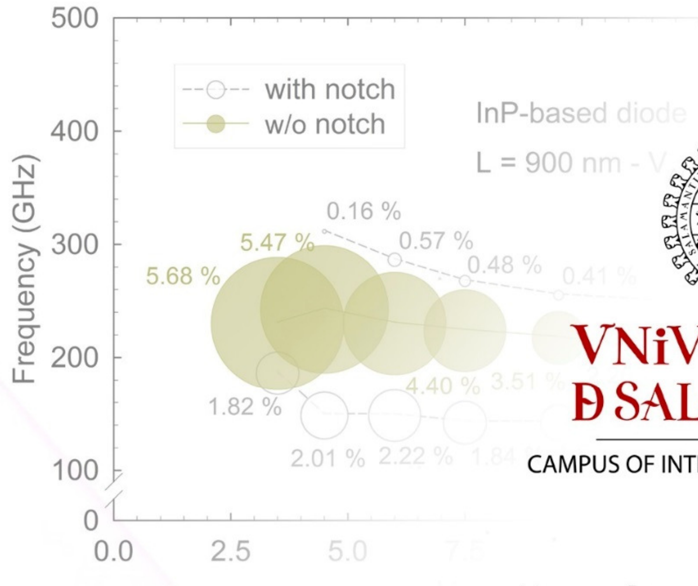

VNiVERSiDAD
Đ SALAMANCA
CAMPUS OF INTERNATIONAL EXCELLENCE

Faculty of Sciences
Department of Applied Physics

Monte Carlo Analysis of Gunn Oscillations and Thermal Effects in GaN-Based Devices

Doctoral Thesis

Sergio García Sánchez

Salamanca, 2015

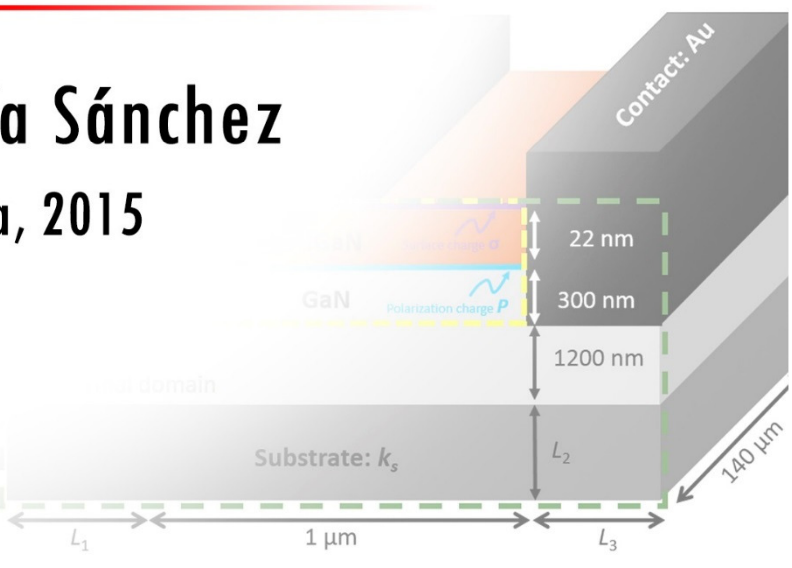
Contact: Au
22 nm
300 nm
1200 nm
GaN
Polarization charge P
Substrate: k_s
L_2
L_1
1 µm
L_3
140 µm

Dª. María Susana Pérez Santos, Profesora Titular de Electrónica del Departamento de Física Aplicada de la Universidad de Salamanca, y

D. Ignacio Íñiguez-de-la-Torre Mulas, Profesor Ayudante Doctor del Departamento de Física Aplicada de la Universidad de Salamanca.

CERTIFICAN:

Que el trabajo de investigación que se recoge en la presente Memoria, titulada *Monte Carlo Analysis of Gunn Oscillations and Thermal Effects in GaN-based devices*, y presentada por **Sergio García Sánchez** para optar al GRADO DE DOCTOR, se ha realizado bajo su dirección en el Área de Electrónica del Departamento de Física Aplicada de la Universidad de Salamanca.

Salamanca, 22 de julio de 2015

María Susana Pérez Santos
Profesora Titular de Electrónica
Departamento de Física Aplicada
Universidad de Salamanca

Ignacio Íñiguez-de-la-Torre Mulas
Ayudante Doctor
Departamento de Física Aplicada
Universidad de Salamanca

A mis padres, a mis hermanos, a mi abuelo.

A quien anima mis días.

I thought it was an adventure, but in reality it was life.

Joseph Conrad.

Agradecimientos - Remerciements

En primer lugar me gustaría manifestar mi más sincero agradecimiento a los directores de esta tesis, Mª Susana Pérez e Ignacio Íñiguez de la Torre, por toda su desinteresada ayuda, permanente dedicación, disponibilidad, atención, paciencia y trato próximo. Gracias por vuestra confianza.

En segundo lugar, agradezco de igual modo a Tomás González y Javier Mateos todas sus valiosas sugerencias, acertados aportes, rigor científico y su participación activa a lo largo de este estudio. Gracias.

Al resto de miembros del Área de Electrónica de la Universidad de Salamanca, Manuel Gutiérrez, María Jesús Martín, Jesús Enrique Velázquez, Yahya Meziani, Óscar García, Vincent Talbo y José Manuel Iglesias. Especial agradecimiento a mis compañeros de despacho Beatriz García, Elena Pascual y Raúl Rengel. A todos vosotros, los que me habéis ayudado a preparar las horas de docencia, con la explicación los experimentos, resolución de dudas, etc., gracias.

Un agradecimiento para Ana Íñiguez de la Torre, David Aurelio, y especialmente, a Diego Pardo por todo su apoyo y ánimo siempre que hemos tenido ocasión de coincidir para *charlar* un poco. Gracias también a toda la gente de la Universidad de Salamanca que me ha prestado ayuda siempre que lo he necesitado.

Agradezco a mis hermanos, Manuel, Rosa María y Alicia García, a mi abuelo Esteban Sánchez, y a mis padres el haber estado pendientes de mí, a mi lado, brindándome su apoyo, de una u otra forma, siendo algo tan imprescindible para poder llevar a buen puerto todos mis sueños.

Especial agradecimiento a todas mis amigas y amigos, de quienes jamás podría olvidarme, especialmente a David Ares, Astrid, Alejando Mulero, Bea Martín, Carolina Fernández, José Miguel Rodríguez y Charlie. Gracias a mis compañeros de Inglés y Francés por sus ánimos. A Mercedes Cruz, por su ánimo y ayuda durante estos últimos años.

Mi más sincero agradecimiento al futuro Doctor en Historia del Arte y mi gran amigo, José María Vicente, con quien he compartido viajes y las mayores locuras que jamás

hubiera pensado. Estos años no hubieran sido lo mismo si tú no hubieras estado a mi lado. ¡Gracias, Chemita!

Pour conclure, j'aimerais remercier tous les membres de l'Institut d'Électronique du Sud (Montpellier), en particulier Luca Varani et Jérémie Torres, pour m'avoir accueilli dans leur groupe de recherche. Merci infiniment.

Je remercie aussi l'Institut D'Électronique de Microélectronique et de Nanotechnologie (IEMN) de Lille, pour m'avoir fourni des mesures expérimentales intégrées dans cette thèse.

Je remercie également toutes les personnes que j'ai connues à Montpellier et avec lesquelles j'ai voyagé, je suis sorti, j'ai pris un café, je suis allé à la patinoire, je suis allé à la plage, je me suis perdu, etc.

Merci à Jean François et à Aurelie Millithaler-Dantigny pour votre aide inconditionnelle quand je suis arrivé à Montpellier et pendant tout mon stage dans cette ville.

Merci à Virginie Verrez, Jérôme Chartet et Samuel Batch, pour prendre soin de moi quand j'étais malade à Avignon, je vous suis vraiment très reconnaissant. Merci à ma famille française, la famille Audéon, de m'avoir invité chez eux et de rendre possible une nouvelle rencontre après 11 ans. Enfin, je souhaite remercier en particulier David Rayeroux, Kévin Nizet, Santi Chuetor, Carlos Molina et Luis Daniel Castro, que j'espère revoir très bientôt.

ABSTRACT

In recent years, the development of GaN technology has made significant inroads into high-power and high-frequency applications with respect to other semiconductor competitors such as GaAs or InP.

In this dissertation, by means of an in-house Monte Carlo tool, we study the possibility of generating Gunn oscillations through vertical n^+nn^+ (without notch) and $n^+n^-nn^+$ (notched) diodes based on InP and GaN with different lengths of the active region and two doping profiles. In general, when the notch accomplishes its role of fixing the onset of charge accumulation near the cathode, the oscillations are of lower frequency and power. For InP-based diodes, the fundamental frequency reaches 140 GHz (notched, L=1.2 µm) and 400 GHz (without notch, L=0.75 µm). For the GaN-based diode with an active length L=1.5 µm, despite the fact that the fundamental harmonic is around 100 GHz, the power spectral density for the 10th harmonic (~1 THz) is still significant. InP diodes with L=0.9 µm offer an efficiency (η) of up to 5.5 % for frequencies around 225 GHz. The generation bands in GaN diodes appear at higher frequencies (up to 675 GHz with η=0.1 %) than in InP.

When circuits work at high powers, thermal models become essential to determine temperature limits with a view to preventing device failure, thus reducing manufacturing costs. In order to include thermal effects in our Monte Carlo code, two techniques have been implemented: (i) a thermal resistance method (TRM), and (ii) an advanced electro-thermal model that solves the steady-state heat diffusion equation, called HDEM. We calibrate/validate our simulator by comparison with experimental measurements of an AlGaN/GaN diode. For the TRM, several thermal resistance values are employed, and for the HDEM different substrates (polycrystalline diamond, diamond, carbide silicon, silicon and sapphire), thicknesses and die lengths are tested. In addition, we include the effect of thermal boundary resistance. Using temperature-independent thermal conductivity in the HDEM allows us to extract an equivalent thermal resistance, R_{th}, for each geometry and substrate material. The extracted R_{th} values are constant with the dissipated power, P_{diss}. However, when a more real temperature-dependent thermal conductivity is employed, R_{th} exhibits a strong dependence on P_{diss}. As final test device, we analyse for an HEMT, the effect of (i) the heat-sink temperature and (ii) gate-length, through electro-thermal simulations.

CONTENTS

Contents 13

Abbreviations and notations 17

List of Figures..21

List of Tables..31

Introduction..33

Chapter 1: Theoretical concepts and modelling tools 45

- 1.1. Gunn Effect..45
  - 1.1.1. Explanation of the phenomenon 46
  - 1.1.2. Dynamics of domain formation in Gunn Diodes..48
  - 1.1.3. Modes of operation of Gunn diodes..52
    - (a) Transit-time dipole-layer mode 52
    - (b) Accumulation-layer mode..53
- 1.2. The Monte Carlo tool 54
  - 1.2.1. Overview..54
  - 1.2.2. Monte Carlo method: inverse transform..55
  - 1.2.3. Single-particle Monte Carlo technique..56
    - (a) Scattering mechanisms 58
    - (b) Semiconductor properties 61
      - (b.1) Indium Phosphide (InP)..61
      - (b.2) Gallium Nitride (GaN)..65
      - (b.3) Aluminium Gallium Nitride ($Al_{0.27}Ga_{0.73}N$)..68
  - 1.2.4. Device simulator 70
    - (a) Physical restrictions 73
    - (b) Modes of operation and analysis of results..74
    - (b.1) Average and instantaneous magnitudes 74
      - (b.2) DC operation mode..74
      - (b.3) DC + AC operation mode..76

(b.4) RLC operation mode 77

(c) The Ramo-Shockley theorem and Fast Fourier Transform (FFT) 78

(c.1) The Ramo-Schockley theorem 78

(c.2) Fast Fourier Transform (FFT) 80

Chapter 2: Comparison of the performance of InP- and GaN-based Gunn Diodes 85

2.1. State of the art 85

2.1. Geometry of vertical diodes 90

2.2. DC bias 92

2.2.1. InP diodes with DS1 92

2.2.2. GaN diodes with DS1 and DS2 97

2.3. DC + AC bias 100

2.3.1. Equivalence of the RLC circuit and single-tone excitation 101

2.3.3. Dependence of efficiency on length, bias conditions and material 103

2.3.4. Results for DS2 108

2.4. Effect of operating temperature 110

2.5. Conclusions 112

Chapter 3: Electro-thermal MC simulations of GaN-based devices 115

3.1. State of the art: Modelling of thermal effects 116

3.2. Self-consistent electro-thermal algorithms 121

3.2.1. Thermal resistance method (TRM) 123

3.2.2. Heat Diffusion Equation Model (HDEM) 124

3.3. Two-terminal devices: diode 129

3.3.1. Isothermal simulations 132

3.3.2. Electro-thermal simulations 135

(a) Thermal resistance method (TRM) 135

(b) Heat Diffusion Equation Model (HDEM) 136

(b.1) Extraction of R_{th} from HDEM 138

(b.2) Dependence on k_s 139

(b.3) Dependence on die lengths (L_1, L_2) ... 141

(b.4) Design rules based on L_1, L_2 and k_s ... 142

(b.5) Thermal boundary resistance (TBR) ... 143

(b.6) Temperature-dependent thermal conductivity ... 146

3.4. Three-terminal device: HEMT ... 150

3.4.1. Isothermal simulations ... 154

3.4.2. Electro-thermal simulations ... 155

(a) Heat-sink temperature analysis ... 161

(b) Gate-length analysis ... 163

(c) Temperature-dependent thermal conductivity ... 166

3.5. Conclusions ... 169

Conclusions and future work ... 173

Conclusions ... 173

Future work ... 174

Appendix. Measurements of HEMTs ... 177

Bibliography ... 185

ABBREVIATIONS AND NOTATIONS

Abbreviations

AC	Alternating current
AlGaAs	Aluminium gallium arsenide
AlGaN	Aluminium gallium nitride
CMOS	Complementary metal-oxide-semiconductor
DUT	Device under test
DC	Direct current
DS1	Doping scheme 1
DS2	Doping scheme 2
DHBT	Double heterojunction bipolar transistor
FFT	Fast Fourier transform
FEM	Finite element method
FDM	Finite difference method
FMA	Frequency of maximum amplitude
FME	Frequency of maximum efficiency
GaAs	Gallium arsenide
GaN	Gallium nitride
HDE	Heat diffusion equation
HDE-MC	Heat diffusion equation - Monte Carlo
HDEM	Heat diffusion equation model
HBVD	Hetero-barrier varactor diodes
HEMT	High-electron-mobility transistor
IMPATT	Impact ionization avalanche transit-time
InAlAs	Indium aluminium arsenide

InGaAs	Indium gallium arsenide
InGaN	Indium gallium nitride
InP	Indium phosphide
LED	Light-emitting diode
LSA	Limited-space-charge accumulation
LU	Lower-upper
MODFET	Modulation-doped field-effect transistor
MMIC	Monolithic millimetre wave integrated circuit
MC	Monte Carlo
NDR	Negative differential resistance
PDR	Percentage of diffusive reflections
PS	Poisson solver
PCD	Polycrystalline diamond
PSD	Power spectral density
RF	Radio frequency
Re(Z)	Real part of the impedance
RTD	Resonant-tunnelling diode
Al_2O_3	Sapphire
SSD	Self-switching diode
Si	Silicon
SiC	Silicon carbide
SLED	Super lattice electronic device
SRS	Surface roughness scattering
THz	Terahertz
TBR	Thermal boundary resistance

TRM	Thermal resistance method
3-D	Three-dimensional
TED	Transferred-electron device
TUNNETT	Tunnel injection transit-time
2-D	Two-dimensional
2DEG	Two-dimensional electron gas
w/o	Without

Relevant notations

E_0	Average electric field
N_D	Carrier concentration
η	DC to AC conversion efficiency
L_{eff}	Dead length
λ_d	Debye’s length
ε_{SC}	Dielectric permittivity
τ_d	Dielectric relaxation time
μ_{dif}	Differential mobility
D_n	Diffusion constant for electrons
P_{DC}	Dissipated power
V_{DS}	Drain-to-source bias
L_{eff}	Effective length
m^*	Effective mass
μ_0	Electron mobility
f	Frequency
$\Delta\nu$	Frequency resolution
V_{GS}	Gate-to-source bias

V_{MC}	Intrinsic Monte Carlo bias
T_{latt}	Lattice temperature
L	Length of the active region
ω_p	Plasma frequency
P	Polarization charge
$P(\nu)$	Power spectral density or energy spectral density
Q	Quality factor
v_{sat}	Saturation velocity
n_s	Sheet carrier density
R_s	Square resistance
σ	Surface charge density
$T_{heat\text{-}sink}$	Temperature of the heat sink
k	Thermal conductivity
R_{th}	Thermal resistance
E_T	Threshold electric field
V_{th}	Threshold voltage
P_{AC}	Time-average AC power
Δt	Time step
v_d	Total average drift velocity
θ	Transformed or apparent temperature
n_0	Uniform equilibrium concentration
λ	Wave length

LIST OF FIGURES

Figure 1: Global GaN semiconductor device market size and forecast, 2011 - 2019 (UDS million). Source: Transparency Market Research Journals. White papers, Primary Interviews. 33

Figure 2: Electromagnetic Spectrum..35

Figure 3: State-of- the-art results from transistor amplifiers, transistor oscillators, and selected active two-terminal devices in the 100-1000 GHz frequency range at room temperature (28). 37

Figure 4: Surface temperature distribution in a double-finger AlGaN/GaN HEMT measured with an infrared microscope (QFI Infrascope II). http://web.mit.edu/kbagnall/www/research.htm..40

Figure 5: Schematic of a vertical Gunn diode. 41

Figure 6: Temperature distribution in an HEMT. 42

Figure 1. 1: (a) Energy band structures of GaAs. (b) Occupation of high valleys. 47

Figure 1. 2: Schematic of the *v*-*E* characteristic showing negative differential mobility for electric fields between E_{th} and E_s. 48

Figure 1. 3: Demonstration of domain formation. (a) *v*-*E* relationship and some critical points. (b) A small dipole grows to (c) a mature domain. (d) Current (Gunn) oscillations. Between t_1 and t_2, the matured domain is annihilated at the anode and another is formed near the cathode (87). 49

Figure 1. 4: Formation of a dipole. Electric field and carrier concentration. 53

Figure 1. 5: Accumulation-layer transit mode under time-invariant terminal voltage (87). 53

Figure 1. 6: Rejection sampling. 56

Figure 1. 7: Simple diagram of the particle motion in real space under a uniform electric field applied in the *x* direction. 57

Figure 1. 8: Flow-chart of the single particle program. 58

Figure 1. 9: Scattering mechanism depending on the physical origin. 60

Figure 1. 10: Band structures of indium phosphide. 62

Figure 1. 11: Microscopic magnitudes calculated at room temperature *vs.* the electric field for InP. (a) Average velocity, (b) valley-occupation, (c) average kinetic energy, and (d) effective mass. A doping of 10^{15} cm^{-3} was employed. 64

Figure 1. 12: Band structures of gallium nitride. 65

Figure 1. 13: Microscopic magnitudes calculated at room temperature *vs.* the electric field for the GaN material. (a) Average velocity, (b) valley-occupation, (c) average kinetic energy, and (d) effective mass. 67

Figure 1. 14: Flow-chart of the two-dimensional MC program. 72

Figure 1. 15: 2D device simulation scheme. 73

Figure 1. 16: (a) DC, (b) DC+AC and (c) RLC modes of operation scheme. 75

Figure 1. 17: Average and instantaneous values. 75

Figure 1. 18: Calculation of the Current PSD from long-time sequences of current density by employing the FFT. Definition of the Frequency of Maximum Amplitude (FMA). 75

Figure 1. 19: (a) DC to AC conversion efficiency, and (b) FME and corresponding efficiency. 76

Figure 1. 20: Schematic representation of electrodes, charges and currents (80). 79

Figure 2. 1: Geometry of the two types of Gunn structures studied. (a) Diode without notch and (b) diode with a 250 nm-length notch placed next to the cathode. The lengths of n^+ contact regions are 100 nm and 300 nm at the cathode and anode, respectively, in both structures. n^+=2×10^{18} cm^{-3}, DS1: n=1×10^{17} cm^{-3} and n^-=2×10^{16} cm^{-3} and DS2: n=5×10^{17} cm^{-3} and n^-=1×10^{17} cm^{-3}. Four different lengths, L=1500, 1200, 900 and 750 nm were simulated, always at room temperature. 91

Figure 2. 2: (a) *I-V* curves for the two types of InP diodes, with and w/o notch, and for four different lengths of the active region, L=750 nm, 900 nm, 1200 nm and 1500 nm, for the DS1. (b) Time-sequences of current density for the structure w/o notch with L=1500 nm for V=2.5 V, 5 V, 7.5 V and 10 V. 93

Figure 2. 3: Current PSD for InP-based diodes (with and w/o notch) with *L*=1500 nm for a bias *V*=5 V. 94

Figure 2. 4: FMA$_1$ and corresponding amplitude of the current PSD *vs.* the bias for InP-based diodes (with and w/o notch) with *L*=1500 nm and for the DS1. 94

Figure 2. 5: FMA$_1$ for $V > V_{th}$ *vs.* bias for different lengths of the active region: *L*=750 nm, 900 nm, 1200 nm and 1500 nm in an InP-based diode for the DS1. (a) Structures w/o notch and (b) structures with notch. 95

Figure 2. 6: (a) Time-sequence of current density, where coloured circles mark the equidistant time moments when the instantaneous profiles of (b) the carrier concentration and (c) the electric field are recorded for a 1.5 µm length InP diode w/o notch and with 8 V applied between contacts. 96

Figure 2. 7: (a) FMA$_n$ and (b) corresponding amplitude of the PSD for the different harmonics n (up to the fifth if it exists) *vs.* bias in an InP diode with length *L*=1500 nm for DS1. The results in structures with and w/o notch are represented by dashed and solid lines, respectively. 97

Figure 2. 8: *I-V* curves for the two types of GaN-diodes, with and w/o notch, and for four different lengths of the active region, *L*=750 nm, 900 nm, 1200 nm and 1500 nm. (a) DS1 and (b) DS2. 97

Figure 2. 9: Current PSD for GaN-based diodes (with and without notch) with *L*=1500 nm for a bias *V*=80 V. (a) DS1, (b) DS2. 99

Figure 2. 10: FMA$_3$ and (b) corresponding amplitude of the PSD *vs.* bias in a GaN diode with length *L*=1500 nm for the DS1 and DS2. Structures with and w/o notch results are represented by dashed and solid lines, respectively. 99

Figure 2. 11: FMA$_1$ for $V > V_{th}$ *vs.* bias for different lengths of the active region (*L*=1500 nm, 1200 nm, 900 nm and 750 nm) in a GaN-based diode with DS2. (a) Structures w/o a notch, (b) structures with a notch. 100

Figure 2. 12: RLC modes of the operation scheme. 101

Figure 2. 13: Time-sequences of current density j_d and applied voltage V_d (t) in a InP n^+nn^+ diode using the DS1 and V_{DC}=7.5 V. (a) Resonant RLC circuit in series with the diode

(R=3x10^{-9} Ωm^2, L=4.7x10^{-23} Hm^2, and C=0.0081F/m^2) and (b) excitation by means of a single tone of frequency of 243 GHz and V_{AC}=1.9 V [Eq. (II.1)]. 103

Figure 2. 14: (a) DC to AC conversion efficiency *vs.* frequency for InP-based diodes (with and w/o notch) with L=900 nm and for the DS1. Single-tone excitation with V_{DC}=12 V and V_{AC}=1.5 V. (b) Real part of the impedance. 104

Figure 2. 15: FME and corresponding efficiency of the different generation bands found in diodes with the DS1 with and w/o notch. The size of the bubbles scales with the maximum of the DC to AC conversion efficiency, η, is indicated for the different generation bands. The dependence on the length of the active region is shown for (a) InP diodes using V_{DC}=12 V and V_{AC}=1.5 V and (b) GaN diodes using V_{DC}=70 V and V_{AC}=10 V. (c) Dependence on the DC bias for L=900 nm and using an AC excitation of V_{AC}=1.5 V for InP and V_{AC}=10 V for GaN. 105

Figure 2. 16: (a) DC to AC conversion efficiency *vs.* frequency for GaN-based diodes (with and w/o notch) with L=1200 nm and for the DS1. Single-tone excitation with V_{DC}=70 V and V_{AC}=10 V. (b) Instantaneous profiles of the carrier concentration along the diode corresponding to a given time within one period of the AC signal for the frequencies at the maximum of the emission bands of FME=175, 318.7, 475 and 637.5 GHz. 107

Figure 2. 17: Results for a GaN diode (with and w/o notch) when DS2 is considered. Dependence of the FME and corresponding efficiency of the different generation bands on (a) the length of the active region (V_{DC}=70 V and V_{AC}=10 V) and (b) DC bias for L=900 nm, using V_{AC}=10 V. The size of the bubbles scales with the maximum of the DC to AC conversion efficiency, η, and is indicated for the corresponding generation band...... 108

Figure 2. 18: (a) Average electric field and (b) U-valley occupation *vs.* position at 25 V for a GaN-based diode with notch with L=900 nm for the DS1 and DS2 schemes............ 109

Figure 2. 19: DC to AC conversion efficiency *vs.* frequency for a GaN-based diode with notch with L=900 nm and for the DS2 and with V_{DC}=70 V. The AC excitations used are V_{AC}=10 V, 8.5 V and 6.5 V. The inset shows the DC to AC conversion efficiency *vs.* frequency for an InP-based diode with notch with L=900 nm, and with V_{DC}=4.5 V. The AC excitations used are V_{AC}=1.5 V and 1.0 V 110

Figure 2. 20: (a) Current power spectral density at 77 V and (b) DC to AC conversion efficiency *vs.* frequency at V_{DC}=70 V and V_{AC}=10 V. A GaN-based diode with notch (DS2), L=0.9 µm and two operating temperatures, 300 K and 500 K, is considered. 111

Figure 3. 1: Flow chart of the electro-thermal simulations. 122

Figure 3. 2: Flow chart of subroutine TRM. 123

Figure 3. 3: Scheme of the electronic and thermal domains. 123

Figure 3. 4: Flow-chart of the HDEM subroutine. 125

Figure 3. 5: Scheme of the resolution of the HDE. 126

Figure 3. 6: (a) AlGaN/GaN diode geometry under study. The area limited by yellow corresponds to the electronic simulated region of the diode and the region limited by green is the thermal domain. (b) Experimental measurements of the *I-V* curve. 129

Figure 3. 7: Simulations of the electronic domain of Figure 3. 6 to analyse the effect on the *I-V* of (a) P and σ (T=300 K and PDR=0 %), (b) the PDR (T=300 K, P=12.12×10^{12} cm^{-2} and σ = -4×10^{12} cm^{-2}) and (d) the lattice temperature (P=12.12×10^{12} cm^{-2}, σ = -4×10^{12} cm^{-2} and PDR=3 %). For the sake of comparison, the experimental values at 300 K are also plotted. (c) Mobility of electrons in the diode as a function of PDR (T=300 K, P=12.12×10^{12} cm^{-2} and σ = -4×10^{12} cm^{-2}). 133

Figure 3. 8: *I-V* curves obtained with the TRM with the thermal resistances indicated in Table 3. 2. The experimental results are also included. The background colours represent the lattice temperature for each bias point according to the Eq. (III.1) in the case of R_{th-2}. 135

Figure 3. 9: (a) *I-V* curve of the diode, showing the results of an initial isothermal simulation and of successive iterations towards convergence of the HDEM. Results for the diode presented in Figure 3. 6. 137

Figure 3. 10: (a) *I-V* curves obtained with the TRM with the thermal resistances indicated in Table 3. 2. The results obtained with the HDEM are also presented. The inset shows the average temperature in the electronic domain of HDEM compared with the TRM temperature at different applied bias. (b) Spatial distribution of the lattice temperature in the electronic domain and (c) in the thermal domain, when the bias is V_{MC}=4 V. 137

Figure 3. 11: (a) *I-V* curves for the TRM (R_{th}=14.07x10^{-3}K·m/W) and the HDEM. The inset shows temperature (average for the HDEM) *vs.* bias. (b) Average temperature, T_{av}, *vs*. dissipated power and linear fitting to extract the corresponding thermal resistance. The solid lines in Figure 3. 11 (a) correspond to the results obtained with the TRM for the estimated thermal resistance. L_1=200 µm, L_2=300 µm and k_s=156 W/(K·m) are considered. 138

Figure 3. 12: (a) Symbols show the *I-V* curves for different substrates: PCD, diamond, silicon carbide, silicon and sapphire. (b) Analysis to evaluate the influence of k_s in the simulations. Average temperature, T_{av}, *vs*. dissipated power and linear fitting to extract the corresponding thermal resistance. The inset shows R_{th} *vs.* 1/k_s. L_1=200 µm and L_2=300 µm. The solid lines of Figure 3. 12 (a) correspond to the results obtained with the TRM for the estimated thermal resistances. 139

Figure 3. 13: Temperature distribution, for a bias of 6 V, to evaluate the influence of k_s: PCD, 2200 W/(K·m); silicon, 156 W/(K·m) and sapphire, 42 W/(K·m) in the simulations. Thermal domain (a), (c) and (e), and electronic domain (b), (d) and (f). L_1=200 µm and L_2=300 µm. 140

Figure 3. 14: Profile of the increase in lattice temperature (ΔT=T_{latt}-T_h) for three different *y*-positions [channel, MC-HDE domain interface and buffer-substrate interface, see Figure 3. 6 (a)] for a bias of 6 V. 141

Figure 3. 15: (a) R_{th} *vs.* the die dimension L_1 for L_2=250 µm, 300 µm and 350 µm. (b) a) R_{th} *vs.* die dimension L_2 for L_1=200 µm. The substrate employed is Si. 142

Figure 3. 16: Systematic analysis to evaluate the influence of k_s, L_1 and L_2 in the simulations. (a) The symbols show the *I-V* curves when the HDEM is employed. The inset shows the variation in the average temperature with respect to the reference diode. (b) T_{av} *vs*. dissipated power and linear fitting to extract the corresponding thermal resistance. The solid lines in Figure 3. 16 (a) correspond to the results obtained with the TRM for the estimated thermal resistances. 142

Figure 3. 17: AlGaN/GaN diode geometry under study. The location of the TBR is indicated. 144

Figure 3. 18: T_{av} *vs*. P_{diss} for three substrates (a) SiC, (b) Si and (c) sapphire. A TBR layer of Δ_{TBR}=15 nm with k_{TBR} =1 and 0.1 W/(K·m) is studied. Note that the case without the TBR layer from Figure 3. 12 is included for the sake of comparison. The insets show the profile of the lattice temperatures in the middle of the diode close to the TBR region for a bias of 10 V. 145

Figure 3. 19: Profile of the lattice temperatures in the middle of the diode close to the TBR region, for a bias of 10 V when we set TBR=15x10^{-8} m^2·K/W. Sets of pairs Δ_{TBR}=15 nm, k_{TBR}=0.1 W/(K·m); Δ_{TBR}=9 nm, k_{TBR}=0.06 W/(K·m) and Δ_{TBR}=3 nm, k_{TBR}=0.02 W/(K·m). 146

Figure 3. 20: Thermal conductivity: $k_i \sim AT^{-\alpha}$ for the reported values in the literature: (a) GaN: A=4400 W·$K^{0.4}$·cm^{-1} and α=1.4 (170), and in (144) A=15 W·$K^{-0.57}$·cm^{-1} and α=0.43, A=2100 W·$K^{0.2}$·cm^{-1} and α=1.2. (b) Si: A=2590 W·$K^{0.3}$·cm^{-1} and α=1.3 (67). (c) Au: A=3.846 W·$K^{-0.965}$·cm^{-1} and α=0.035 (67). (d) For AlGaN, k is almost constant within the 300 K - 400 K, 30 W/(K·m) range. The thermal conductivity, when the same functional α=1.3 is considered, is also plotted (crosses) for all materials satisfying Eq. (III.25).....147

Figure 3. 21: T *vs.* Θ when Eq. (III.25) is satisfied...148

Figure 3. 22: (a) *I-V* curves for the diode presented in Figure 3. 6 using the temperature-dependent thermal conductivity model. The experimental measurements and the calculations with constant thermal conductivity are also included for the sake of comparison. The inset shows the T_{av} *vs*. dissipated power for the reference structure and the temperature-dependent thermal conductivity model. (b) Profile of temperature along a vertical section (*x*-length=1 µm) for constant conductivity and the temperature-dependent model using Eq. (III.25) at V_{MC}=10 V. Inset: Zoom of the electrical domain (shadowed region) with the carrier concentration on the right axis (for the temperature-dependent thermal conductivity model). 148

Figure 3. 23: *I-V* curves with and w/o TBR. The inset shows the TBR [Eq. (III.24)] *vs. T* when the thermal conductivity of Eq. (III.25) is considered. 149

Figure 3. 24: AlGaN/GaN HEMT geometry under study. The gate has a length of 250 nm. The area limited in yellow corresponds to the electronic simulated region of the diode and the region limited in green is the thermal domain. 151

Figure 3. 25: (a) Output characteristics (top curve V_{GS}=-2 V, step 1.0 V). (b) Transfer characteristics, (c) transconductance g_m *vs.* V_{GS}, and (d) g_d *vs.* V_{GS} for V_{DS}=3 V, 6 V and 8 V. 152

Figure 3. 26: Spatial profiles of (a) electron concentration, (b) energy, (c) longitudinal velocity, and (d) rates of optical polar phonon scatterings for V_{DS}=8 V V_{GS}=-2 V in the HEMT. The position of the gate contact is also indicated. 154

Figure 3. 27: (a) Transfer characteristics and (b) transconductance g_m *vs.* V_{GS} for V_{DS}=3 V, 6 V and 8 V of HEMTs with the geometry of Figure 3. 24. In both graphics, isothermal simulations at 300 K, 500 K and 700 K are taken into account. 155

Figure 3. 28: (a) I_D-V_{DS} characteristics of the HEMT of Figure 3. 24. Lines: HDEM, symbols: TRM (R_{th}=14.25x10^{-3} K·m/W). (b) Average (dashed lines) and peak (solid lines) temperature with HDEM. Temperature when the TRM is used (symbols). For the HDEM L_1=L_3=200 µm, L_2=300 µm and an Si substrate are considered. 156

Figure 3. 29: Drain conductance g_d *vs.* V_{GS} for V_{DS}=3 V, 6 V and 8 V for curves obtained with the HDEM. 156

Figure 3. 30: Average temperature *vs.* dissipated power for the results of Figure 3. 28 (a). 157

Figure 3. 31: Comparison of isothermal simulations and results obtained on employing the HDEM. (a) Transfer characteristics, (b) transconductance g_m, (c) temperature *vs*. dissipated power and (d) temperature *vs.* V_{GS} (HDEM simulation). V_{DS}=6 V. The inset in Figure 3. 31 (c) shows the equivalence between the HDEM and the TRM. 158

Figure 3. 32: Temperature profile in the channel for the HDEM and TRM *vs*. horizontal length at V_{DS}=6 V and V_{GS}=-4.2 V. 159

Figure 3. 33: Mobility of electrons in a diode as a function of temperature (PDR=0 %, P=14.12×10^{12} cm^{-2}and σ = -4×10^{12} cm^{-2}). 159

Figure 3. 34: Microscopic characteristics in channel *vs*. horizontal length at V_{DS}=6 V and V_{GS}=-4.2 V. (a) Energy, (b) velocity and (c) optical polar phonon scattering rate. 160

Figure 3. 35: Comparison between the HDEM and the TRM when heatsinks with temperatures of 50 K, 100 K, 200 K and 300 K are considered. (a) Transfer characteristics of the current density I_D. The inset shows the average temperature *vs.* dissipated power. (b) Transconductance g_m. *vs.* V_{GS}. V_{DS}=6 V. 161

Figure 3. 36: Temperature profile inside the device along the channel for the HDEM *vs*. horizontal length at V_{DS}=6 V and V_{GS}=-4.2 V. Two heat sinks of temperatures 50 K and 100 K are considered..162

Figure 3. 37: Microscopic characteristics of the carrier concentration and velocities through the channel for the particular case in which the same dissipated power of 10950 W/m is obtained. We consider heat sinks with temperatures of 50 K (V_{GS}=-2.8 V, V_{DS}=6 V) and 300 K (V_{GS}=-4.6 V, V_{DS}=6 V), respectively...162

Figure 3. 38: AlGaN/GaN HEMT geometry under study. The HEMT on the left has a gate-length of 125 nm, and the HEMT on the right has a gate-length of 60 nm. The area limited by yellow corresponds to the electronic simulated region of the diode and the region limited by green is the thermal domain..163

Figure 3. 39: Comparison of transfer characteristics of HEMT-L$_g$250, HEMT-L$_g$125 and HEMT-L$_g$60 when isothermal (at 300 K) and electro-thermal (HDEM) simulations are performed. (a) I_D *vs.* V_{GS}. (b) g_m. V_{DS}=6 V. 164

Figure 3. 40: Microscopic characteristics in the channel *vs*. horizontal length at V_{DS}=6 V and V_{GS}=-3 V. Isothermal (300 K) and electro-thermal (HDEM) simulations are compared. (a) Carrier concentration. (b) Velocity. The vertical dashed line indicates the end of the gate...165

Figure 3. 41: (a) Peak temperature *vs.* V_{GS}. (b) Position where hot spots are located with respect to the gate *vs.* V_{GS}. V_{DS}=6 V...166

Figure 3. 42: Carrier concentration in the channel *vs*. horizontal length at V_{DS}=6 V and V_{GS}-6 V and -3 V for the HEMT with a gate length of 250 nm.......................................166

Figure 3. 43: Average temperature *vs.* dissipated power (V_{GS} is swept from -2 V to -9 V) for the two models: temperature-independent thermal conductivity *vs.* temperature-dependent thermal conductivity. 167

Figure 3. 44: Temperature-independent *vs.* temperature-dependent thermal conductivity models. (a) Transfer characteristics I_D *vs.* V_{GS}. The inset shows the average temperature *vs.* $V_{GS.}$ (b) Transconductance g_m. V_{DS}=6 V.. 168

Figure A. 1: Geometry of the HEMTs. HEMT A (left), HEMT B (right) characterized. ... 177

Figure A. 2: Experimental measurements. Current density I_D *vs.* drain-to-source bias V_{DS}. 178

Figure A. 3: Experimental measures of HEMTs A and B of wafer 1. Current density I_D *vs.* drain-to-source bias V_{DS} when V_{GS} is swept from 0 V to -6 V, ΔV=1 V. I_D *vs.* V_{GS} for V_{DS}=2 V, 3 V, 4 V and 5 V. Transconductance g_m *vs.* V_{GS} for V_{DS}=5 V. 179

LIST OF TABLES

Table 1: Some electronic sources at THz frequencies. 36

Table 1. 1: Conditions for Gunn oscillations for GaAs, InP and GaN materials (87,88)...52

Table 1. 2: InP electron properties. 63

Table 1. 3: GaN electron properties..66

Table 1. 4: $Al_{0.27}Ga_{0.73}N$ electron properties. 69

Table 2. 1: Debye length for the different doping levels under analysis.........................91

Table 2. 2: τ_d and ω_p for different doping levels, where InP and GaN are taken into account. 92

Table 2. 3: Recapitulation of the main results obtained in Chapter 2...........................113

Table 3. 1: Electro-thermal simulators, institutions and researchers that employ them. 118

Table 3. 2: Values of the thermal resistances used in the TRM. 135

Table 3. 3: Values of the thermal conductivity at 300 K used in the simulation for the different materials. 136

INTRODUCTION

In the last decade, Gallium Nitride (GaN) semiconductors and their alloys (AlGaN, InGaN) have emerged as the most promising materials for applications at high power and microwave frequencies (1-3). This has led to much effort being devoted to the study of this technology, and in the future huge further investment is anticipated. In order to provide some data, we focus our attention on the trends and forecasts published by the Transparency Market Research (4). According to this, the global GaN semiconductor devices market was US$ 379.82M in 2012, and it is estimated to reach US$ 2,203.73M by the end of 2019, as shown in Figure 1.

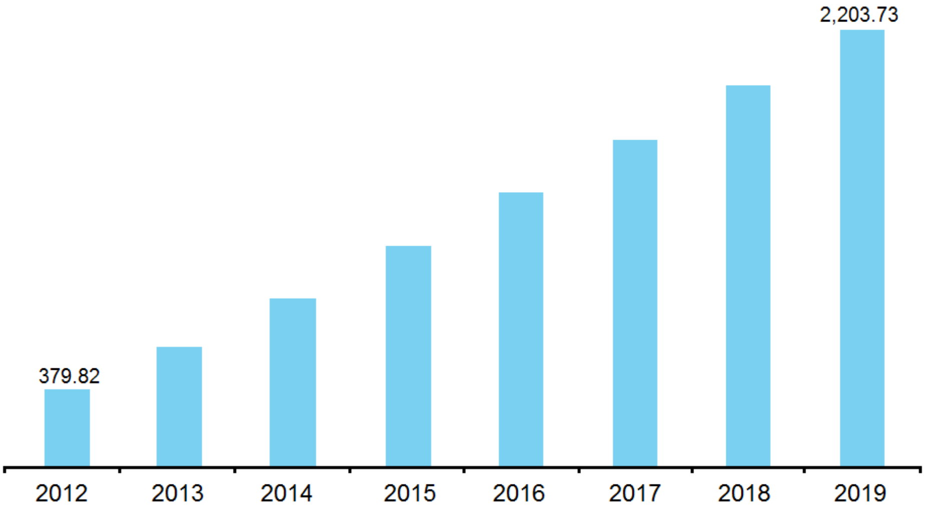

Figure 1: Global GaN semiconductor device market size and forecast, 2011 - 2019 (UDS million). Source: Transparency Market Research Journals. White papers, Primary Interviews.

The high breakdown electric field of GaN (~3.3 MV/cm) makes it an excellent material for working at very high powers, as GaN-based devices can simultaneously support high current (~10 A) and high voltages (~100 V) (1,5-8). This material has another advantage with respect to other competitors because it can be combined with silicon-based substrates that have excellent thermal conductivities (1). In addition, when higher temperatures are involved, some properties of nitrides, such as their elevated chemical and thermal stability and radiation hardness, make them robust and ideal candidates for work in aggressive environments (9,10).

GaN has potential and current uses in a wide range of applications. Initially, it seemed that GaN technology would only be affordable mainly for military purposes, and it was limited in civilian use. However, the evolution of the technology and the reduction in materials costs have made GaN-based devices an economical option even for commercial use.

GaN circuits can cover a huge working frequency band(1). The rise in communication technologies has encouraged research into and the development of power amplifiers in the micro-wave range, where high power amplification is required. The key applications in this area are mainly commercial wireless infrastructures (base stations), broadband radar systems and narrow band general purpose amplifiers, and public mobile radios (12-15). The applications of GaN are also suitable for the manufacture of laser diodes emitting in the ultraviolet (16). The near ultra-violet spectral range can be accessed using a GaN or an InGaN active region, from 363 nm (GaN) to longer wavelengths (16). Furthermore, the alloy indium gallium nitride (InGaN) is the light-emitting layer in modern blue and green LED_S and it is often grown on a GaN buffer on a transparent substrate (Si or SiC). To sum up, thanks to GaN technology, the invention of efficient blue light-emitting diodes has been possible, enabling bright and energy-saving white light sources. For this discovery, the Nobel Prize in Physics 2014 was awarded jointly to Isamu Akasaki, Hiroshi Amano and Shuji Nakamura. Some applications of LEDs include backlights for mobile appliances, traffic signals, displays, or automotive applications.

Thus, within the current context of great interest in GaN-based devices, this dissertation aims to explore Gunn diodes as submillimeter-frequency power sources and to develop an efficient electro-thermal simulator able to analyse thermal issues in high-power HEMTs. Below we shall briefly discuss these two main topics.

---

[1] Satellite or radar communications operate in a range of frequencies from hundreds of MHz to ten GHz, reaching up to the terahertz region (11).

Sources in the THz range

An existing challenge in high-frequency (high-speed) electronics is the use of GaN to make solid-state devices with the main objective of obtaining sources, amplifiers and detectors in the THz range (17-19). The wavelength of radiation in the terahertz band (T-rays) is located in the electromagnetic spectrum between microwaves and infrared frequencies (100 GHz < f < 10 THz, 3 mm > λ >30 μm) (20), as can be observed in Figure 2. In other words, it is located between the limits of the Electronics and Optics domains (21-23). In recent years, this frequency band has aroused much scientific interest owing to its multiple potential applications. A significant part of the interest raised by THz radiation is due to its different degree of absorption by many materials of interest. For example, this radiation is able to penetrate a large number of non-conductive materials. It can pass through dielectrics such as clothing, paper, paperboard, wood, walls, plastic and ceramic objects (non-polar molecules) (24). Fog and clouds can also be penetrated, but it is not the case for metal, water or ammonia (polar molecules). As a consequence, THz wavelengths are considered to be of great interest for different applications in diverse fields such as medical imaging, biology, security, telecommunications, pharmacy, sensors, quality control mechanisms and in the aerospace industry, etc. (25-27). Insufficient of THz technology nowadays is due to the lack of compact sources based on solid-state devices able to operate at room temperature. In addition, the low cost, portability and power of such sources devices would make their applications feasible in a broad context.

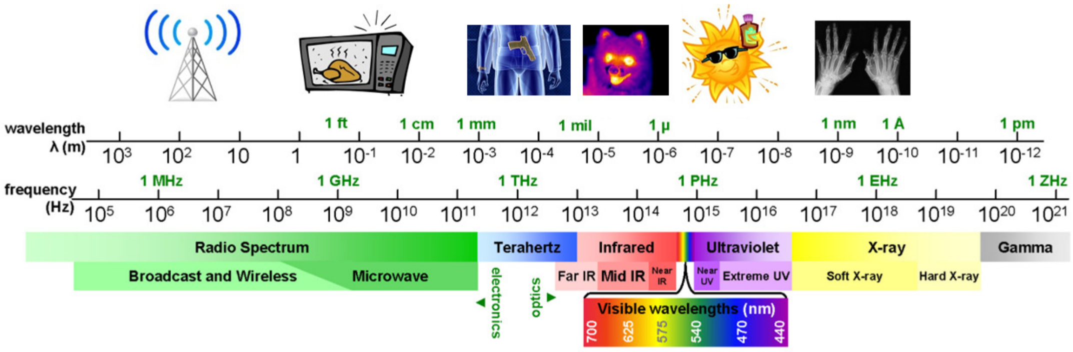
wavelength
λ (m)
1 ft
1 cm
1 mm
1 mil
1 μ
1 nm
1 Å
1 pm
10³ 10² 10 1 10⁻¹ 10⁻² 10⁻³ 10⁻⁴ 10⁻⁵ 10⁻⁶ 10⁻⁷ 10⁻⁸ 10⁻⁹ 10⁻¹⁰ 10⁻¹¹ 10⁻¹²
frequency
(Hz)
1 MHz
1 GHz
1 THz
1 PHz
1 EHz
1 ZHz
10⁵ 10⁶ 10⁷ 10⁸ 10⁹ 10¹⁰ 10¹¹ 10¹² 10¹³ 10¹⁴ 10¹⁵ 10¹⁶ 10¹⁷ 10¹⁸ 10¹⁹ 10²⁰ 10²¹
Radio Spectrum
Terahertz
Infrared
Ultraviolet
X-ray
Gamma
Broadcast and Wireless
Microwave
electronics
optics
Far IR
Mid IR
Near IR
Near UV
Extreme UV
Soft X-ray
Hard X-ray
Visible wavelengths (nm)
700
625
575
540
470
440

Figure 2: Electromagnetic Spectrum.

In order to achieve signals in the THz region, different electronic sources based on semiconductor devices have been studied. In 2010, H. Eisele presented a paper about the state-of-the-art of electronic sources that have either demonstrated substantial amounts of output power or have strong potential in the production of significant output powers at frequencies above 300 GHz (28). As is well known, Eisele remarked that the performance of electronic sources generally improves when they are cooled to cryogenic temperatures. However, cryogenic temperatures tend to be incompatible with many consumer applications. Thus, for a fair comparison of performance his review focuses on room-temperature operation(2).

Frequency multipliers			**Oscillators with transistors**			**Active two-terminal devices**		
Technology	Frequency	Power	Technology	Frequency	Power	Technology	Frequency	Power
GaAs Schottky varactor and varistor diodes (29-31)	0.1 - 1.2 GHz (29-31)	~µW	MMIC (32-34)	94 GHz (32)	427 mW	RTD InAs/AlSb (35)	360 GHz	90 W/cm^2
	1.2 THz (31)	100 µW						
	1.5 -1.6 THz (31)	15 µW-20 µW		217.5 - 220 GHz (33)	> 50 mW	InGaAs/AlAs (36)	342 GHz	23 µm
	1.9 THz (31)	3 µW		338 GHz (34)	10 mW	GaInAs/AlAs (37)	831 GHz	> 1 µW
InP-based HBVD* (38-40)	0.1 - 1.2 GHz.	~µW	InP-based HBTs (41)	> 300 GHz	35 -115 mW	GaAs-based TUNNETT (42)	202 GHz	10 mW
							210 GHz	9 mW
							235 GHz	4 mW
GaN-based devices (31,43,44)	270 - 300 GHz (44)	125 mW	InP DHBT** (45)	330 GHz	2.3 mW/m^2	GaN-based TUNNETT (46)	200 GHz	160 mW
	0.1 THz (31,43)	~mW	AlGaN/GaN-HEMT	40 GHz (47)	10.5 W/mm		300 GHz	30 mW
				4 GHz (48)	40 W/mm			

* Hetero-barrier varactor diodes (HBVD). **Double heterojunction bipolar transistor (DHBT)

Table 1: Some electronic sources at THz frequencies.

A brief summary of these sources is conveniently expanded, with special attention given to the power and frequency properties, as presented in Table 1 and discussed below.

I. One of the sources studied involves *frequency multipliers*. These have been manufactured using different technologies and configurations: varactor and varistor diodes, hetero-barrier varactor diodes (HBVD) or double heterojunction

---

[2] Technological advances are described in ref. (28)

bipolar transistors (DHBTs). In particular, those based on GaAs Schottky diodes have been employed for many decades at submillimeter wavelengths, mainly when all-solid-state solutions were required. For these GaAs Schottky diodes, expected longer-term performance improvements for multiplier chains are 139 µW (at 1.6 THz) and 32 µW (at 2.4 THz) (49), assuming room-temperature operation and a pump source with 150 mW at the W-band (75-110 GHz) (28).

With the advent of GaN-based millimeter wave-power amplifiers, output powers of 125 mW in the frequency range of 270 GHz - 300 GHz were produced (44); the output power has been multiplied by a factor of 1000 in comparison with GaAs and InP technology. Considering the new developments, as well as recent advances in the thermal management of frequency multipliers (31,43), the continuous progress of power amplifiers around or above 0.1 THz (31,50), and the prospect of high-breakdown voltage GaN Schottky diodes for submillimeter-wave multipliers (31,51,52), it is clear that coherent electronic sources have the potential to deliver milliwatts of tunable single-mode power well into the terahertz range.

II. Another possible technology to achieve frequencies in the THz range involves *oscillators with transistors* (28). Figure 3 summarizes the state-of-the-art results from transistor-based power amplifiers for oscillators and compares them with active two-terminal devices that have yielded more than 10 mW above 300 GHz without the use of power-combining (28).

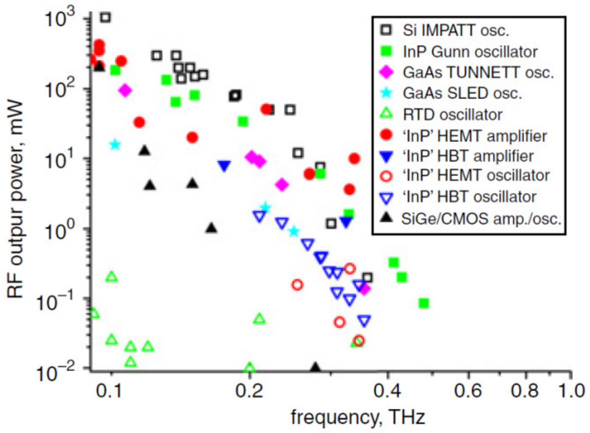

Figure 3: State-of- the-art results from transistor amplifiers, transistor oscillators, and selected active two-terminal devices in the 100-1000 GHz frequency range at room temperature (28).

The performance of monolithic millimetre-wave integrated circuits (MMICs) approaches the output powers, in the 100 GHz -260 GHz frequency range, that so far have only been possible with Si impact ionization transit-time (IMPATT) diodes (28,53,54). InP/InGaAs heterojunction bipolar transistors (HBTs) are the preferred devices for THz amplifiers and oscillators in comparison with AlGaAs/GaAs HBTs because they provide higher operating frequencies (28).

The rapid development of radio frequency-powered electronics requires the introduction of wide band-gap materials (such as GaN or Si) due to its potential in high-output power density, high operation voltage and high input impedance. In the last decade, GaN-based RF-powered devices have undergone substantial progress in many aspects, from materials growth, processing technology, device structure, to MMIC design. Output power density has reached 40 W/mm (48), more than one order of magnitude higher than GaAs (47).

III. Another possible technology available for working in the THz range is that of *active two-terminal devices* [see Figure 3 (28)]. These were the first solid-state devices ever to be used in microwave oscillators and their great advantage is that they are simpler to manufacture in comparison with three-terminal devices. Active two-terminal devices generate output power by providing a negative differential resistance (NDR) at the frequency of interest. Devices that are relevant at submillimeter waves are resonant-tunnelling diodes (RTDs), tunnel-injection transit-time devices (TUNNETT), super lattice electronic devices (SLEDs) and transferred-electron devices (TEDs, also called Gunn devices) (28), the latter being the object of study of this dissertation. Entry to the THz range through the NDR is still a challenging issue. For this purpose, Gunn devices are also currently being explored. For example, InP Gunn devices in a third-harmonic mode yielded 330 mW at 412 GHz and 86 mW at 479 GHz at room temperature (28). In addition, THz oscillations in an $In_{0.53}Ga_{0.47}As$ submicron planar Gunn diode have been observed for the first time, operating at a fundamental frequency above 300 GHz (55). Moreover, an AlGaAs/GaAs-based planar Gunn diode oscillator with a fundamental frequency operation of 120 GHz has been built, which is the highest fundamental frequency for a GaAs-based Gunn diode (56).

It is predicted that, owing to the electronic properties of GaN, GaN-based devices will be perfect candidates for working as sources in the THz range. However, despite the huge efforts made in recent years, continuous-wave Gunn oscillations have not yet been observed experimentally in GaN diodes (57,58). Some hints pointing to “bias” oscillations were obtained for GaN Gunn diodes in the presence of an inductance series (58). Although there are several modelling works where Gunn structures have been analysed (59), there are no systematic studies in which the performances of vertical diodes with different materials, lengths, bias conditions and doping levels have been compared. In Chapter 2 of this dissertation, InP- and GaN-based devices will be analysed with the main objective of addressing the best conditions to achieve Gunn oscillation in both materials.

Thermal effects in GaN-based devices

In just a short time, transistors based on nitrides have become ideal candidates for work at high temperatures [AlGaN/GaN HEMTs begin to fail in the operating temperature range of 500 °C and InAlN/GaN HEMTs can operate up to 900 °C, (60)], high output power [8.4 W/mm with a power-added efficiency of 28 % at 8 GHz in AlGaN/GaN HEMTs (2)], and low noise, and they also have the possibility of working at high frequencies, covering a huge part of the electromagnetic spectrum (ranging from 1 GHz to 100 GHz).

One of the most important aspects leading to the degradation in GaN-transistors is the elevated temperatures reached inside the device. For GaN-based microwave power devices, the thermal behaviour due to the self-heating effect is a major limitation because power dissipation is very high (61). Thermal effects play a more significant role in the performance of existing GaN-based HEMTs as compared to GaAs-based HEMTs (62). Since GaN-based devices have grown in popularity, many researchers are currently investigating safe operating temperatures for GaN-based devices. Among other mechanism as (nonradioactive) recombination heat or convention (63), the power dissipation due to Joule effect is usually the main origin of the increase of the device temperature. This temperature rise affects adversely the performance of the device, its reliability, and its lifetime (64). Accordingly, it is crucial to consider thermal effects in computational models, such as in experimental characterization, with the main goal of designing strategies to reduce their negative consequences. As an example, in Figure 4 the surface temperature distribution in a double-finger AlGaN/GaN HEMT measured with an infrared microscope is shown[3]. Also, thermal models become essential to know the temperature limits to avoid device breakdown, thus avoiding manufacturing costs. The typical methods used to study the effect of high temperatures include thermal modelling with the finite element method (FEM) and the finite difference method (FDM) software packages. There are also commercial modelling tools that allow electro-thermal simulations of a wide range of electronic devices to be carried out, such as the Silvaco Atlas (http://www.silvaco.com), Sentaurus Device (http://www.synopsys.com), COMSOL Multiphysics® (http://www.comsol.com), etc.

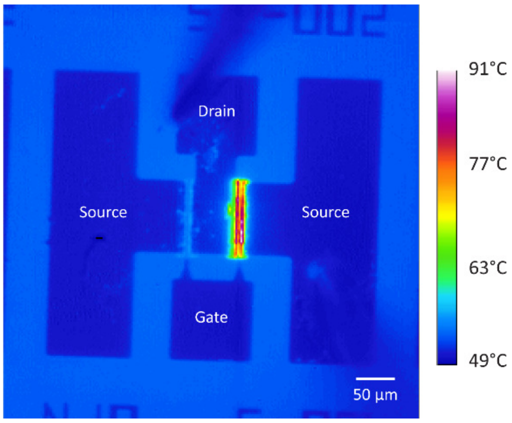

Figure 4: Surface temperature distribution in a double-finger AlGaN/GaN HEMT measured with an infrared microscope (QFI Infrascope II). http://web.mit.edu/kbagnall/www/research.htm.

Commercial software and home-made simulators can include thermal effects via different alternatives, ranging from simple models that consider an approach based on a thermal resistance (65) to others that take into account the heat diffusion equation (HDE) (66-68), and those that employ the Boltzmann equation for phonons (69).

In our particular case, we shall couple the thermal resistance and the HDE approaches with MC electronic simulators. It is important to point out that electronic transients in semiconductor systems are of the order of picoseconds, whereas thermal transients for the HDE may be of the order of nanoseconds, microseconds, or even longer (70). Performing MC computations of the duration of thermal transients would not be feasible (70). Albeit, it will not be necessary for thermal transients to be reached when the static

---

[3] http://web.mit.edu/kbagnall/www/research.htm.

direct current (DC) electro-thermal characteristics are investigated. In this case, the steady-state HDE is a good approximation.

Thesis Outline

The Research Group on Semiconductor Devices of the University of Salamanca, (http://campus.usal.es/~gelec), is one of the leading research groups in academia carrying out simulations of micro- and nano-devices based on the MC method (71). Their MC simulator includes, intrinsically at microscopic level, the physical phenomena on which devices base their operation (band structures of the materials, scattering mechanisms, self-consistency of the electric field, etc.). With these simulations it is possible to predict the performance of the device and to establish design rules prior to its manufacture. The technique is used to simulate devices that operate at high frequency, for example, self-switching diodes (SSDs) (72), InGaAs/InAlAs planar diodes (73) and, in particular in this dissertation, Gunn diodes based on materials with negative differential mobility (InP or GaN) (74,75) and AlGaN/GaN HEMTs (76-78).

This thesis is distributed in the following 3 chapters:

In Chapter 1, the theoretical concepts and modelling tools are presented. The Gunn effects, the dynamics of domain formation in Gunn diodes and the main modes of operation of these diodes are explained. Then, we introduce the Monte Carlo tool. The methods employed (i) to know the microscopic characteristics of the materials under analysis (InP, GaN), and (ii) to study complete electronic devices are described. Finally, the techniques used for processing the results are discussed.

In Chapter 2, the MC simulator is used to explore the possibility of enhancing the emission power and the oscillating frequency in InP- and GaN-based Gunn $n^{+}nn^{+}$ devices (see Figure 5).

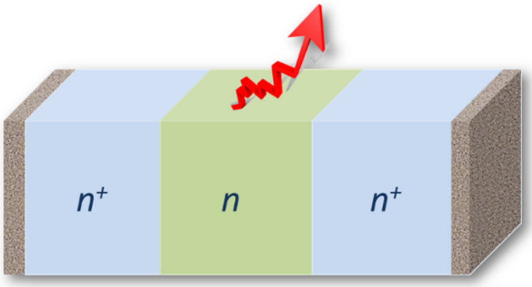

Figure 5: Schematic of a vertical Gunn diode.

These devices will provide us with frequencies close to the THz regime, avoiding the need to use multiplication stages. Different lengths of the active region and doping profiles will be considered. First, a study under DC bias conditions is carried out, analysing the time sequences of current densities, the spectrum of the signals, etc. Secondly, we perform a study of the devices when a bias condition $V_{DC}+V_{AC}\cos(\omega t)$ is applied between its terminals: the AC power generated, the frequency of the generation bands and the DC to AC conversion efficiency are analysed. The main conclusions are summarized at the end of the chapter.

In Chapter 3, we focus our attention on the inclusion of thermal effects in an in-house ensemble MC tool self-consistently coupled with a two-dimensional (2D) Poisson solver. We present the two self-consistent thermal algorithms implemented, one based on a thermal resistance method, and the other based on the self-consistent resolution of the HDE. The HDE is solved for both temperature-independent and temperature-dependent thermal conductivities. Once the tool is ready, we corroborate/calibrate our results with experimental DC measurements of an un-gated AlGaN/GaN device. Isothermal and electro-thermal (thermal resistance method *vs.* HDEM) results are compared. Different die lengths and substrates are simulated, providing some rules for design purposes. Thermal boundary resistance effects are also included. Once the electro-thermal simulator has been calibrated, we analyse an AlGaN/GaN HEMT, as illustrated in Figure 6 showing a typical temperature distribution in a HEMT.

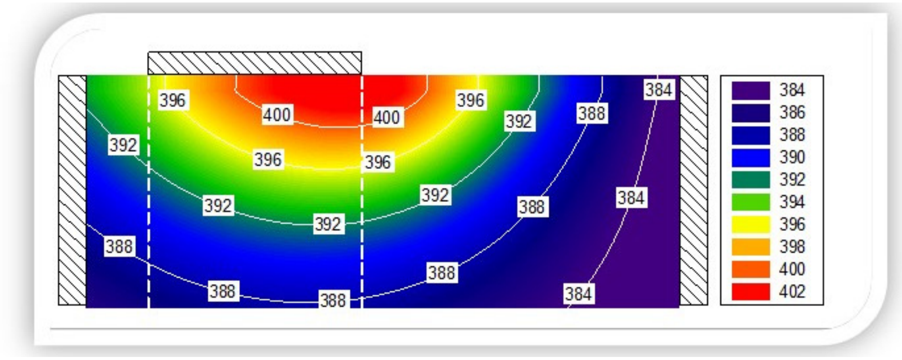

Figure 6: Temperature distribution in an HEMT.

Isothermal simulations and electro-thermal simulations are also compared by analysing the current density, transconductance, and other quantities. Hot-spots are studied under different bias conditions, heat-sink temperatures, and gate lengths. Finally, we conclude Chapter 3 by discussing the main contributions and the most significant achievements.

The thesis ends by summarising the main conclusions and future work.

CHAPTER 1: THEORETICAL CONCEPTS AND MODELLING TOOLS

In this chapter, we briefly introduce the theoretical concepts and modelling tools necessary for an accurate understanding of this dissertation. Firstly, the Gunn effect is presented through an explanation of the phenomenon, its dynamics and the different modes of operation. Secondly, we describe the Monte Carlo (MC) simulator, which uses software developed over the past 20 years by the members of the "Research Group in Semiconductor Devices of the University of Salamanca". An overview and the description of the MC technique are introduced, followed by the single-particle MC procedure. The MC simulator takes into account the scattering mechanisms, the physical restrictions or the properties of the materials. We provide the microscopic magnitudes at room temperature of average velocity, valley-occupation, average kinetic energy, and effective mass for InP and GaN materials. We end with the details of the two-dimensional device simulator and the different modes of operation that it supports. We specify the procedures necessary to analyse the Gunn oscillations, the alternating current (AC) power generation from direct current (DC), the DC to AC conversion efficiency, and the calculation of impedance.

1.1. Gunn Effect

As a starting point, a historical review concerning Gunn oscillations is presented. For a complete study, readers are referred to the works presented in refs. (79,80). In 1954, after the invention of the transistor, Shockley (81) suggested that a Negative Differential Resistance (NDR) semiconductor-based device with two terminals could have advantages over transistors, particularly at high frequencies. In 1961, Ridley and Watkins (82) described a method to achieve negative incremental resistance based on the heating, through an electric field, of electrons that were originally in a sub-band of high mobility and light mass. When electrons had the proper temperature they could occupy other band with high energy, low mobility, and high effective mass.

This theory was further developed by Hilsum in 1962 (83). However, he was unable to have his theoretical studies verified experimentally owing to the reduced quality of the GaAs-diodes then available.

In 1963, while studying noise in semiconductors, J. B. Gunn discovered the phenomenon that bears his name (84). He observed the existence of periodic fluctuations in the current through GaAs- and InP-based diodes when a bias higher than a critical value was applied between their terminals. At the time, Gunn did not link this observation to Ridley and Watkins' theories. It was in that same year that Ridley predicted the creation of an electric-field domain that was travelling continuously along in the crystal; it was formed in the cathode and it disappeared when it reached the anode.

Finally, H. Kroemer (85) proposed that the negative differential mobility would be linked to Ridley-Watkins and Hilsum's ideas. Their theory was based on the intervalley transfer mechanisms in the conduction band from low energy and high mobility electrons in the lower valley at equilibrium to another valley with greater energy and lesser mobility.

1.1.1. Explanation of the phenomenon

The phenomenon of Gunn oscillations is due to the transfer of conduction electrons from a high-mobility, low-energy valley to lower-mobility and higher-energy satellite valleys (86,87). In order to have this electron transfer effect, the semiconductor must have a key property: *the energy minima* (*with the mobilities mentioned above*) *must be close in the conduction band.*

The operation of Gunn diodes is based on the presence of a negative incremental resistance. Taking into account this phenomenon, circuit theory says that they are able to generate energy instead of dissipate it.

For a better understanding of this phenomenon, we focus our attention on the energy-band structure of GaAs, presented in Figure 1. 1 (a). The InP energy-band structure, with the exception of different values of the effective masses or bandgap, is similar to that of GaAs bands. Although the GaN energy-band structure is different for GaAs- and InP-materials [as will be described in section 1.2.3 (b.2)], the explanation for the phenomenon is the same.

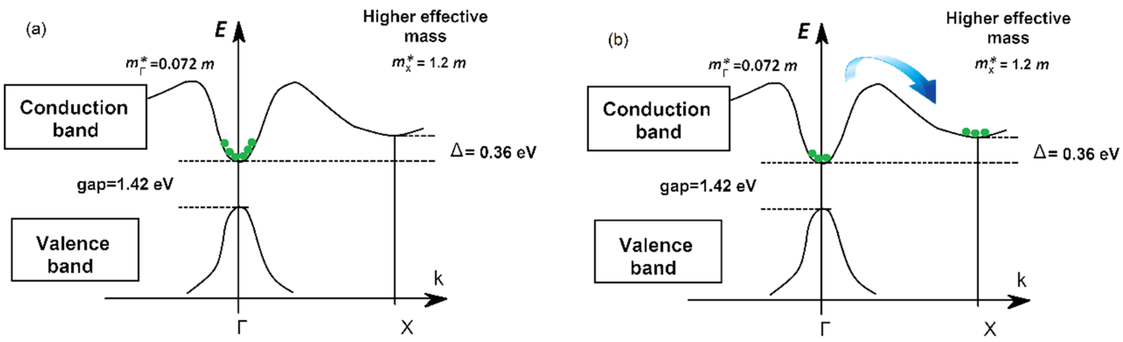
(a)
E
Higher effective mass
m^*_Γ=0.072 m
m^*_X = 1.2 m
Conduction band
Δ= 0.36 eV
gap=1.42 eV
Valence band
k
Γ
X
(b)
E
Higher effective mass
m^*_Γ=0.072 m
m^*_X = 1.2 m
Conduction band
Δ= 0.36 eV
gap=1.42 eV
Valence band
k
Γ
X

Figure 1. 1: (a) Energy band structures of GaAs. (b) Occupation of high valleys.

Under equilibrium conditions all electrons are in the absolute minimum of the conduction band, as illustrated in Figure 1. 1 (a). If a weak electric field, *E*, is applied over the equilibrium conditions, carriers (in *n* density) moving at the minimum of the Γ-valley will contribute to the current with an elevated mobility, μ_Γ, due to their small effective mass (86,87). It may be assumed that:

$$J = e\mu_\Gamma nE. \qquad \text{(I. 1)}$$

If the electric field increases, the velocity of the carriers also rises and so does their energy. There will come a time at which some electrons will acquire enough energy, and start to occupy higher valleys, as shown in Figure 1. 1 (b), and they begin to move with lower mobility as a result of a higher effective mass.

If we consider only two valleys (Γ and L) the total density of the carriers will be $n=n_\Gamma+n_L$,

and the current density can be written as:

$$J = e(\mu_\Gamma n_\Gamma + \mu_L n_L)E = e\left(\frac{\mu_\Gamma n_\Gamma + \mu_L n_L}{n_\Gamma + n_L}\right)nE = env_d, \qquad \text{(I. 2)}$$

where μ_Γ and μ_L are the electron mobilities in the Γ- and L- valleys, respectively, n_Γ and n_L are the carrier densities in each of these valleys, and v_d is the total average drift velocity.

While the carriers are in the Γ-valley, the average drift velocity will become greater with the electric field, and it will start to decrease when the onset of intervalley transfer mechanisms begins. For a specific electric field (threshold electric field, E_T), the velocity reaches its maximum value. For electric fields higher than the threshold electric field, electrons possess negative differential mobility, $\mu_{dif} = dv_d/dE < 0$, and the material presents a negative differential resistance (86,87) (see Figure 1. 2). Evidently, Figure 1. 2 is a simplification, and clearly, the real characteristics have a smooth shape due to other scattering mechanisms.

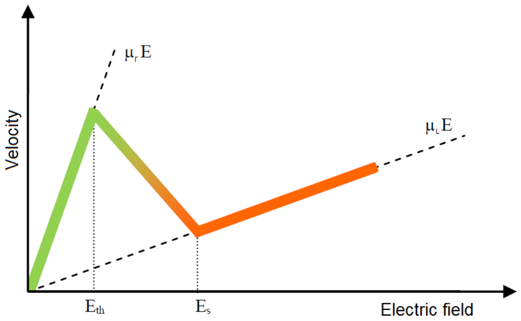

Figure 1. 2: Schematic of the *v-E* characteristic showing negative differential mobility for electric fields between E_{th} and E_s.

The conditions necessary for the appearance of negative differential mobility in a material, and therefore for Gunn oscillations to happen, are as follows (86,87):

- The lattice temperature has to be low enough, so that in the absence of electric field electrons will remain in the absolute minimum of the conduction band.
- The value of the effective mass in the absolute minimum of the conduction band has to be the lowest value of all valleys.
- The separation energy between the conduction band minima must be lower than the GAP energy to avoid impact ionization mechanisms before intervalley transfer occurs.

1.1.2. Dynamics of domain formation in Gunn Diodes

Unlike other various physical causes giving rise to a negative differential resistance, a semiconductor exhibiting bulk negative differential mobility is inherently unstable, because random fluctuation in the carrier density at any point in the semiconductor produces a momentary space charge that grows exponentially with time (87). In many cases, and under these particular conditions, the formation of domains and the appearance of oscillations in the current may occur. The concept of domain formation and Gunn oscillation is demonstrated qualitatively in Figure 1. 3 (87).

In a transfer electron device, instability starts with a dipole consisting of excess electrons (negative charge) and depleted electrons (positive charge), as shown in Figure 1. 3 (b). The dipole may arise from many possibilities, such as doping inhomogeneity, material defects, or random noise. This dipole sets up a higher field for the electrons at that location ($E > E_0$,E_0 being the average electric field in the structure with $E_0 > E_T$). This higher field slows these electrons down relative to the others outside the dipole. As a result, the region of excess electrons will grow because the electrons trailing behind the dipole are arriving with a higher velocity. By the same token, the region of depleted electrons (positive charge) also grows because electrons ahead of the dipole leave with a higher velocity.

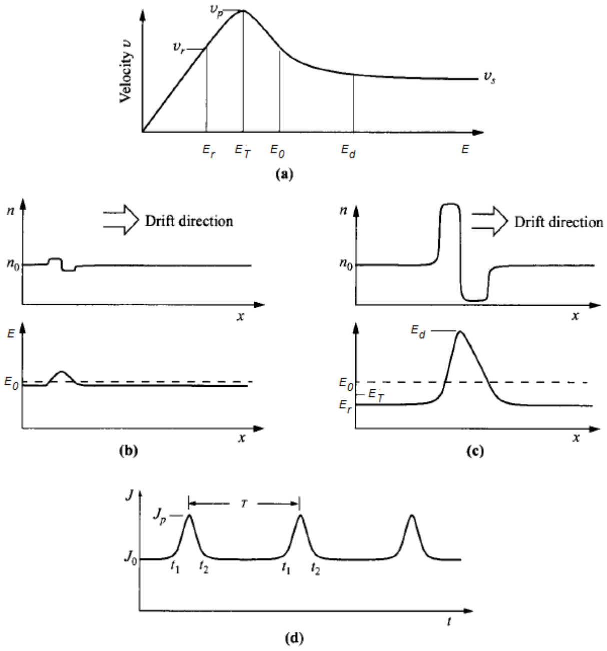

Figure 1. 3: Demonstration of domain formation. (a) *v*-*E* relationship and some critical points. (b) A small dipole grows to (c) a mature domain. (d) Current (Gunn) oscillations. Between t_1 and t_2, the matured domain is annihilated at the anode and another is formed near the cathode (87).

As the dipole grows, the field at that location also increases, but only at the expense of the field everywhere else outside the dipole. The field inside the dipole is always above E_0, and its carrier velocity decreases monotonically with field. The field outside the domain is lower than E_0, and its carrier velocity passes through the peak value and then decreases as the field is lowered. When the field outside the dipole decreases to a certain value, the velocities of the electrons inside and outside the dipole are the same [Figure 1. 3 (a), Figure 1. 3 (c)]. At this point, the dipole ceases to grow and is said to mature to a domain, usually still near the cathode. The domain then transits from near the cathode to the anode (87). The current waveform is shown in Figure 1. 3 (d). At t_2, a domain is completely formed. At t_1, the domain reaches the anode, and before another domain is formed the electric field throughout jumps to E_0. During the formation of a domain (t_1 - t_2), the field outside the dipole passes through the value of E_T where the peak velocity occurs. This causes a current peak. The current pulse width corresponds to the interval between the annihilation of the domain at the anode and the formation of a new domain. The period *T* corresponds to the transit time of the domain from cathode to anode. Typically, the displacement of the domain takes place at about the speed of the saturation velocity (the velocity reached for the highest electric fields, v_s).

The formation of charge accumulation domains can be explained formally through the corresponding equations as follows (86,87). Our standing point is the one-dimensional continuity equation for electrons without recombination, given by:

$$\frac{\partial n}{\partial t} = \frac{1}{e}\frac{\partial J}{\partial x} \ . \tag{I. 3}$$

If there is a small local fluctuation in the number of the majority of carriers *n* from the uniform equilibrium concentration, n_0, the locally created space-charge density is $n - n_0$. The Poisson equation and the current-density equation are:

$$\frac{\partial E}{\partial x} = \frac{-e(n - n_0)}{\varepsilon_{SC}} \ , \tag{I. 4}$$

$$J = e n_0 v_d + e D_n \frac{\partial n}{\partial x} \ , \tag{I. 5}$$

where E is the electric field, ε_{SC} the dielectric permittivity of the semiconductor, and D_n is the diffusion constant for electrons. Differentiating Eq.(I. 5) with respect to *x*, the following is obtained:

$$\frac{\partial J}{\partial x} = en_0 \frac{\partial v_d}{\partial E}\frac{\partial E}{\partial x} + \; eD_n \frac{\partial^2 n}{\partial x^2}, \tag{I. 6}$$

And, inserting Poisson's equation, Eq.(I. 4) yields:

$$\frac{\partial n}{\partial t} = -\frac{n - n_0}{\varepsilon_{SC}/en_0\mu_{dif}} + D_n \frac{\partial^2 n}{\partial x^2}, \tag{I. 7}$$

$\mu_{dif=\partial v_d/\partial E}$ being the differential mobility.

To conclude, we can solve Eq.(I. 7) by separation of variables, by taking $n(x,t) = n_1(x)n_2(t)$. The temporary solution of the space charge density created locally is:

$$n - n_0 = (n - n_0)_{t=0}e^{-t/\tau_d}, \tag{I. 8}$$

where τ_d is the dielectric relaxation time, given by:

$$\tau_d = \frac{\varepsilon_{SC}}{en_0\mu_{dif}} \tag{I. 9}$$

τ_d represents the time constant for the decay of the space charge to neutrality if the differential mobility is positive. However, if the semiconductor exhibits a negative differential mobility, any charge imbalance will grow with a time constant equal to $|\tau_d|$ instead of decaying. For large space-charge growth, this growth factor must be greater than unity, making $t/|\tau_d| > 1$. The maximum time required by a domain to pass through the whole active length is $t_{max} = L/v_s$, where L is the length of the active region, and v_s is the average drift velocity (typically known as the saturation velocity). Therefore, the following condition must be satisfied $L/(v_s|\tau_d|) > 1$, or:

$$n_0 L > \frac{\varepsilon_{SC} v_s}{e|\mu_{dif}|} \; . \tag{I. 10}$$

to achieve Gunn oscillations.

Table 1. 1 summarizes the conditions necessary to achieve Gunn oscillations in GaAs, InP and GaN materials. It merits special attention, as we shall see in Chapter 2.

Material	*Conditions for Gunn oscillations*
GaAs and InP	$n_0L > 10^{12}$ cm^{-2}
GaN	$n_0L > 8 \times 10^{12}$ cm^{-2}

Table 1. 1: Conditions for Gunn oscillations for GaAs, InP and GaN materials (87,88).

1.1.3. Modes of operation of Gunn diodes

Since Gunn first observed microwave oscillations in GaAs- and InP-transferred electron devices in 1963, several modes of operation have been studied: the ideal uniform-field mode, the transit-time dipole layer mode, the quenched dipole-layer mode, the accumulation-layer mode, and the limited-space-charge accumulation (LSA) mode (87). As in Chapter 2, we shall find two of these modes of operation: the transit-time dipole-layer mode and the accumulation-layer mode; these models are detailed below.

(a) Transit-time dipole-layer mode

When the n_0L product is greater than 10^{12} cm^{-2} for GaAs and InP, and bigger than 8×10^{12} cm^{-2} for GaN, we have the mode described mathematically above when a space-charge perturbation in the material increases exponentially in space and time to form mature dipole layers that propagate to the anode. The dipole is usually formed near the cathode contact, since the largest doping fluctuation and space-charge perturbation exists there. The space-charge perturbation grows quickly, and ahead of the accumulation region of slow electrons (heavy electrons located in the upper valleys) a depletion region is formed, which originates a dipole because the charge is negative in the accumulation region and it is positive in the depletion region. A zone of strong electric field is created between these two regions, as shown in Figure 1. 4. This electric field changes the velocity of electrons that constitute the dipole-accumulation domain. The velocity becomes steady when the velocities of (i) electrons in valleys of high effective mass (low mobility) in the domain, and (ii) of the electrons in lower valleys (high mobility) in the rest of the device are equal. The cyclic formation and subsequent disappearance at the anode of the fully developed dipole layers are what give rise to the experimentally observed Gunn oscillations.

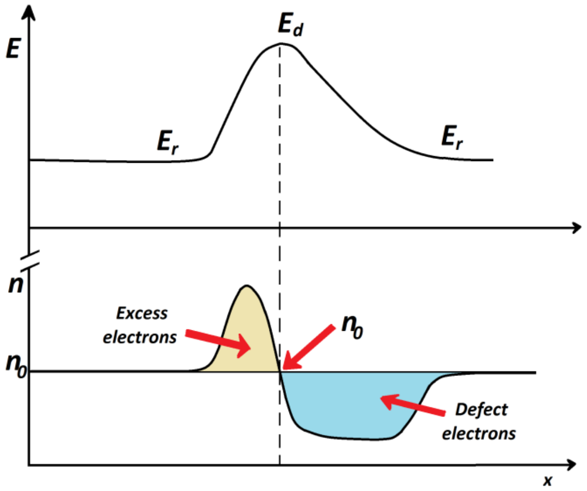
E
E_d
E_r
E_r
n
n_0
Excess electrons
n_0
Defect electrons
x

Figure 1. 4: Formation of a dipole. Electric field and carrier concentration.

(b) Accumulation-layer mode

The main difference between the accumulation-layer mode and the dipole-layer mode is that in a lightly doped or short sample, when Eq. (I. 10) is not satisfied, the mode exhibits only an accumulation of electrons without a depleted region of a positive charge. When a uniform field is applied to such a device, the accumulation-layer dynamics can be understood in a simplified manner, as shown in Figure 1. 5.

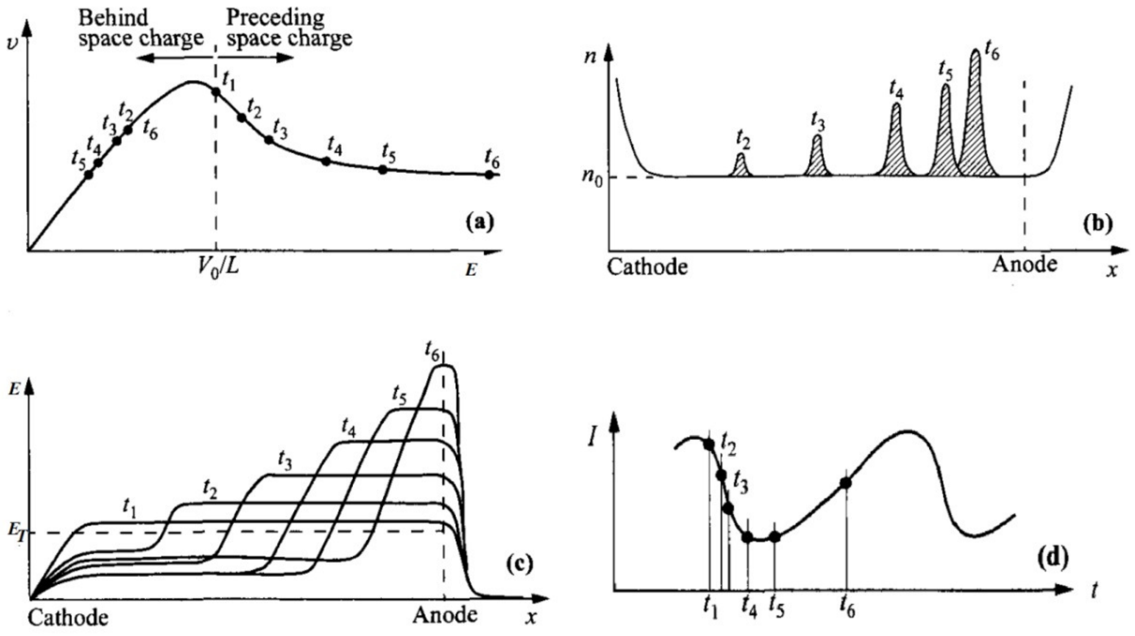
Behind space charge
Preceding space charge
v
V_0/L
E
(a)
n
n_0
Cathode
Anode
x
(b)
E
E_T
Cathode
Anode
x
(c)
I
t
(d)
t_1
t_2
t_3
t_4
t_5
t_6

Figure 1. 5: Accumulation-layer transit mode under time-invariant terminal voltage (87).

At time t_1, an accumulation layer (i.e., excess electrons) is injected from the cathode so that the field distribution splits into two parts, as illustrated at time t_2. The velocities on both sides of the accumulation layer have been altered in the direction shown in Figure 1. 5 (a). Since the terminal voltage is assumed to be constant, the area under each electric-field curve of Figure 1. 5 (c) should be equal. As the accumulation layer propagates toward the anode, this equality can only be maintained if the velocities on both sides of the accumulation layer fall, as dictated by the velocity-field curve and indicated at times t_3,t_4, and t_5. Eventually, the accumulation layer reaches the anode at time t_6, and disappears there. The field near the cathode rises through the threshold, another accumulation layer is injected, and the process repeats. The smooth current waveform is shown in Figure 1. 5 (d). In this particular example, the accumulation charge continues to grow along the device length.

1.2. The Monte Carlo tool

1.2.1. Overview

The main objective of this section is to present the Monte Carlo (MC) method, which will be employed to simulate the devices described in Chapters 2 and 3. Simulations are abstractions of reality, the process of imitating being a real phenomenon with a set of mathematical formulas. It is the initial step in the design, thereby avoiding having to carry out excess testing, and hence allowing substantial savings in costs.

A series of procedures that handle complex probability distributions by employing random numbers are grouped under the term *Monte Carlo method* or *Monte Carlo simulation*. This method provides solutions to an abundance of physical problems involving experiments with statistical samples in a computer.

The Monte Carlo simulation was created to solve integrals that cannot be tackled by analytical methods. The method receives its name from the capital of the Principality of Monaco, since Monte Carlo is *the capital of games of chance*, where a roulette is taken as a generator of random numbers. Although Lord Kelvin used MC-like methods in 1901, the name and the systematic development of Monte Carlo methods as is currently know, can be dated from around 1944, which coincides with the development of the computer.

The effective use of Monte Carlo methods as a research tool is due to Stanislaw Ulam, while he was working on nuclear weapons projects at the Los Alamos National

Laboratory. From that moment on, and as a consequence of the fast evolution of computers, the Monte Carlo method started to find use in different fields of science.

In electronics, the Monte Carlo method consists of a microscopic treatment through which the dynamics of carriers moving inside a semiconductor material subjected to the action of a self-consistent electric field and the crystalline lattice is studied (89,90).

This section will attempt to give a general idea of the MC tool employed here. More details about the simulator can be found in dissertations published over the last 20 years by the Research Group on Semiconductor Devices of the University of Salamanca (from 1994 [T. González] up to 2012 [A. Íñiguez-de-la-Torre]) (80,91-95).

1.2.2. Monte Carlo method: inverse transform

To obtain the values of different physical magnitudes that obey complex probability distributions, we shall make use of random distributions. This procedure is known as the Monte Carlo method, and will be described below (96).

Let us consider $p(\Phi)$ and $p(\boldsymbol{r})$, the normalized density probability functions associated with complex physical distribution and random distribution, respectively. In general, we can establish the identity:

$$\int_0^{\Phi} p(\Phi')d\Phi' = \int_0^{r} p(r')dr' \, . \tag{I. 11}$$

By employing the uniform distribution $p(r) = 1$, for r between 0 to 1, the next expression is obtained:

$$r = \int_0^{\Phi} p(\Phi')d\Phi' \; \rightarrow \; \Phi = \Phi(r) \; . \tag{I. 12}$$

In this way, the inversion of this expression provides us with random values of Φ through values of r, which r is a random number uniformly distributed between 0 and 1. When the integral of Equation (I. 12) is impossible to evaluate analytically, or the resulting expression cannot be inverted, different techniques are possible allowing its inversion: importance sampling, rejection sampling, the Metropolis method, and Gibbs sampling (97). We shall explain rejection sampling. This method was proposed by John Von Neumann (98) and can be applied if the conditions (see Figure 1. 6):

(a) The variable only takes values in the range [*a*,*b*].

(b) The density function $f(x)$ is fenced in a rectangle of altitude *c*.

$$f(x) = \begin{cases} \leq c, x \in [a,b] \\ 0, \text{otherwise} \end{cases},$$

are met.

If both indicated conditions are satisfied, the values of a random variable are simulated according to the following procedure. First, two random numbers with uniform distributions U_1 and U_2 are generated, where U_1 must lie within the interval [*a*, *b*], and U_2 within the interval [0, *c*]. As can be observed in Figure 1. 6, the values of U_1 and U_2 define a point *P* of coordinates (U_1, U_2), which will be included inside the rectangle where the density probability function has been delimited. Secondly, we shall apply the next criterion. If the point *P* obtained is inside the area that covers *f*(*x*), *x* is given by *x* = U_1, ignoring the point in other cases; that is to say, if *P* were outside the area covered by the density function. In this way the values of *x* follow the distribution *f*(*x*).

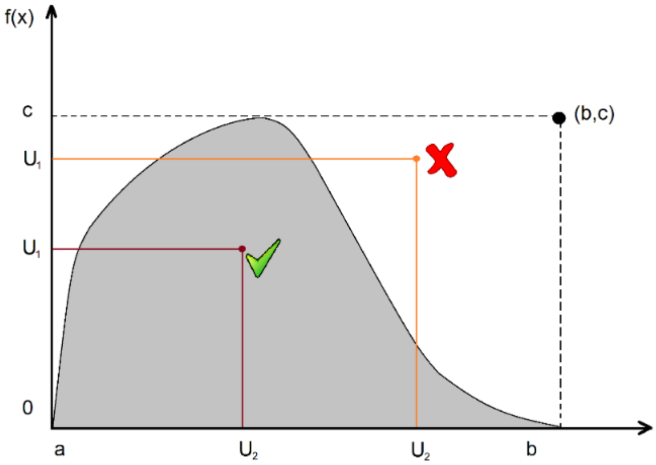

Figure 1. 6: Rejection sampling.

1.2.3. Single-particle Monte Carlo technique

The basic philosophy underlying the single-particle Monte Carlo technique, applied to charge transport in semiconductors, consists of simulating the motion of a free particle inside the crystal. It is intended so that the free flight of the particle accelerated by an applied electric field between intermediate instantaneous random scattering events can be studied. Describing Figure 1. 7 in more detail, the algorithm generates random free-flight times for the only particle; it determines the state after each free flight; it randomly chooses from amongst the different scattering mechanisms at the end of the free flight; it computes the final energy and momentum of the particle after scattering, and -finally- it reiterates the routine for the subsequent free flight. The flow chart of the single-particle MC simulator is shown in Figure 1. 8. By monitoring the particle motion at different points during the simulation, it is possible to estimate the magnitudes of several physical parameters for the particle statistically, such as the distribution function, average drift velocity, average energy, etc.

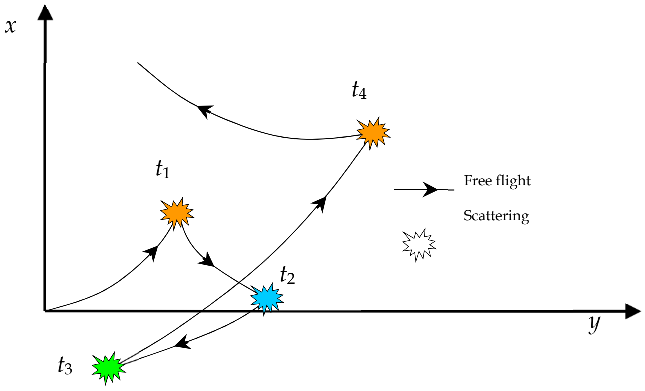

Figure 1. 7: Simple diagram of the particle motion in real space under a uniform electric field applied in the *x* direction.

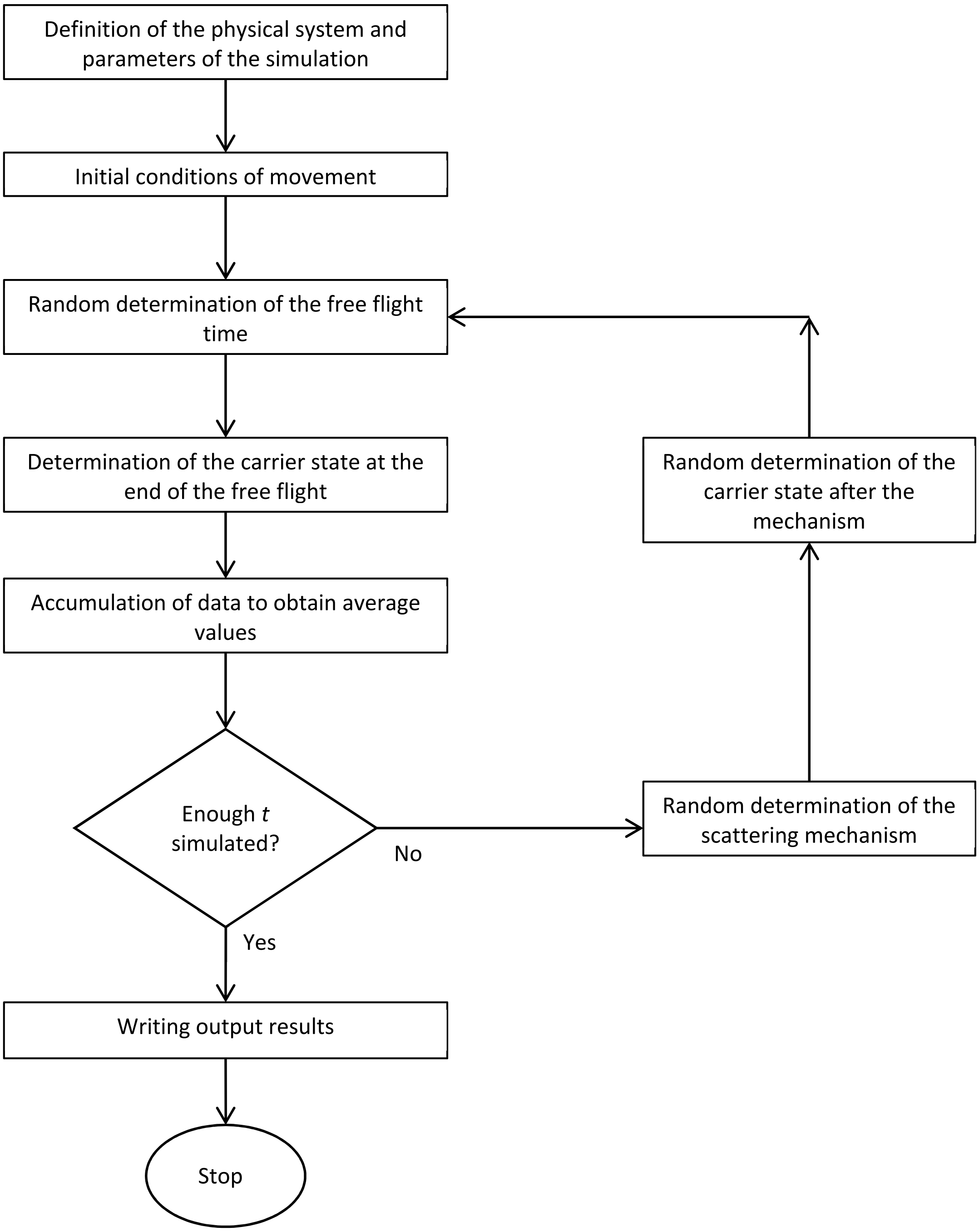
Definition of the physical system and parameters of the simulation
Initial conditions of movement
Random determination of the free flight time
Determination of the carrier state at the end of the free flight
Accumulation of data to obtain average values
Enough *t* simulated?
No
Yes
Random determination of the scattering mechanism
Random determination of the carrier state after the mechanism
Writing output results
Stop

Figure 1. 8: Flow-chart of the single particle program.

(a) Scattering mechanisms

A carrier inside a crystal with a certain effective mass would be uniformly accelerated by the electric field. However, inside the crystal there are impurities and vibrations of the atoms of the lattice that cause electrons to undergo collisions, called scattering mechanisms.

Details of the scattering mechanisms that can take place inside the crystals according to different criteria can be found below:

Depending on the electron's energy after the interaction:

- *Elastic*: The electron conserves its energy after undergoing scattering, e.g. ionized impurities scattering, electron-electron scattering.
- *Inelastic*: The electron gains or transfers energy in the collision, e.g. phonon scattering, optical (polar) scattering.

Depending on the wave vector before and after the scattering:

- *Isotropic*: The wave-vector of the electron after the collision does not depend on the direction of the initial wave-vector. The probability of the final state is the same in all directions, e.g. optical (non-polar) scattering, intervalley scattering.
- *Anisotropic*: The direction of the final wave-vector is dependent on the initial wave-vector of the electron. The probability of the final state tends to be higher when the angle between the incident wave-vector and the outgoing wave-vector is not very different, e.g. phonon scattering, acoustic (non-polar) scattering.

Depending on the physical origin:

Figure 1. 9 summarizes the scattering mechanisms considered in our simulator according to a classification from a physical origin(4).

- *Scattering with defects*: Within this classification, we stress the interaction with ionizing impurities. It is a Coulombic interaction, elastic and anisotropic. In our MC simulator it is evaluated by using the Brooks-Herring model (99). Dislocation scattering is usually typical in the GaN layer, and alloy scattering only appears in ternary materials (100).
- *Carrier-carrier scattering*: This mechanism is important in materials with a very high free-carrier concentration due to its proximity, meaning that carriers interact among themselves as a consequence of the electrostatic charge that they transport. In this work, it is not taken into account.

---

[4] The inclusion of generation recombination processes and impact ionization scattering is out of the scope of this thesis.

- *Lattice scattering*: This refers to the interactions with the phonons that arise as a result of the vibrations of the lattice. They are divided into intravalley and intervalley events, depending on the final state of the carrier after the collision (same energy valley as the initial state or not, respectively). The intravalley mechanisms generally involve phonons with a small wave vectors, whereas intervalley mechanisms involve phonons with a large wave vector. Furthermore, intervalley mechanisms are classified as equivalent or non-equivalent, depending on whether the valley in which the final state is found is of the same type as the initial one or not.

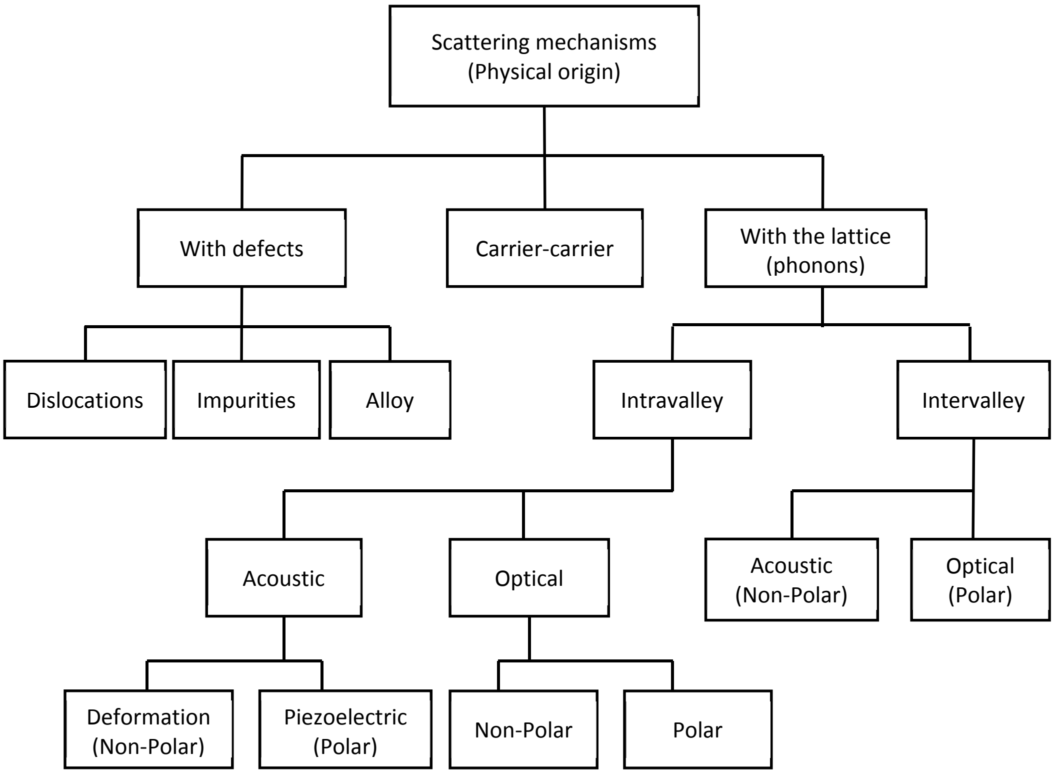
Scattering mechanisms
(Physical origin)
With defects
Carrier-carrier
With the lattice
(phonons)
Dislocations
Impurities
Alloy
Intravalley
Intervalley
Acoustic
Optical
Acoustic
(Non-Polar)
Optical
(Polar)
Deformation
(Non-Polar)
Piezoelectric
(Polar)
Non-Polar
Polar

Figure 1. 9: Scattering mechanism depending on the physical origin.

We remark the importance of including in our work the non-equivalent intervalley transfer mechanisms, these being responsible for the production of Gunn oscillations.

- **Intervalley**: (equivalent and non-equivalent). Inelastic and isotropic processes.
- **Acoustic** (non-polar): Elastic and anisotropic.
- **Piezoelectric**: Elastic and anisotropic.
- **Optical polar**: Inelastic and anisotropic.

- **Optical non-polar**: Inelastic and isotropic. This scattering only takes place in the L-valleys and therefore is not considered in GaN-based simulations.

For further details on the issues addressed of this section, we again refer readers to dissertations carried out by the Research Group on Semiconductor Devices of the University of Salamanca (80,91-95).

(b) Semiconductor properties

In this section, the most significant physical properties associated with the electrons of some of the materials under analysis are presented. The details of the band diagrams are also provided. To analyse the microscopic characteristics associated with the different materials (velocity, valley-occupation, effective mass and energy), the single-particle MC simulator was employed.

The conduction bands of the materials considered here will be modelled by a three- non-parabolic, spherical, valley model, whose energy-wave vector relation is approximated by:

$$\varepsilon(\boldsymbol{k})\big(1+\alpha\varepsilon(\boldsymbol{k})\big)=\gamma(\boldsymbol{k})=\frac{\hbar^2k^2}{2m^*} \ , \qquad \text{(I. 13)}$$

where m^* is the effective mass at the bottom valley, and α is the non-parabolicity coefficient.

(b.1) Indium Phosphide (InP)

Indium phosphide is a binary direct semiconductor composed of indium and phosphorus. Under normal conditions, InP crystallizes in the zinc-blende structure (101).

❖ Energy diagram-bands

The energy band diagrams are presented in Figure 1. 10. The first conduction sub-band presents three minima. The absolute minimum is located at the centre of the first Brillouin zone (Γ-point, 1.344 eV above the maximum of the valence-band). The second minimum is located at the L-point (at 0.86 eV from the Γ-valley, with four equivalent valleys), and the third is located at the X-point (at 0.96 eV from the Γ-valley) (101). For the modelling of transport phenomena at low electric fields (lower than 100 KV/cm), it would suffice to consider the Γ-valley, four equivalent L-valleys, and three equivalent X valleys, given that the larger conduction bands will be completely deserted.

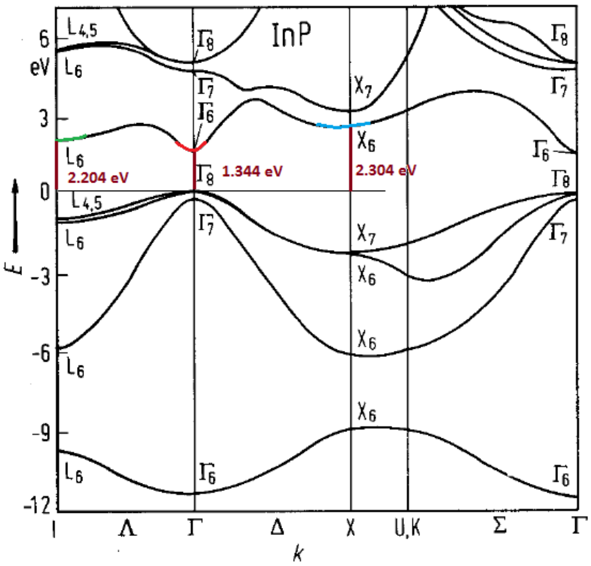

Figure 1. 10: Band structures of indium phosphide.

This material shows the necessary conditions for the existence of the negative differential mobility zone, and hence Gunn oscillations: (i) the value of the effective mass in the absolute minimum of the conduction band is the lowest one in all valleys m^*/m=0.078, and (ii) the separation energy between the conduction band minima is lower than the bandgap energy (Table 1. 2). The parameters employed for the simulation of the electrons are summarized in Table 1. 2 (101).

Symbol	***InP***
Density (Kg/m^3)	4790.0
Sound velocity (*m/s*)	5130.0
Optic dielectric constant (*HF*)	9.56
Static dielectric constant (*LF*)	12.4
Polar optical phonon energy (*eV*)	0.0422
Non-Polar optical phonon energy (*eV*)	0.0432
Band GAP (*eV*)	1.344
Lattice constant (*Å*)	5.8687

	Γ	**L**	**X**
Effective mass(m^*/m_0)	0.078	0.26	0.325
Non-parabolicity coefficient(eV^{-1})	0.83	0.23	0.38
Energy from Γ valley (*eV*)	0.0	0.86	0.96
Number of equivalent valleys	1	4	3
Acoustic def. potential (*eV*)	6.5	6.5	6.5
Optic def. potential (*eV*)	0.0	6.7	0.0
Intervalley def. potential (10^{10} *eV/m*)			
from Γ to	0.0	10.0	10.0
from L to	10.0	10.0	9.0
from X to	10.0	9.0	9.0
Intervalley phonon energy (*eV*)			
from Γ to	0.0	0.0278	0.0299
from L to	0.0278	0.0290	0.0293
from X to	0.0299	0.0293	0.0299

Table 1. 2: InP electron properties.

- Microscopic characteristics of the material

The microscopic characteristics of electronic transport at room temperature (velocity, average kinetic energy, valley-occupation and effective mass) are shown in Figure 1. 11. The velocity exhibits a linear zone for low electric fields, with a mobility of μ=5400 cm^2/V·s. The maximum value reached, 2.3x10^{7}cm/s, corresponds to an electric field of 13 kV/cm, this electric field being when the intervalley transfer mechanisms become important. Because carriers move to higher valleys, the effective mass that they acquire is greater, and, as a consequence, their velocity is reduced, saturating at high electric fields (0.91x10^7 cm/s). It is also possible to observe, when the saturation velocity is reached, the onset of the X-valley occupation. However, Γ- valley occupation is always the highest.

The scattering mechanisms considered in this material are:

- Lattice scattering: intervalley, acoustic, optical (polar and non-polar).
- Scattering with defects.

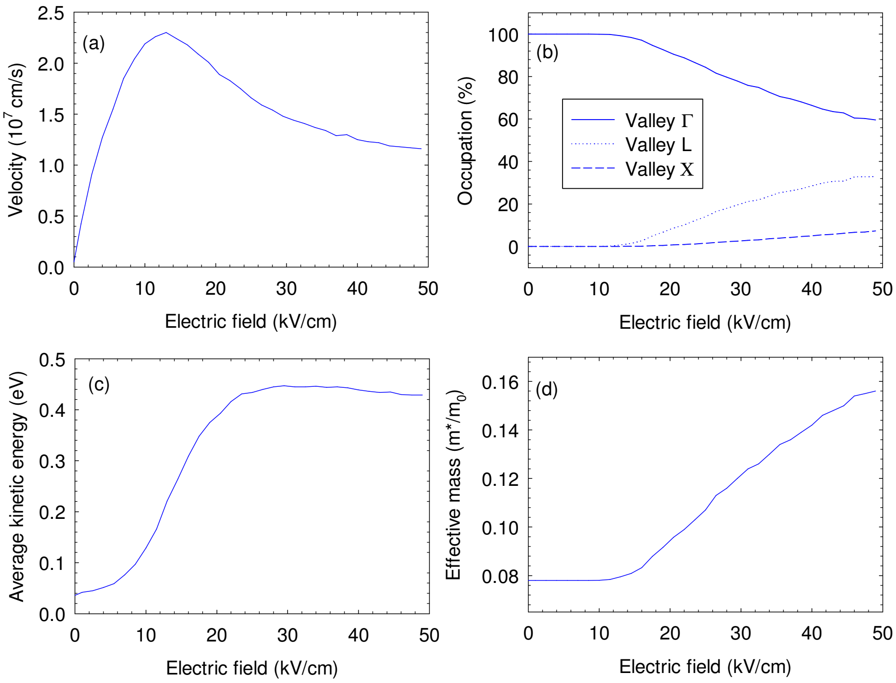

Figure 1. 11: Microscopic magnitudes calculated at room temperature *vs.* the electric field for InP. (a) Average velocity, (b) valley-occupation, (c) average kinetic energy, and (d) effective mass. A doping of 10^{15} cm^{-3} was employed.

(b.2) Gallium Nitride (GaN)

Historically, the GaN direct bandgap semiconductor was one of the first III-V-compound semiconductors to be studied (102). Nitrates of group III can crystallize in three types of structures: wurtzite, zinc-blende and rocksalt (103). The wurtzite structure (α-GaN) is the stable phase of GaN at ambient pressure. A zinc-blende phase (β-GaN) is very close in energy and can be stabilized by epitaxial growth on cubic substrates. In Figure 1. 12 the band-structures of the wurtzite-GaN considered in our simulations are depicted. As indicated above, a three-, non-parabolic spherical, valley model is taken into account (Γ_1, U and Γ_3 valleys). The lowest point of the conduction band is located at the Γ point (Γ_1-valley), 3.44 eV above the absolute maximum of the conduction band, also located at the Γ point. The next minimum is located between the M and L points, leading to a valley (six equivalents) called the U-valley, at 2.2 eV from the minimum of the Γ_1-valley. The next minimum is located in the Γ_3-valley at 2.4 eV from the minimum of the Γ_1-valley. This material, like InP, has optimum conditions for Gunn oscillations to be produced. Although a five-valley model for the study of transport properties would be most accurate, the three-valley model is an excellent approximation for the range of voltages applied in the devices presented in this dissertation. Therefore we do not take into consideration the K- and M-valleys because their occupancy is negligible.

The parameters of the electrons are summarized in Table 1. 3 (101).

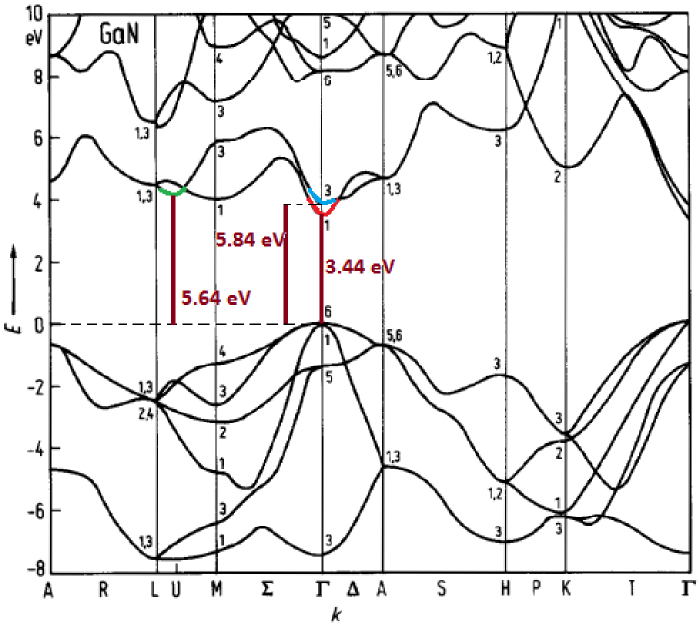

Figure 1. 12: Band structures of gallium nitride.

Symbol	*GaN*
Density (Kg/m^3)	6150.0
Sound velocity (*m/s*)	6560.0
Optic dielectric constant (*HF*)	5.35
Static dielectric constant (*LF*)	8.9
Polar optical phonon energy (*eV*)	0.09120
Non-Polar optical phonon energy (*eV*)	0
Band GAP (*eV*)	3.44
Lattice constant (*Å*)	5.185

	Γ_1	U (M-L)	Γ_3
Effective mass(m^*/m_0)	0.22	0.39	0.28
Non-parabolicity coefficient(eV^{-1})	0.37	0.50	0.22
Energy from Γ valley (*eV*)	0.0	2.2	2.4
Number of equivalent valleys	1	6	1
Acoustic def. potential(*eV*)	8.3	8.3	8.3
Optic def. potential (*eV*)	0.0	0.0	0.0
Intervalley def. potential (10^{10} *eV/m*)			
from Γ to	0	10.0	10.0
from L to	10.0	10.0	10.0
from X to	10.0	10.0	0
Intervalley phonon energy (*eV*)			
from Γ to	0	0.09120	0.09120
from L to	0.09120	0.09120	0.09120
from X to	0.09120	0.09120	0

Table 1. 3: GaN electron properties.

❖ Microscopic characteristics of the material

The microscopic characteristics of electronic transport at room temperature, and for a doping of 10^{15} cm^{-3}, are shown in Figure 1. 13. This material requires higher electric fields to ensure the intervalley transfer mechanisms, and hence to work in a negative differential mobility zone, due to the properties of their energy-bands.

The velocity presents a linear zone for lower electric fields with lower mobility in comparison with the InP material, μ=900 cm^2/V·s. The maximum velocity reached is 2.53x10^7 cm/s for an electric field of 210 kV/cm. Note that this velocity is higher than for InP, and has a threshold electric field one order of magnitude greater. The saturation velocity is 1.43x10^7 cm/s, higher than the InP saturation velocity (0.91x10^7 cm/s). For electric fields higher than 665 kV/cm, the U-valley shows the greatest occupation. The effective mass remains almost constant in the region in which the intervalley scattering mechanisms are not important (electric fields lower than 220 KV/cm).

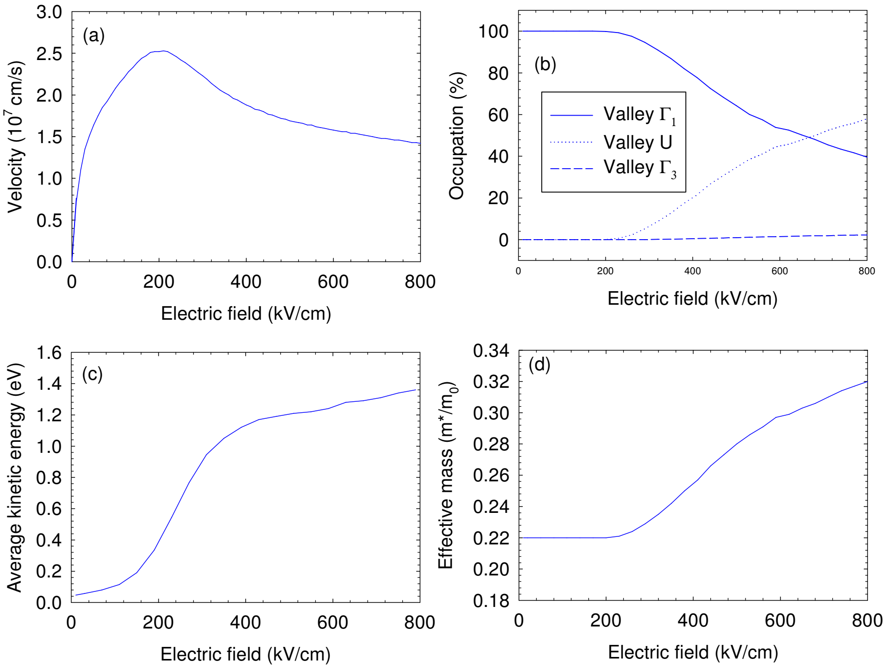

Figure 1. 13: Microscopic magnitudes calculated at room temperature *vs.* the electric field for the GaN material. (a) Average velocity, (b) valley-occupation, (c) average kinetic energy, and (d) effective mass.

The scattering mechanisms considered in this material are:

❖ Lattice scattering: intervalley, acoustic, optical (polar).

❖ Scattering with defects, piezoelectric scattering, dislocation scattering, and alloy scattering.

(b.3) Aluminium Gallium Nitride ($Al_{0.27}Ga_{0.73}N$)

We address the $Al_{0.27}Ga_{0.73}N$ material in a less exhaustive manner. It is an alloy of aluminium nitride (27 %) and gallium nitride (73 %). Its microscopic characteristics are not included in this section since electronic transport in this layer is not important in the heterostructures presented in Chapter 3.

The parameters of this material are summarized in Table 1. 4 (101).

The scattering mechanisms considered in this material are the same as those in GaN:

- Lattice scattering: intervalley, acoustic, optical (polar).
- Scattering with defects, piezoelectric scattering, dislocation scattering and alloy scattering.

Symbol	***$Al_{0.27}Ga_{0.73}N$***
Density (*Kg/m^3*)	5361.6
Sound velocity(*m/s*)	7235.0
Optic dielectric constant (*HF*)	5.1934
Static dielectric constant (*LF*)	8.792
Polar optical phonon energy (*eV*)	0.09336
Non-Polar optical phonon energy (*eV*)	0
Band GAP (*eV*)	4.07720
Lattice constant (*Å*)	5.12965

	Γ_1	**U (M-L)**	**Γ_3**
Effective mass(m^*/m_0)	0.2524	0.4116	0.307
Non-parabolicity coefficient (*eV^{-1}*)	0.34570	0.37445	0.23890
Energy from Γ valley (*eV*)	0.0	1.93	2.427
Number of equivalent valleys	1	6	1
Acoustic def. potential(*eV*)	8.624	8.624	8.624
Optic def. potential (*eV*)	0.0	0.0	0.0
Intervalley def. potential(*10^{10} eV/m*)			
from Γ to	0	10.0	10.0
from L to	10.0	10.0	10.0
from X to	10.0	10.0	0
Intervalley phonon energy (*eV*)			
from Γ to	0	0.09336	0.09336
from L to	0.09336	0.09336	0.09336
from X to	0.09336	0.09336	0

Table 1. 4: $Al_{0.27}Ga_{0.73}N$ electron properties.

1.2.4. Device simulator

In order to study the behaviour of transients, a synchronous simulation of a reasonable number of particles is indispensable. This is called an *ensemble* Monte Carlo, in which the above algorithm is repeated for each particle. The flow chart is shown in Figure 1. 14. Over each time-step, the individual carriers are simulated independently of the others. However, within a real semiconductor device, it is also essential to solve the Poisson equation to account for the spatial distribution of charge. Inductive magnetic effects have been neglected as the electron speed is much smaller than the speed of light. Consequently, it becomes necessary to self-consistently couple both the transport model and the Poisson solver (PS). For this purpose, a spatial grid is needed to solve the PS. In this simulation framework, the particle-based *ensemble* is carried out over a reasonably small time-step, Δt=1 fs, under the action of a self-consistent electric field (solution of the previous iteration) with the appropriate boundary conditions. At the end of each time interval, the PS for the next time-step is applied again using the frozen configuration of charges obtained from the *ensemble* Monte Carlo, as shown in Figure 1. 15.

Although a 3-D simulator would be the ideal tool to simulate the electronic transport (104), our two dimensional MC tool allows us to simulate properly different technologies, from vertical structures (Gunn diodes) to planar devices (transistors). Our simulator is a very-well calibrated model and provides macroscopic results that are in very good agreement with experimental studies. Boundary conditions, such as polarization and surface charges, are included (95). The electric field is computed by LU decomposition (105) of the PS in a finite differences approach. To obtain more information, we refer readers to ref. (95).

Apart of the MC technique, we point out that there are other electronic transport models, such as Drift-Diffusion (106) or Hydrodynamic (107) types, which have also been widely used to study transport in a large variety of semiconductor devices. While the MC method is stochastic, the latter two formulations are deterministic and involve the solution of coupled systems of partial differential equations (108). In the MC technique, the physics enters through the description of the semiconductors band structures (i.e., kinematics) and the scattering behaviour (i.e., dynamics) (108). In the deterministic approaches, the physics is lumped into parameterized mobilities, diffusion constants, and lifetimes. For this reason, access to the physics is more straightforward in a MC approach. However, in the MC methods significantly longer computer execution times are required (108).

Prior to the present contribution, the two-dimensional tool was only designed to perform isothermal simulations. One of our efforts has been the implementation of thermal effects though two algorithms in the MC code: one based on a thermal resistance, and the other based on the resolution of the HDE. To facilitate the reading of this manuscript, these two methods will be discussed in detail in Chapter 3.

In addition, different subroutines have been implemented in the MC software to apply different modes of operation: the DC mode, DC + AC mode, and RLC mode. These approaches are summarized succinctly in section 1.2.4 (b).

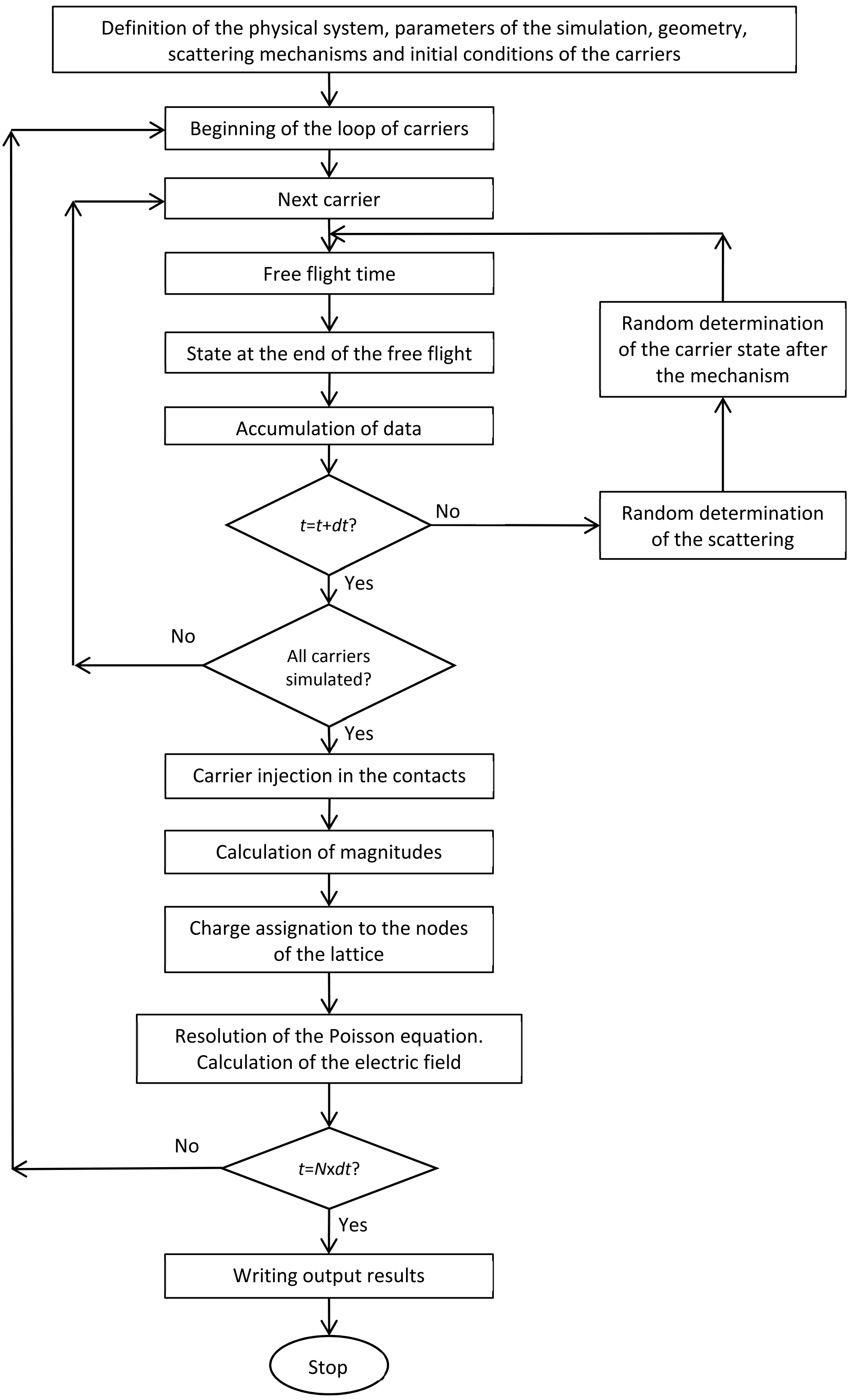
Definition of the physical system, parameters of the simulation, geometry, scattering mechanisms and initial conditions of the carriers
Beginning of the loop of carriers
Next carrier
Free flight time
State at the end of the free flight
Accumulation of data
t=t+dt?
No
Random determination of the scattering
Random determination of the carrier state after the mechanism
Yes
All carriers simulated?
No
Yes
Carrier injection in the contacts
Calculation of magnitudes
Charge assignation to the nodes of the lattice
Resolution of the Poisson equation. Calculation of the electric field
t=Nxdt?
No
Yes
Writing output results
Stop

Figure 1. 14: Flow-chart of the two-dimensional MC program.

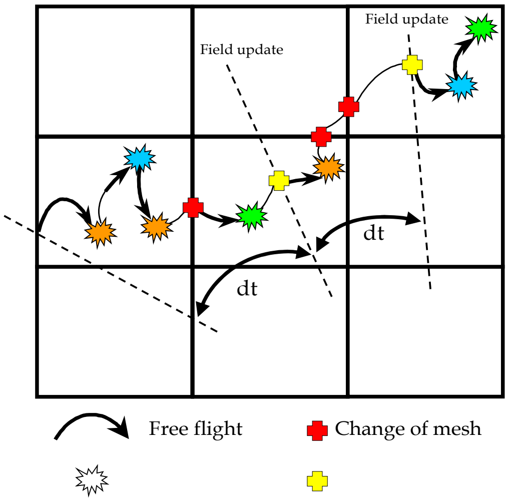

Figure 1. 15: 2D device simulation scheme.

(a) Physical restrictions

To correctly reproduce the performance and behaviour of the device with our MC tool, the following conditions must be satisfied (80).

- The time-step, Δt, will be limited by the plasma frequency ω_p (109) and by the dielectric relaxation time τ_d (107), whose expressions are:

$$\omega_p = \sqrt{\frac{q^2 N_D}{\varepsilon_0 \varepsilon_r m^*}} \ , \qquad \text{(I. 14)}$$

$$\tau_d = \frac{\varepsilon_0 \varepsilon_r}{q N_D \mu_0} \ , \qquad \text{(I. 15)}$$

μ_0 being electron mobility, q electron charge, $\varepsilon_0\varepsilon_r$ the dielectric constant, N_D the carrier concentration, and m^* the effective mass. The time-step, Δt, must satisfy the following condition:

$$\omega_p \Delta t < 2 \ y \ \Delta t < \tau_d \ . \qquad \text{(I. 16)}$$

- The mesh sizes must always be lower than the Debye length (80),

$$\lambda_d = \sqrt{\frac{\varepsilon_0 \varepsilon_r k_B T}{q^2 N_D}} \ , \qquad \text{(I. 17)}$$

k_B being the Boltzmann constant and T the lattice temperature.

Neumann boundary conditions (the difference between the normal components of the respective electric displacements must be equal to any surface charge) are imposed in the semiconductor boundaries so that current only flows in/out of the device through the contacts in which a Dirichlet condition (where the potential is fixed) is imposed.

(b) Modes of operation and analysis of results

(b.1) Average and instantaneous magnitudes

The number of iterations must be sufficient to reach the stationary regime (or, in other words, stable oscillations). During the simulation, different magnitudes (current density, electric field, valley occupation, velocity, potential, etc.) are accumulated to calculate their instant and average values.

In this way, the instant value of a magnitude A in the $\boldsymbol{r}$ position, related to the p mesh, $A_p(\boldsymbol{r})$, where there are $N_p(t)$ carriers, will be (71):

$$A_p(\boldsymbol{r},t) = \frac{1}{N_p(t)} \sum_{i=1}^{N_p(t)} A_i(t)\,, \qquad \text{(I. 18)}$$

where $A_i(t)$ is the value of A for particle i at instant t.

An average over the time of all instant values of the A_p magnitude [calculated from Eq. (I. 18)] is made to determine the average value of A_p in the $\boldsymbol{r}$ position, $\overline{A_p(r)}$ after a transient period.

(b.2) DC operation mode

Typically, when one is interested in studying the stationary behaviour of the *I-V* curves of a diode (or other device), it is necessary to perform a DC analysis. For this, we shall employ the DC mode of operation, implemented in our simulator, whose scheme is depicted in Figure 1. 16 (a). By employing this mode, a constant bias V_{DC} is applied between the Device Under Test (DUT) terminals. When a DC bias V_{DC} is applied to the DUT terminals the average current density, J_A [obtained from the long-time sequences of the current density by employing Eq. (I. 18)], can be plotted and analysed, see Figure 1. 17. The DC dissipated power is given by Ohm’s law, $P_{DC}=V_{DC} \times J_A$.

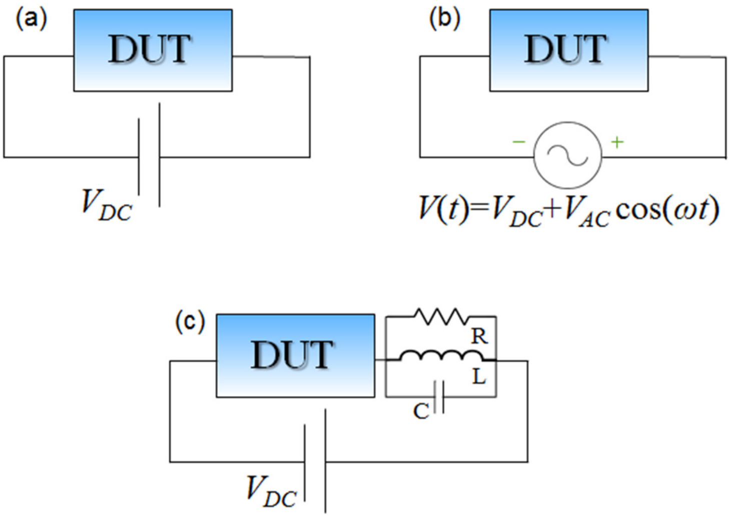
(a)
DUT
V_{DC}
(b)
DUT
$V(t)=V_{DC}+V_{AC}\cos(\omega t)$
(c)
DUT
R
L
C
V_{DC}

Figure 1. 16: (a) DC, (b) DC+AC and (c) RLC modes of operation scheme.

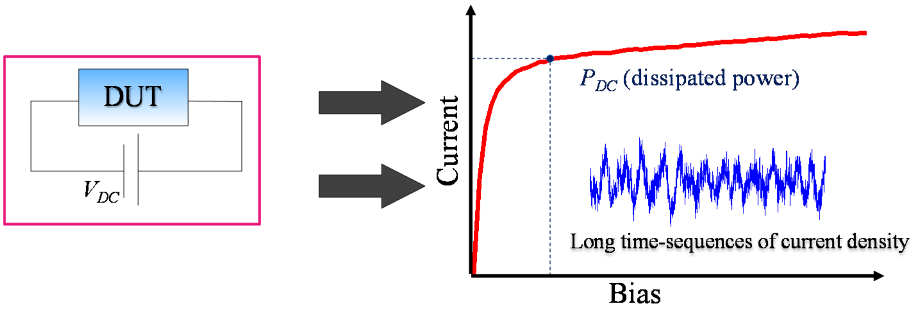
DUT
V_{DC}
Current
P_{DC} (dissipated power)
Long time-sequences of current density
Bias

Figure 1. 17: Average and instantaneous values.

To study the dynamics of the device, as in the case of the time-domain current density to evaluate Gunn oscillations, we need to analyse the frequency spectrum of the long-time sequences of the signal through the Fourier transform, Figure 1. 18.

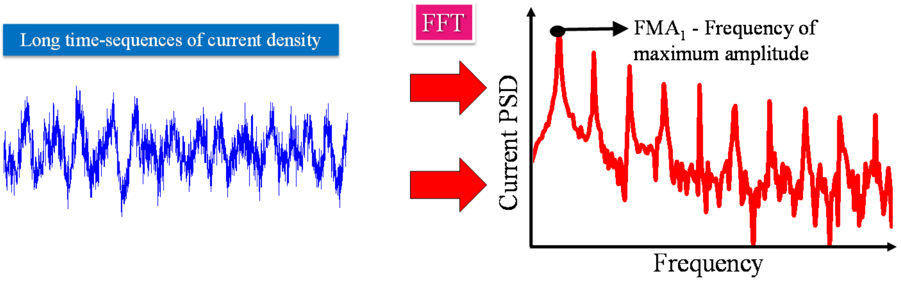
Long time-sequences of current density
FFT
FMA_1 - Frequency of maximum amplitude
Current PSD
Frequency

Figure 1. 18: Calculation of the Current PSD from long-time sequences of current density by employing the FFT. Definition of the Frequency of Maximum Amplitude (FMA).

In our particular case, we shall employ the Fast Fourier Transform (FFT), described in section 1.2.4 (c.2). We define the frequency at which the amplitude of the power spectral density (PSD) has a remarkable peak as the Frequency of Maximum Amplitude, FMA.

(b.3) DC + AC operation mode

When we wish to calculate the DC to AC conversion efficiency, or the impedance of the devices addressed in this thesis, one possible technique is to apply sinusoidal signals. For this, we created the DC + AC mode of operation. In our tool it is implemented by applying a time-dependent bias $V_{DC} + V_{AC}\cos(\omega t)$ between the DUT terminals. Its scheme is shown in Figure 1. 16 (b).

We define the DC to AC conversion efficiency according the following formula:

$$\eta = -\frac{P_{AC}}{P_{DC}}\,, \qquad \text{(I. 19)}$$

P_{AC} being the time-average AC power, defined by:

$$P_{AC} = \overline{(V(t) - V_A)(J(t) - J_A)}\,, \qquad \text{(I. 20)}$$

$V(t)$ being the instantaneous potential between the DUT terminals, V_A its average value, and $J(t)$ the instantaneous value of the current density.

- If $\eta > 0$ $(P_{AC} < 0)$→ The diode generates AC power from DC.
- If $\eta < 0 (P_{AC} > 0)$→ The diode consumes power (resistive behaviour)

To analyse the number of generation bands, the DC to AC conversion efficiency (η) *vs.* frequency is represented in Figure 1. 19 (a). The frequency at which the maximum efficiency is achieved is defined by the FME.

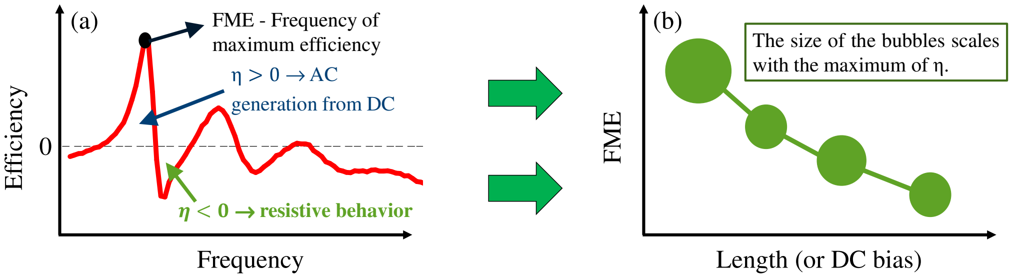

Figure 1. 19: (a) DC to AC conversion efficiency, and (b) FME and corresponding efficiency.

We shall also analyse the frequency (and its corresponding efficiency) *vs.* the length of the diodes (or the applied DC bias), depending on the situation, as shown in Figure 1. 19 (b). We remark that the size of the bubbles scales with the maximum of η.

Next, the method to calculate the impedance is presented. We apply a signal between the diode terminals with a harmonic component, $V(t) = V_{DC} + V_{AC}\cos(\omega t)$. The impedance of the diode is (110):

$$Z(\omega) = R(\omega) + jX(\omega)\,, \tag{I. 21}$$

where R is the resistance and X the reactance. These parameters are determined by the following expressions:

$$R(\omega) = \frac{V_{AC} I_R(\omega)}{I_R^2(\omega) + I_X^2(\omega)}\,, \tag{I. 22}$$

$$X(f) = \frac{V_{AC} I_X(\omega)}{I_R^2(\omega) + I_X^2(\omega)}\,, \tag{I. 23}$$

with $I_R(\omega)$ being the real part of the Fourier transform of the current, and $I_X(\omega)$ its imaginary part:

$$I_R\,(\omega) = \frac{1}{T}\int_0^T I(t)\cos(\omega t)\,dt\,, \tag{I. 24}$$

$$I_X(\omega) = \frac{1}{T}\int_0^T I(t)\sin(\omega t)\,dt\,. \tag{I. 25}$$

(b.4) RLC operation mode

Another possible alternative for calculating DC to AC conversion efficiency could come from the use of a proper resonant cavity coupled with the DUT. Under specific conditions, this resonant cavity could provide a quasi-sinusoidal signal of the same amplitude as that of the single-tone excitation of the DC + AC mode. However, from the point of view of manufacture, this is not always possible. In our particular case, we shall consider as a resonant cavity a simple parallel RLC resonant circuit connected in series with the DUT, as shown in Figure 1. 16 (c). More details are explained in section 2.3.1.

(c) The Ramo-Shockley theorem and Fast Fourier Transform (FFT)

(c.1) The Ramo-Schockley theorem

Calculation of the instant current is critical in the analysis of the static and dynamic characteristics, and noise, in an electronic device. The easiest and most intuitive way for calculating it would be to count the particles that enter/leave the device through a contact per unit of time. The main problem of this method is that, to be reliable, it requires many iterations. Furthermore, this technique does not allow us to calculate in a precise way the current at each instant of time and hence record its possible temporal fluctuations. Therefore, the use of a more precise method will allow a better analysis of the dynamic characteristics and noise.

We refer to the Ramo-Schockley theorem (111,112), originally developed for the calculation of the induced charge on any electrode of a vacuum tube, which can be considered as having no space charge within the apparatus. This theorem has also been extended to cases with the presence of stationary space charge (113), with inhomogeneous dielectric media (114), when there are electrodes with a variable potential involved (115), when the presence of mechanisms with extreme temporal dependence is included, and when there are Auger processes, photoexcitation, Shockley-Read-Hall recombination, etc. (116,117).

This is a very robust procedure for calculating the contribution to the current at a given electrode from all electrons that move inside the device. In this way, the movement of a charge carrier contributes to the current at the terminals although it does reach the contacts physically. The current calculated will be more precise and will have higher statistical significance. When the potentials of the electrodes are fixed, the change in position of the electron produces a variation in the contact charges (the lines of forces of the electric field change, and hence the density of charge in the terminals must be updated), which must be reflected in a current through the device. Thus, the contribution to the current is gradual, although when the electron leaves the device, the total contribution will evidently be the same as if we had taken into account its contribution only at the moment of its exit.

We consider a system (see Figure 1. 20) where *M* arbitrarily shaped electrodes are located in an inhomogeneous medium whose dielectric constant may vary in space.

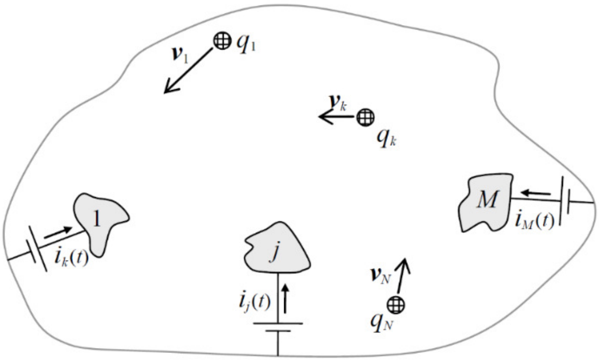

Figure 1. 20: Schematic representation of electrodes, charges and currents (80).

There are also *N* charged particles in the medium. The *M* electrodes are maintained at potentials by external power supplies. Using the superposition principle, we can calculate at each instant *t* the induced charge on the j^{th} electrode as a summation of the charge of each particle, q_k, weighted by a non-dimensional geometric factor $W_j^*(\boldsymbol{r}_k)$ that corresponds to the potential at the position of the particle *k*, $\boldsymbol{r}_k$, when the j^{th} electrode is kept at unit potential while all other electrodes are grounded and all the mobile and fixed charges are removed from our system (114). We thus have:

$$Q_j = -\sum_{k=1}^{N} q_j W_j^*(\boldsymbol{r}_k) \ . \qquad \text{(I. 26)}$$

To find the current flowing in the j^{th} electrode, we differentiate Eq. (I. 26) with respect to time:

$$i_j(\mathrm{t}) = \frac{dQ_j}{dt} \ , \qquad \text{(I. 27)}$$

obtaining the final form of current $i_j(t)$ in the quasi-static approximation:

$$i_j(\mathrm{t}) = -\sum_{k=1}^{N} q_j \boldsymbol{v}_k \overline{\nabla} W_j^*(\boldsymbol{r}_k) \, , \qquad \text{(I. 28)}$$

where $\boldsymbol{v}_k$ is the velocity of the k^{th} charged particle at time t (114). This current is solely contributed by the movements of the N charged particles with fixed potentials at electrodes.

Additionally, we have taken into account the current induced due to the time-varying potentials of the electrodes through capacitive coupling between electrodes, i_{Dj} (t), defined by:

$$i_{Dj}(\mathrm{t}) = -\sum_{p=1}^{M} C_{jp} \frac{\Delta V_p}{\Delta t} \;, \qquad \text{(I. 29)}$$

where C_{jp} is the diode geometrical capacitance between the j^{th} and p^{th} contacts, and ΔV_p is the increase in potential in the p^{th} electrode (114).

Therefore, the total current flowing in the j^{th} electrode denoted by i_{jT} (t) is:

$$i_{jT}(t) = i_j(\mathrm{t}) + i_{Dj}(\mathrm{t}) = -\sum_{k=1}^{N} q_j \boldsymbol{v}_k \overline{\nabla} W_j^*(\boldsymbol{r}_k) + \sum_{p=1}^{M} C_{jp} \frac{\Delta V_p}{\Delta t} \;. \qquad \text{(I. 30)}$$

In our simulations we will work with the total current density, $j_T(t)$, defined as:

$$j_T(t) = \frac{i_T(t)}{A}, \qquad \text{(I. 31)}$$

where A is the cross-section to the current.

For the diodes presented in Chapter 2, the total current density of Eq. (I. 32) will be named as j_d ($j_T(t) \equiv j_d$). For this study, Eq. (I. 30) can be simplified accordingly to:

$$j_d = j_v\,(t) + C_d \frac{dV_d}{dt} = -\frac{1}{L_T} \sum_{k=1}^{N} q v_k + C_d \frac{dV_d}{dt}\,, \qquad \text{(I. 32)}$$

where $j_v(t)$ is the drift current density, C_d the diode geometrical capacitance between the contacts, L_T the total length, and V_d the voltage applied between the diode terminals.

(c.2) Fast Fourier Transform (FFT)

By about 1750 Daniel Bernoulli was convinced that an *arbitrary* function could be represented by a Fourier series. Although Fourier series were used around this time by

Euler, d'Alembert, Lagrange and others, the general question of which functions could be represented by Fourier series was not settled. The majority opinion was far too conservative and definitely opposed to Bernoulli, and it was not until Fourier's 1811 paper on the propagation of heat that reasonably convincing arguments were given to state that a fairly arbitrary function could be represented by a Fourier series. Undoubtedly, Fourier's proofs could be, and indeed were, criticized for a lack of rigour. The results he obtained with his methods were impressive, however, and encouraged research in the right direction. Thus, in 1829, after being influenced by Fourier's work, Dirichlet gave some fairly general sufficient conditions for a function to have a Fourier series representation. From the 1850's onwards, research into Fourier series was carried out by Riemann, Cantor, and many others. This work finally culminated in Lebesgue's introduction of his integral and its applications to Fourier series, and in Hilbert's expansion of a function into a series of eigenfunctions of compact self-adjoint operator in the early 1900's. The Fourier transform was introduced by Fourier in his 1811 paper with a limiting argument based on Fourier series. Even today, the same argument is used in many textbooks to serve as a motivation (118).

The Fourier transform was further developed by Cauchy and Poisson. Over the years a number of special 'singular' Fourier transforms have been introduced. The culmination of this work is Schwartz' very beautiful theory of temperature distributions and the corresponding Fourier transform (118).

Regardless of whether $F(t)$ is periodic or not, a complete description of $F(t)$ can be given using sines and cosines (119). If $F(t)$ is not periodic it requires all frequencies to be present if it is to be synthesised. A non-periodic function may be thought of as a limiting case of a periodic one, where the period tends to infinity, and consequently the fundamental frequency tends to zero. The harmonics are more and more closely spaced and at the limit there is a continuum of harmonics, each of infinitesimal amplitude: $a(\nu)d\nu$, for example. The summation sign is replaced by an integral sign and we have that:

$$F(t) = \int_{-\infty}^{\infty} a(\nu)d\nu\cos(2\pi\nu t) + \int_{-\infty}^{\infty} b(\nu)d\nu\sin(2\pi\nu t) \qquad \text{(I. 33)}$$

or, equivalently:

$$F(t) = \int_{-\infty}^{\infty} a(v) \cos\big(2\pi vt + \theta(v)\big)\ dv \ , \tag{I. 34}$$

or, again:

$$F(t) = \int_{-\infty}^{\infty} \psi(v) e^{2\pi ivt} dv \quad . \tag{I. 35}$$

Just as with Fourier series, the function $\psi(v)$ can be recovered from $F(t)$ by inversion. This is the cornerstone of Fourier's theory because, astonishingly, the inversion has exactly the same form as the synthesis, and we can write, if $\psi(v)$ is real and $F(t)$ is symmetric (119):

$$\psi(v) = \int_{-\infty}^{\infty} F(t) e^{-2\pi ivt} dt \quad , \tag{I. 36}$$

so that not only $\psi(v)$ is the Fourier transform of $F(t)$, but $F(t)$ is the Fourier transform of $\psi(v)$. The two together are called a 'Fourier pair'. The variables that appear in the Fourier transform, t and v, are often time and frequency variables, respectively. The square of the spectrum, $P(v)$, is commonly called power spectrum, spectral density, power spectral density, or energy spectral density.

$$P(v) = |F(v)|^2 \ . \tag{I. 37}$$

The power spectrum of a signal is the power of that signal at each frequency, v, that it contains. This magnitude is of special interest in the spectral analysis of current oscillations.

Discrete Fourier Transform (DFT)

If one wishes to obtain the Fourier transform of a given function, it may happen that the function is defined in terms of a continuous independent variable, as is most often the case in books, especially in lists of transform pairs. But it may also happen that function values are given only as discrete values of the independent variable, as with physical measurements made at regular time intervals. Regardless of the form of the given function, if the transform is evaluated by numerical computing, the values of the transform will be available only at discrete intervals (120). The DFT allows us to evaluate the Fourier transform of functions sampled at fixed intervals during sequences of finite duration. Let us consider a function *f*(*x*), discretized in *N* samples, $\{f(x_0), f(x_0+\Delta x), f(x_0+2\Delta x), \dots, f(x_0+(N-1)\Delta x)\}$, separated by Δx.

The DFT is expressed by:

$$F(n\Delta v)=\frac{1}{N}\sum_{m=0}^{N-1} f(x_0+m\Delta t)e^{-j2\pi\frac{nm}{N}}\ , \tag{I. 38}$$

with *n*=0, 1, 2, …, *N*-1. The obtainable frequency resolution is equal to the inverse of the time duration during which a signal is being observed,

$$\Delta v=\frac{1}{N\Delta t}\,. \tag{I. 39}$$

Fast Fourier Transform (FFT)

Direct computation of an *N*-point DFT requires almost $O(N^2)$ complex arithmetic operations (121). An arithmetic operation involves a multiplication and an addition. However, this complexity can be significantly reduced by developing efficient algorithms. Two standard radix successive doubling algorithms are developed for the FFT: Decimation-in-Time (DIT) and Decimation-in-Frequency (DIF). The advantage of these methods is that they are able to compute the discrete Fourier transform much better than other available algorithms. In general, fast algorithms reduce the computational complexity of an *N*-point DFT to about $Nlog_2N$ complex arithmetic operations. Additional advantages are reduced storage requirements and reduced computational error due to finite bit length arithmetic (121).

In order to understand why doubling algorithms are more efficient, the DIT operation is discuss below. The DIT algorithm is based on decomposing an *N*-point sequence (assume $N=2^l$, *l*=integer) into two *N*/2-point sequences (one of even samples and another of odd samples) and obtaining the *N*-point DFT in terms of the DFTs of these two sequences. Just alone, this operation results in some savings in the arithmetic operations. Further savings can be achieved by decomposing each of the two *N*/2 point sequences into two N/4 points DFTs. This process is repeated until two-point sequences are obtained (121).

For our calculations, the doubling algorithm described in ref. (105) was implemented. The long time-sequences of the current density can be studied, Figure 1. 18, and by employing the FFT (taking into account 2^{17}=131072 iterations and Δt=1 fs), the current Power Spectral Density (PSD) is obtained. The frequency resolution is 7.62 GHz.

CHAPTER 2: COMPARISON OF THE PERFORMANCE OF InP- AND GaN-BASED GUNN DIODES

Since the 1960s, when the Gunn effect was discovered, and in view of the existence of a negative differential resistance (NDR) (82,84,122), some materials such as GaAs or InP have been used in the electronics industry to manufacture vertical structures working as emitters, sources and amplifiers in the millimeter region of the electromagnetic spectrum (22,23). Currently, other wide-band gap materials such as GaN have been employed for these purposes, but without success (57,58). Even though there are several works where vertical structures have been analysed (59), there is a lack of systematic studies aimed at comparing the abilities of the different materials of vertical diodes with and without (w/o) a notch. This will be the main theme of this chapter. We shall carry out a numerical comparison between the performances of InP- and GaN-based vertical diodes: DC bias conditions, DC to AC conversion efficiency, and power spectral density. Oscillation frequencies from 130 GHz up to 400 GHz have been predicted in structures w/o notch for InP at the fundamental harmonic frequency. For GaN, a large number of harmonics are generated, reaching frequencies up to 2 THz. It is found that InP diodes with a length of the active region of 900 nm provide efficiencies of up to 5.5 % at frequencies ∼225 GHz. Several bias conditions, doping profiles and different lengths of the active region will be considered. The effect of heating in GaN-based diodes will also be addressed.

2.1. State of the art

Gunn diodes were introduced by J. B. Gunn at the *Solid State Device Research Conference* (84) in 1963. He studied the current-voltage characteristic of GaAs- and InP-based devices. He discovered that when a constant bias was applied between the diode terminals, and after the electric field had surpassed a critical value (threshold electric field), spontaneous current oscillations appeared inside the device (123). GaAs- and InP-based Gunn diodes of a length of the active region ∼1 µm are classically used to generate signals up to a few hundred GHz [∼200 GHz (22,23,124)]. A detailed studied of the behaviour of these devices, focusing attention mainly on InP-based devices, one of the objectives of this dissertation, can be found in the following papers:

- ***V. Gruzinskis et al.*** (1993) (22): These authors present a theoretical analysis of the transport characteristics exhibited by a n^+nn^+ InP-based diode with a length of the active region of 1 µm under a stable generation of microwave power. By employing a kinetic and a hydrodynamic approach, frequency ranges for generation (100 GHz < f < 200 GHz) are estimated and the predicted DC-AC conversion efficiencies (∼4 %) are in good agreement with the experimental results (125,126). Moreover, they found a maximum increase in the generation frequency up to values in the 600 GHz - 800 GHz range when the length of the active region was reduced to sizes between 300 nm and 200 nm.
- ***V. Gruzinskis et al.*** (1994) (23): In their work, they developed a closed hydrodynamic model and the associated numerical procedures for simulating hot-carrier transport in submicron semiconductor devices (lengths of the active region 0.72 µm, 0.9 µm and 1 µm). The results were compared with a standard MC approach. In InP-based diodes, they achieved a wide band tuning of the generation frequency from 100 GHz up to 200 GHz. Power generation of 150 mW at 140 GHz for a 1 μm-long InP device was predicted.
- ***Kamoua R.*** (1998) (127): The author develops a harmonic-balance technique for the analysis of high-frequency TED oscillators. The nonlinear behaviour of the TED is modelled according to the ensemble MC approach to semiconductor device simulation. His results are in very good agreement with experimental data from InP TED oscillators operation at 131.7 GHz and 151 GHz in the fundamental mode and at 188 GHz in the second-harmonic mode. For the fundamental frequencies of 131.7 GHz and 151 GHz, the output RF power reaches 55 mW and 135 mW, respectively.

However, the intrinsic characteristics of GaAs and InP make it impossible, experimentally, for them to reach the THz range. One of the limitations of these materials arises from their saturation velocity (v_S=0.91x10^7 cm/s for GaAs and v_S=1.16x10^7 cm/s for InP), which is not very high; this parameter is crucial for oscillation frequencies close to the THz range to be reached. In addition, these materials have a low threshold and breakdown electric fields (88), so the application of high bias is not possible and hence the power level delivered is small. The solution may come from the use of nitrides, such as GaN, with a higher threshold electric field and saturation velocity. According to the predictions of several authors (128,129), technological efforts to manufacture GaN diodes able to support the high bias voltage required to operate under negative differential resistance conditions will be necessary to successfully achieve high power oscillations in the 200-400 GHz range. Indeed, so far experimental evidence of oscillations has not been achieved in GaN vertical diodes, mostly because of the proximity of the metal contacts and the very high applied voltages required for operation beyond the threshold field, which typically cause the diodes to burn out before oscillating (57,58). The following references provide more details of the design of GaN-based devices:

- ***E. Alekseev et al.*** (2000) (88): Hydrodynamic dynamic simulations were used to carry out the harmonic power analysis of GaAs and GaN n^+nn^+ diode oscillators in order to evaluate their large-signal microwave characteristics. GaN diodes (with a length of the active region of 3 µm) offer twice the frequency capability of GaAs Gunn diodes (87 GHz *vs*. 40 GHz), while their output power density is 2x10^5 W/cm^2 compared to ~10^3 W/cm^2 for GaAs structures.
- ***V. Gruzinskis et al.*** (2001) (130): These authors studied electron transport and microwave power generation in the 200-300 GHz frequency range by $n^+n^-nn^+$ zinc-blende GaN and $n^+pnn^-n^+$ wurtzite GaN structures by means of Monte Carlo (MC) particle simulation. They predicted (for diodes ~1 µm) that at room temperature in the 230-250 GHz frequency range more than 350 mW of microwave power can be delivered by the $n^+pnn^-n^+$ wurtzite GaN structure in the continuous wave operation mode and over 1.3 W in the pulsed mode. Their simulations of 1 µm-long notched $n^+n^-nn^+$ zinc-blende GaN transfer electron

devices in a parallel resonant circuit with a standard 50 Ω load resistor at 300 K produced 0.5 W of microwave power at 240 GHz [this power is more than three times greater than the theoretically predicted peak power of 150 mW at 140 GHz for a 1 μm-long InP device (23)].

- ***R. P. Joshi et al.*** (2003) (131): Oscillators based on bulk wurtzite GaN are presented in MC-based studies. The authors examined two structures: (i) devices with the conventional single notch structure, and (ii) repetitive structures with serial segments to fashion a "multiple domain" device. Although they did not examine a multiple domain structure in the context of GaN Gunn diodes, they did mention that theoretical predictions for GaAs Gunn oscillators call for an N^2 scaling in output power with the number of segments, N (132). Conversion efficiencies of up to about 2 % can be attained at 300 K and would be around 1.45 % at 450 K. The room temperature value was higher than that reported for GaAs devices (133). They predicted peak power outputs of 0.68 W and 0.52 W at 300 K and 400 K (higher values than those predicted in other materials, about 0.15 W for InP). A reduction in the operating frequency with increasing temperature (from 300 K up to 450 K) was observed due to a lower drift velocity, from 140 GHz to 110 GHz.
- ***C. Sevik et al.*** (2004) (134): The dynamics of large-amplitude Gunn domain oscillations from 120 GHz to 650 GHz was studied by means of MC simulations in GaN $n^+n^-nn^+$ channels. The main finding was that by increasing the notch width, GaN Gunn diodes could be operated with greater efficiency at their second harmonic frequency (~1 % for 240 GHz) than at the fundamental (~0.7 % for 110 GHz). Thus, the notch width can be adjusted to enhance AC to DC conversion efficiency at higher harmonics more efficiently than the fundamental frequency.
- ***C. Sevik et al.*** (2004) (129): These authors investigated the efficiency and harmonic enhancement trends in GaN-based Gunn diodes by means of an ensemble MC. They studied the effects of a doping notch and its position within the active channel which favours a doping notch positioned next to the cathode. The width of the notch can be optimized to enhance the higher-harmonic operation without degrading its performance at the fundamental mode. They showed that, as a general trend, the variations of temperature, channel doping,

and the notch width primarily affected the phase angle between the current and voltage wave forms rather than the amplitude of oscillations.

- ***R. F. Macpherson et al.***(2008) (128): These authors carried out simulations of GaN Gunn diodes at various doping levels and temperatures, reaching frequencies up to 300 GHz via the MC technique in a diode with a transit region of 1.11 µm doped at 1.5 x 10^{23} m^{-3} and a notch of length 0.15 µm doped at 0.5x10^{23} m^{-3}. For their particular analysis, the authors stated that a good approximation is that the frequency varied linearly with temperature. In order to provide some data, the expected variations of frequency would be 40 GHz over a temperature range of 150 K.
- ***R. F. Macpherson et al.***(2008) (135): In this work, the use of doping spikes by employing the MC technique was compared with notched devices in GaN Gunn diodes. Their results suggest that the use of a doping spike is a feasible alternative to a doping notch in the design of a GaN-based Gunn diode. For a diode with a transit region of 1.05 µm, the device (with a doping spike or with a notch) works at a frequency of ∼230 GHz. The diode with a doping spike operates similarly to a realistic notched device, with only a small decrease in AC-DC conversion efficiency.
- ***L. Yang et al.*** (2012) (59): The authors described a comparative investigation on sub-micrometer InN and GaN Gunn diodes with an ATLAS simulator from Silvaco, working at THz frequencies. The results showed that 0.3 µm - 1 µm Gunn diodes with a diode area of 500 µm^2 could generate fundamental frequencies of around 200-800 GHz and AC currents of several hundred of mA. InN diodes exhibited more stable oscillation, whereas GaN diodes generated higher oscillation frequencies in both the dipole-domain and accumulation-domain modes due to the different negative differential resistance characteristics of high-field transport. Notch-doped Gunn diodes generated oscillations at a dipole-domain mode, whereas uniformly doped Gunn diodes generated oscillations at an accumulation-domain mode, regardless of whether they were based on InP or GaN. Moreover, the oscillation in dipole-domain mode was more stable than that in the accumulation-domain mode for both the GaN and InN Gunn diodes.

Furthermore, InN was more suitable for short Gunn diodes to achieve higher frequencies as compared with GaN (InN has lower *N*x*L* limit).

- ***C. F. Dalle*** (2015) (136): The potential of vertical differentiated GaN-transferred electron devices (TED) was compared with that of the base flat doping profile TEDs for the generation of AC power sources at 1 THz. The author employed a 1-D numerical physical macroscopic model based on the energy-momentum approach. Different structures were optimized: n^+nn^+, $n^+n^-nn^+$, $n^+nn^-nn^+$, n^+pnn^+. AC-emitted power in the 180 mW - 210 mW range was predicted for the n^+nn^+, $n^+n^-nn^+$, and n^+pnn^+. The results of the comparison revealed that while the differentiated doping profile TEDs slightly improved both the RF performance and electronic limitation, above all they significantly improved the thermal limitation resulting from the high DC bias conditions imposed by the GaN material threshold electric field.

As an alternative to GaAs, InP and GaN vertical diodes, planar structures such as InGaAs/InAlAs (73), GaAs/AlGaAs (55,137,138) and InGaAs/AlGaAs planar diodes (139) and GaN/AlGaN self-switching-diodes (SSDs) (72) are currently being investigated.

2.1. Geometry of vertical diodes

For our analysis, two types of Gunn diodes were chosen, without (n^+nn^+) and with ($n^+n^-nn^+$) a notch, depicted in Figure 2. 1. The diode with a notch contains a lightly-doped n^- region adjacent to the cathode, which aims to create a high electric field zone, promoting the onset of charge accumulation domains in the cathode. This n^- region always has a fixed length of 250 nm, which is considered to be included in the transit region length *L*. In both types of structure, the transit or active region is sandwiched between two heavily doped n^+ ohmic contact regions, whose lengths are 100 nm and 300 nm at the cathode and anode, respectively. This asymmetry is considered because, while the cathode n^+ region is always at equilibrium, for high bias electrons enter the anode n^+ region with high energies and many of them are in upper valleys, a certain length being necessary for them to thermalize before reaching the anode.

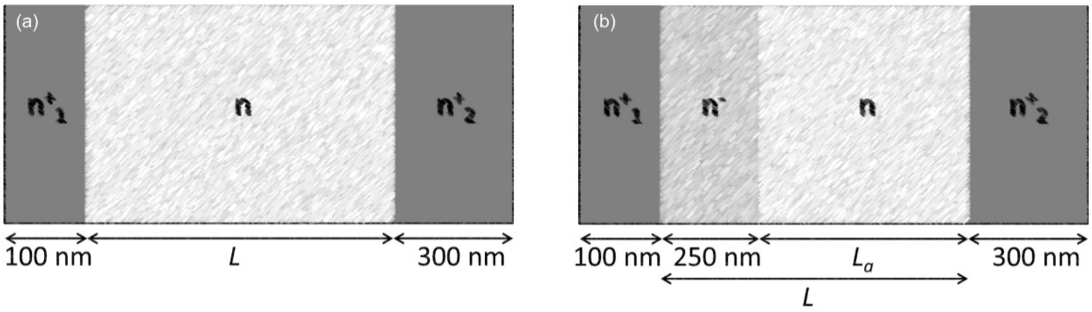

Figure 2. 1: Geometry of the two types of Gunn structures studied. (a) Diode without notch and (b) diode with a 250 nm-length notch placed next to the cathode. The lengths of n^+ contact regions are 100 nm and 300 nm at the cathode and anode, respectively, in both structures. n^+=2×10^{18} cm^{-3}, DS1: n=1×10^{17} cm^{-3} and n^-=2×10^{16} cm^{-3} and DS2: n=5×10^{17} cm^{-3} and n^-=1×10^{17} cm^{-3}. Four different lengths, L=1500, 1200, 900 and 750 nm were simulated, always at room temperature.

Systematic MC simulations were performed for four different lengths of the active region (L=1500 nm, 1200 nm, 900 nm and 750 nm), two doping levels, and two materials (InP and GaN). In the case of the structures with a notch, the length of this region (always 250 nm) is included in L. The vertical length is 10 nm. The current density is normalized with this length.

Regarding doping levels, we considered two doping schemes, denoted as DS1 and DS2. For DS1 we used n=1×10^{17} cm^{-3} and n^-=2×10^{16} cm^{-3} while for DS2 we used n=5×10^{17} cm^{-3} and n^-=1×10^{17} cm^{-3}. It should be noted that a ratio of n/n^-=5 was kept. The contact regions were always doped at n^+=2×10^{18} cm^{-3}.

Certain physical restrictions must be imposed in our simulations. One of them is that the mesh size must be less than the Debye length, as indicated in Chapter 1. The corresponding values of the Debye length according to the carrier concentration, N_D, and the material properties are summarized in Table 2. 1. The dimension of the employed meshes in the discretization of the diode for both technologies (InP and GaN) are close to the Debye lengths of the GaN material.

N_D(10 ^{18} cm $^{-3}$)	λ_d InP (nm)	λ_d $GaN(nm)$
0.02	29.76	25.21
0.1	13.31	11.28
0.5	5.95	5.04
2.0	2.97	2.52

Table 2. 1: Debye length for the different doping levels under analysis.

In addition, the time-step Δt used in the simulations must be lower than the characteristic time of the faster process involved in our study (as was also mentioned in Chapter 1). In Table 2. 2 the values of $2/\omega_p$ y τ_d for the cases under analysis are shown.

	InP		GaN	
$N_D(10^{18}$ cm $^{-3})$	$2/\omega_p$ (ps)	τ_d(fs)	$2/\omega_p$ (ps)	τ_d(fs)
0.02	1.55	63.4	2.20	273
0.1	0.69	12.6	0.99	54.6
0.5	0.31	2.53	0.44	10.9
2.0	0.15	0.63	0.22	2.73

Table 2. 2: τ_d and ω_p for different doping levels, where InP and GaN are taken into account.

As has been mentioned, a time-step *Δt* of 1 fs was used in the simulations. For this time-step, and in the particular case of N_D=2x10^{18} cm^{-2} and for the InP material, the condition imposed in Eq. (I. 16) is not satisfied. This will not affect our MC simulations because the access areas (contacts) are not decisive in the effects studied.

2.2. DC bias

In this section, we report the Monte Carlo simulations carried out to study the ability to generate Gunn oscillations of diodes based on InP and GaN with different lengths of the active region and two doping profiles by applying DC bias conditions between the diode terminals(5).

2.2.1. InP diodes with DS1

First, the dependence of the current density on the applied bias for InP-based diodes with and w/o notch, for DS1 and different lengths of the active region, *L*=750 nm, 900 nm, 1200 nm and 1500 nm, is shown in Figure 2. 2 (a).

---

[5] The number of iterations was *N*=150000.

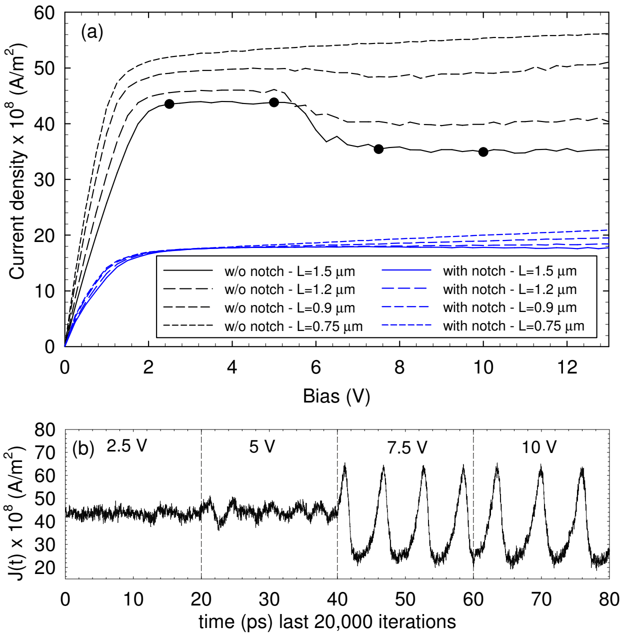

Figure 2. 2: (a) *I*-*V* curves for the two types of InP diodes, with and w/o notch, and for four different lengths of the active region, *L*=750 nm, 900 nm, 1200 nm and 1500 nm, for the DS1. (b) Time-sequences of current density for the structure w/o notch with *L*=1500 nm for *V*=2.5 V, 5 V, 7.5 V and 10 V.

Gunn instabilities appear once the current saturation has been reached, since the main origin of this effect is the onset of intervalley transfer mechanisms (82,84,122). In the diodes w/o notch, an abrupt decrease in the average current density for a bias of around 5 V is obtained, even if Gunn oscillations are already present for lower voltages. In order to investigate the physical mechanism in the device that originates the current drop, the time-sequences of current density for *V*=2.5 V, 5 V, 7 V and 10 V are plotted for the longer diode in Figure 2. 2 (b). A transition in the oscillation regime at 5 V is observed, from the accumulation-layer mode to transit-time dipole-layer mode (87). In the accumulation-layer mode, the time-sequences of the current density have a sinusoidal-like shape. However, once the transit-time dipole-layer mode appears, the current exhibits an asymmetric nature, leading to a decrease in the average current density. In the notched structures the presence of the higher resistive n^- region lowers the value of the current in the *I*-*V* characteristics of Figure 2. 2 (a).

To study the behaviour of the frequency domain and the spectral purity of the Gunn oscillations obtained, Figure 2. 3 shows the PSD [defined in Section 1.2.4 (b.2)] of the current in a diode with *L*=1500 nm, with and w/o notch, when a bias *V*=5 V is applied. The notched structure provides a higher number of harmonics, with frequencies of

FMA_1=152.6 GHz, FMA_2=297.5 GHz, FMA_3=450.1 GHz and FMA_4=595.1 GHz for the first, second, third and fourth harmonic, respectively. The diode w/o notch only shows a clear harmonic with FMA_1=213.6 GHz.

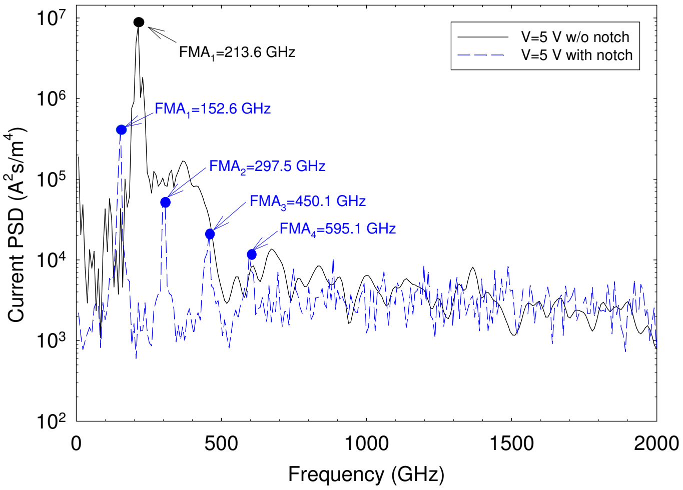

Figure 2. 3: Current PSD for InP-based diodes (with and w/o notch) with *L*=1500 nm for a bias *V*=5 V.

It is noteworthy that the diode with notch offers higher spectral purity but the power of the first harmonic is more than one order of magnitude smaller in comparison with the structure w/o notch, as expected from the lower current level. The frequency and amplitude of the most significant peak of the PSD, FMA_1, versus bias are represented in Figure 2. 4.

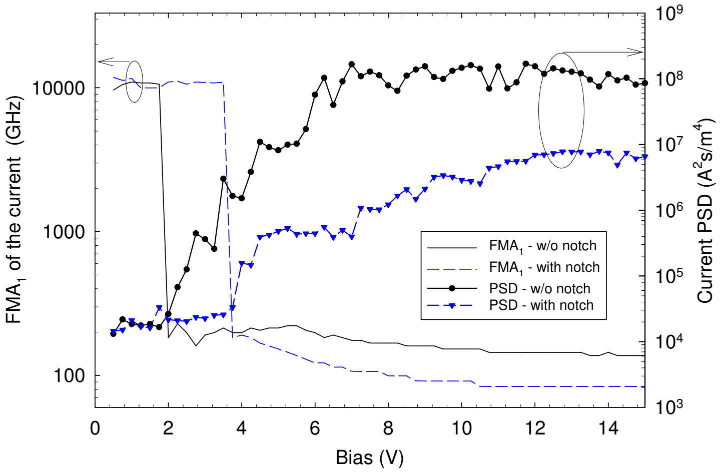

Figure 2. 4: FMA_1 and corresponding amplitude of the current PSD *vs.* the bias for InP-based diodes (with and w/o notch) with *L*=1500 nm and for the DS1.

In general, for all devices and lengths (not shown here), at low bias FMA_1 lies in the terahertz region and is related to plasma effects (140). In particular, for the structure of

Fig. 4, FMA$_1$ is around 10 THz when bias ≤ 3 V. However, as bias increases, a significant shift in that peak (from high to low frequency) takes place, together with a huge bump in amplitude. In fact, this strong change in behaviour occurs when Gunn oscillations start, and it is therefore possible to define a threshold voltage, V_{th}, for this effect. For the structure with notch, V_{th} is 3.75 V, and for the diode w/o notch $V_{\mathrm{th}}=2$ V. In this latter device, a saturation of the amplitude of the most significant peak of the current PSD is also observed from a bias around 7.5 V, indicating the existence of a mature oscillation.

The bias dependence of the value of FMA$_1$ for different lengths of the active region (L=1500 nm, 1200 nm, 900 nm and 750 nm) in diodes with and w/o notch is shown in Figure 2. 5 for $V>V_{\mathrm{th}}$. When the length of the active region is reduced, the frequency obviously increases because carriers must travel a smaller distance to reach the anode. In diodes w/o notch, Figure 2. 5 (a), oscillation frequencies are in the 130 GHz up to 400 GHz range. More detailed inspection reveals that frequency can be estimated as v_{sat}/L_{eff}, where $L_{eff}=L-L_d$, with L_{eff} being the effective length and L_d the dead length. We have estimated for $v_{sat}=1.16\times10^7$ cm/s that, irrespective of the length of the channel, L_{eff} is about 40 % of the total length.

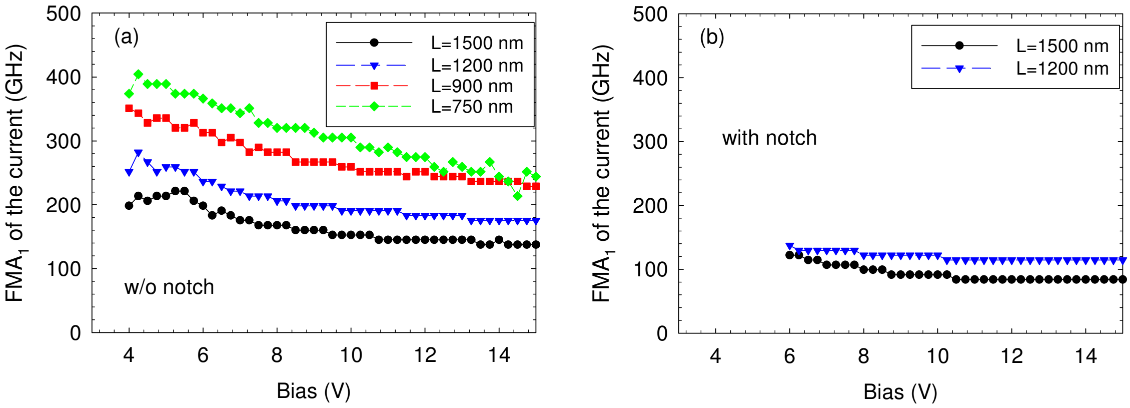

Figure 2. 5: FMA$_1$ for $V>V_{th}$ *vs.* bias for different lengths of the active region: L=750 nm, 900 nm, 1200 nm and 1500 nm in an InP-based diode for the DS1. (a) Structures w/o notch and (b) structures with notch.

To illustrate this phenomenon, the time-sequence of current density, the instantaneous carrier concentration, and the electric field profiles are plotted for a 1.5 µm-InP diode w/o notch for five time-points spaced evenly in the same period, in Figure 2. 6 (a), Figure 2. 6 (b) and Figure 2. 6 (c), respectively. As can be observed, the charge-accumulation domain is being formed well inside the active region, which has already been detected in other structures (141). We reproduce the accumulation-layer transit mode plot depicted in Section 1.1.3 (b) in Figure 1. 5.

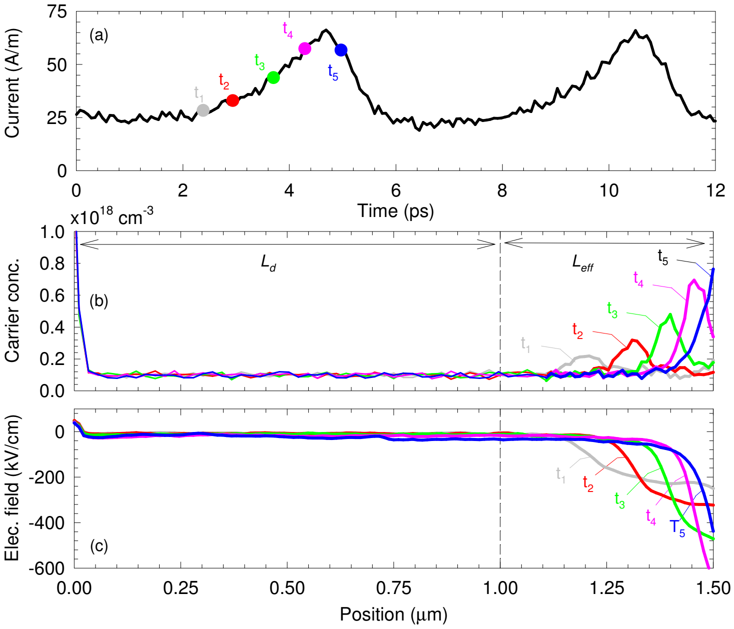

Figure 2. 6: (a) Time-sequence of current density, where coloured circles mark the equidistant time moments when the instantaneous profiles of (b) the carrier concentration and (c) the electric field are recorded for a 1.5 µm length InP diode w/o notch and with 8 V applied between contacts.

Regarding diodes with notch [Figure 2. 5 (b)] for lengths of 750 nm and 900 nm, although the condition $n_0L>10^{12}$ cm^{-2} is satisfied (87) no Gunn oscillations are observed. For the longer diodes, lower oscillation frequencies are found, in the 80-140 GHz range. Now, the oscillation frequency can be estimated roughly as v_{sat}/L because the notch creates a high electric field that fixes the domain onset. From the point of view of manufacturing, notched devices can easily tune the frequency by designing them with the proper length of the active region. Also, for a given length, diodes w/o notch provide higher oscillation frequencies in comparison with structures with notch.

To conclude the study of InP-based diodes, in Figure 2. 7 (a) we analyse FMA$_n$ (up to n=5, if it exists) and its amplitude versus bias [Figure 2. 7 (b)] when L=1500 nm. The notched structure provides a higher number of harmonics, but the frequencies are lower and their power is also lower (by one or two orders of magnitude). For example, at 10 V in a diode w/o notch, FMA$_3$=450 GHz, while in the structure with notch to obtain such high frequency it is necessary to reach the fifth harmonic, FMA$_5$=442 GHz. In addition, for the previous case the structure with notch generates harmonics with higher spectral purity with respect to the diode w/o a notch, but the PSD is reduced by a factor ~30.

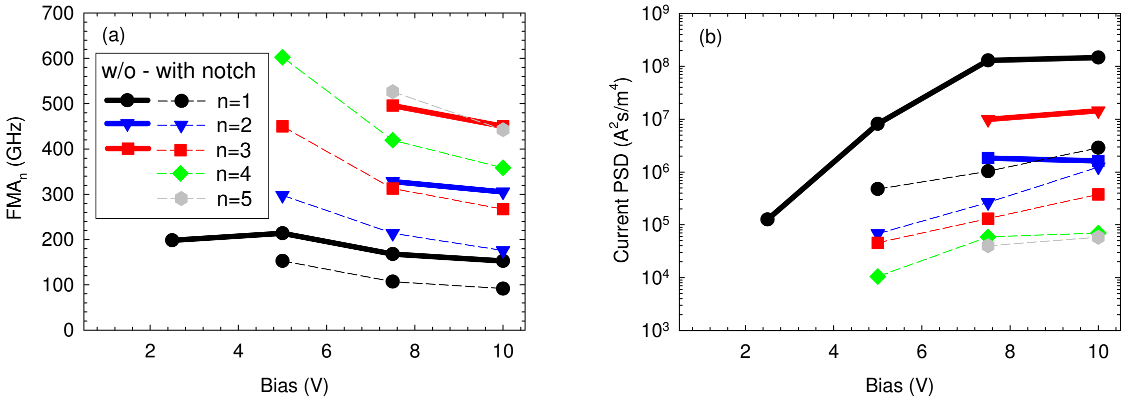

Figure 2. 7: (a) FMA_n and (b) corresponding amplitude of the PSD for the different harmonics n (up to the fifth if it exists) *vs.* bias in an InP diode with length *L*=1500 nm for DS1. The results in structures with and w/o notch are represented by dashed and solid lines, respectively.

2.2.2. GaN diodes with DS1 and DS2

Once the DC study in InP-based diodes had been carried out, the next step consisted of an analysis of the dependence of the current density on the bias for GaN-diodes with DS1 and DS2, with and without notch, with different lengths of the active region: 750 nm, 900 nm, 1200 nm and 1500 nm, as shown in Figure 2. 8 (a) and Figure 2. 8 (b), respectively.

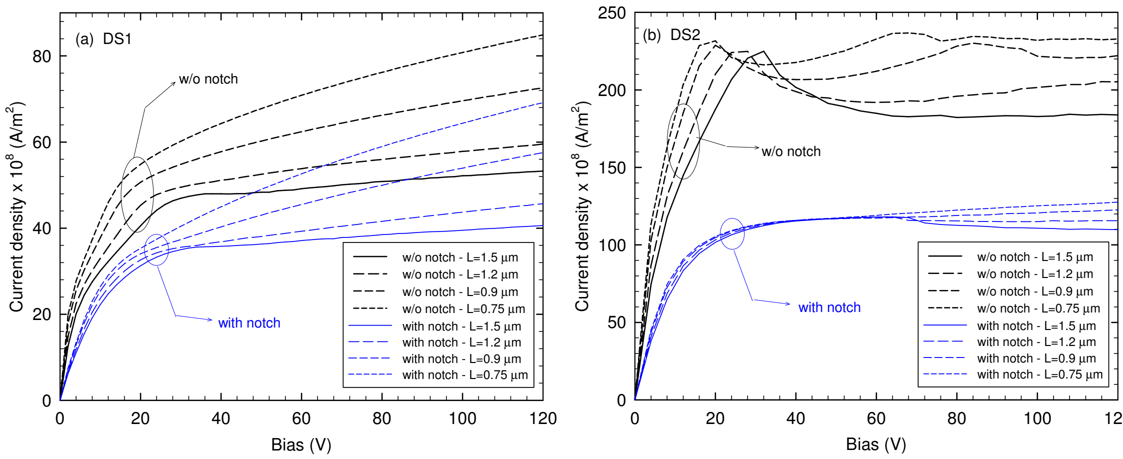

Figure 2. 8: *I-V* curves for the two types of GaN-diodes, with and w/o notch, and for four different lengths of the active region, *L*=750 nm, 900 nm, 1200 nm and 1500 nm. (a) DS1 and (b) DS2.

It should be noted that for GaN the applied bias is higher than for InP because intervalley transfer and negative differential mobility in GaN appear at much higher electric fields.

Finally, while in InP-based diodes the notch limits the current density for DS1, which in saturation is essentially the same for all the lengths, such is not the case in GaN for the same doping level. This is an indication that this notch in the GaN diodes is not effective and will presumably not fix the position of the domain onset. In order to boost the effect of the notch in the GaN diodes, a second doping scheme, DS2, where the doping of the n^- and n regions was larger, was considered. Note that the concentration ratio between the n and n^-regions (n/n^-=5) is the same for DS1 and DS2, but that the gradient in the latter scheme is higher, thus increasing the electric field in the notch beyond the threshold value (E_T=210 kV/cm). The results are summarized in Figure 2. 8 (b). First, two main differences with respect to the case of DS1 [Figure 2. 8 (a)] can be observed: (i) diodes without notch exhibit a more visible negative incremental resistance zone and (ii) when present, the notch limits the current in the diodes, as happened in the InP structures, such that the saturation current is the same, independently of the length. This indicates that with the doping values of DS2 the notch is more effective. To confirm this, we analysed the current PSD for DS1 and DS2 in Figure 2. 9 (a) and Figure 2. 9 (b), respectively. For DS1, similar current power spectral densities and a strikingly high number of harmonics (reaching ~2 THz) were achieved in both structures, with and w/o notch. Note that for the InP diode with the same doping scheme (DS1) [Figure 2. 3] only four harmonics are observed in the notched diode and only the fundamental one in the structure w/o notch. The GaN diode with notch (and DS1) provided a slightly lower FMA$_1$ (~180 GHz) with respect to the structure w/o notch. However, for higher-order harmonics the difference between the corresponding FMA$_n$ increased. Note that in contrast to InP, in GaN the amplitude of the harmonics was very similar for both structures (with and w/o notch). As mentioned above, this could indicate that the notch in these devices was not effective. However, with DS2, Figure 2. 9 (b), the notch is more effective and it really is the fixing the point of the formation of the domain close to the cathode. Thus, as in InP for DS1 where the notch is effective, the PSD and the FMA$_1$ in notched structures are clearly smaller. For example, FMA$_1$ is 99 GHz and 140 GHz for structures with and w/o notch, respectively and, as for InP, the diode with notch shows a higher number of harmonics (the tenth reaching 1 THz). Furthermore, the current PSD does not decay significantly up to the third harmonic, its extraction being more feasible.

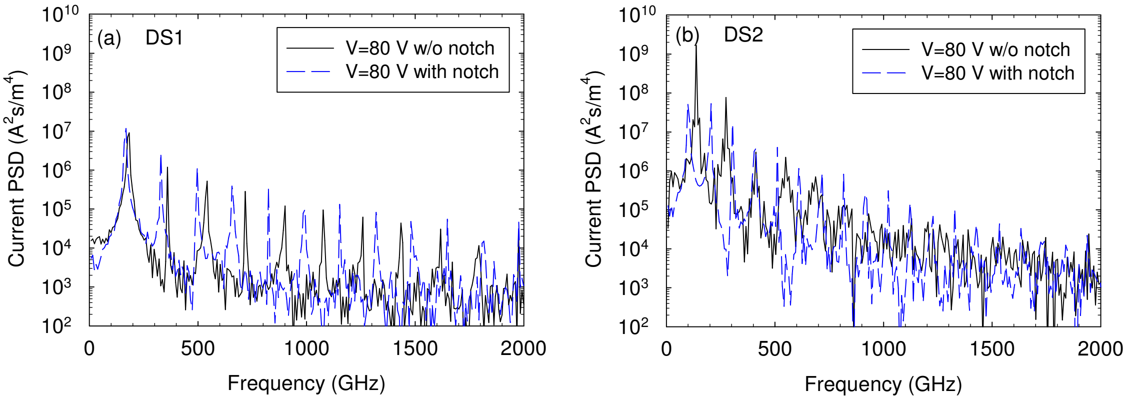

Figure 2. 9: Current PSD for GaN-based diodes (with and without notch) with *L*=1500 nm for a bias *V*=80 V. (a) DS1, (b) DS2.

We now focus attention only on the third harmonic of the current. In Figure 2. 10 (a) and (b) we represent the dependence of FMA_3 and the corresponding values of the PSD on the bias, respectively, for a diode with a length of 1500 nm and the DS1 and DS2 doping schemes. Higher FMA_3 values (460 GHz-580 GHz) are achieved with DS1 in both types of diode, with and w/o notch, in comparison with DS2, which provides an FMA_3 of about 280 GHz-442 GHz. The main difference between DS1 and DS2 oscillation frequencies is that whereas in the first case the values of FMA_3 in diodes with and w/o notch are very similar, for the DS2 scheme larger differences are observed. This again shows that the notch for the DS2 is more effective. The amplitude of the current PSD at FMA_3 [Figure 2. 10 (b)] is one or two orders of magnitude higher for the DS2, as expected from its higher current density values.

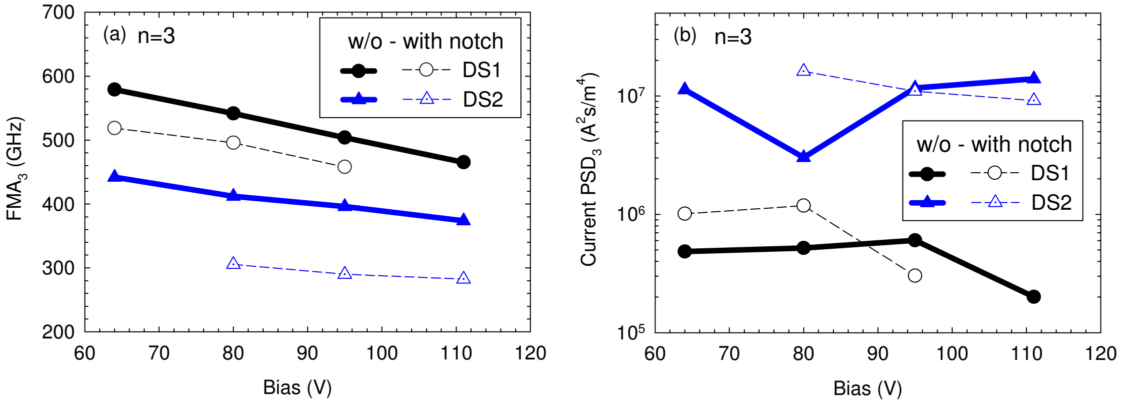

Figure 2. 10: FMA_3 and (b) corresponding amplitude of the PSD *vs.* bias in a GaN diode with length *L*=1500 nm for the DS1 and DS2. Structures with and w/o notch results are represented by dashed and solid lines, respectively.

The non-trending data-point at 80 V seen in Figure 2. 10 (b), for the DS2 in the structure without a notch, is attributed to the non-linearities of the devices that affect the DC and AC response separately. To conclude, Figure 2. 11 shows the bias dependence of FMA_1 in DS2 diodes for L=750 nm, 900 nm, 1200 nm and 1500 nm. As described for InP (Figure 2. 5) when L is reduced, for diodes w/o and with notch, FMA_1 increases, in this case reaching a maximum value of around 300 GHz. Although GaN diodes are expected to attain higher fundamental frequencies than InP diodes, the longer effective transit length L_{eff} of ~65 % observed in GaN structures leads to slower Gunn oscillations.

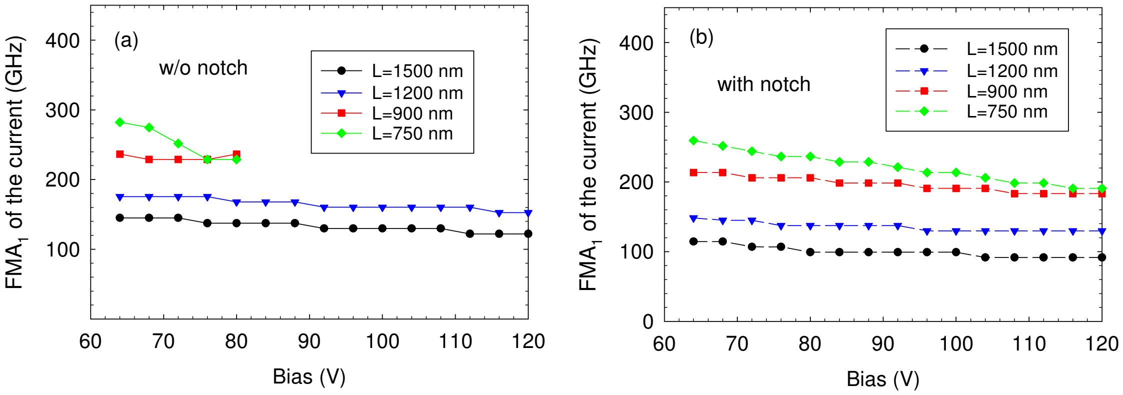

Figure 2. 11: FMA_1 for $V > V_{th}$ *vs.* bias for different lengths of the active region (L=1500 nm, 1200 nm, 900 nm and 750 nm) in a GaN-based diode with DS2. (a) Structures w/o a notch, (b) structures with a notch.

As expected, notched diodes provide lower FMA_1. While for this doping scheme the condition $n_0L>8\times10^{12}$ cm^{-2} is fulfilled in all cases (87,88), note that the structures with notch [Figure 2. 11 (b)] exhibit Gunn oscillations for all lengths and for all bias ranges, while diodes without a notch [Figure 2. 11 (a)] do not oscillate for ≥ 80 V in the case of L=750 nm and 900 nm. Therefore, short notched diodes can generate signals with higher power and very high frequency at higher biases. In this context, it is interesting to consider the threshold voltages V_{th} for Gunn oscillations: structures w/o a notch exhibit lower values of V_{th} and decrease with L (from 36 V for L=1500 nm to 20 V for L=750 nm) while in the diodes with a notch V_{th} is higher and remains constant with L at 38 V.

2.3. DC + AC bias

Once the DC analysis has been concluded, in this part of the work simulations under DC + AC bias conditions in InP- and GaN-based diodes are carried out to optimize their oscillation frequency and the DC to AC conversion efficiency. We show that equivalent operating conditions are achieved by direct application of a sinusoidal AC voltage superimposed over the DC bias and by simulation of the intrinsic device coupled with the consistent solution of a parallel RLC resonant circuit connected in series(6).

2.3.1. Equivalence of the RLC circuit and single-tone excitation

We shall demonstrate that in some cases the excitation obtained through an equivalent resonant circuit, by proper selection of the R, L and C parameters, and the operation of the diode under a single-tone excitation like that of Eq. (II.1), are equivalent.

$$V_d(t) = V_{DC} + V_{AC}\cos(2\pi f t)\,. \tag{II.1}$$

For this purpose, we shall compare the value of the signal applied between the diode terminals $V_d(t)$ calculated from Eq. (II.1) with the one obtained when only the DC bias is applied but the diode is connected in series with a parallel RLC resonant circuit, see Figure 2. 12.

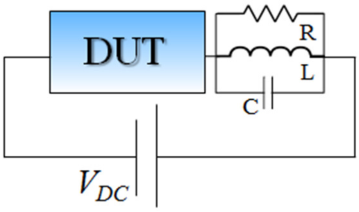

Figure 2. 12: RLC modes of the operation scheme.

The equations of such a circuit can be written as follows (142)

$$V_{DC} = V_d + V_C\,, \tag{II.2}$$

where V_d and V_C are the voltage drops at the terminals of the diode and the RLC circuit, respectively. We need to solve the Poisson equation together with the external circuit equations. The total current density flowing through the diode is

$$j_d = \mathrm{C}\frac{dV_\mathrm{C}}{dt} + j_\mathrm{L} + \frac{V_\mathrm{C}}{\mathrm{R}}\,, \tag{II.3}$$

with j_L the current density flowing through the inductance L:

---

(6) The number of iterations taken into account was *N*=300000.

$$V_{\mathrm{C}} = \mathrm{L}\frac{dj_{\mathrm{L}}}{dt}. \tag{II.4}$$

Taking into account the generalized Ramo-Shockley Theorem (114), discussed in Section 1.2.5, and by considering a finite differences technique and a time-independent source signal, we have:

$$V_d(t) = \frac{-j_v(t) + \frac{\mathrm{C_d}}{\Delta t}V_d(t-\Delta t) + \frac{V_{DC}}{\mathrm{R}} + j_L(t-\Delta t) + \frac{\Delta t}{\mathrm{L}}V_{DC} + \frac{\mathrm{C}}{\Delta t}V_d(t-\Delta t)}{\frac{\mathrm{C_d}}{\Delta t} + \frac{1}{\mathrm{R}} + \frac{\Delta t}{\mathrm{L}} + \frac{\mathrm{C}}{\Delta t}}\ . \tag{II.5}$$

$V_d(t)$ is updated at each time-step (Δt) by using this expression before solving the Poisson equation in the device (142).

Figure 2. 13 shows the direct equivalence between the parallel RLC circuit and the single-tone excitation. Here, an InP diode w/o notch, with DS1 and at *L*=900 nm, is considered. In Figure 2. 13 (a) we plot the results for a simulation using V_{DC}=7.5 V, R=3x10^{-9} Ωm^2, L=4.7x10^{-23} Hm^2, and C=0.0081 F/m^2, affording a quality factor *Q*∼40 [a parameter that describes how under-damped an oscillator or resonator is (143)].

In Figure 2. 13 (b) a single-tone scheme of 243 GHz and V_{AC}=1.9 V, with V_{DC}=7.5 V, is used. As is clear, both operating conditions are equivalent as long as the values considered for R, L and C in the resonant circuit lead to a quasi-sinusoidal signal of the same amplitude as that of the single-tone excitation [Figure 2. 13 (b)]. A phase shift slightly greater than π/2 between the current density and the applied voltage appears, which means that the diode exhibits a positive efficiency η in such conditions. In the case of the use of the resonant RLC circuit, the mean current density is I_m=39x10^8 A/m^2 and η=1.9 %, while on applying the single-tone we obtain, I_m=38.2 x10^8 A/m^2 and η=2.0 %. Consequently, and for this particular case, both methods are essentially equivalent. In the subsequent analysis, in order to be systematic, and at the expense of providing results that in some cases could correspond to non-realistic conditions, below we shall make use of the single-tone excitation [Eq. (II.1)] because it is less time-consuming than the resonant-circuit simulation. Indeed, in the above case the *Q* factor of the parallel RLC resonant circuit is large enough to filter out the other possible harmonics and thus provide a pure sinusoidal excitation. However, in other cases it would not be possible to replicate a pure sinusoidal excitation by using the simple parallel RLC circuit considered here. This would require including a further band-pass filter. However, circuit design is out of the scope of this thesis.

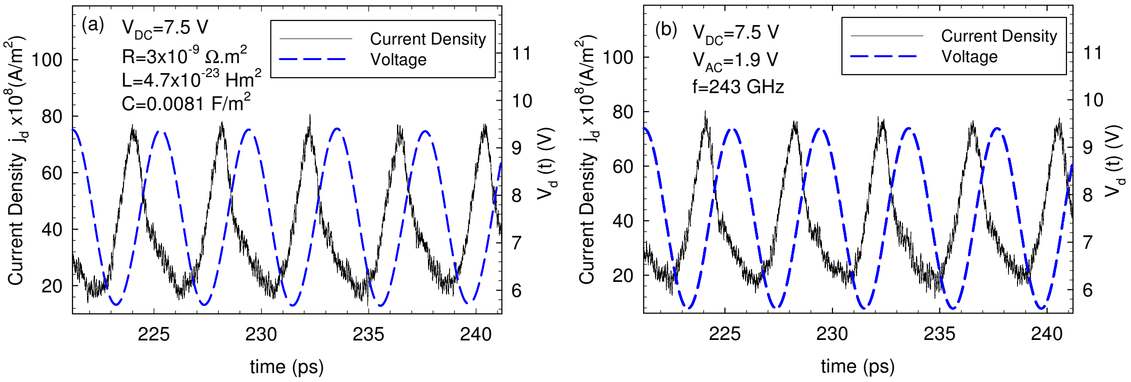

Figure 2. 13: Time-sequences of current density j_d and applied voltage V_d (t) in a InP n^+nn^+ diode using the DS1 and V_{DC}=7.5 V. (a) Resonant RLC circuit in series with the diode (R=3x10^{-9} Ωm^2, L=4.7x10^{-23} Hm^2, and C=0.0081F/m^2) and (b) excitation by means of a single tone of frequency of 243 GHz and V_{AC}=1.9 V [Eq. (II.1)].

Thus, the results obtained under the single-tone excitation illustrate the intrinsic potential of the diodes to generate signals at different frequency bands, but obtained under optimum conditions, which in some cases may not be affordable experimentally in a straightforward way.

2.3.3. Dependence of efficiency on length, bias conditions and material

In order to analyse the performance of the diodes operating as emitters, the DC to AC conversion efficiency, η (explained in Section 1.2.5), was evaluated by means of the superposition of a single-tone sinusoidal potential of amplitude V_{AC} at a DC bias of V_{DC}[7]. The dependence of η on the frequency f of the AC excitation for an InP-based diode with L=900 nm (DS1) and with V_{DC}=12.0 V and V_{AC}=1.5 V is shown in Figure 2. 14 (a). Higher frequencies are achieved in the diode without notch in comparison with the diode with notch for the first generation band. This is basically because the notch fixes the onset of the charge accumulation domain in the cathode region while in the diode w/o notch it takes place well inside the active region.

In the case of the diode with notch, three bands with η>0, indicating the generation of AC power, are observed. The FME (frequency of maximum efficiency) for the first generation band is FME_1=137 GHz with an efficiency of 0.92 %; for the second generation band FME_2=238 GHz, with still a competitive efficiency of η=0.28 %; and the third one FME_3=369 GHz, with an efficiency of 0.03 %. The bands potentially suitable for oscillations match the range of frequencies where the real part of the impedance is negative [Re(Z)<0], as can be observed in Figure 2. 14 (b) (110). The exact values for the diode notch are 71-156 GHz and 206-275 GHz, where we have identified the presence of one or two charge accumulation domains inside the diode's active region.

---

[7] All results of this section are for the DS1.

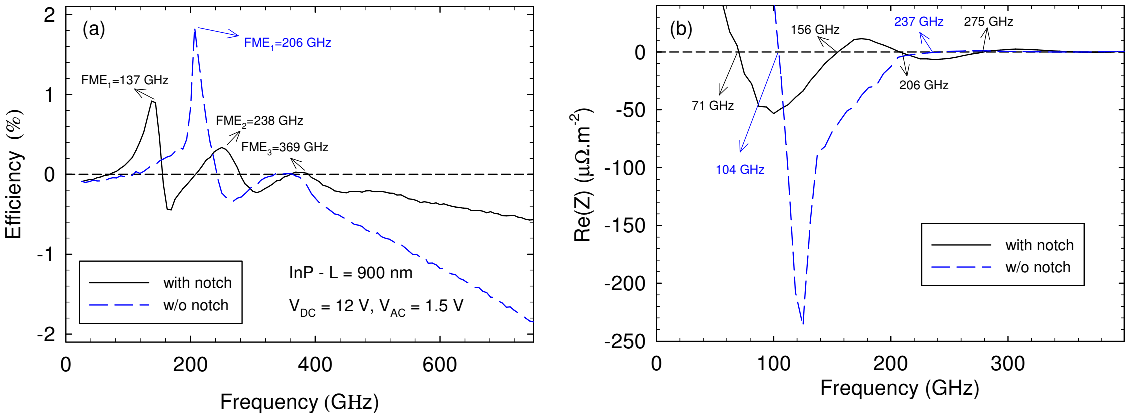

Figure 2. 14: (a) DC to AC conversion efficiency *vs.* frequency for InP-based diodes (with and w/o notch) with L=900 nm and for the DS1. Single-tone excitation with V_{DC}=12 V and V_{AC}=1.5 V. (b) Real part of the impedance.

For the diode without notch, we identify only one range, where Re(Z)<0, to be 104-237 GHz. A value of 1.84 % for efficiency is achieved for the first generation band at 206 GHz. It is remarkable that in all cases, as was found in refs. (22,23), the top limit (zero crossing) of the first negative band of the real part of the impedance approaches the self-oscillation frequency (DC analysis) of the diode, [see Figure 2. 5].

Below we report a systematic study of the frequency of the oscillations and the conversion efficiency, η, by comparing the dependence on the length and the DC bias for both semiconductors, InP and GaN, using DS1. Figure 2. 15 shows the values of FMEs in the different generation bands as a function of diode length (studying up to the third generation band, if it exists).

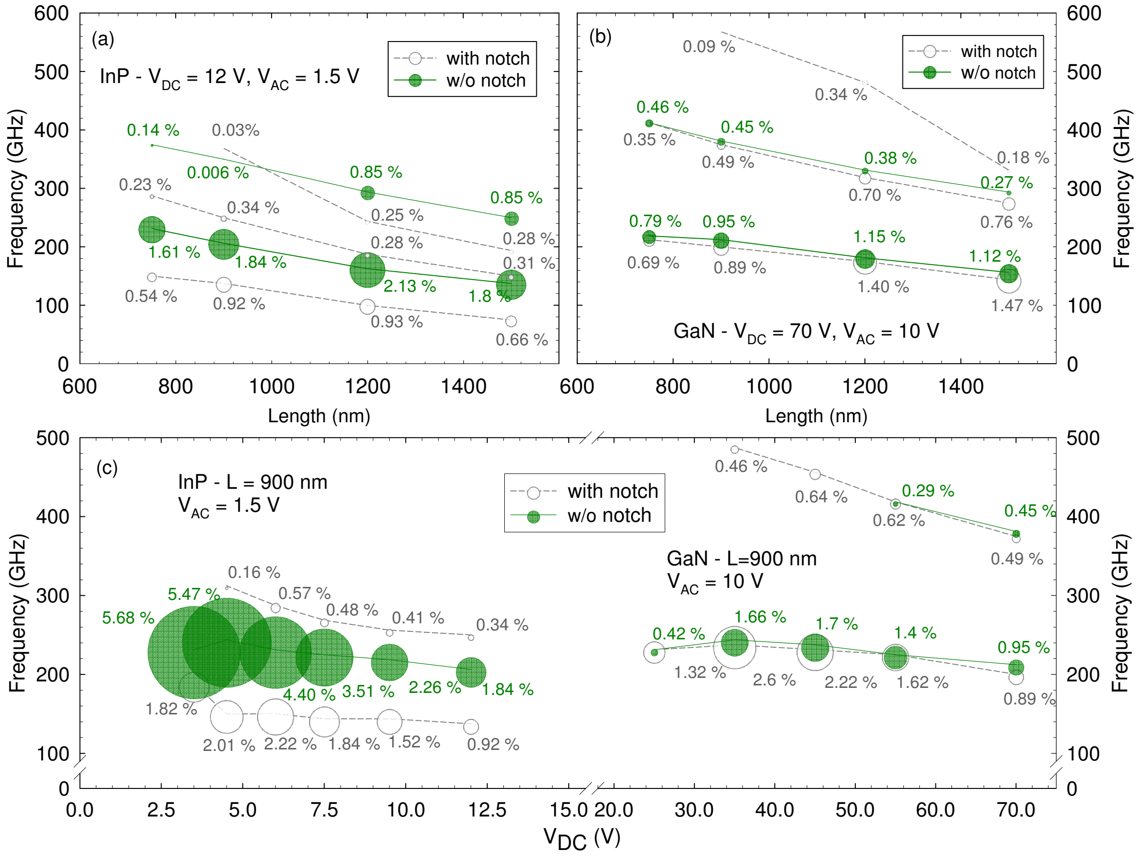

Figure 2. 15: FME and corresponding efficiency of the different generation bands found in diodes with the DS1 with and w/o notch. The size of the bubbles scales with the maximum of the DC to AC conversion efficiency, *η*, is indicated for the different generation bands. The dependence on the length of the active region is shown for (a) InP diodes using V_{DC}=12 V and V_{AC}=1.5 V and (b) GaN diodes using V_{DC}=70 V and V_{AC}=10 V. (c) Dependence on the DC bias for *L*=900 nm and using an AC excitation of V_{AC}=1.5 V for InP and V_{AC}=10 V for GaN.

In the case of InP, for V_{DC}=12.0 V and V_{AC}=1.5 V, the FMEs lie in the 70-400 GHz range [Figure 2. 15 (a)]. As explained before regarding to Figure 2. 14 (a), the absence of notch provides better performance in terms of the values of *η* and FME for the first generation band. In all cases the shorter the active region, the higher the FME, but efficiency remains nearly constant. It is remarkable that in diodes w/o notch for *L*=900 nm and 1500 nm the value of *η* in the first generation band is similar (1.84 %), but the FME of the oscillations is 68.75 GHz higher for the shorter one.

For GaN [Figure 2. 15 (b)] we used V_{DC}=70 V and V_{AC}=10 V, and we obtained FMEs between 100 and 600 GHz. In this case, in contrast to InP there is no significant difference between the results in the presence and absence of notch. This phenomenon is due to the ineffectiveness of the notch at fixing the nucleation of the high-field domain.

Therefore, the notch does not determine the location of the onset of charge accumulation. This onset of charge accumulation takes place at the same position inside the active region irrespectively of the presence or absence of notch. In GaN, electrons have higher effective mass than in InP, and they move more slowly and are subject to many scattering mechanisms inside the notch. Thus, for the n^-n gradient of DS1, and even if the electric field is quite high in the notch, they do not gain enough energy to rise to the upper U-valleys. The highest efficiency, 1.47 %, is achieved with a length of L=1500 nm but for a small FME of 143 GHz, while the length that provides the highest FME, 568 GHz (third generation band), is L=900 nm, but gives a very low efficiency of 0.09 %. Finally, the diode with notch, with L=1200 nm, even shows a fourth generation band, with a FME of 638 GHz but with very low efficiency of 0.04 % (not included in this Figure; this case will be studied later, in Figure 2. 16).

Regarding the effect of the bias conditions on the frequency of the oscillations, Figure 2. 15 (c) offers the results for L=900 nm in InP and GaN diodes up to the second generation band. Let us start with the InP case, where V_{AC}=1.5 V and V_{DC} is swept from 3.5 V up to 12 V. The range of FMEs found is 100-320 GHz. Diodes without notch display only one generation band in the range 206-243 GHz, while diodes with notch exhibit more than one band in almost all the situations. The most relevant result is that the DC to AC conversion efficiencies achieved without notch are high, above 5 %, than those obtained with notch. For diodes without notch, as a general feature the higher the V_{DC} value, the lower the efficiency and the FME as a consequence of the higher electric field inside the structure (with the only exception of V_{DC}=3.5 V, the voltage at which the oscillations are close to disappearing and the FME decreases). However, when the diode has a notch, it fixes the oscillation frequency, and the FME shows practically no dependence on V_{DC} for the first generation band, while the efficiency decreases for higher V_{DC}, as in the previous case. Again, for V_{DC}=3.5 V a different behaviour is found and only one generation band exists. The maximum efficiency for the first generation band is 2.22 %, corresponding to an FME of 150 GHz and a bias V_{DC}=6 V. For this bias, it is also observed that η in the second generation band takes the highest value, 0.57 %, at 288 GHz.

In the case of GaN, we consider V_{AC}=10 V, and V_{DC} is swept from 25 V up to 70 V, values notably higher than in InP diodes. In this case, the range of FMEs achieved is much larger, between 100 and 500 GHz. Again, the presence of the notch does not seem to be effective since there is no significant difference between the results concerning the structures with and without notch. This means that the domain is always created inside the active region (at similar distance from the anode) and not in the vicinity of the cathode. As a consequence, in the two cases for the first generation band η and the FME decrease with the increase in V_{DC}, with FME in the 200-243 GHz range. For V_{DC} <35 V, efficiency begins to decrease until the oscillation disappears completely since electrons do no gain enough energy to be in the negative differential mobility region. Even if the FMEs are the same, the diodes with notch provide higher efficiency in all cases, except for V_{DC}=70 V in the first generation band. It is expected that increasing the doping levels will improve the role played by the notch, and this is studied in next section.

To conclude the study of the DS1, in Figure 2. 16 (a) we show the efficiency *vs*. frequency for GaN-based diodes with L=1200 nm (V_{DC}=70 V and V_{AC}=10 V).

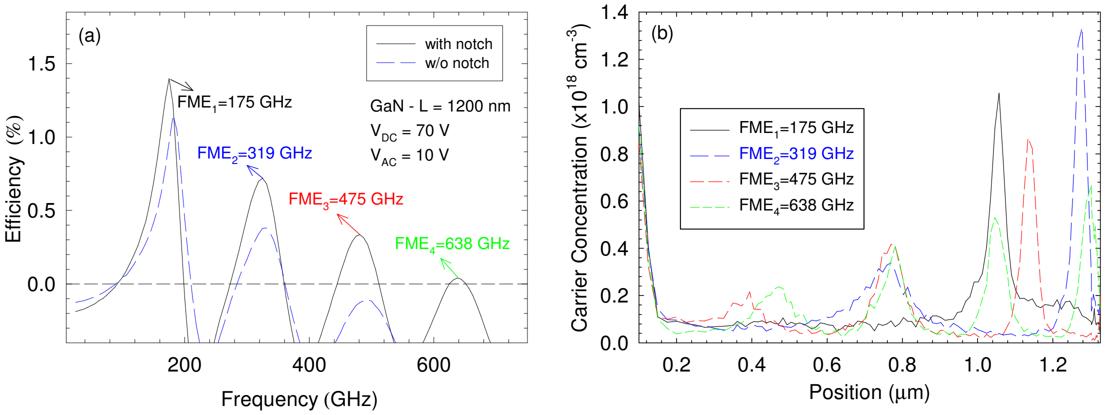

Figure 2. 16: (a) DC to AC conversion efficiency *vs.* frequency for GaN-based diodes (with and w/o notch) with L=1200 nm and for the DS1. Single-tone excitation with V_{DC}=70 V and V_{AC}=10 V. (b) Instantaneous profiles of the carrier concentration along the diode corresponding to a given time within one period of the AC signal for the frequencies at the maximum of the emission bands of FME=175, 318.7, 475 and 637.5 GHz.

As mentioned above, in this particular case a fourth generation band appears at 638 GHz in the notched diode. In Figure 2. 16 (b) instantaneous profiles of carrier concentration along the diode with notch are plotted for different frequencies of the AC excitation, with FME=175, 319, 475 and 638 GHz (FMEs of each generation band). As expected, an increasing number (from 1 to 4) of charge domains drifting along the active region is observed for increasing frequencies of the AC excitation. The generation bands and the associated FMEs are not equally separated since the nucleation of several domains reduces the so-called dead space.

2.3.4. Results for DS2

We now consider, only for GaN, the second doping scheme, denoted as DS2, where the doping of the n^- and n regions is larger. In Figure 2. 17 (a) we again analyse the dependence of the FME and maximum efficiency on length.

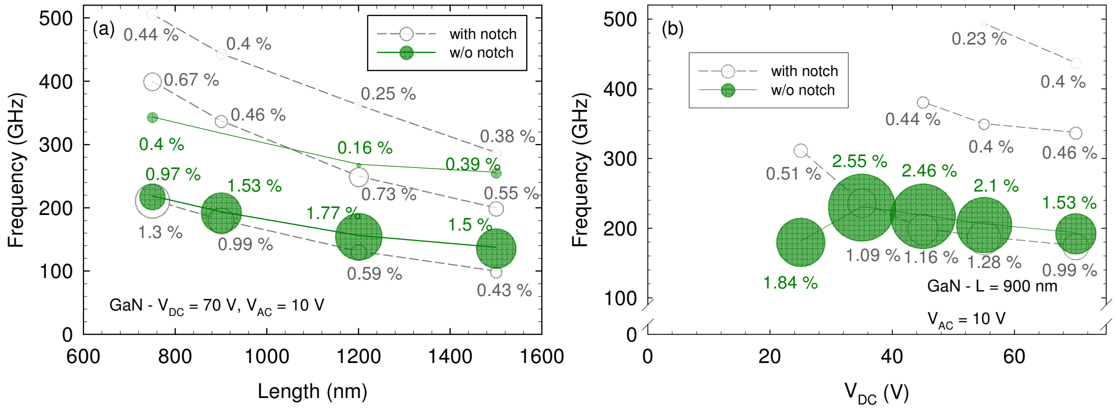

Figure 2. 17: Results for a GaN diode (with and w/o notch) when DS2 is considered. Dependence of the FME and corresponding efficiency of the different generation bands on (a) the length of the active region (V_{DC}=70 V and V_{AC}=10 V) and (b) DC bias for L=900 nm, using V_{AC}=10 V. The size of the bubbles scales with the maximum of the DC to AC conversion efficiency, η, and is indicated for the corresponding generation band.

For this particular case, there are noticeable differences between both types of diodes, with and without notch, being more prominent in the longer structures (L=1200 and 1500 nm). With DS2, although the concentration ratio between the n and n^- regions is the same (n/n^-=5), the gradient is higher, thus increasing the electric field in the notch beyond the threshold value (E_T=210 kV/cm), see Figure 2. 18 (a). A significant electron transfer from the Γ_1 valley to the U valley inside the notch is observed, Figure 2. 18 (b), such that its presence is actually effective at fixing the point of formation of the domain. For the device with notch, up to a third generation band is visible, 500 GHz being reached with significant efficiency.

Furthermore, for *L*=900 nm even the sixth generation band has been identified (shown in Figure 2. 19), with an FME of 675 GHz, and for *L*=750 nm the fifth one reaching 688 GHz (not shown in the graphic).

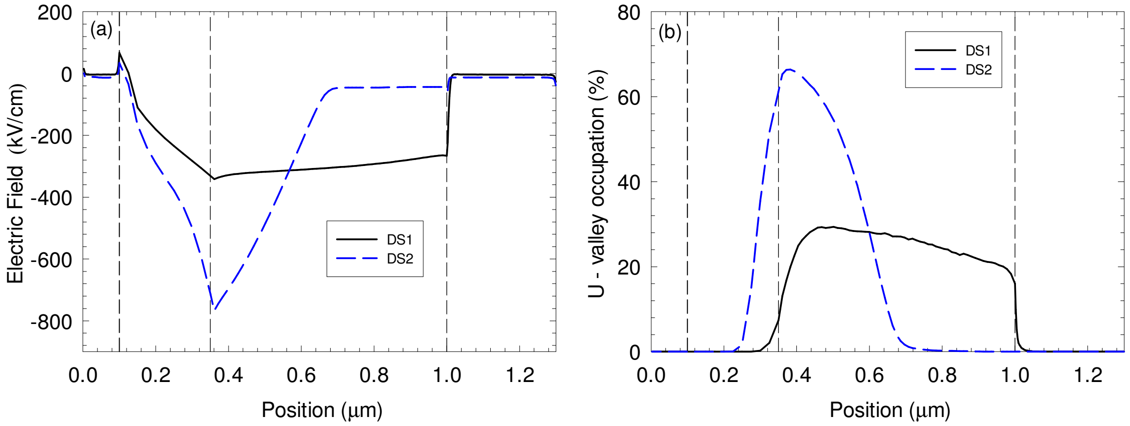

Figure 2. 18: (a) Average electric field and (b) U-valley occupation *vs.* position at 25 V for a GaN-based diode with notch with *L*=900 nm for the DS1 and DS2 schemes.

Figure 2. 17 (b) shows the FME *vs.* the DC bias V_{DC} in the diode with *L*=900 nm (with and without notch) when V_{AC}=10 V, and V_{DC} is swept from 25 V up to 70 V. Only one generation band is observed in the diode without notch, where the best η is obtained for 35 V. Indeed, higher DC to AC maximum conversion efficiencies and FMEs are obtained for decreasing bias, down to 35 V. However it is the structure with notch that, for a bias of 25 V, provides the highest FME (312 GHz), although with less efficiency. It is remarkable that FMEs close to 500 GHz in the third generation band can be achieved when V_{DC} is 55 V with an efficiency of 0.23 %.

Finally, to study the effect of the amplitude of the AC excitation, V_{AC}, we calculated the values of η for a GaN-based diode with notch and *L*=900 nm for the DS2, Figure 2. 19. Three values of V_{AC}=6.5 V, 8.5 V and 10 V were considered, with V_{DC}=70 V. The number of generation bands is determined by V_{DC} when a moderated level of the bias V_{AC} is applied. When the V_{AC} component is reduced, a lower η, but at slightly higher FMEs, is achieved for the first and second generation bands. The same behaviour was observed for the DS1 in InP diodes (see inset of Figure 2. 19). For higher generation bands, the FMEs do not vary significantly. We hope that such excellent predictions for GaN diodes can be confirmed experimentally soon.

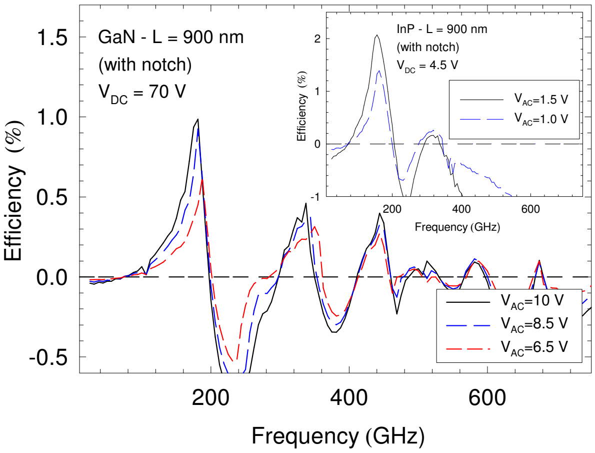

Figure 2. 19: DC to AC conversion efficiency *vs.* frequency for a GaN-based diode with notch with *L*=900 nm and for the DS2 and with V_{DC}=70 V. The AC excitations used are V_{AC}=10 V, 8.5 V and 6.5 V. The inset shows the DC to AC conversion efficiency *vs.* frequency for an InP-based diode with notch with *L*=900 nm, and with V_{DC}=4.5 V. The AC excitations used are V_{AC}=1.5 V and 1.0 V

2.4. Effect of operating temperature

Since GaN devices will likely be used for high-power applications, it is necessary to study the effect of high temperature in their operation. Self-heating effects could be substantial at the high power values used in the diodes, and could deteriorate their performance. We simulate the diode with a notch, with *L*=900 nm, for the second doping scheme, under DC bias conditions (77.07 V) and DC+AC bias conditions, at V_{DC}=70 V and V_{AC}=10 V (Figure 2. 20).

For DC bias conditions, Figure 2. 20 (a) it should be noted that although the fundamental harmonics are around ∼200 GHz for both temperatures (300 K and 500 K), a significant PSD is obtained for the 10th harmonic (∼2 THz). At 500 K, the frequency of the harmonics is slightly lower but the PSD does not vary significantly in comparison with the result obtained at room temperature.

Under DC + AC bias conditions, Figure 2. 20 (b), it can be observed that in comparison with the result obtained at room temperature, the FMEs are smaller for the different bands and η is slightly lower. This effect evidently takes place because of the smaller drift velocity of electrons at higher temperature. In any case, a fifth generation band where the FME is 625 GHz with an efficiency of 0.06 %, and a fourth one with η=0.15 % at 475 GHz, are still obtained.

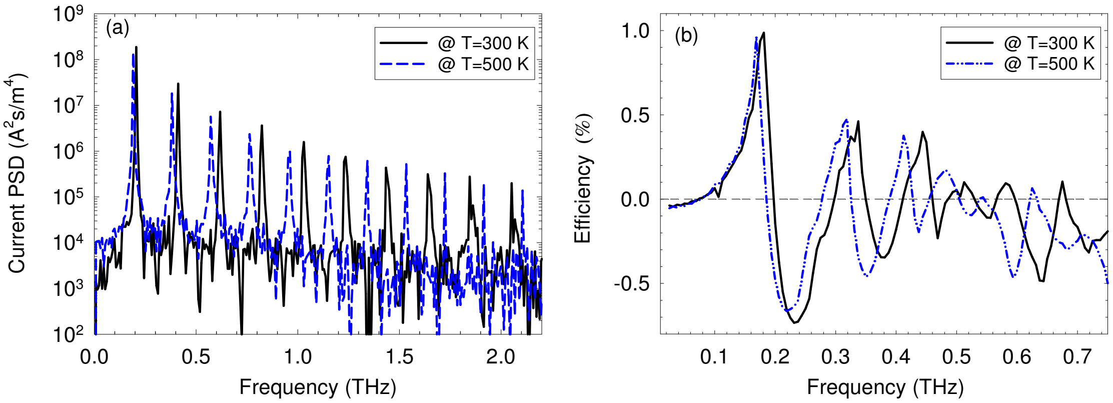

Figure 2. 20: (a) Current power spectral density at 77 V and (b) DC to AC conversion efficiency *vs.* frequency at V_{DC}=70 V and V_{AC}=10 V. A GaN-based diode with notch (DS2), L=0.9 µm and two operating temperatures, 300 K and 500 K, is considered.

2.5. Conclusions

In this chapter we have made a numerical comparison between InP-and GaN-based vertical diode performances under DC and DC+AC bias conditions. The main conclusions are summarized below.

- By means of MC simulations, the equivalence between the operation of a diode connected in series with a resonant circuit and the direct application of a signal consisting of the superposition of a sinusoidal AC component to the DC bias has been proved in a particular example case, in which the feedback signal obtained from the RLC circuit was essentially sinusoidal. The latter technique has been used to analyse the performance of InP and GaN structures.
- GaN has high threshold and breakdown electric fields and thus requires higher bias (one order of magnitude higher than InP) for negative differential mobility to be achieved, which implies the possibility of generating higher AC power at the expense of an also higher DC consumption. However, in order to actually extract the predicted AC power, an appropriate RLC circuit and tuneable band-pass filters should be designed to accomplish such ideal conditions. Mismatch, losses, heating effects, diode parasitic capacitances, etc. may additionally degrade the performance foreseen by MC simulations.
- The generation bands in GaN diodes occur at higher frequencies than in InP, corroborating the expectations of obtaining emissions near the so-called terahertz gap.
- When the amplitude of the single-tone AC excitation is reduced, a lower η but at slightly higher FMEs is achieved for the first and second generation bands.
- Overall, it is found that notched structures provide (i) a higher number of harmonics, (ii) more generation bands and (iii) higher spectral purity, at the expense of a lower frequency for the first harmonics.
- Although thermal effects lead to a reduction in the FMEs and the generation of fewer harmonics, the diodes studied here are still operative and their expected figures of merit are very promising in terms of high-frequency emission and power generation.

- Table 2. 3 recapitulates the main results obtained in this chapter.

			InP (DS1)[8]	**GaN (DS1)**	**GaN (DS2)**[9]
Does the notch fix the domain near the cathode?			Yes	No	Yes
DC	L_{eff}		40 %	-	65 %
	V_{th} (L=1500 nm)	with notch	3.75 V	32 V	38 V
		w/o notch	2 V	32 V	36 V
	FMA_1range (w/o notch)		130 GHz < FMA_1< 400 GHz. (all L).	150 GHz < FMA_1< 330 GHz. (L=0.9, 1.2, and 1.5µm).	120 GHz < FMA_1< 290 GHz. (all L).
	FMA_1range (with notch)		85 GHz < FMA_1< 140 GHz. (L=1.2 and 1.5µm).	150 GHz < FMA_1< 244 GHz. (L=0.9, 1.2, and 1.5µm).	120 GHz < FMA_1< 260 GHz. (all L).
	Number of harmonics (L=1500 nm, V_{DC}=5 V)		Up to the fourth, F MA_4~600 GHz (with notch). Only the fundamental, FMA_1 ~210 GHz (w/o notch).	Larger number of harmonics than InP-diodes	
				The tenth harmonic reaches 1 THz	Higher spectral purity
DC + AC	η and *FME*		η up to 5.5 % for FME_1 ~225 GHz. (L=0.9 µm, w/o notch)	The best result achieved is a FME of about 600 GHz for GaN-based diodes, with L≈1 µm.	η=0.1 % in a 0.9 µm-long GaN diode in the sixth generation band (675 GHz).

Table 2. 3: Recapitulation of the main results obtained in Chapter 2.

---

[8] For DS1 n=1×10^{17} cm^{-3} and n^-=2×10^{16} cm^{-3}.

[9] For DS2 n=5×10^{17} cm^{-3} and n^-=1×10^{17} cm^{-3}.

CHAPTER 3: ELECTRO-THERMAL MC SIMULATIONS OF GaN-BASED DEVICES

The development of technology using AlGaN/GaN, thanks to their outstanding electronic properties and improved maturity of device manufacture, has in the last few years made a significant inroad into high-power and high-frequency applications with respect to other semiconductor competitors such GaAs (55,137,138). In spite of the strong potentiality of AlGaN/GaN-based devices and the good thermal conductivity of GaN (144), excessive overheating is still an important challenge for their reliability and extensive practical use, as it produces a significant degradation of the main figures of merit (145). Furthermore, thermal effects are boosted by the thermal boundary resistance (TBR) that appears in the growth process of dissimilar materials. However, to date the modelling of the TBR effects is still an open problem. Three types of substrates are commonly used in GaN-based devices: sapphire (Al_2O_3), silicon (Si) and silicon carbide (SiC). Sapphire and silicon suffer from low-medium thermal conductivity and high lattice mismatch density with GaN, while mono-crystalline SiC has high thermal conductivity and stability but is very expensive (61) and also has full of defects.

This chapter focuses on the development of an electro-thermal simulator able to analyse the thermal effects that are essential for the correct modelling of GaN-based devices (61,66,70,144,146,147). The aim is to expand the abilities of our in-house semi-classical Monte Carlo (MC), proven to be a very powerful tool to investigate electron transport and optimize the static, dynamic and noise operation of semiconductor devices (148), by including self-heating effects through (i) a thermal resistance method (TRM) and (ii) an advanced electro-thermal model. We shall validate the tool and analyse its potential by comparing simulations with experimental direct-current (DC) measurements of an un-gated $Al_{0.27}Ga_{0.73}N$/GaN heterostructure.

Second, we shall analyse thermal effects in high electron-mobility transistors (HEMTs). Self-heating has a more significant effect on GaN HEMTs as compared to GaAs HEMTs due to the higher gate and drain voltage ranges that can be applied to GaN HEMTs without inducing breakdown, and their better current handling capability, which results in higher average heat generation (147). In particular, AlGaN/GaN HEMTs are exceptional devices for multiple commercial and military applications (149).

This chapter is organized as follows. The state of the art is presented in Section 3.1. Two self-consistent thermal algorithms are introduced in Section 3.2. One is based on a thermal resistance method, and the other is used to solve the heat diffusion equation model (HDEM) under two scenarios for the thermal conductivity to be temperature-independent and temperature-dependent. In Section 3.3 we analyse a diode. Here, the device structure and isothermal simulations are presented and the results will be compared with experimental measurements. This section includes a systematic isothermal study of the influence of several physical parameters of the heterolayer that provide the initial electronic calibration of the tool. Following this, we run the electro-thermal simulations. The potentials and comparisons between both models and the influence of die dimensions and thermal conductivities of the substrate are analysed in detail, with emphasis on the spatial distribution of temperature. The effect of the inclusion of the thermal boundary resistance and the role of the temperature dependence of thermal conductivity are also examined. In Section 3.4 we carry out a MC analysis of HEMTs. Isothermal simulations are investigated by studying the basic output characteristics and some microscopic properties of electron transport. Later, the electro-thermal simulations are presented and compared. The effect of gate-length, cooling and also the role of the temperature dependence of thermal conductivity will be studied. Finally, the conclusions are reported in Section 3.5.

3.1. State of the art: Modelling of thermal effects

Since GaN-based electronics have grown in popularity (1,2), many research groups have recognized the importance of analysing thermal effects in GaN-based devices with thermal models (61,66,144). In this section we offer a brief summary of the state of the art by describing some of the most relevant works of modelling in which self-heating effect are taken into consideration. This effort was the starting point to perform the work described in this chapter.

In Table 3. 1 we summarize some methods or software that implement thermal effects, and the corresponding institutions and researchers that employ these techniques.

Method	***Research Group***	***Researchers***
Monte Carlo	Institute of Microwave and Photonics, School of Electronic and Electrical Engineering, University of Leeds, Leeds, U.K.	T Sadi, R W Kelsall, N J Pilgrim, W Batty (66,70,147,150).
	Center for Applied Physics Research, Tabriz University, Tabriz, Iran.	A Asgari, M Kalafi (151).
	School of Electrical, Electronic and Computer Engineering, The University of Western Australia, Crawley, Australia.	L Faraone (151).
	Department of Electrical Engineering and Center for Solid State Electronics Research Arizona State University, Tempe, USA.	D Vasileska, A Ashok, S M Goodnick, F A Alessio, D Guerra, D Ferry, M Saraniti (152,153).
	Frescale Inc, Tempe, AZ, USA.	O L Hartin (152).
	Department of Physics, University of Aberdeen, King's College, Aberdeen, UK	R F Macpherson, G M Dunn (128).
	Research Group on Semiconductor devices. Department of Applied Physics, University of Salamanca, Spain	T González, J Mateos, S Pérez, I Íñiguez-de-la-Torre, S García (65,76).
Hydrodynamic	Advanced Material and Device Analysis Group, Institute for Microelectronics, TU Wien, Gusshausstr. Vienna, Austria	S Vitanov, V Palankovski (144).
	Fraunhofer Institute for Solid-State Physics (IAF), Tullastr. Freiburg, Germany.	S Maroldt, R Quay (144).
	Shanghai Institute of Technical Physics, Chinese Academy of Sciences, Shanghai, China.	X D Wang, W D Hu, X S Shen, W Lu (154).
Drift-diffusion and hot electron	Shanghai Institute of Technical Physics, Chinese Academy of Sciences, Shanghai, China.	X D Wang, W D Hu, X S Shen, W Lu (154).

Commercial simulator		
COMSOL®	ISOM and Departamento. Ingeniería Electrónica, ETSI Telecomunicación, Universidad Politécnica de Madrid, Madrid, Spain.	A Wang, F Calle (146).
	CEI Campus Moncloa, UPM-UCM, Madrid, Spain.	M J Tadjer (146).
	Institut d'Electronique de Microélectronique et de Nanotechnologie, Lille University, Villeneuve d'Ascq, France.	X Tang, M Rousseau, N Defrance, V Hoel, A Soltani, J De Jaeger (61).
	PICIGIDA International, Parc de Villejust, Courtabocuf Cedex, France	R Langer (61).
Silvaco Atlas	Department of Information Engineering, University of Parma, Parma, Italy.	F Giuliani, N Delmonte, P Cova, R Menozzi (155).
	Department of Electrical Engineering and Computer Science, Massachusetts Institute of Technology, Cambridge, UK.	F Gao, H Lo, R Ram, T Palacios (156).
DESSIS	Air Force Research Laboratory, Materials Directorate, Wright-Patterson Air Force Base, USA. Semiconductor Research Center, Wright State University, Dayton,, USA.	E R Heller (157).
	Air Force Research Laboratory, Sensors Directorate, Wright-Patterson Air Force Base, USA.	A Crespo (157).
ANSYS	Key Laboratory for Wide Band-Gap Semiconductor Materials and Devices, School of Microelectronics, Xidian University, Xi'an, China.	Y Liyuan, A Shan, C Yonghe, C Mengyi, Z Kai, M Xiaohua, H Yue (158).

Table 3. 1: Electro-thermal simulators, institutions and researchers that employ them.

Authors that use the ***MC technique*** develop electro-thermal simulators which use an iterative procedure that self-consistently couple the MC electronic transport with the solution of the heat diffusion equation (HDE) (62,66,147,150,153). Different devices have been be studied, such as AlGaN HEMTs (62,66), *n*-type 0.15 µm gate $In_{0.15}Ga_{0.85}As/Al_{0.28}Ga_{0.72}As$ HEMTs (150), or submicrometer Si/SiGe modulation-doped field-effect transistors (MODFETs) (147). Usually, the relationships between the thermal drop effect observed in the electro-thermal I_D-V_{DS} characteristics of the devices and the microscopic properties of electron transport and the temperature profiles are studied.

Some authors analyse the effect of growing the material on various substrate materials, such as SiC, Si, GaN, and sapphire (66). For sapphire substrates a huge current reduction occurs upon the inclusion of thermal self-consistency and very high peak temperatures, which shows that this type of substrate is not ideal for use in high-power applications (66). SiC was seen to be the most suitable substrate for high-power applications as compared to Si, GaN and sapphire substrates, providing the highest thermally self-consistent current and the lowest peak temperature under the same biasing conditions (66). The reduction in the length of the semiconductor die is seen to affect the peak temperature values without significantly altering the temperature range (62). In general, simulations are validated with experimental measurements. We want to point out that there are already pioneer groups(10) that focus their research interest in the development of electro-thermal MC models. These models are needed for studying submicrometer and nanoscale GaN-based heterostructures. Therefore, the inclusion of heating effects will become essential in our simulator for the correct and more accurate modelling of this kind of devices. For a proper calibration of our in-house simulator, the inclusion of experimental validations will become very important. The electro-thermal software will also allow us to consider the presence of the effect of the thermal boundary resistance, as we will see in this chapter.

In addition, with the drift-diffusion, thermodynamic, hydrodynamic or hot-electron methods, a similar analysis can be made. For example, we can remark, as an example, the work reported by (S. Vitanov et al, 2010) (144), in which authors describe two-dimensional hydrodynamic simulations of AlGaN/GaN HEMTs at high temperatures (425 K). The simulator is calibrated against the measurement data of a real device and delivers good predictive results for the DC and RF characteristics.

Moreover, there exists commercial software that takes into account the inclusion of heating effects. We highlight Sentaurus, COMSOL® and Silvaco ATLAS.

---

[10] Institute of Microwave and Photonics, School of Electronic and Electrical Engineering, University of Leeds, UK, or the Department of Electrical Engineering and Center for Solid State Electronics Research Arizona State University, Tempe, USA.

- **Sentaurus Device** (http://www.synopsys.com): Sentaurus offers different transport models such as Drift Diffusion or Hydrodynamic. In the case of the latter, it is possible to calculate the potential, electron densities, electron temperatures, and the lattice temperatures simultaneously for a particular device and geometry. For example, the thesis work of ref. (159) uses Sentaurus to calculate the temperature distributions for carriers and lattice simultaneously.
- **COMSOL Multiphysics®** (http://www.comsol.com): this is a finite-element analysis, solver and simulation software package for several applications in physics and engineering, especially coupled phenomena, or multiphysics. The Semiconductor Module allows detailed analysis of semiconductor device operation at the fundamental physics level. The module is based on the drift-diffusion equations, using isothermal or non-isothermal transport models. It is useful for simulating a range of practical devices. Of interest in this sense is ref. (61), in which the authors describe a predictive physical-thermal model to analyse the physical and thermal phenomena observed in experiments. They found that compared with Si substrate, composite SopSiC substrates and SiCopSiC substrates present better thermal resistances, especially at high dissipated power densities. The simulation results are validated by experimental results. From the simulation data it is concluded that polycrystalline diamond and mono-crystalline SiC substrates appear to be the best candidates in terms of thermal dissipation, the composite and bulk GaN substrates, with few dislocations, bring improvements in comparison with the Si substrate, especially for high dissipated power densities. Another application is the one provided by authors of ref. (146), in which they use a finite element method implemented in COMSOL to investigate the potential reduction in self-heating effects induced by a capped diamond layer.
- **Silvaco ATLAS** (www.silvaco.com): this enables device technology engineers to simulate the electrical, optical, and thermal behaviour of semiconductor devices. Atlas includes different methods to solve electron transport: drift diffusion, energy balance and hydrodynamic models. It includes the Thermal Packaging Simulator. Thermal 3D is a general heat-flow simulation module that predicts heat flow from any power generating devices (not limited to semiconductor

devices), typically through a substrate and into the package and/or heat sink via the bonding medium. The operating temperatures for packaged and heat-sinked devices or systems can be predicted for the design and optimization phase or for general system analysis. For example, a case study can be found in ref. (156), where the authors combine self-consistent electro-thermal simulations of AlGaN/GaN HEMTs obtained with the Silvaco Atlas commercial device simulator with a fully coupled piezoelectric-thermal model developed in MATLAB. This combination offers an effective method to calculate the stress and elastic energy in GaN-based device transistors under operating conditions. The results show that the role of lattice heating is as important as the electric field as regards the mechanical properties of AlGaN/GaN HEMTs, and it should be carefully considered for the prediction of reliability of GaN-based transistors.

Although electronic transport models, such as the Energy-Balance (61), Drift-Diffusion (106) or Hydrodynamic (107) types, are used extensively, as can be seen MC algorithms have also been widely used to study transport in a large variety of semiconductor devices. Even though the MC technique requires greater computational effort, its main advantage is that it can provide an accurate description of electron transport in real short-gate transistors, where non-stationary effects and ballistic effects may arise. In fact, this chapter could be considered as a preliminary work for the confirmation of the validity of electro-thermal models and the calibration of their parameters for subsequent used in the simulation of transistors. Henceforth, we include thermal effects in our MC tool, first to replicate the experimental *I-V* curves and second to provide design strategies to reduce their negative consequences.

3.2. Self-consistent electro-thermal algorithms

Figure 3. 1 shows the flow chart of the electro-thermal simulations. The first step consists of the data input process, where the user defines the necessary parameters to run the MC program. They are provided from several files that contain different types of information where the geometry of the device under analysis, the parameters of the materials that form the heterostructure layer, the scattering mechanism, the different bias conditions, etc., are indicate

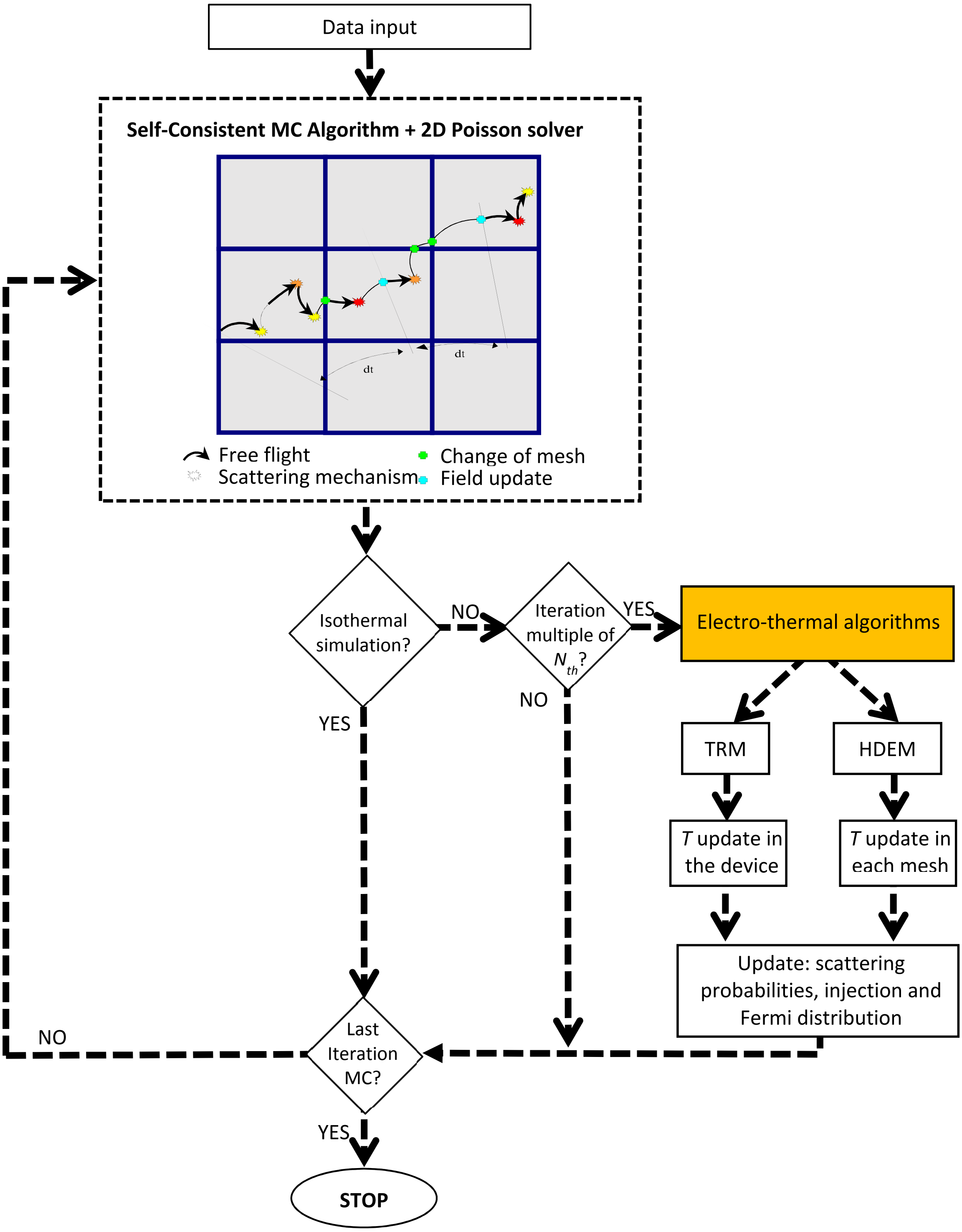
Data input
Self-Consistent MC Algorithm + 2D Poisson solver
dt
dt
Free flight
Scattering mechanism
Change of mesh
Field update
Isothermal simulation?
NO
Iteration multiple of N_{th}?
YES
Electro-thermal algorithms
NO
YES
TRM
HDEM
T update in the device
T update in each mesh
Update: scattering probabilities, injection and Fermi distribution
NO
Last Iteration MC?
YES
STOP

Figure 3. 1: Flow chart of the electro-thermal simulations.

Two different self-consistent techniques are incorporated in our MC simulator: (i) a thermal resistance method (TRM), and (ii) an electro-thermal model, where the steady-state heat diffusion equation (HDE) is solved, henceforth called HDEM. We wish to point out that in both models the temperature is updated during the simulation time (every N_{th} time-steps) and the inelastic scattering mechanisms in each mesh are re-calculated accordingly. In addition, other parameters used in the MC code are also updated, such as energy emission and absorption events.

3.2.1. Thermal resistance method (TRM)

The first approach is based on a thermal resistance method (see flow-chart of Figure 3. 2). This model is based on the use of an ad-hoc thermal resistance, R_{th} (65), and is only considered in the electronic domain (region where the electronic transport is solved), delimited by yellow region in Figure 3. 3.

If the TRM is employed, the user has to provide, via an input file, the value of the thermal resistance and the number of time-steps N_{th} in which the temperature must be updated.

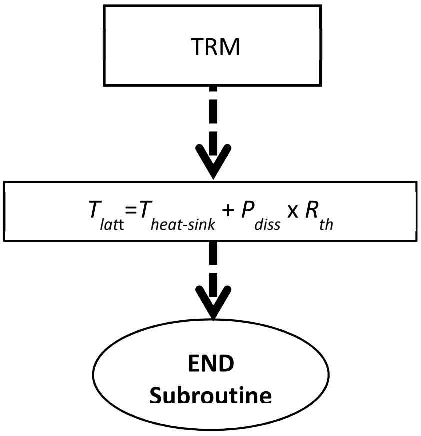

Figure 3. 2: Flow chart of subroutine TRM.

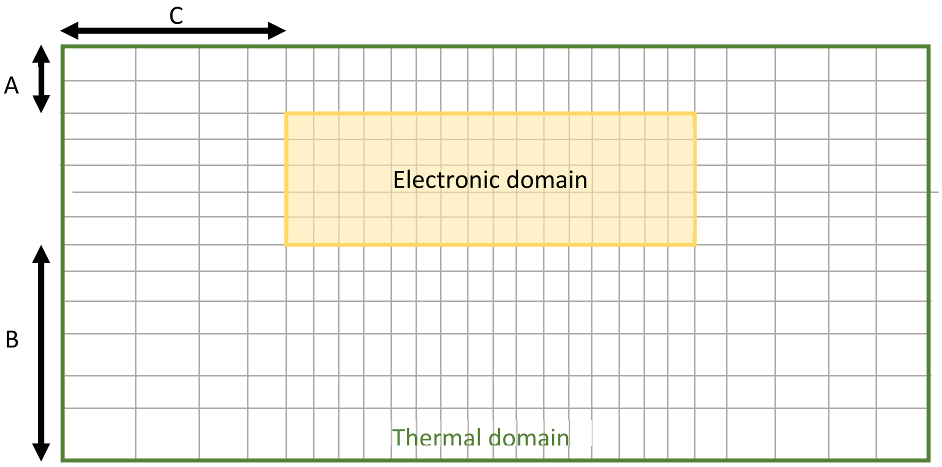

Figure 3. 3: Scheme of the electronic and thermal domains.

The algorithm is as follows: at each bias point (V_{MC}), we simulate the whole device at **a uniform constant lattice temperature**, T_{latt}, during a given number of time-steps N_{th} and then the average MC current density, I_{MC}, is evaluated. At this point, T_{latt} is updated according to the expression:

$$T_{latt} = T_{heat-sink} + I_{MC} \cdot V_{MC} \cdot R_{th} \ , \qquad \text{(III.1)}$$

where V_{MC} is the intrinsic MC bias, and $T_{heat\text{-}sink}$ is the temperature of the heat sink. In this model, the lattice temperature varies at each operating point, depending on the power of the device (I_{MC}xV_{MC}).

The simulation is then performed at the new T_{latt} during the next N_{th} steps, where T_{latt} is updated again. This method allows the lattice temperature to be adapted in a self-consistent way to the total dissipated power within the device. We chose an updating time of 5000 time-steps of 1 fs each. This time is a trade-off between a large number of total iterations, N_T, that allows for a reduction in stochastic fluctuations in the calculation of the electron current and a small one that produces an excessive computational time due to the frequent number of temperature updates.

3.2.2. Heat Diffusion Equation Model (HDEM)

In this section we describe the more sophisticated method introduced before and called HDEM (see flow-chart of Figure 3. 4). This method considers the whole device (called the thermal domain and delimited by green lines in Figure 3. 3). In this case, the user need to build an input file to define the geometry of the thermal domain, the heat-sink temperature, the thermal conductivities, N_{th}, and the values of the number of meshes *A*, *B* and *C* (see Figure 3. 3) to combine the thermal and electronic domains.

We couple our MC tool with the solution of the steady-state HDE (66-68) (where radiation and convection losses are neglected):

$$\nabla[k(r,T)\nabla T(r)] = -G(r) \ , \qquad \text{(III.2)}$$

where $T(r)$ and $G(r)$ are the temperature and the dissipated power density, respectively, at position r and $k(r,T)$ is the temperature-dependent and inhomogeneous thermal conductivity. With our MC approach, only a steady state solution can be achieved, because typically the thermal relaxation time is much longer (several orders of magnitude) than the electronic one, which, from a computational point of view, makes the analysis of thermal transients practically unaffordable (in the range of ns to µs) using the time-step necessary to ensure a correct electronic description (about fs) (66,70).This is why the time dependence is ignored in the thermal equations, and only the DC results are provided.

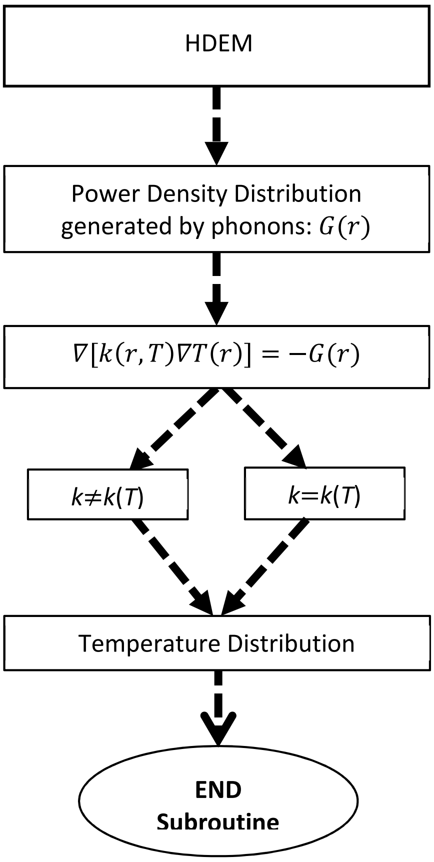
HDEM
Power Density Distribution generated by phonons: $G(r)$
$\nabla[k(r,T)\nabla T(r)] = -G(r)$
$k \neq k(T)$
$k = k(T)$
Temperature Distribution
END Subroutine

Figure 3. 4: Flow-chart of the HDEM subroutine.

Two cases will be analysed (see flow chart of Figure 3. 4): (i) a simple one, where thermal conductivity is assumed to be temperature-independent: $k(T)=k(T_0)$, and (ii) a second and more realistic one including a temperature-dependent thermal conductivity for each material. For the first case, since thermal conductivity is piecewise homogeneous, Eq. (III.2) yields a linear Poisson-like equation.

In the second case Eq. (III.2) can be linearized through the Kirchhoff variable transformation (66-68):

$$\theta = T_0 + \frac{1}{k(T_0)} \int_{T_0}^{T} k(\alpha)\, d\alpha, \qquad \text{(III.3)}$$

where T_0 is a reference temperature and θ is the transformed or apparent temperature. In both cases, Eq. (III.2) yields a linear two-dimensional Poisson-like equation that can be written as:

$$\frac{\partial^2 \Sigma}{\partial x^2}+\frac{\partial^2 \Sigma}{\partial y^2}=-\frac{G(x,y)}{k(T_0)}, \qquad \text{(III.4)}$$

where Σ will be T or θ for temperature-independent and temperature-dependent thermal conductivities, respectively.

Figure 3. 5 shows the scheme employed to resolve the HDE. By using discretization (through a straightforward finite-difference technique using five points), and by resolving the resulting system, the temperature associated with each node can be determined.

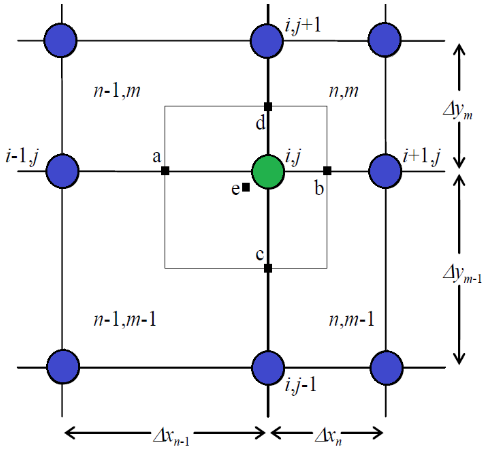

Figure 3. 5: Scheme of the resolution of the HDE.

The procedure is as follows. Our system consists of *nxm* meshes of different sizes and (*n*+1)x(*m*+1) nodes. The resolution of the HDE is carried out in two stages. First, the power assignment is made, where the dissipated power due to the phonons at each mesh of the device is calculated. This power is used in the second stage, which consists of the resolution of the resulting system of equations from the discretization of Eq. (III.4), see Eq. (III.5).

$$\begin{aligned}
&\Sigma_{i,j-1}\frac{2(\Delta x_n+\Delta x_{n-1})}{\Delta y_{m-1}}+\Sigma_{i-1,j}\frac{2(\Delta y_m+\Delta y_{m-1})}{\Delta x_{n-1}}-\\
&-\Sigma_{i,j}2\left[(\Delta x_n+\Delta x_{n-1})\left(\frac{1}{\Delta y_m}+\frac{1}{\Delta y_{m-1}}\right)+(\Delta y_m+\Delta y_{m-1})\left(\frac{1}{\Delta x_n}+\frac{1}{\Delta x_{n-1}}\right)\right]+\\
&+\Sigma_{i+1,j}\frac{2(\Delta y_m+\Delta y_{m-1})}{\Delta x_n}+\Sigma_{i,j+1}\frac{2(\Delta x_n+\Delta x_{n-1})}{\Delta y_m}= \qquad \text{(III.5)}\\
&=-\left(\frac{G_{n-1,m-1}\Delta x_{n-1}\Delta y_{m-1}}{k(T_0)_{n-1,m-1}}+\frac{G_{n,m-1}\Delta x_n\Delta y_{m-1}}{k(T_0)_{n,m-1}}+\frac{G_{n-1,m}\Delta x_{n-1}\Delta y_m}{\varepsilon k(T_0)_{n-1,m}}+\frac{G_{n,m}\Delta x_n\Delta y_m}{k(T_0)_{n,m}}\right).
\end{aligned}$$

It is noteworthy that the temperature Σ is a magnitude associated with the nodes (subscript *i*, *j*). The dissipated power (*G*) and the thermal conductivity $k(T_0)$ correspond to the meshes (subscript *n*, *m*) of the discretization. Using this technique in all the nodes of the lattice, (*n*+1)x(*m*+1), linear equations are obtained. Given that this is a pentadiagonal system, the *LU* factorization method (105) is employed. The exact solution of the temperature Σ in the different nodes in which the device has been discretized is obtained. We need to calculate the temperature associated with each mesh because our MC tool works with this magnitude. The temperature in the mesh *n*,*m* will be:

$$\Sigma_{n,m} = (\Sigma_{i,j} + \Sigma_{i+1,j} + \Sigma_{i,j+1} + \Sigma_{i+1,j+1})/4 \,. \qquad \text{(III.6)}$$

In this approximation, the thermal domain (green region in Figure 3. 3) of the simulated devices is larger than the electronic intrinsic region (yellow region in Figure 3. 3). The last key point is the coupling of both domains, electronic and thermal. We calculate the steady-state solution by an iterative procedure as follows. First the dynamics of the particles in the electronic domain is simulated with the MC algorithm during an initial transient time of 10 ps (sufficient for a steady-state to be reached) and at room temperature. Next, the power density distribution *G*(*r*) is averaged and computed every 20 ps to update the geometry-dependent temperature in the thermal domain via the solution of Eq. (III.4). The new temperature distribution is then used to run the subsequent MC iteration, where all inelastic scattering mechanisms, energy emission and absorption events are recorded to calculate *G*(*r*) again. Enough iterations of the HDE-MC solver are done in order to reach a convergence of the electro-thermal solution(11).

The following bullet points describe the different boundary conditions when temperature-independent and temperature-dependent thermal conductivities are considered.

- **Boundary conditions [*k*≠*k*(*T*)]**

  Dirichlet boundary conditions to T are imposed at the bottom heat sink.

  At the surface between two regions of different materials, γ, the Neumann boundary condition is used:

---

[11] The singular number of iterations to reach a convergence will be indicated in the corresponding section for each calculation.

$$k_1(T)\hat{n}\frac{\partial T}{\partial r_n}\bigg|_\gamma = k_2(T)\hat{n}\frac{\partial T}{\partial r_n}\bigg|_\gamma . \qquad \text{(III.7)}$$

Where $\hat{n}$ is the normal unit vector of γ, and r_n stands for a vector normal to γ.

Furthermore, the continuity of *T* across γ is satisfied (67). Adiabatic conditions are imposed at the top and side boundaries of our thermal device:

$$k_1(T)\frac{\partial T}{\partial r_n}\bigg|_\gamma = 0 . \qquad \text{(III.8)}$$

- **Boundary conditions [*k*=*k*(*T*)]**

Dirichlet boundary conditions on T can be expressed in terms of θ by means of Eq. (III.3). If the heat-sink temperature is the same as T_0, θ will be equal to T_0.

At the surface between two regions of different materials, γ, the continuity conditions must be transformed according to the Kirchhoff transformation, Eq. (III.3), under which Eq. (III.7) is invariant due to the equality

$$k_1(T_0)\hat{n}\frac{\partial \theta}{\partial r_n}\bigg|_\gamma = k_2(T)\hat{n}\frac{\partial T}{\partial r_n}\bigg|_\gamma . \qquad \text{(III.9)}$$

Thus, for θ we can write:

$$k_1(T_0)\frac{\partial \theta}{\partial r_n}\bigg|_\gamma = k_2(T_0)\frac{\partial \theta}{\partial r_n}\bigg|_\gamma . \qquad \text{(III.10)}$$

Unfortunately, the continuity of θ across γ is not invariant under the Kirchhoff transformation and θ is not defined uniquely (67). The problem can be solved simply by assuming a thermal conductivity with the same functional dependence on *T* for all regions, i.e. $k_i(T) = C_i\, f(T)$, with C_i a characteristic constant for each material. Such an assumption renders the apparent temperature continuous and possibilities a correctly resolution of the HDE. Thanks to this, we keep the same subroutine in the code for both models, *T* and θ; and for the last one, we merely need to introduce the variable transformation of Eq. (III.3).

Adiabatic conditions are imposed at the top and side borders of our thermal device:

$$k_1(T_0)\left.\frac{\partial\theta}{\partial r_n}\right|_{\gamma} = 0\,. \qquad \text{(III.11)}$$

It is well-established that the thermal conductivity, k_i, in semiconductor devices for non-cryogenic device applications depends on temperature according to:

$$k_i(T) \sim AT^{-\alpha}. \qquad \text{(III.12)}$$

where A and α are characteristics parameters of each material (67). This dependence will be used for a temperature-dependent thermal conductivity analysis. Taking into account this functional dependence, the real temperature T can be calculated simply by applying the inverse transform from Eq. (III.3):

$$T = T_0\left[1 + \frac{(\theta - T_0)(1-\alpha)}{T_0}\right]^{\frac{1}{1-\alpha}}. \qquad \text{(III.13)}$$

3.3. Two-terminal devices: diode

In this section we shall study a two-terminal structure. Figure 3. 6 (a) shows the geometry of the $Al_{0.27}Ga_{0.73}N$/GaN diode under analysis, manufactured and measured at the Institut D'Électronique de Microélectronique et de Nanotechnologie (IEMN) in Lille, France.

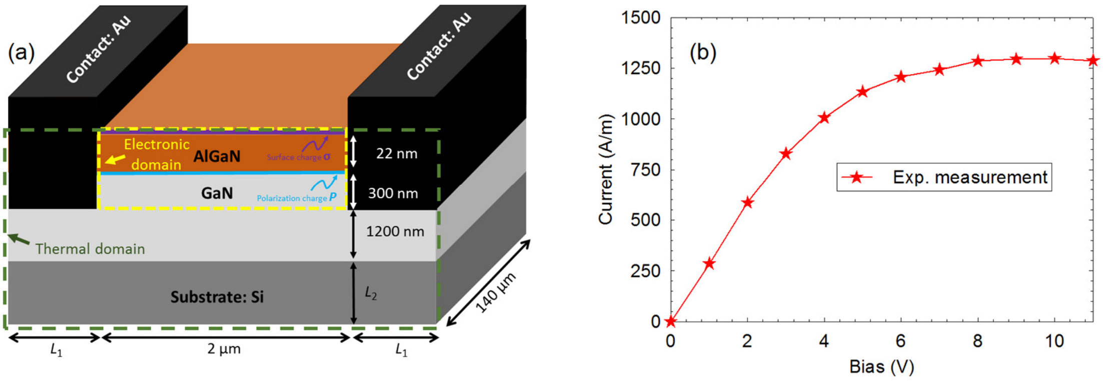
(a)
Contact: Au
Contact: Au
Electronic domain
AlGaN
Surface charge σ
GaN
Polarization charge P
22 nm
300 nm
1200 nm
Thermal domain
Substrate: Si
L2
140 µm
L1
2 µm
L1
(b)
Current (A/m)
1500
1250
1000
750
500
250
0
Bias (V)
0
2
4
6
8
10
Exp. measurement

Figure 3. 6: (a) AlGaN/GaN diode geometry under study. The area limited by yellow corresponds to the electronic simulated region of the diode and the region limited by green is the thermal domain. (b) Experimental measurements of the *I-V* curve.

The structure is a 22-nm-thick un-doped $Al_{0.27}Ga_{0.73}N$ barrier layer grown on top of a 1.5-µm-thick un-doped GaN buffer. The substrate is a 300 µm thick layer of Si. The length between the contact terminals is 2 µm and the width of the structure is 140 µm. The measured experimental values in equilibrium of the sheet electron density, n_s, the mobility, μ, and the sheet resistance, R_s, of the epilayer are 8×10^{12} cm^{-2}, 1000 cm^2/V·s and 780.2 Ω/sq, respectively at 300 K. The measured contact resistance is R_C=0.4 Ω·mm (considered constant with temperature).The experimental measurement of the *I-V* curve of the diode is shown in Figure 3. 6 (b).

The real top electrodes are implemented in the simulations as vertical contacts, with the proper injection and potential profiles across the heterolayer. To use this approach, an initial simulation at equilibrium, and with the contacts located at the top (as in a real device), is made with a view to obtaining the potential and concentration profiles along the vertical layers. A detailed description can be found in refs. (95,160). To simulate the AlGaN/GaN heterolayer correctly, we incorporate the influence of spontaneous and piezoelectric surface polarization charges (161-164):

$$P_{Al_xGa_{1-x}N/GaN}(x) = P^{sp}_{GaN} - P^{sp}_{Al_xGa_{1-x}N}(x) - P^{pz}_{Al_xGa_{1-x}N}(x). \qquad \text{(III.14)}$$

where the superscript *sp* refers to the spontaneous polarization charge, and *pz* to the piezoelectric charge. This charge is incorporated in the simulation as a boundary condition in the Poisson equation that affects the nodes of separation between both materials. The term x refers to the molar fraction of Al; that is, 0.27.

In order to estimate the value of these charges, initially we have followed the theoretical calculus developed in ref. (164). This is an *ab initio* calculus that provides the following expressions for the charges in which we are interested:

$$P^{sp}_{GaN} = -0.034\,, \qquad \text{(III.15)}$$

$$P^{sp}_{Al_xGa_{1-x}N}\,, = -0.090\,x - 0.034\,(1-x) + 0.019\,x(1-x), \qquad \text{(III.16)}$$

$$P^{pz}_{Al_xGa_{1-x}N}(x) = xP^{pz}_{AlN}[\varepsilon(x)] + (1-x)P^{pz}_{GaN}[\varepsilon(x)]\,, \qquad \text{(III.17)}$$

where

$$P^{pz}_{AlN} = -1.808\,\varepsilon\; + 5.624\,\varepsilon^2 \text{ for } \varepsilon < 0\,, \qquad \text{(III.18)}$$

$$P^{pz}_{AlN} = -1.808\,\varepsilon - 7.888\,\varepsilon^2 \text{ for } \varepsilon > 0\,, \qquad \text{(III.19)}$$

$$P^{pz}_{GaN} = -0.918\,\varepsilon + 7.559\,\varepsilon^2\,, \qquad \text{(III.20)}$$

with $\varepsilon(x)$ the strain rate, given by:

$$\varepsilon(x)=\frac{[a_{GaN}-\mathrm{a}(x)]}{\mathrm{a}(x)}\ , \qquad \text{(III.21)}$$

where a_{GaN} and $\mathrm{a}(x)$ are the lattice constants of the GaN and the alloy $Al_xGa_{1-x}N$, without strain, respectively. At the same time, $\mathrm{a}(x)$ can be estimated as (in nm) (163):

$$a(x)=0.31986-0.00891x\ . \qquad \text{(III.22)}$$

From these expressions it is possible to calculate the value of $P_{Al_xGa_{1-x}N/GaN}(x)$ for any molar fraction of Al in the layer of the AlGaN of the heterojunction. In particular, for the case where x=0.27, the value employed in the simulations of the heterojunction studied, we have that $P_{Al_xGa_{1-x}N/GaN}$=14.12x10^{12} cm^{-2}.

In addition, a surface charge density σ is included at the top of the AlGaN layer; it appears as a result of polarization charges partially compensated by charges trapped at surface states. Both types of charges lead to an enhancement of the accumulation of electrons n_s in the channel, satisfying -when the applied voltage is zero- the neutrality condition $P + \sigma + n_s = 0$. For the structures under analysis in this section, a new scattering is considered: the surface roughness scattering (SRS), being a key parameter for the simulation of heterostructures (160). These SRS mechanisms reduce mobility, and hence to reproduce the experimental results correctly the effect of interface roughness in the heterojunctions must be introduced in our 2-D MC simulator. In the literature it is possible to find advanced models for roughness scattering that consider the dependence of the probability on the electron wave vector (165,166). In our case, as a first approximation we have implemented a simpler global model in which a given fraction of electron reflections at the heterojunction is treated as diffusive (instead of specular) (160). Each time an electron reaches the surface, the diffusive or specular character of the reflection is determined by means of a random number. The intensity of the SRS is controlled by the percentage of diffusive reflections (PDR) (160) with respect to the total number. Here, we are using phonon populations at thermal equilibrium with electrons throughout the simulation domain (66), and hence the Bose-Einstein distribution is always used for the electron-phonon scattering rate (167). Indeed, if self-heating is included, the influence of hot-phonons is found to have relatively little impact (168).

External series resistance R_c can be introduced through the boundary conditions, modifying the potential at the contact by the voltage drop across the resistance R_c (115). In ref. (115) a simple post-processing approach to incorporate the contact and probe resistances in the MC simulated *I-V* characteristics is described. This approximation will be taken into account in our un-gated diodes: the experimental bias will be calculated from our intrinsic MC bias, V_{MC}, by taking $V=V_{MC} + 2R_C \times I_{MC}$, with I_{MC} the MC current density.

3.3.1. Isothermal simulations

Electronic conduction occurs mainly in the channel [where the two-dimensional electron gas (2DEG) is located], and hence simulations will be only run in the so called electronic domain that includes the channel and its vicinity. In this section, we shall consider isothermal simulations. The MC tool will be calibrated by adjusting the parameters of the simulator, such as PDR, σ or *P,* in order to reproduce the experimental measurements (under equilibrium conditions and at room temperature) of n_s and μ. The mobility is given by:

$$\mu = 1/(R_s q n_s) \ , \qquad \text{(III.23)}$$

with R_s the square resistance, and q the electron charge. In order to obtain the value of μ with the simulations, the following procedure will be considered. We fix n_s with different sets of P and σ, and for each n_s we simulate diodes with different lengths at low bias. For each length we calculate the diode resistance, R_d, through the slope V_{MC} *vs.* I_{MC}. By fitting R_d *vs*. the length of the diode, and by extrapolating the length to zero, we obtain R_s.

We used 150000 iterations in the simulation with a time-step of Δt=1 fs. Figure 3. 7 summarizes the effect of P and σ, PDR and temperature on the *I-V* curve. We also plot the experimental values for comparison.

First, at 300 K, and without roughness scattering (PDR=0 %), in Figure 3. 7 (a) we investigate five different sets of values for P and σ providing, at equilibrium, sheet carrier densities of n_s=10×10^{12} cm^{-2}, 8×10^{12} cm^{-2} and 6×10^{12} cm^{-2}.

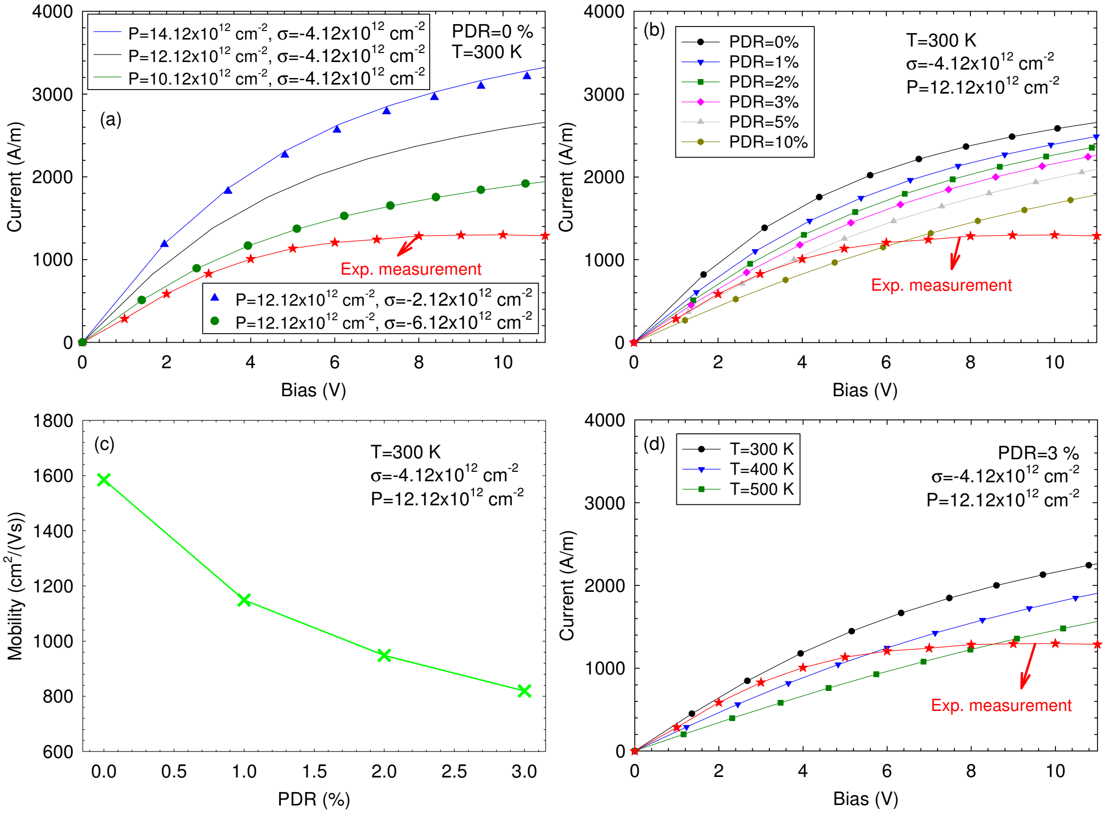

Figure 3. 7: Simulations of the electronic domain of Figure 3. 6 to analyse the effect on the *I-V* of (a) *P* and σ (*T*=300 K and PDR=0 %), (b) the PDR (*T*=300 K, $P=12.12\times10^{12}$ cm^{-2} and σ = -4×10^{12} cm^{-2}) and (d) the lattice temperature ($P=12.12\times10^{12}$ cm^{-2}, σ = -4×10^{12} cm^{-2} and PDR=3 %). For the sake of comparison, the experimental values at 300 K are also plotted. (c) Mobility of electrons in the diode as a function of PDR (*T*=300 K, $P=12.12\times10^{12}$ cm^{-2} and σ = -4×10^{12} cm^{-2}).

In this structure, it is proved that two pairs of *P* and σ that provide the same n_s (neutrality condition at equilibrium) offer almost the same current density. This is due to charge conservation. For example, the sets ($P=12.12\times10^{12}$ cm^{-2} and σ = $-\ 6.12\times10^{12}$ cm^{-2}, green symbols) and ($P=10.12\times10^{12}$ cm^{-2} and σ = $-\ 4.12\times10^{12}$ cm^{-2}, green line), which at equilibrium provide $n_s=6\times10^{12}$ cm^{-2} almost reproduce the same *I-V* curve. Evidently, when n_s is reduced (by adjusting *P* and σ) the current density decreases remarkably. The calculated sheet resistance and the electron mobility are R_s=325, 460 and 787 Ω/sq and μ=1920 cm^2/(V·s), 1600cm^2/(V·s) and 1324 cm^2/(V·s) for $n_s=10\times10^{12}$ cm^{-2}, 8×10^{12} cm^{-2} and 6×10^{12} cm^{-2}, respectively. In all cases, the increase in mobility in the GaN channel with respect to that found in the bulk material [900 cm^2/(V·s)] comes from the action of (i) the Pauli exclusion principle [accounted for in our simulations by the rejection of scattering events (148)] and (ii) the screening of ionized impurities and dislocation scatterings, which have an important influence in the GaN channel carrier dynamics due to the highly degenerated accumulation of electrons.

Our models overestimate the experimental value of the mobility [around 1000 cm^2/(V·s)], which can be attributed to the absence of SRS in these simulations. Thus, in Figure 3. 7 (b) we study these effects by sweeping PDR from 0 % up to 10 % (n_s=8×10^{12}cm^{-2} and T=300 K). As expected the current level decreases as PDR increases. In addition, as PDR is higher the current does not saturate, and the behaviour does not follow the experimental trend. Concerning mobility, Figure 3. 7 (c), a very strong dependence on PDR appears for low values, while beyond 2 % the decrease in mobility is less pronounced. We also checked the effect of increasing the density of dislocations from 0.15×10^{10} cm^{-2} up to 0.30×10^{10} cm^{-2} (with a strong effect on carrier dynamics in bulk GaN); no significant influence in this heterostructure due to the screening effect of the high carrier density in the channel was observed. Finally, we selected values of P=12.12×10^{12} cm^{-2} and σ= - 4.12×10^{12} cm^{-2}and a PDR=3 %, providing n_s=8×10^{12} cm^{-2}, μ=819 cm^2/V·s and R_s=952 Ω/sq (very similar to the experimental ones at 300 K). In order to investigate the influence of temperature, Figure 3. 7 (d) shows the results from 300 K to 500 K. If we look at the simulated curve for T=300 K it shows a good agreement with the measurements at low bias, while for voltages above 4-5 V the difference is remarkable. Conversely, for high voltages the measured current is close to the one obtained from simulations but at higher temperatures, 400 K (V=5.5 V) and 500 K (V=8.5 V). These facts suggest that our isothermal simulations are not capable of reproducing the whole experimental I-V curve. For this, it is necessary to implement the self-consistent thermal models (TRM and HDEM), which provide different lattice temperatures for each bias point. The results depicted in Figure 3. 9 (d) show that from 0 V to 5.6 V temperature should change from 300 K to 400 K, and in the range of 5.6 V to 8.5 V from 400 K to 500 K.

3.3.2. Electro-thermal simulations

In this section we present both electro-thermal models: TRM(12) and the HDEM(13). We shall study how to extract the thermal resistance R_{th} from the HDEM, the dependence on k_s, and die lengths L_1 and L_2. The effect of the thermal boundary resistance is also explored.

(a) Thermal resistance method (TRM)

Figure 3. 8 shows the DC response obtained for six values of the thermal resistance (see Table 3. 2) used in the TRM to analyse the effect of self-heating. These values are of the order of 10^{-2} K·m/W, well within the range of typical values for HEMTs (65,151).

$R_{th\text{-}1}$=12×10^{-3} (K·m/W)	$R_{th\text{-}2}$=14×10^{-3} (K·m/W)
$R_{th\text{-}3}$=16×10^{-3} (K·m/W)	$R_{th\text{-}4}$=18×10^{-3} (K·m/W)
$R_{th\text{-}5}$=20×10^{-3} (K·m/W)	$R_{th\text{-}6}$=22×10^{-3} (K·m/W)

Table 3. 2: Values of the thermal resistances used in the TRM.

The background colours in Figure 3. 8 represent the lattice temperature for $R_{th\text{-}2}$ according to Eq. (III.1).

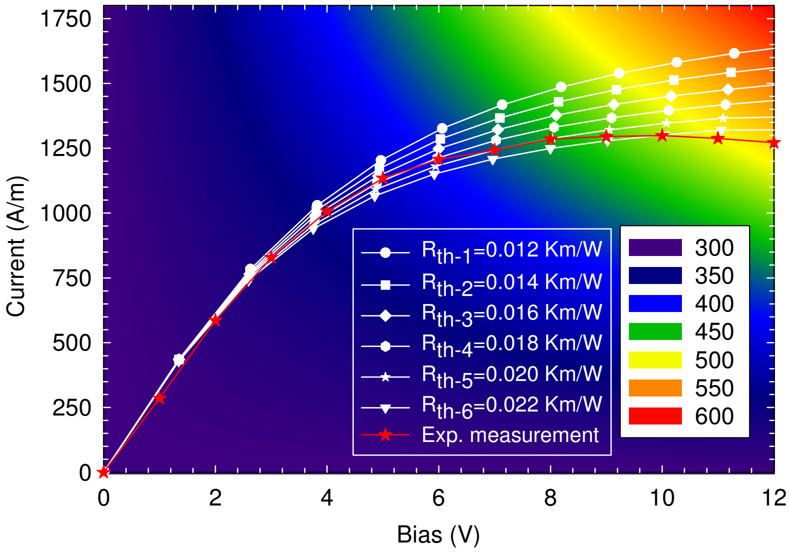

Figure 3. 8: *I-V* curves obtained with the TRM with the thermal resistances indicated in Table 3. 2. The experimental results are also included. The background colours represent the lattice temperature for each bias point according to the Eq. (III.1) in the case of $R_{th\text{-}2}$.

---

[12] 150000 iterations.

[13] 300000 iterations.

The current values for the six thermal resistances under analysis are similar for low bias, up to 2.5 V, because the dissipated power is insignificant and therefore the increase in temperature is small ($T \sim 327$ K at V_{MC}=2 V for 18x10^{-3} K·m/W). At higher voltages the temperature reaches values as high as 494 K, 516 K, 536 K, 555 K, 573 K and 590 K at V_{MC}=10 V for the $R_{\text{th-1}}$, $R_{\text{th-2}}$, $R_{\text{th-3}}$, $R_{\text{th-4}}$, $R_{\text{th-5}}$ and $R_{\text{th-6}}$, respectively. Good agreement with the experimental result is achieved up to ∼6 V with $R_{\text{th-4}}$=0.018 K·m/W, but the saturation level of the experimental current is not well reproduced.

Although this model provides an acceptable approximation, it does not replicate the real operation conditions because temperature is kept constant along the whole device. For this reason, a more complex physical model will be explored in the next section.

(b) Heat Diffusion Equation Model (HDEM)

The HDEM allows us to calculate a local temperature map and identify hot spots inside the device. It is important to note that the source of the heating (corresponding to lattice phonon emission) is only provided by the electronic domain, but Eq. (III.4), used to calculate the temperature distribution, is solved in the complete thermal domain taking into account the heat flow in the whole device. The thermal conductivities of the different materials, at room temperature, are reported in Table 1. We chose a reference structure with L_1=200 µm. For the substrate, a Si layer with a thickness of L_2=300 µm is considered. A heat-sink at room temperature (T=300 K) is located at the bottom of the structure.

Material	k^{300} ($W \cdot K^{-1} \cdot m^{-1}$)
$Al_{0.27}Ga_{0.73}N$	30 (169)
GaN	130 (144)
Polycrystalline SiC	300 (61)
Si	156 (67)
Au	315 (67)
Diamond	1000 (146)
Sapphire	42 (66)
Polycrystalline diamond (*PCD*)	2200(61)

Table 3. 3: Values of the thermal conductivity at 300 K used in the simulation for the different materials.

Figure 3. 9 (a) shows the isothermal (at room temperature) *I-V* curve and those obtained at different iterations of the MC simulation when the lattice temperature is updated according to the protocol explained in Section 3.2.2. For low bias, up to 4 V, the current converges to its thermally self-consistent value in the second iteration of the solution of the HDEM. For higher potentials, and for this particular case, it is necessary to perform at least four iterations, at which the current does not differ visibly from the previous one, thus indicating the convergence of the algorithm.

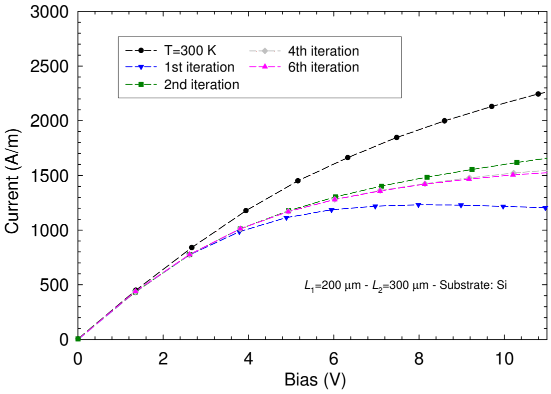

Figure 3. 9: (a) *I-V* curve of the diode, showing the results of an initial isothermal simulation and of successive iterations towards convergence of the HDEM. Results for the diode presented in Figure 3. 6.

In Figure 3. 10 (a) we superimpose the *I-V* curve obtained with the HDEM over the ones obtained before with the TRM.

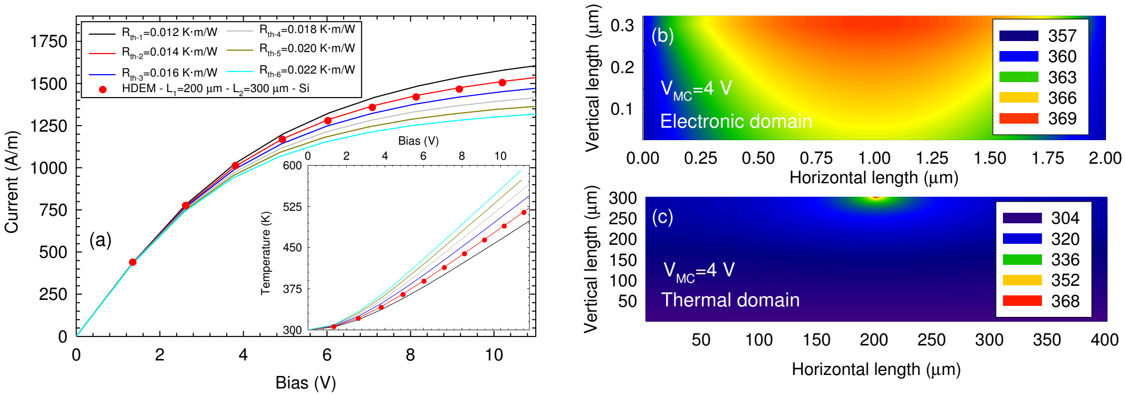

Figure 3. 10: (a) *I-V* curves obtained with the TRM with the thermal resistances indicated in Table 3. 2. The results obtained with the HDEM are also presented. The inset shows the average temperature in the electronic domain of HDEM compared with the TRM temperature at different applied bias. (b) Spatial distribution of the lattice temperature in the electronic domain and (c) in the thermal domain, when the bias is V_{MC}=4 V.

It is striking that the TRM with R_{th-2} and the HDEM (circle symbols) provide almost same results. In particular, if we focus on a bias of 5 V (corresponding to V_{MC}=4 V), both methods give the same value of the current density, ~1170 A/m, and the dissipated power generated by phonons, ~4.6 K·W/m. However, the value was obtained under different conditions: while the lattice temperature is constant (T~365 K) for the TRM, for the HDEM it changes with position, as shown in the map of the electronic domain plotted in Figure 3. 10 (b). A detailed scrutiny reveals that the maximum, minimum and average temperatures are T_{max}=369 K, T_{min}=358 K and T_{av}=365 K, respectively. We wish to stress that T_{av} is almost the same as the T_{latt} obtained from the TRM, as shown in the inset of Figure 3. 10 (a). Figure 3. 10 (c) shows the lattice temperature in the complete thermal domain. As can be observed, the high temperature region is concentrated in the vertical position in the 300 µm to 250 µm range, and remains close to the temperature of the sink (T=300 K) in the rest of the thermal domain.

(b.1) Extraction of R_{th} from HDEM

The comparison between both electro-thermal models in the previous section suggests the possibility of extracting an R_{th} from HDEM. Using the structure presented in Figure 3. 6 with L_1=200 µm, L_2=300 µm and Si-substrate (k_S), the I-V curve and the average temperature as a function of the dissipated power are plotted in Figure 3. 11 (a) and (b), respectively.

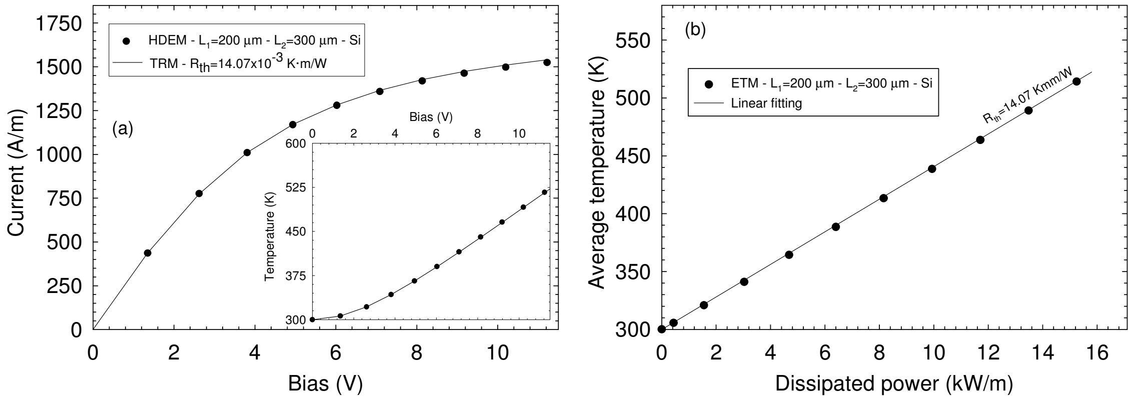

Figure 3. 11: (a) I-V curves for the TRM (R_{th}=14.07x10^{-3}K·m/W) and the HDEM. The inset shows temperature (average for the HDEM) *vs.* bias. (b) Average temperature, T_{av}, *vs.* dissipated power and linear fitting to extract the corresponding thermal resistance. The solid lines in Figure 3. 11 (a) correspond to the results obtained with the TRM for the estimated thermal resistance. L_1=200 µm, L_2=300 µm and k_S=156 W/(K·m) are considered.

Figure 3. 11 (b) allows us to extract the values of R_{th} used in the TRM from the HDEM. For this, we make a linear fitting of the average temperature *vs.* dissipated power. The slope of the linear regression provides R_{th}. To check the equivalence between both models, we use the extracted value of R_{th} in the TRM. As we can see from the solid lines of Figure 3. 11 (a) the TRM *I-V* curves provide the same results as the simulations with the HDEM.

The inset in Figure 3. 11 (a) shows the TRM temperature and the average temperature from the HDEM *vs.* bias. As can be observed, both temperatures are almost the same, meaning that the two models are equivalent. Once the R_{th} of a structure has been extracted with the HDEM, the TRM can be used to optimize the thermal properties of the device because it is faster and requires less resources. However, note that with the TRM only a global value of the lattice temperature is calculated, while with the HDEM a local temperature map can be analysed, it being possible to identify hot spots inside the device that could be important in more complex devices such as HEMTs.

(b.2) Dependence on k_s

In Figure 3. 12 we plot, the *I-V* curves, Figure 3. 12 (a), and the average temperature in the electronic domain (T_{av}) *vs.* dissipated power, Figure 3. 12 (b) for devices grown on different substrates (PCD, diamond, Si, SiC and sapphire).

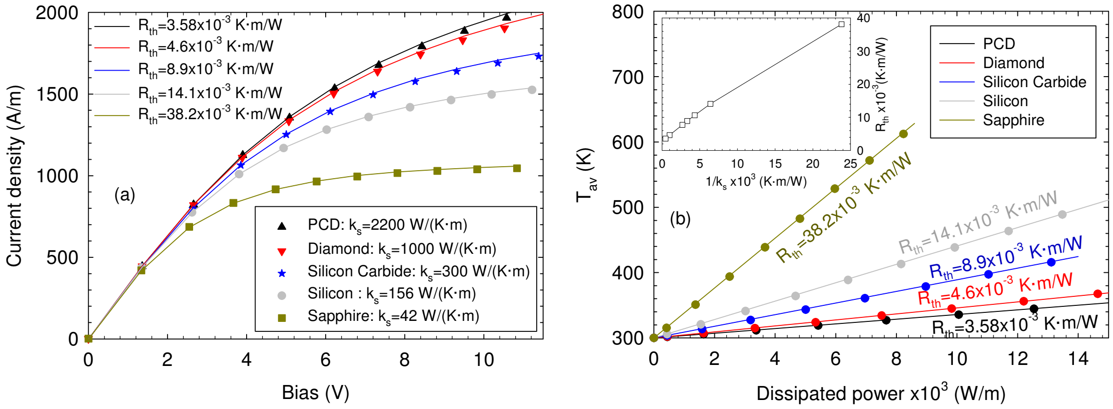

Figure 3. 12: (a) Symbols show the *I-V* curves for different substrates: PCD, diamond, silicon carbide, silicon and sapphire. (b) Analysis to evaluate the influence of k_s in the simulations. Average temperature, T_{av}, *vs.* dissipated power and linear fitting to extract the corresponding thermal resistance. The inset shows R_{th} *vs.* $1/k_s$. L_1=200 µm and L_2=300 µm. The solid lines of Figure 3. 12 (a) correspond to the results obtained with the TRM for the estimated thermal resistances.

For the lowest values of k_s, self-heating becomes crucial: the substrate exhibits a significant influence on the current saturation level; note that for V_{DS}=8 V, T_{av}=612 K for sapphire and T_{av}=438 K for Si. In the case of materials with high k_s (PCD and diamond), although the PCD substrate has a thermal conductivity more than two-fold higher than the diamond substrate, the current level does not change significantly. This reflects the fact that both substrates are excellent heat conductors. In fact, at high power (V_{DS}=8 V) the devices operate with similar T_{av} (355 K and 365 K for PDC and diamond, respectively).

In Figure 3. 12 (b) the extracted values of R_{th} are indicated: R_{th}=38.2x10^{-3} K·m/W, R_{th}=14.1x10^{-3} K·m/W, R_{th}=8.9x10^{-3} K·m/W, R_{th}=4.6x10^{-3} K·m/W and R_{th}=3.58x10^{-3} K·m/W for sapphire, Si, SiC, diamond and PCD, respectively. As expected, R_{th} is inversely proportional to k_s, see inset of Figure 3. 12 (b). Once again, such estimated values for the thermal resistances will provide, in a TRM based model, the same *I-V* curves [see solid lines of Figure 3. 12 (a)] as those obtained from the simulations with the HDEM.

Figure 3. 13 plots the lattice temperature in the thermal and electronic domains for the PCD, Si, and sapphire substrates for a bias of 6 V.

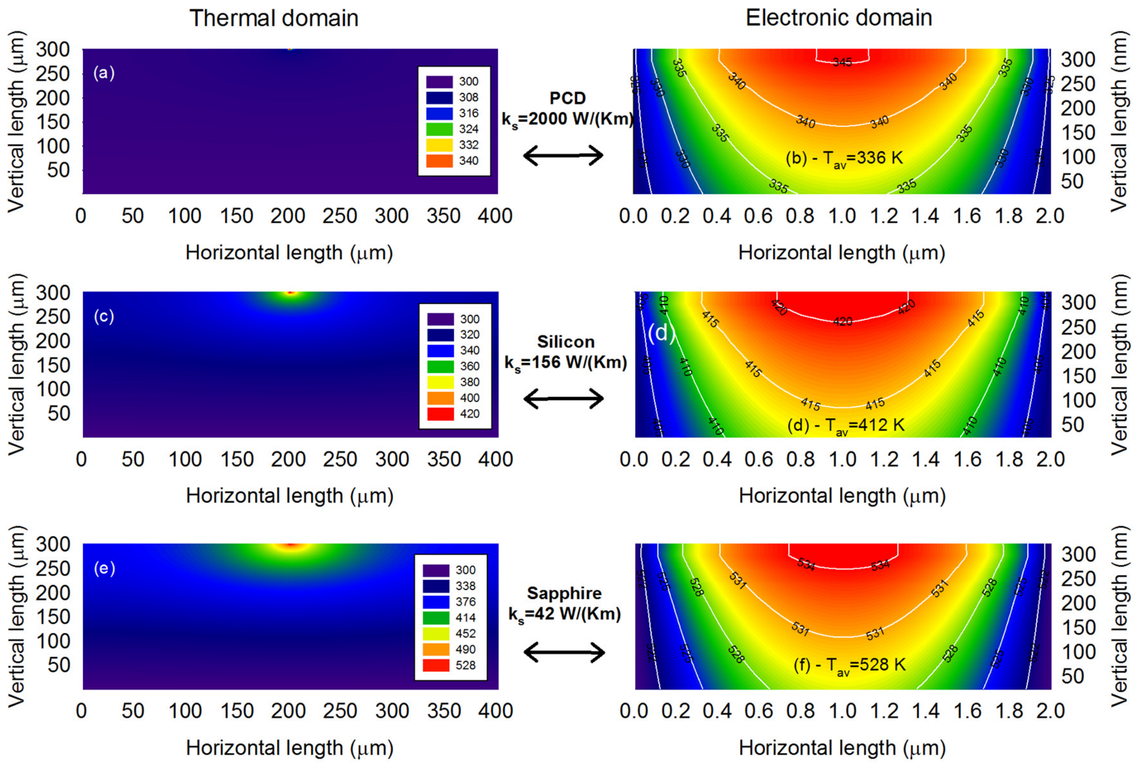

Figure 3. 13: Temperature distribution, for a bias of 6 V, to evaluate the influence of k_s: PCD, 2200 W/(K·m); silicon, 156 W/(K·m) and sapphire, 42 W/(K·m) in the simulations. Thermal domain (a), (c) and (e), and electronic domain (b), (d) and (f). L_1=200 μm and L_2=300 μm.

A strong degradation of the device operation may take place with the sapphire substrate due to the very high temperatures reached as a consequence of the poor thermal conductivity [Figure 3. 13 (e), (f)] in comparison with Si [Figure 3. 13 (c), (d)] and PCD [Figure 3. 13 (a), (b)]. In the electronic domain, the average temperatures are T_{av}=528 K, T_{av}=412 K and T_{av}=336 K (T_{max}=535 K, 422 K and 345 K) for the sapphire, Si and PCD, respectively. In all cases, the temperature peak is well located in the GaN two-dimensional electron gas (2DEG) of the diode.

In Figure 3. 14 we represent the profiles of the increase in lattice temperature for the same bias (6 V) at three different *y*-positions (channel, MC-HDE domain interface, and buffer-substrate interface).

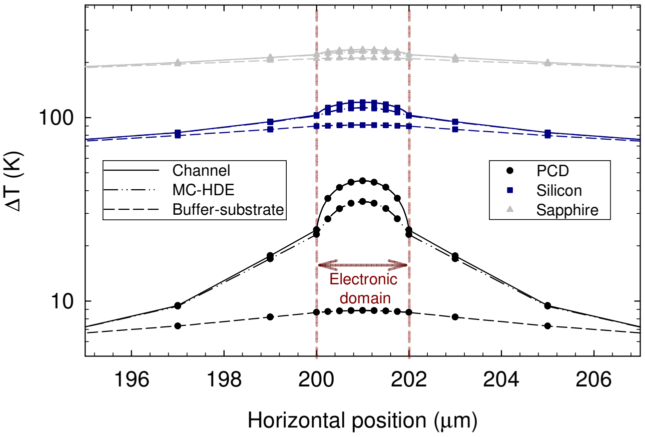

Figure 3. 14: Profile of the increase in lattice temperature ($\Delta T = T_{latt} - T_h$) for three different *y*-positions [channel, MC-HDE domain interface and buffer-substrate interface, see Figure 3. 6 (a)] for a bias of 6 V.

It is noteworthy that when thermal conductivity is low (for sapphire) the lattice temperature for the three layers is almost the same and constant in the electronic domain and vicinities. The sapphire material causes a huge rise in temperature. For the sapphire, and if the die length is too short, the contacts will be subjected to high temperatures (which could damage them), in comparison with the cases of diamond or PCD substrates. As a consequence, the substrate exerts a strong influence over the thermal management of the device.

(b.3) Dependence on die lengths (L_1, L_2)

In Figure 3. 15 (a) we analyze R_{th} *vs*. the die dimension L_1 for L_2=250 μm, 300 μm and 350 μm. For low values of L_1, R_{th} increases enormously, whereas for high values of L_1, R_{th} can be considered almost constant. For a given L_1, Figure 3. 15 (b), as L_2 is increased the thermal resistance becomes higher, as expected, and therefore the heat flux generated by the phonons is dissipated less efficiently because the heat sink is further away from the electronic domain. R_{th} is in the 12-23x10^{-3} K·m/W range.

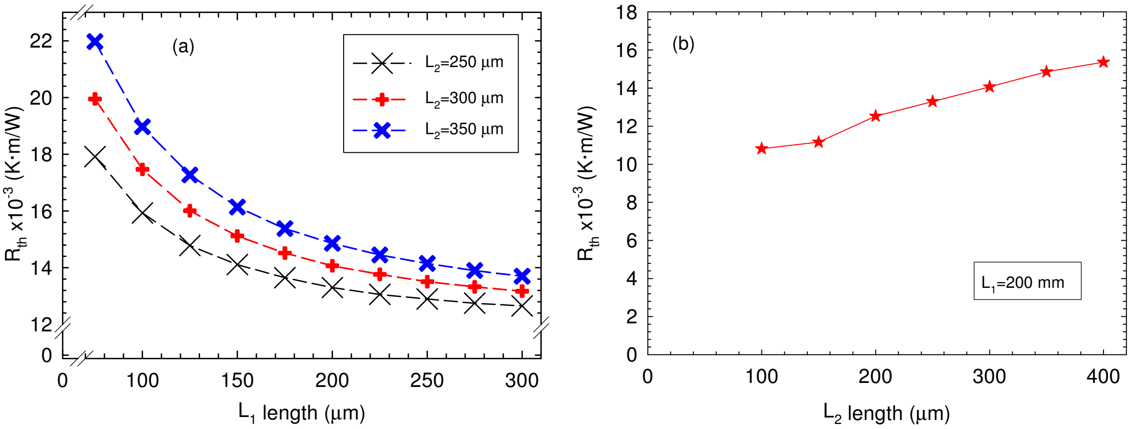

Figure 3. 15: (a) R_{th} *vs.* the die dimension L_1 for L_2=250 μm, 300 μm and 350 μm. (b) a) R_{th} *vs.* die dimension L_2 for L_1=200 μm. The substrate employed is Si.

(b.4) Design rules based on L_1, L_2 and k_s

By taking the structure presented in Figure 3. 6 as a reference, we have made a systematic analysis to evaluate the influence of (i) k_s, (ii) L_2 and (iii) L_1 on the results when they are modified by a factor 2 with respect to the reference values. That is, k_s=300 W/(K·m), L_1=100 μm and L_2=150 μm. The symbols in Figure 3. 16 (a) show the *I-V* curves calculated with the HDEM.

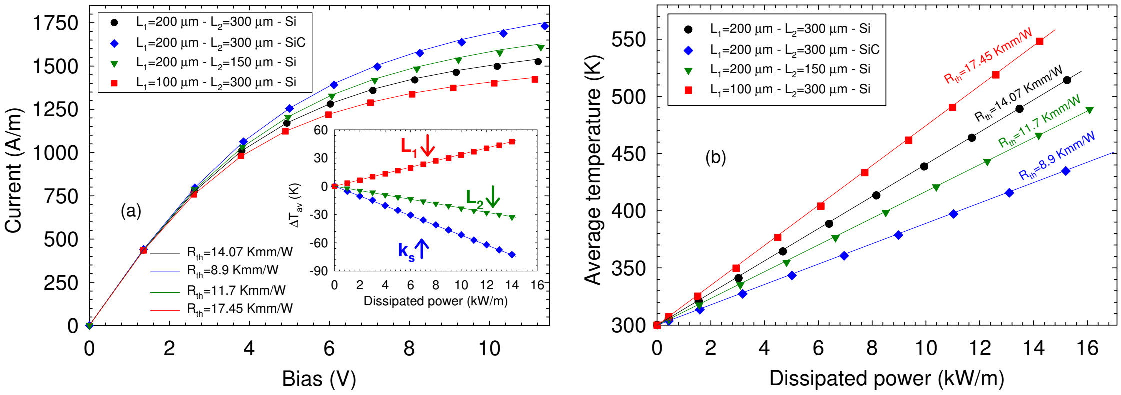

Figure 3. 16: Systematic analysis to evaluate the influence of k_s, L_1 and L_2 in the simulations. (a) The symbols show the *I-V* curves when the HDEM is employed. The inset shows the variation in the average temperature with respect to the reference diode. (b) T_{av} *vs.* dissipated power and linear fitting to extract the corresponding thermal resistance. The solid lines in Figure 3. 16 (a) correspond to the results obtained with the TRM for the estimated thermal resistances.

In addition, in the inset of Figure 3. 16 (a) we plot the average temperature difference with respect to the reference diode, ΔT_{av}, as a function of the dissipated power. Although k_s, L_1 and L_2 are modified by a factor ∼2, the parameters that have the strongest impact on temperature are k_s, then L_1, and finally L_2. The calculated slopes are -5.2, 3.4 and -2.3 K·m/kW, respectively. Regarding the dependence on k_s, a higher current is achieved for the SiC-substrate than for Si due its better thermal conductivity and hence less self-heating in the structure. Regarding L_2, when this is decreased from 300 µm down to 150 µm, the power generated by the phonons is dissipated more efficiently because the heat sink is closer to the electronic domain. Finally, with respect to L_1, if this is reduced down to 100 µm, the current decreases due to a stronger and more uniform self-heating. Also, it is possible to extract, Figure 3. 16 (b), the equivalent thermal resistance. In Figure 3. 16 (a) it may be seen that by that employing such estimated values for the thermal resistances in the TRM (lines) model, the same *I-V* curves are obtained as in the simulations with the HDEM (symbols).

This analysis leads to the following recommendations. When possible, for manufacturing purpose: (i) employ high-thermal conductivity substrates, (ii) reduce substrate depth and (iii) design a long enough die to guarantee low temperature in the contact areas. We checked that values of L_1 smaller than 100 µm result in very high temperatures >700 K at V_{MC}∼10 V.

(b.5) Thermal boundary resistance (TBR)

Thermal effects are boosted by the thermal boundary resistance (TBR). The TBR is a measure of the opposition that an interface exerts against the heat flow due to different phonon dynamics and poor crystalline quality near the boundary. The TBR can be measured by employing 3-D micro-Raman thermography (170). In order to include TBR effects in semiconductor device simulators, different techniques are used, ranging from those based on 3-D finite-difference models (170) to others that employ a continuity condition for a finite interfacial conductance between the layers of interest (171). However, to date the modelling of the TBR effects is still an open problem.

Our approach to take into account the effect of TBR is very simple: we included a small layer of thickness Δ_{TBR} of a material with low thermal conductivity, k_{TBR}, between the GaN-buffer and the substrate (see Figure 3. 17*,* yellow layer).

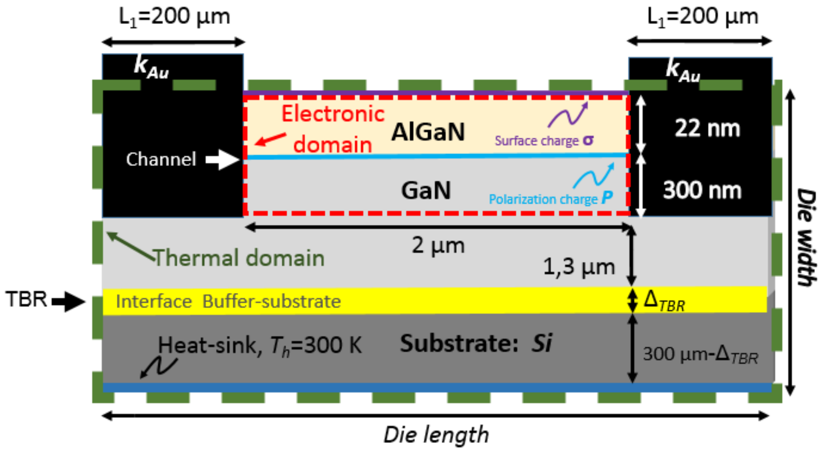
L$_1$=200 µm
L$_1$=200 µm
k_{Au}
k_{Au}
Electronic domain
AlGaN
Surface charge σ
22 nm
Channel
GaN
Polarization charge P
300 nm
Die width
Thermal domain
2 µm
1,3 µm
TBR
Interface Buffer-substrate
Δ_{TBR}
Heat-sink, T_h=300 K
Substrate: Si
300 µm-Δ_{TBR}
Die length

Figure 3. 17: AlGaN/GaN diode geometry under study. The location of the TBR is indicated.

In this framework, the value of the simulated TBR will be:

$$\mathrm{TBR} = \Delta_{\mathrm{TBR}}/k_{TBR} \qquad \text{(III.24)}$$

The effect of the TBR is analysed by choosing three substrates, SiC, Si and sapphire. A layer of thickness Δ_{TBR}=15 nm is introduced at the buffer-substrate interface. Simulations were performed by considering two temperature-independent thermal conductivities (k_{TBR}) of 1 and 0.1 W/(K·m) for this layer. According to Eq. (III.24), the TBR is equal to 1.5x10^{-8} and 15x10^{-8} m^2·K/W, this being consistent with the values reported experimentally (170). The TBR for GaN on sapphire has been suggested to be higher than for SiC and Si because the interface between the epitaxial films and their growth substrate contains nucleation layers and areas with a high concentration of defects and impurities. In addition, there is still considerable uncertainty in the device material parameters and their temperature dependences (170). We point out that the TBR increases with temperature. For example, in ref. (170), it was found a TBR of 3.3x10^{-8} m^2·K/W at 150 K and a TBR of 6.5x10^{-8} m^2·K/W at 275 K at the GaN/SiC interface.

In Figure 3. 18 (a), (b) and (c), we analyse T_{av} *vs.* P_{diss} for SiC, Si and sapphire. The insets show the profile of the lattice temperatures in the middle of the structures at the buffer-substrate interface. As expected, SiC exhibits better thermal behaviour than Si, and sapphire, and therefore, lower temperatures are obtained inside the device. If the TBR is very high (further obstructing the exit of the thermal flow from the device), it can be the critical parameter for the design of an appropriate heat sink. Note that the discontinuity ΔT at the interface increases when a higher conductivity substrate is chosen (by way of example, for a TBR=15x10^{-8} m^2·K/W, and at a bias of 10 V, ΔT of 142 , 125 K and 70 K are obtained for SiC Si, and sapphire, respectively). SiC is the most sensitive to the changes in the TBR. Remarkably, it may occur that a device grown on a substrate with poor k_s but with a good thermal interface resistance (low TBR) exhibits better thermal behaviour than another grown on a substrate with an excellent k_s but with a high TBR. This behaviour is also reflected in the values of R_{th} obtained, which are in the 9-17x10^{-3}K·m/W, 14-21x10^{-3} K·m/W, and 38-41x10^{-3} K·m/W ranges for SiC and Si, and sapphire, respectively.

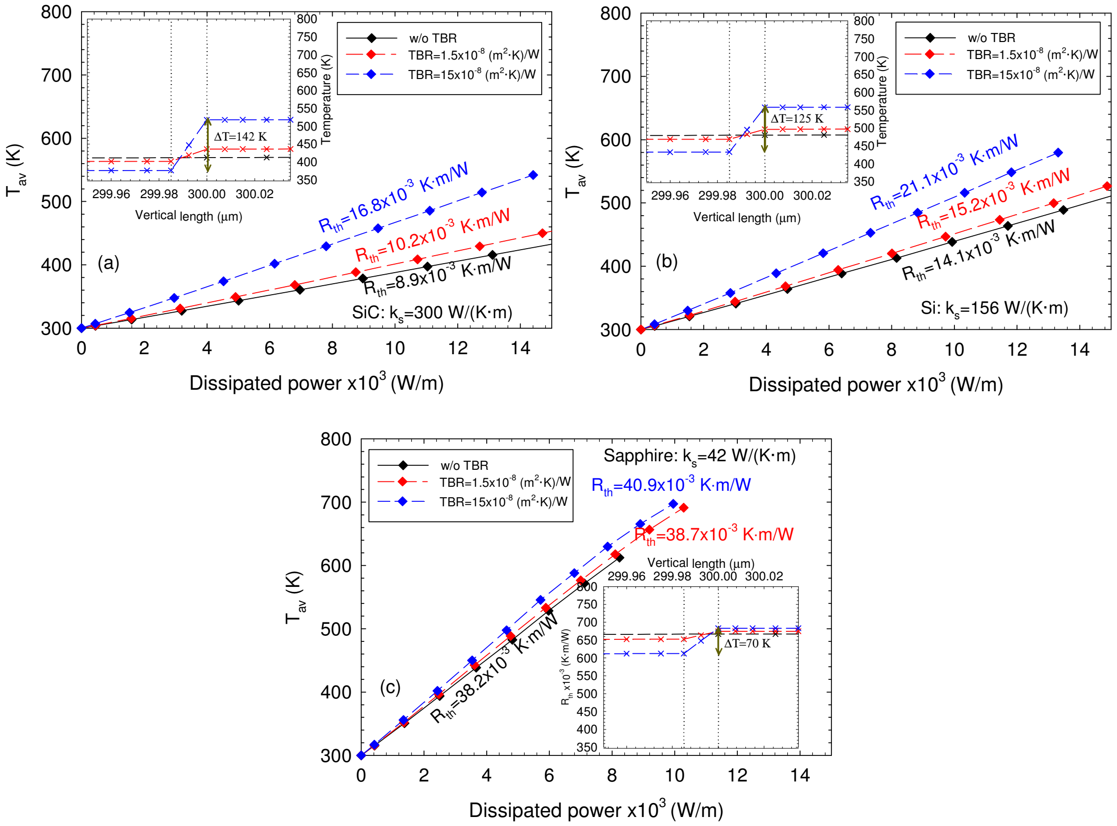

Figure 3. 18: T_{av} *vs.* P_{diss} for three substrates (a) SiC, (b) Si and (c) sapphire. A TBR layer of Δ_{TBR}=15 nm with k_{TBR} =1 and 0.1 W/(K·m) is studied. Note that the case without the TBR layer from Figure 3. 12 is included for the sake of comparison. The insets show the profile of the lattice temperatures in the middle of the diode close to the TBR region for a bias of 10 V.

Below, in Figure 3. 19, we analyse the effect of Δ_{TBR} and k_{TBR} on Eq. (III.24), providing the same TBR (15x10^{-8} m^2·K/W). For this, we explore the profile of the lattice temperature close to the TBR region in the middle of the diode of Figure 3. 17. The sets [Δ_{TBR}=15 nm, k_{TBR}=0.1 W/(K·m)], [Δ_{TBR}=9 nm, k_{TBR}=0.06 W/(K·m)] and [Δ_{TBR}=3 nm, k_{TBR}=0.02 W/(K·m)] are studied in Figure 3. 19. Note that the temperature discontinuity is 125 K in all three cases. This demonstrates that, given a constant TBR, its effects can be introduced in the simulations by adjusting the pairs Δ_{TBR} and k_{TBR}.

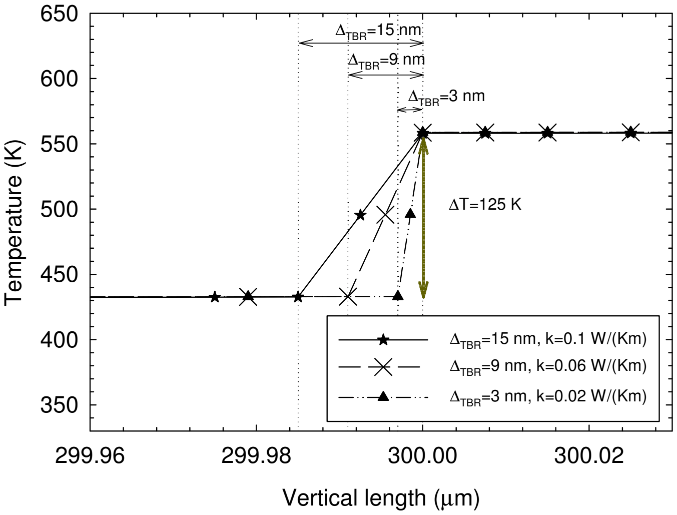

Figure 3. 19: Profile of the lattice temperatures in the middle of the diode close to the TBR region, for a bias of 10 V when we set TBR=15x10^{-8} m^2·K/W. Sets of pairs Δ_{TBR}=15 nm, k_{TBR}=0.1 W/(K·m); Δ_{TBR}=9 nm, k_{TBR}=0.06 W/(K·m) and Δ_{TBR}=3 nm, k_{TBR}=0.02 W/(K·m).

(b.6) Temperature-dependent thermal conductivity

Up to this point, we have considered temperature-independent thermal conductivity for all the materials. However, this is not completely realistic, since it is well known that thermal conductivity depends on temperature, according to Eq. (III.12). There is a significant discrepancy in the reported values for the thermal conductivity of GaN. As an example, A=4400 W·K$^{0.4}$·cm^{-1}, α=1.4 are used in (170), and in (144) two different models are proposed: A=15 W·K$^{-0.57}$·cm^{-1}, α=0.43, and A=2100 W·K$^{0.2}$·cm^{-1}, α=1.2. These dependences on thermal conductivity are plotted in Figure 3. 20 (a)[14].

For the silicon substrate, the experimental data are well reproduced by A=2590 W·K$^{0.3}$·cm^{-1} and α equals 1.3 (67), Figure 3. 20 (b). For Au, the dependence is given by the parameters A=3.846 W·K$^{-0.965}$·cm^{-1} and α=0.035 (67), Figure 3. 20 (c). Finally, for AlGaN, k is almost constant within the 300 K - 400 K range, with a value of about 30 W/(K·m) (169), see Figure 3. 20 (d). It is very important to note that the same functional relationship [same value of α of Eq. (III.12)] must be used for all the materials in order to fulfil the temperature continuity when using the Kirchhoff transformation (67). We choose α=1.3, which corresponds to the most relevant layer (Si) for the solution of the heat flow equation. Therefore, the temperature-dependent thermal conductivity for all semiconductors is:

---

[14] We assume that thermal conductivity is not dependent on layer thickness. However, some properties of the materials, such as dislocation density (especially for GaN or diamond samples) and thermal conductivity, can vary significantly with sample thickness, as ref. (172) describes.

$$k_i(T) \approx k_i^{300} \cdot \left(\frac{300\ K}{T}\right)^{1.3}. \qquad \text{(III.25)}$$

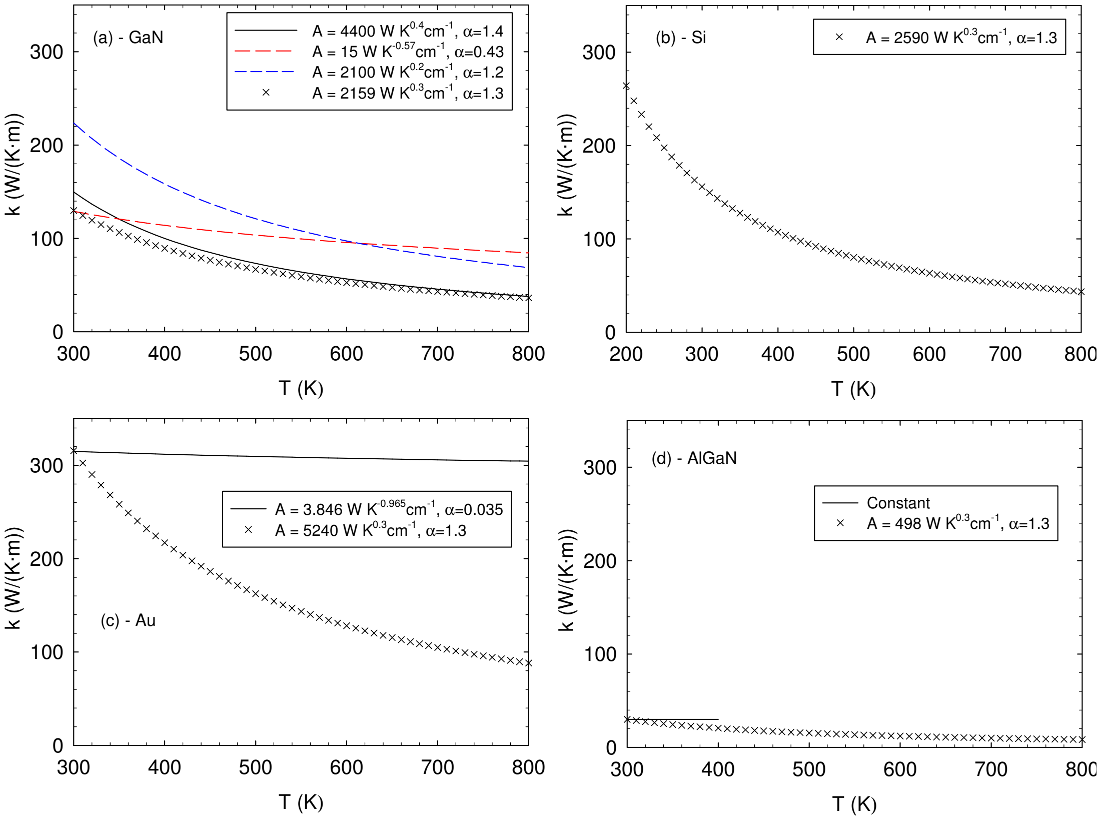

Figure 3. 20: Thermal conductivity: $k_i{\sim}AT^{-\alpha}$ for the reported values in the literature: (a) GaN: A=4400 W·K$^{0.4}$·cm^{-1} and α=1.4 (170), and in (144) A=15 W·K$^{-0.57}$·cm^{-1} and α=0.43, A=2100 W·K$^{0.2}$·cm^{-1} and α=1.2. (b) Si: A=2590 W·K$^{0.3}$·cm^{-1} and α=1.3 (67). (c) Au: A=3.846 W·K$^{-0.965}$·cm^{-1} and α=0.035 (67). (d) For AlGaN, k is almost constant within the 300 K - 400 K, 30 W/(K·m) range. The thermal conductivity, when the same functional α=1.3 is considered, is also plotted (crosses) for all materials satisfying Eq. (III.25).

The thermal conductivity of Eq. (III.25) *vs.* temperature is also represented for all materials, see crosses in Figure 3. 20. For the GaN and AlGaN materials, thermal conductivity is well reproduced while for Au this approximation does not replicate the real dependence; in particular at high temperatures. However, the contacts will usually be close to 300 K, so the approach is justified. Figure 3. 21 shows the relationship between *T* and *Θ* given by Eq. (III.13) when Eq. (III.25) is used.

In Figure 3. 22 (a) we plot a comparison of the results obtained from the simulation with temperature-independent and temperature-dependent thermal conductivities for the diode in Figure 3. 6.

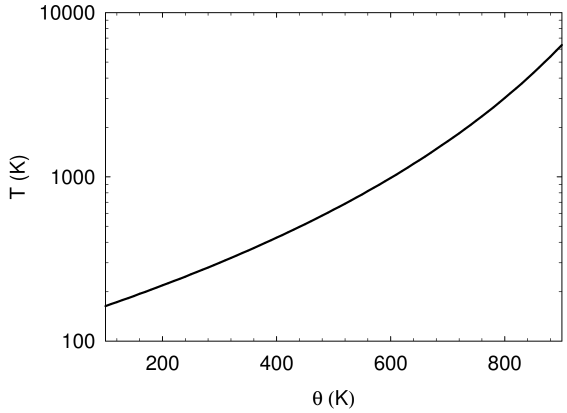

Figure 3. 21: *T vs. Θ* when Eq. (III.25) is satisfied.

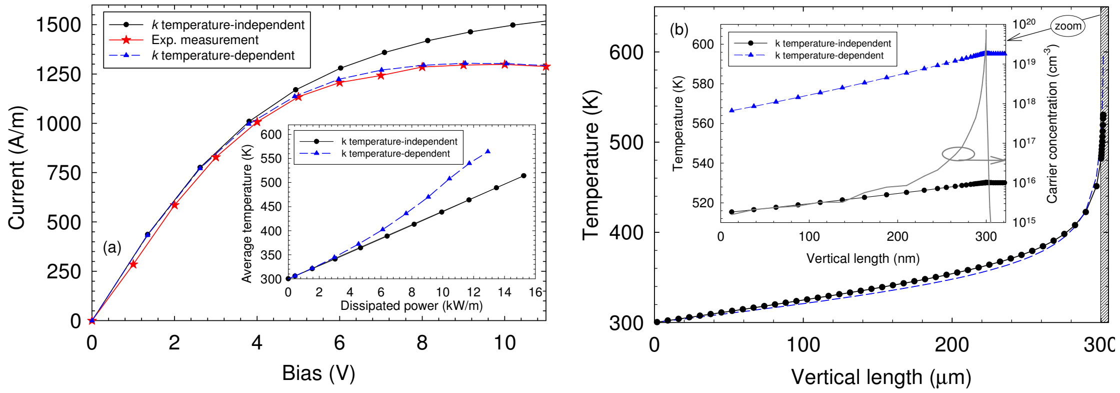

Figure 3. 22: (a) *I-V* curves for the diode presented in Figure 3. 6 using the temperature-dependent thermal conductivity model. The experimental measurements and the calculations with constant thermal conductivity are also included for the sake of comparison. The inset shows the T_{av} *vs*. dissipated power for the reference structure and the temperature-dependent thermal conductivity model. (b) Profile of temperature along a vertical section (*x*-length=1 μm) for constant conductivity and the temperature-dependent model using Eq. (III.25) at V_{MC}=10 V. Inset: Zoom of the electrical domain (shadowed region) with the carrier concentration on the right axis (for the temperature-dependent thermal conductivity model).

The temperature-dependent thermal conductivity model reproduces the experimental saturation region at high voltages very satisfactorily: the current density decreases. It can be noted from the inset in Figure 3. 22 (a) that for the temperature-dependent thermal conductivity models it is not possible to define a constant thermal resistance because T_{av} is non-linear with the dissipated power. Therefore, carrying out a TRM simulation is not straightforward and the HDEM scheme is required. Within this temperature-dependent thermal conductivity, higher temperatures are reached inside the device as a result of the decrease in thermal conductivity with increasing temperature. To show this effect, Figure 3. 22 (b) presents, at V_{MC}=10 V, the vertical profile of the temperature in the middle of the diode (x-length=1 µm) for the simulation with constant conductivity and for the temperature-dependent thermal conductivity model. Near the heat sink, both approaches provide almost the same temperature, but around 20 µm below the GaN-substrate interface the temperature starts to increase significantly, and this increase is even more abrupt for the temperature-dependent model. The difference in temperature between the two models can be observed better in the inset of Figure 3. 22 (b), where only the electronic domain is presented (300 nm from the top of the whole device). Note that on the right axis we also plot the carrier concentration to help identify where the 2DEG is located.

To conclude this section, we simulate the effect of the TBR. We model the temperature-dependent thermal conductivity [Eq. (III.25)] for a TBR of thickness Δ_{TBR}=15 nm by considering the parameter A=1.6605 W·K$^{0.3}$·cm^{-1} [k_{TBR}=0.1 W/(K·m) at 300 K)]. Figure 3. 23 plots the current density as a function of bias.

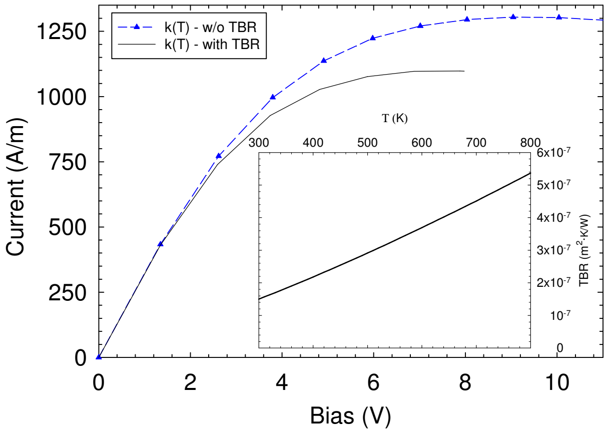

Figure 3. 23: *I-V* curves with and w/o TBR. The inset shows the TBR [Eq. (III.24)] *vs.* *T* when the thermal conductivity of Eq. (III.25) is considered.

When the TBR is included, and for biases higher than 2 V, the current is lower in comparison with the results w/o TBR. The TBR layer elicits an increase of the temperature inside the device being and becomes more pronounced as bias is increased. The simulation becomes unstable for a bias around 8 V as a consequence of the very high temperatures due to the combination of the reduction in thermal conductivity and the block of the heat flow by the TBR. The increase in TBR with temperature is shown in the inset of Figure 3. 23. Consideration of the TBR may be very important for realistic device modelling.

3.4. Three-terminal device: HEMT

In this section we examine the effects of heating in submicrometer HEMTs using an electro-thermal MC method. We analyse the characteristics of the transistor by considering isothermal and electro-thermal simulations. For the electro-thermal ones, we shall study the effect of the heat-sink temperature and the gate length.

The structure of the layers and the geometry of the HEMT used as reference are shown in Figure 3. 24. The distance between the drain-source contacts is 1 µm. The structure is a 22-nm-thick un-doped $Al_{0.27}Ga_{0.73}N$ barrier layer grown on top of a 1.5-µm-thick un-doped GaN buffer grown on Si. The development of the technology in recent years has led to the addition of more layers in the manufacture of HEMTs. We remark (i) the introduction of an Aluminium Nitride (AlN) spacer layer between the AlGaN and GaN as one way to improve the 2DEG density, mobility, and drain current (173), and (ii) AlN has traditionally been used as an interlayer to grow high-quality GaN on Si (174)(15). These layers have been disregarded in our simulations, but our simplistic and symmetric structure is a good choice to analyse the electron transport and thermal effects in GaN-based HEMTs in detail.

The gate (Schottky contact) is positioned in the middle of the structure, and has a length of 250 nm. Current through a Schottky contact is mainly caused by thermionic emission

---

[15] The role of the AlN seed layer is to structurally decouple the top GaN layer from the underlying Si substrate. The AlN layer induces a compressive stress in the GaN layers grown subsequently, partially counterbalancing both the growth and the thermally induced tensile stress and hence preventing cracking. Furthermore, the use of AlN nucleation layers in HEMTs reduces parasite conduction in the substrate and leads to a better pinch-off condition.

of carriers over the barrier. Quantum mechanical tunnelling and barrier lowering due to image force could be an important effect to be taken into account. For simplicity, and because our objective was to study the thermal behaviour, these effects were not taken into account in our simulator. Thus, our Schottky contact will only act as point of exit for electrons that are able to surpass the barrier of potential imposed by this contact. The Schottky potential barrier can be implemented simply by a shift in the gate-to-source bias, V_{GS}. This means that $V_{GS}(experimental)=V_{GS}(MC)+V_{\varphi}$. The Schottky potential barrier, V_{φ}, is typically in the 0.5 V-1.5 V range (for different metal work functions) (175). We shall not compare our MC results with experimental measurements, so neither the V_{φ} nor the external contact resistance are included in the present study.

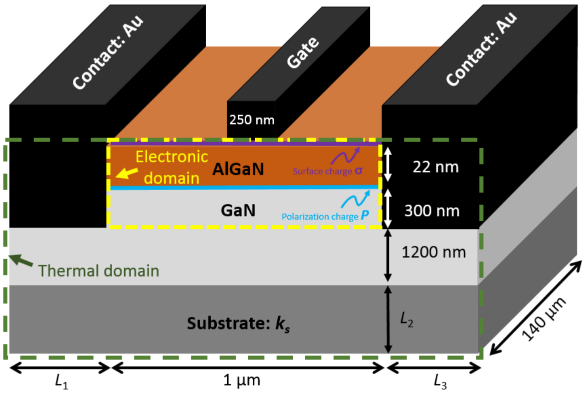

Figure 3. 24: AlGaN/GaN HEMT geometry under study. The gate has a length of 250 nm. The area limited in yellow corresponds to the electronic simulated region of the diode and the region limited in green is the thermal domain.

Between the AlGaN and GaN layers, the theoretical polarization charge P=14.12x10^{16} m^{-2}, obtained from Equation (III.14), is considered. A surface charge density σ=-4.12x10^{16} m^{-2} is placed at the top of the AlGaN layer. Under equilibrium conditions, n_S will be 10x10^{16} m^{-2} ($n_s=P-\sigma$). This value was chosen following some experimental guidelines for HEMTs manufactured in Lille and characterized during a research stay of the author at the Institut d'Électronique du Sud (IES) in Montpellier. A comparison of I-V and g_m obtained from experimental measurements and MC simulations is out of the scope of this work, because this is a preliminary work designed to introduce thermal effects in the MC tool, and also because the manufactured devices were too long and would require excessive computational times. In addition, we did not know all the heterostructure details accurately. Despite this, the HEMTs characterization campaign in Montpellier is summarized in the appendix.

The simulation results of the transistor depicted in Figure 3. 24 at room temperature are plotted below. The developed electro-thermal models are not considered yet. In Figure 3. 25 (a) we show the current I_D *vs.* V_{DS} for gate-to-source biases of -2 V up to -7 V, ΔV_{GS}=1 V, when PDR=0 % and PDR=3 %. The different operation regimes can be differentiated: cut-off (OFF-state operation), triode, and saturation (ON-state operation). When the potential applied to the gate-to source becomes more negative, the slope in the triode region is lower. As is the case for the diodes, the current level decreases as PDR increases from 0 % to 3 %, and the current saturates at higher drain-to-source biases. At PDR=0 %, the saturation starts when 1 V<V_{DS}<2 V, and at PDR=3% the saturation begins to be reached when 1 V<V_{DS}<3 V. For more negative gate-to-source biases (i) saturation starts at lower V_{DS} bias, and (ii) the current level begins to be independent of the value of PDR.

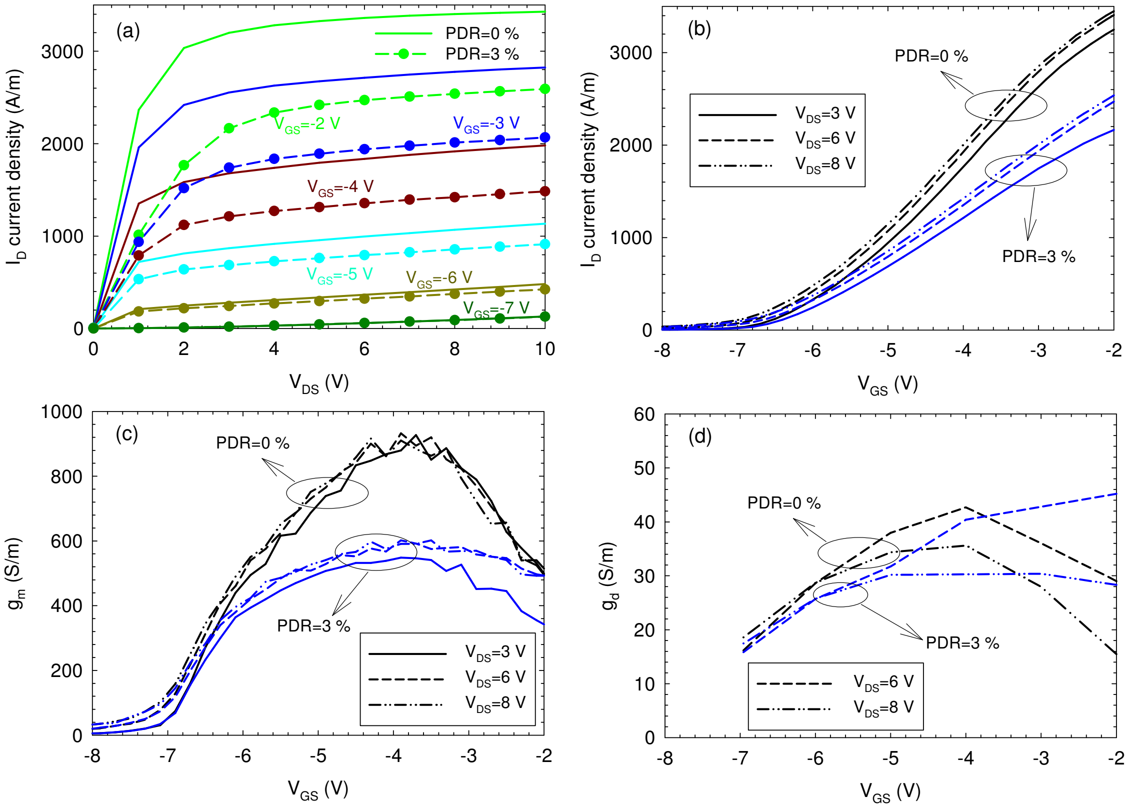

Figure 3. 25: (a) Output characteristics (top curve V_{GS}=-2 V, step 1.0 V). (b) Transfer characteristics, (c) transconductance g_m *vs.* V_{GS}, and (d) g_d *vs.* V_{GS} for V_{DS}=3 V, 6 V and 8 V.

Figure 3. 25 (b) shows the values of the current density I_D *vs.* V_{GS} when V_{DS} is kept constant at 3 V, 6 V, and 8 V. It may be seen that the characteristics are almost the same for V_{DS}=6 V and V_{DS}=8 V. The slope of this curve allows us to define another parameter of interest: namely transconductance (g_m). This parameter gives an idea of the control that the gate-to-source bias has over the drain current. For a field-electric transistor, transconductance is evaluated as:

$$g_m = \left.\frac{\partial I_D}{\partial V_{GS}}\right|_{V_{DS}} . \qquad \text{(III.26)}$$

Figure 3. 25 (c) summarizes g_m *vs.* V_{GS}, corresponding to the DC curves of Figure 3. 25 (b), when V_{DS} is 3 V, 6 V, and 8 V. For PDR=0 %, and for the three biases, V_{DS}, g_m takes its maximum value at V_{GS}=-4 V. We stress that under these particular conditions, g_m is~900 S/m, a high value with respect to the typical values for GaN HEMTs (65). This is due to the fact that the MC provides typically higher mobilities than the experimental ones, and in addition, we were considering the following conditions: PDR=0 %, isothermal temperature of 300 K in the whole device, and the absence of external resistances. For PDR=3 %, g_m takes its maximum value at ~600 S/m, well within the range of typical values for GaN HEMTs (65,176).

Also, the drain conductance, g_d, is analysed, defined as:

$$g_d = \left.\frac{\partial I_D}{\partial V_{DS}}\right|_{V_{GS}} . \qquad \text{(III.27)}$$

We represent g_d *vs.* V_{GS} for V_{DS}=6 V and 8 V. For PDR=0 %, g_d takes its maximum value at V_{GS}=-4 V; and the same trend is observed in both potentials. In contrast, for PDR=3% the same shape is not observed. At V_{DS}=8 V, for V_{GS}>-5 V, g_d remains almost constant; in contrast with V_{DS}=6 V, in which g_d increases as V_{GS} becomes larger. For simplicity, and because we are not going to make a comparison with the experimental results, from now on, we consider a roughness scattering of PDR=0 %.

In order to shed light on the behaviour of the device, and taking advantage of the capability of the microscopic MC simulations, Figure 3. 26 shows the spatial distribution of the main internal quantities [electron concentration (a), energy (b) and longitudinal velocity (c)] and scattering mechanisms (optical polar phonons, d) for V_{DS}=8 V and V_{GS}=-2 V (typical conditions for ON-state operation).

We remark that under these conditions electrons are not completely confined to the region near the heterojunction, Figure 3. 26 (a), but are also injected deep into the GaN layer (which increases drain conductance). This effect could be avoided by the use of a double heterojunction[16]. In addition, we can see the real-space transfer phenomenon in the AlGaN layer. As expected, hot carriers appear in the channel at the drain side of the gate, reaching energies close to 2 eV and exhibiting an important velocity overshoot (up to almost 6x10^7 cm/s). Scattering with optical phonons is also maximum in this region, which could lead to the self-heating effect, which will be studied later by considering the HDEM.

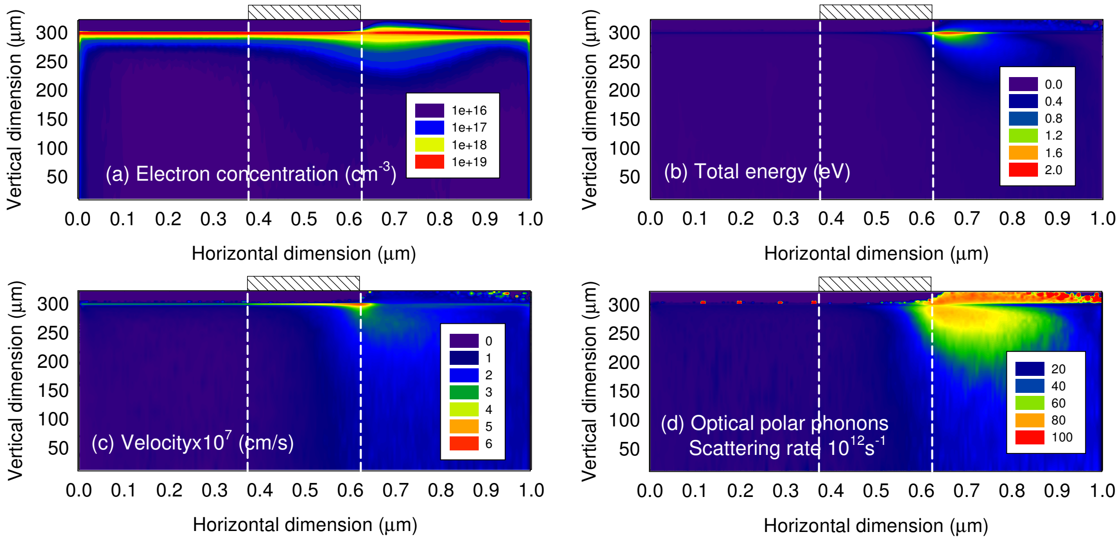

Figure 3. 26: Spatial profiles of (a) electron concentration, (b) energy, (c) longitudinal velocity, and (d) rates of optical polar phonon scatterings for V_{DS}=8 V V_{GS}=-2 V in the HEMT. The position of the gate contact is also indicated.

3.4.1. Isothermal simulations

In this section we consider that the whole device has a homogenous temperature; this means that all the meshes of the discretisation have the same temperature. To this end, we shall compare the results of isothermal simulations at 300 K, 500 K and 700 K.

---

[16] In double heterojunctions, the channel is separated from the buffer layer by a second heterojunction at the bottom of the channel. The additional barrier leads to better carrier confinement and buffer isolation, as well as improved device performance, such as a lower buffer leakage current and a higher-power gain cut-off frequency (177).

Figure 3. 27 (a), and (b) shows the transfer characteristics (I_D *vs.* V_{GS}) and the transconductance, g_m, respectively, for V_{DS}=3 V, 6 V and 8 V. With these V_{DS} we have low-, medium- and high-dissipated power inside the device. The gate-to-source bias is swept from -2 V to -9 V. The effects of temperature are more prominent for the less negative gate-source potentials. As temperature is increased, the maximum of g_m is shifted to higher V_{GS}, and, for the same V_{GS} and V_{DS}, the current density and g_m are also reduced. The control of the gate over the drain current is partially lost. For a given temperature, when the transistor is clearly operating in the saturation regime (V_{DS}=6 V and 8 V), the current density and the transconductance are similar.

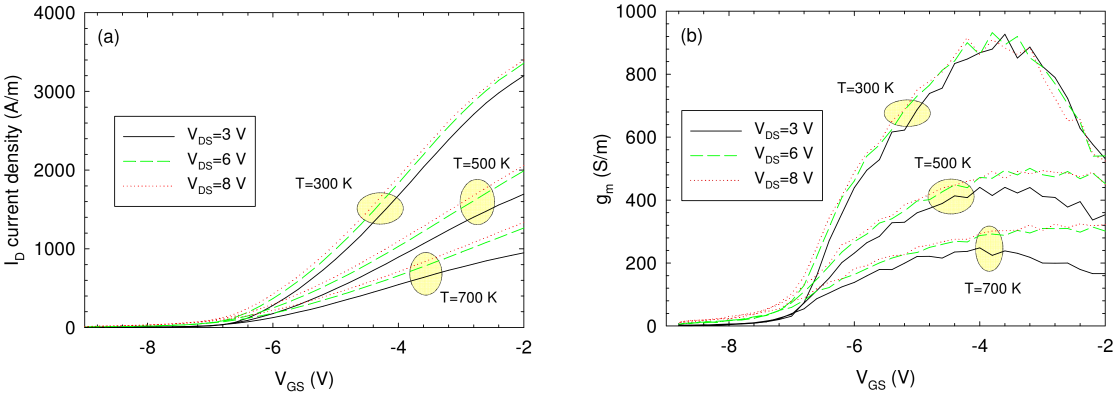

Figure 3. 27: (a) Transfer characteristics and (b) transconductance g_m *vs.* V_{GS} for V_{DS}=3 V, 6 V and 8 V of HEMTs with the geometry of Figure 3. 24. In both graphics, isothermal simulations at 300 K, 500 K and 700 K are taken into account.

3.4.2. Electro-thermal simulations

In this section, we study the geometry of the transistor shown in Figure 3. 24 by considering L_1=L_3=200 µm, L_2=300 µm, and Si substrate. We compare isothermal results with simulations where the TRM and HDEM (temperature-independent thermal conductivity) are employed.

In Figure 3. 28 (a) (lines) the I_D-V_{DS} characteristics of the HEMT when the HDEM is taken into consideration are shown. The thermal drop in current density I_D (negative slope on I_D) for the gate-to-source biases of -2 V, -3 V and -4 V is due to self-heating effects, and is a phenomenon not observed with isothermal simulations.

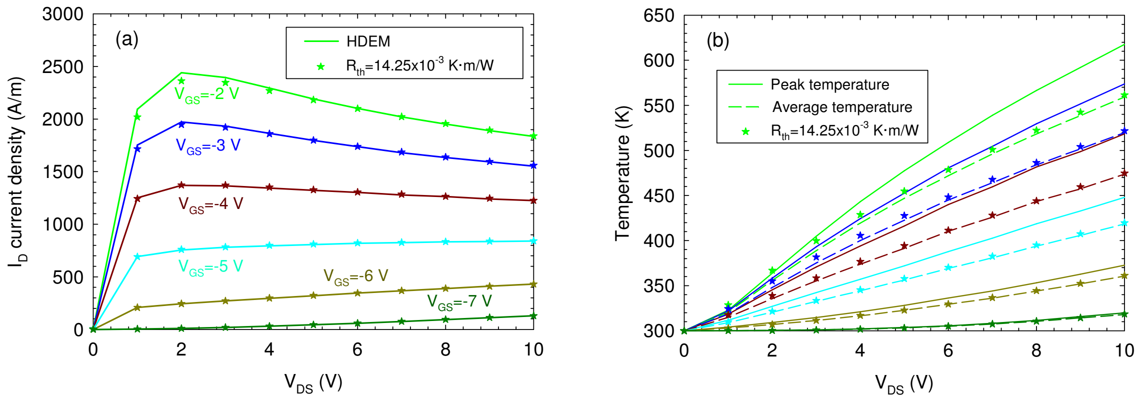

Figure 3. 28: (a) I_D-V_{DS} characteristics of the HEMT of Figure 3. 24. Lines: HDEM, symbols: TRM (R_{th}=14.25x10^{-3} K·m/W). (b) Average (dashed lines) and peak (solid lines) temperature with HDEM. Temperature when the TRM is used (symbols). For the HDEM L_1=L_3=200 µm, L_2=300 µm and an Si substrate are considered.

To complete the analysis, in Figure 3. 29 we represent the drain conductance g_d *vs.* V_{GS} for V_{DS}=3 V, 6 V and 8 V for the I_D-V_{DS} curves obtained with the HDEM in Figure 3. 28 (a).

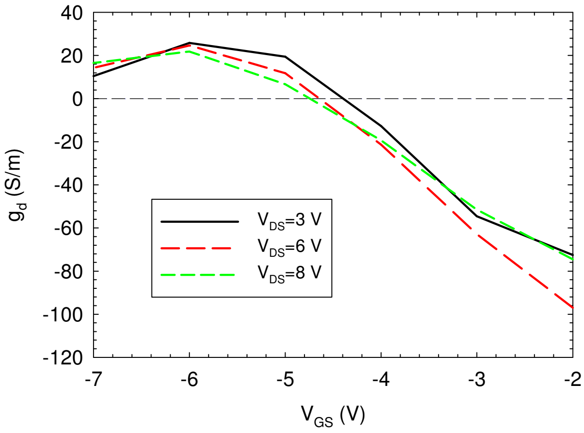

Figure 3. 29: Drain conductance g_d *vs.* V_{GS} for V_{DS}=3 V, 6 V and 8 V for curves obtained with the HDEM.

It is explicitly observed that, at V_{DS}=3 V, g_d reaches negative values for gate-to-source biases V_{GS}>-4.4 V, whereas for V_{DS}=6 V and 8 V g_d is seen for V_{GS}>-4.7 V. In the extreme case (V_{DS}=10 V, V_{GS}=-2 V) a peak temperature rise of 317 K above the ambient temperature (300 K) is achieved, see Figure 3. 28 (b). As V_{GS} is reduced, the average and peak temperatures become closer to each other. Measurements(17) of temperature distribution in AlGaN/GaN heterostructures typically afford up to 500 K (178,179).

---

[17] Micro-Raman spectroscopy (178) or the combination of an atomic force microscope and thermal probe (179).

Therefore, the high temperatures, as high as 600 K, reached in our simulations may be used as a predictive tool to avoid failure/burnout in real HEMTs devices.

Figure 3. 30 shows the average temperature *vs*. the dissipated power for different V_{GS}. This plot allows us to calculate R_{th} as explained in Section 3.3.2. We obtain similar values of R_{th} for all cases, and the mean value is R_{th}=14.25x10^{-3} K·m/W. Using such estimated R_{th} the TRM-based model provides the same I_D-V_{DS} values [see symbols of Figure 3. 28 (a)] as with the HDEM. Note that the TRM temperature and the average temperature from the HDEM are almost the same [see symbols in Figure 3. 28 (b)].

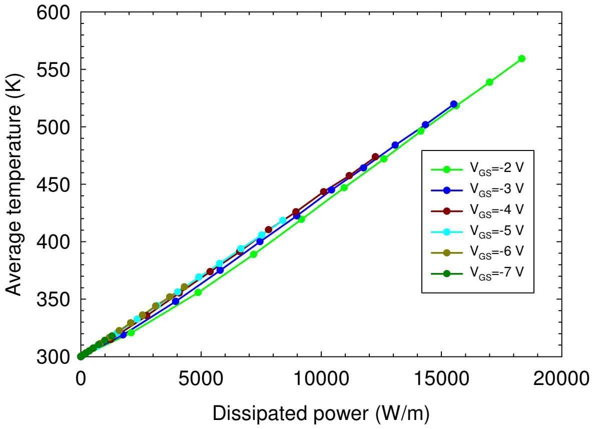

Figure 3. 30: Average temperature *vs.* dissipated power for the results of Figure 3. 28 (a).

Regarding the transfer characteristics (I_D *vs.* V_{GS}) and g_m, Figure 3. 31 (a) and (b) shows those calculated with the isothermal simulations (from 300 K to 700 K) and with HDEM simulations for V_{DS}=6 V. Related to the values of I_D *vs.* V_{DS}, Figure 3. 31 (a), HDEM provides almost the same trend as the simulated curve at T=300 K at low gate-to-source biases, V_{GS}<-5.5 V; and for T=400 K in the -4.5 V<V_{GS}<-4 V range. We focus our attention on V_{GS}=-4.2 V because the isothermal simulation (400 K) gives exactly the same current density, 1217 A/m, as the HDEM (square symbol). This is because the HDEM average temperature is also 400 K [square symbol of Figure 3. 31 (c)]. However, although the current is the same, it is striking that the value of g_m is different, see square symbols of Figure 3. 31 (b). This means, at V_{GS}=-4.2 V, g_m(HDEM)=494 S/m≠g_m(400K)=615 S/m. However, it is observed that at V_{GS}=-4.2 V g_m(HDEM)≈g_m(500 K). The maximum of g_m(HDME)=500 S/m, well within the range of typical values of manufactured AlGaN/GaN HEMTs (176), is reached at V_{GS}=-5 V. At very low dissipated powers (in the particular cases of V_{GS}<-7 V) the HDEM provides the same g_m as isothermal simulations.

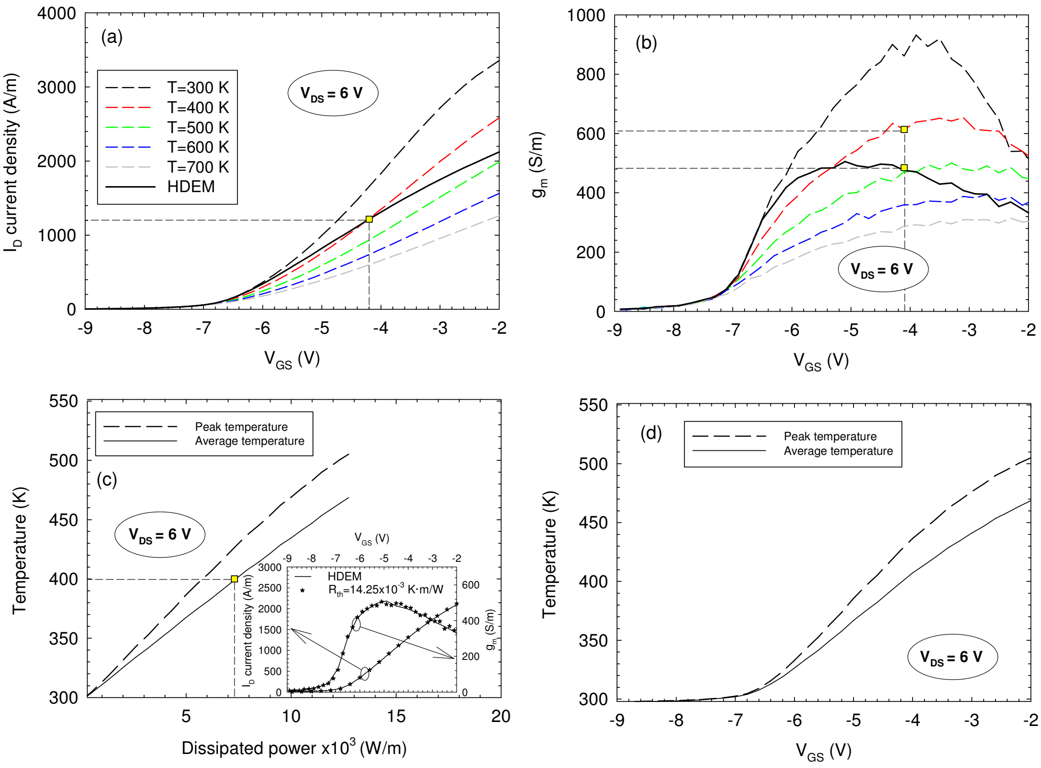

Figure 3. 31: Comparison of isothermal simulations and results obtained on employing the HDEM. (a) Transfer characteristics, (b) transconductance g_m, (c) temperature *vs.* dissipated power and (d) temperature *vs.* V_{GS} (HDEM simulation). V_{DS}=6 V. The inset in Figure 3. 31 (c) shows the equivalence between the HDEM and the TRM.

In Figure 3. 31 (c) we analyse the average and peak temperature *vs.* the dissipated power at V_{DS}=6 V obtained with the HDEM [solid curve in Figure 3. 31 (a)]. For high power, the difference between the average and peak temperatures is greater. Furthermore, it can be seen better in Figure 3. 31 (d) than in Figure 3. 31 (c) that when the gate-to-source bias becomes more negative the increment in peak temperature above the average temperature is reduced. Finally, by means of TRM with the extracted value of R_{th}=14.25x10^{-3} K·m/W (from Figure 3. 30) we obtain the same transfer characteristic as the one provided by the HDEM, as can be seen in the inset of Figure 3. 31 (c). This equivalence indicates that the behaviour of the device is dominated by the average temperature that fixes the level of the current.

In order to demonstrate that the electronic dynamics responds to the average temperature(18), Figure 3. 32 shows the profile of the temperature in the channel for the

---

[18] Note that effects of local variation in temperature on piezoelectric charges, strain, etc., are not considered in our simulator.

HDEM and TRM *vs*. horizontal length at V_{DS}=6 V and V_{GS}=-4.2 V. Whereas in the TRM the temperature is constant (~400 K) the HDEM provides a profile of the temperature in the 385 K - 425 K range. However, this temperature range does not have a significant influence on electron transport because the mobility of 2DEG (see Figure 3. 33) does not change too much: from 1300 cm^2/(V·s) at 385 K down to 900 cm^2/(V·s) at 425 K [$\Delta\mu$=400 cm^2/(V·s)]. We conclude that both models provide the same behaviour, but we wish to highlight the importance of the HDEM in accurately extracting the value of R_{th}.

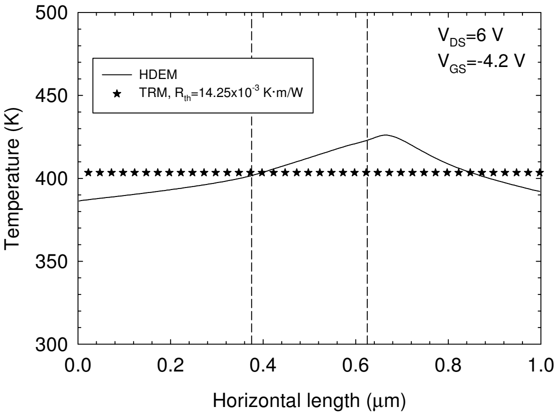

Figure 3. 32: Temperature profile in the channel for the HDEM and TRM *vs*. horizontal length at V_{DS}=6 V and V_{GS}=-4.2 V.

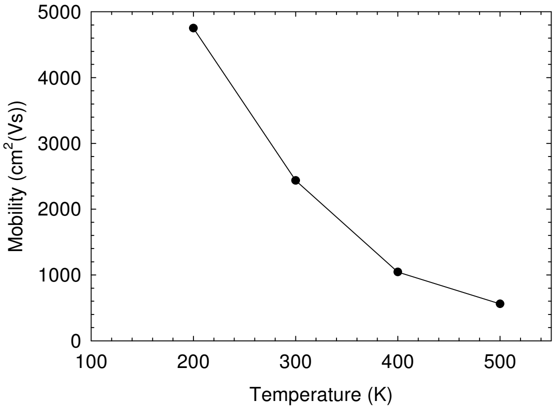

Figure 3. 33: Mobility of electrons in a diode as a function of temperature (PDR=0 %, P=14.12×10^{12} cm^{-2}and σ = -4×10^{12} cm^{-2}).

Returning to the particular bias of V_{DS}=6 V and V_{GS}=-4.2 V, where HDEM, TRM and isothermal simulation at 400 K gave the same current value (1217 A/m), we analyse the profiles of energy, velocity, and optical polar scattering rate along the channel, see Figure 3. 34 (a), (b) and (c), respectively. We compare the isothermal profiles at 300 K, 400 K and 500 K with those obtained with the TRM and HDEM electro-thermal models. Both electro-thermal models (HDEM and TRM) provide the same profiles of energy and velocity, even though temperature with the HDEM is not constant. At these biases, the average temperature of the HDEM and the temperature of the TRM are ~400 K (see Figure 3. 32), and it is found that the microscopic magnitudes agree with those obtained from the isothermal simulations at a temperature of 400 K. For all cases, hot carriers appear in the channel at the drain side of the gate. It is remarkable for the HDEM and the TRM that energies near 1.9 eV are reached, exhibiting an important velocity overshoot [up to 5x10^7 cm/s, well within the range of typical values of simulations of AlGaN/GaN HEMTs (176)]. Regarding the optical polar phonon scattering range, it is seen that as the temperature is higher, more polar phonon scattering mechanisms take place.

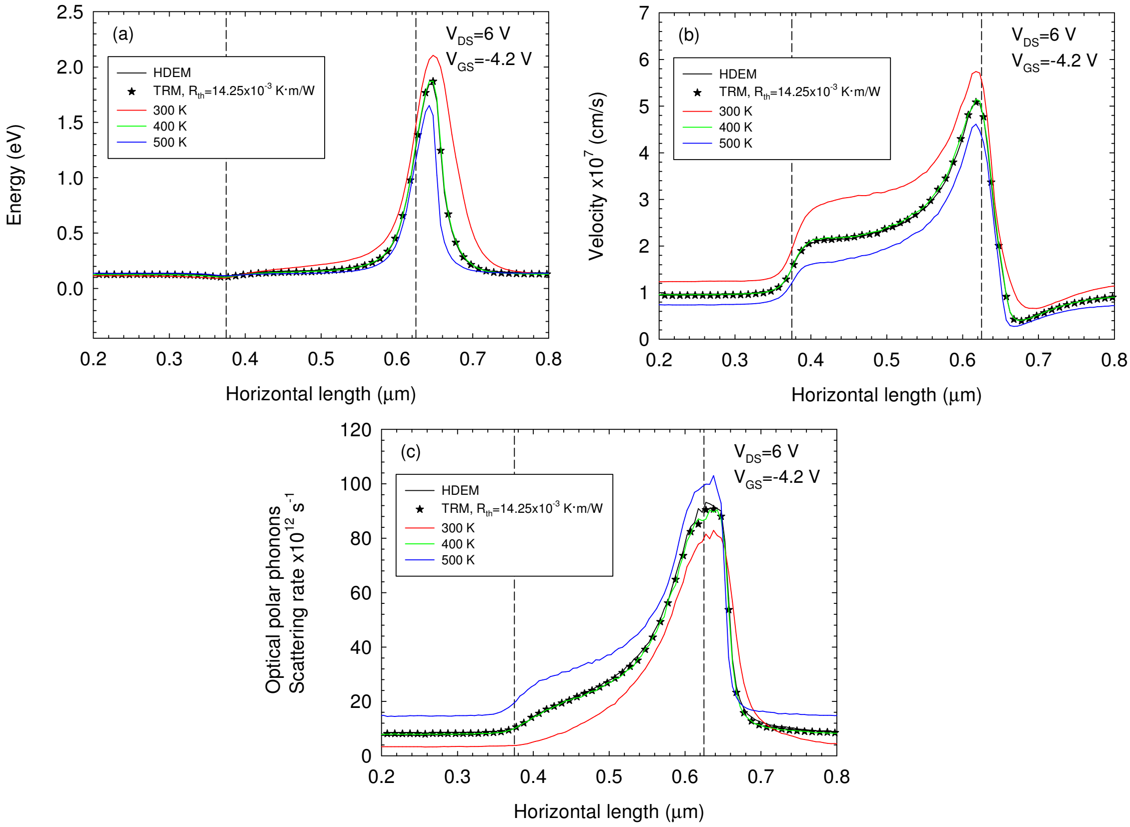

Figure 3. 34: Microscopic characteristics in channel *vs*. horizontal length at V_{DS}=6 V and V_{GS}=-4.2 V. (a) Energy, (b) velocity and (c) optical polar phonon scattering rate.

We highlight the fact that although the HDEM works at a temperature in the 385 K - 425 K range in the channel (Figure 3. 32), the optical polar phonon scattering rate is almost the same as (i) that obtained at the isothermal temperature of 400 K, and (ii) that obtained with the TRM, which operates at 403 K.

(a) Heat-sink temperature analysis

In the previous section we saw that the TRM and the HDEM are equivalent when the temperature in the electronic domain is higher than 300 K. The fact that the mobility changes considerably at low temperatures (see Figure 3. 33) leads us to explore whether both models also give similar results when the devices are cooled. For this purpose, we considered heat sinks with temperatures of 50 K, 100 K and 200 K in the HEMT of Figure 3. 24. In all cases, the value of temperature-independent thermal conductivity at 300 K in Table 3. 3 was used for the different materials.

In Figure 3. 35 (a) and (b) we plot the curve I_D *vs.* V_{GS} and the transconductance for the HDEM, respectively, for V_{DS}=6 V (lines) for the four heat-sinks.

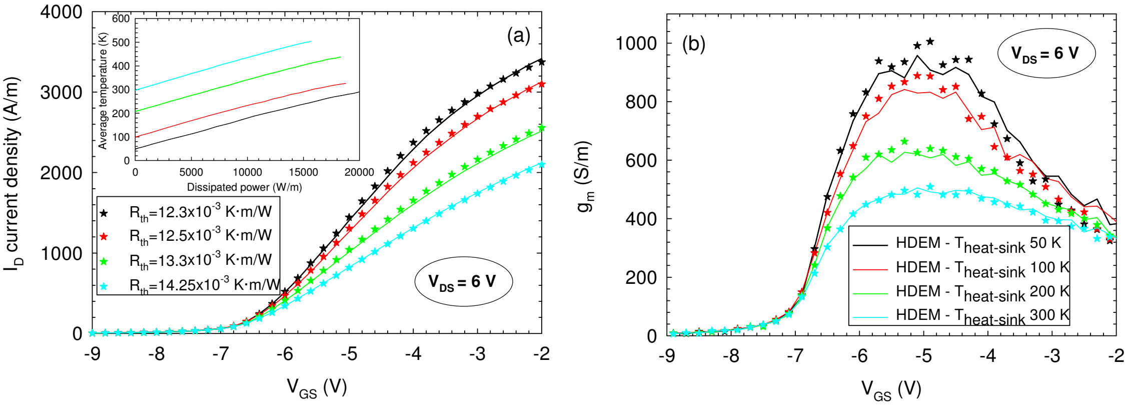

Figure 3. 35: Comparison between the HDEM and the TRM when heatsinks with temperatures of 50 K, 100 K, 200 K and 300 K are considered. (a) Transfer characteristics of the current density I_D. The inset shows the average temperature *vs.* dissipated power. (b) Transconductance g_m. *vs.* V_{GS}. V_{DS}=6 V.

Following Section 3.3.2 (b), by fitting the average temperature *vs.* dissipated power of the HDEM [see inset of Figure 3. 35 (a)], four thermal resistances with values of 12.3x10^{-3} K·m/W, 12.5x10^{-3} K·m/W, 13.3x10^{-3} K·m/W and 14.25x10^{-3} K·m/W for the heat-sinks with 50 K, 100 K, 200 K and 300 K, respectively, are extracted. By the use of the R_{th} obtained in the TRM [star symbols in Figure 3. 35 (a) and (b)], it is possible to replicate the I_DV_{DS} curves and g_m. Thus, we demonstrate again that both models are equivalent.

However, the HDEM allows us to analyse the temperature along the channel for the particular bias conditions of V_{GS}=-4.2 V and V_{DS}=6 V and the heat sinks with 50 K and 100 K, Figure 3. 36.

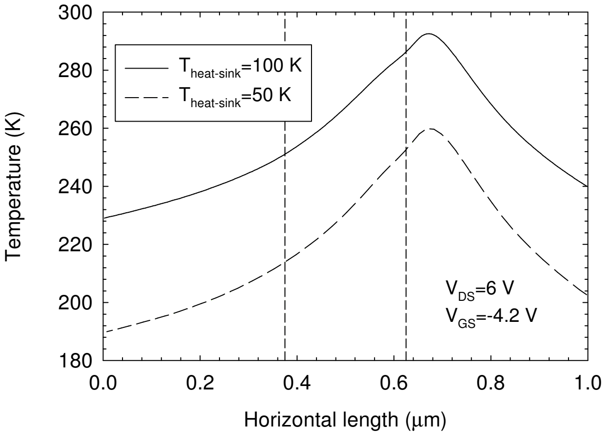

Figure 3. 36: Temperature profile inside the device along the channel for the HDEM *vs*. horizontal length at V_{DS}=6 V and V_{GS}=-4.2 V. Two heat sinks of temperatures 50 K and 100 K are considered.

The device works at temperatures ranging from 190 K - 260 K (Δ*T*=70 K) and 230 K - 290 K (Δ*T*=60 K), for the heat sinks with 50 K and 100 K, respectively. Although the temperature inside the device varies significantly, it seems that the level of the current is also determined by the average temperatures of 230 K and 262 K in these working conditions. We also checked the profiles of velocity, carrier concentration, energy, etc., verifying that HDEM and TRM show the same values.

To analyse why the extracted thermal resistance is different for each heat sink, we now study the profiles of the carrier concentration and velocities from HDEM [Figure 3. 37 (a) and (b)] when the same dissipated power of 10950 W/m (V_{DS}=6 V, I_D=1825 A/m) is obtained.

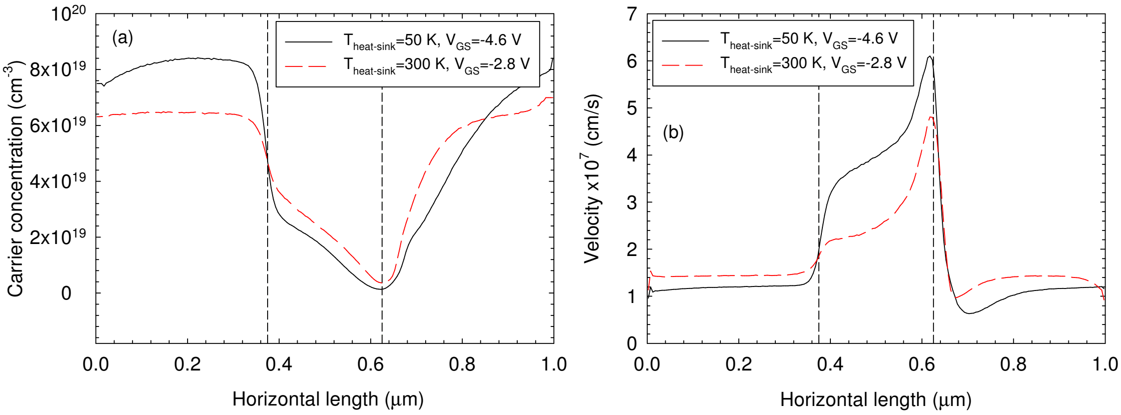

Figure 3. 37: Microscopic characteristics of the carrier concentration and velocities through the channel for the particular case in which the same dissipated power of 10950 W/m is obtained. We consider heat sinks with temperatures of 50 K (V_{GS}=-2.8 V, V_{DS}=6 V) and 300 K (V_{GS}=-4.6 V, V_{DS}=6 V), respectively.

We focus our attention on the heat sinks with 50 K (V_{GS}=-4.6 V) and 300 K (V_{GS}=-2.8 V), respectively. Although the dissipated power (JxV_{DS}) is the same, they exhibit different microscopic characteristics. For the heat sink with 50 K, an important velocity overshoot (6.1x10^7 cm/s) can be observed. This indicates that a more ballistic transport takes place in this region in comparison with the heat sink with 300 K, where the peak velocity is 4.8x10^7 cm/s. It is found that $\Delta T=T_{av}-T_{heat\text{-}sink}$ is not the same for the different heat-sinks: $\Delta T_{heat\text{-}sink\text{-}300\text{ K}}$=156 K ≠ $\Delta T_{heat\text{-}sink\text{-}50\text{ K}}$ =135 K, which means that the extracted values of R_{th} are not equal, as can be deduced from Eq. (III.1). Thus, the fact of not having identical electronic dynamics inside the device acquires special relevance at low temperatures (higher ΔT) and affects the value of R_{th}.

(b) Gate-length analysis

In this section, we examine the gate-length effect for isothermal and electro-thermal (HDEM) simulations. For this, we compare the HEMT in Figure 3. 24 (HEMT-L_g250) with the HEMTs shown in Figure 3. 38 (HEMT-L_g125 and HEMT-L_g60).

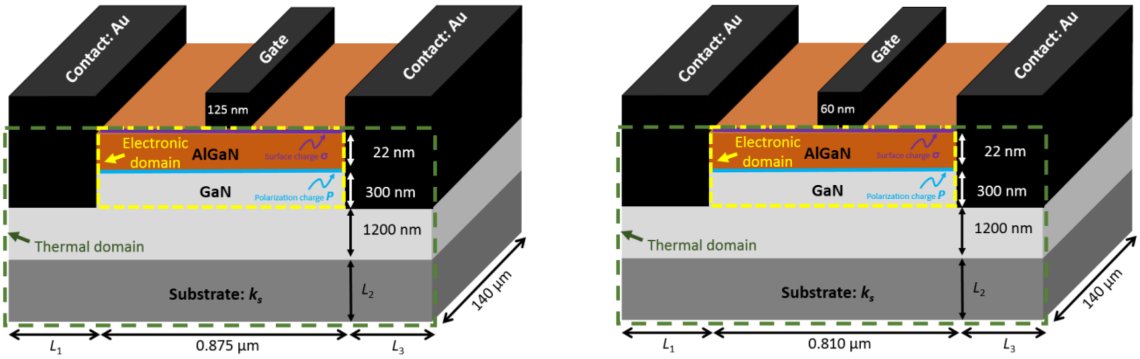
Contact: Au
Gate
Contact: Au
125 nm
Electronic domain
AlGaN
Surface charge σ
GaN
Polarization charge P
22 nm
300 nm
1200 nm
Thermal domain
Substrate: k_s
L_2
140 µm
L_1
0.875 µm
L_3
Contact: Au
Gate
Contact: Au
60 nm
Electronic domain
AlGaN
Surface charge σ
GaN
Polarization charge P
22 nm
300 nm
1200 nm
Thermal domain
Substrate: k_s
L_2
140 µm
L_1
0.810 µm
L_3

Figure 3. 38: AlGaN/GaN HEMT geometry under study. The HEMT on the left has a gate-length of 125 nm, and the HEMT on the right has a gate-length of 60 nm. The area limited by yellow corresponds to the electronic simulated region of the diode and the region limited by green is the thermal domain.

The new simulated HEMTs have gate-lengths of 125 nm and 60 nm (extremely short, but chosen to analyse the theoretical effect of smaller gate-lengths). We consider Si as substrate. We point out that our HEMTs do not have been scaled. In order to make a comparison between the different HEMTs, we keep the same source-to-gate and gate-to-drain distances. The distances between the drain-source contacts are 875 nm and 810 nm, respectively. We shall compare isothermal (300 K) and electro-thermal (HDEM) simulations. The transfer characteristics of HEMT-L_g250, HEMT-L_g125 and HEMT-L_g60 at V_{DS}=6 V are summarized in Figure 3. 39: (a) I_D *vs.* V_{GS}, and (b) g_m *vs.* V_{GS}.

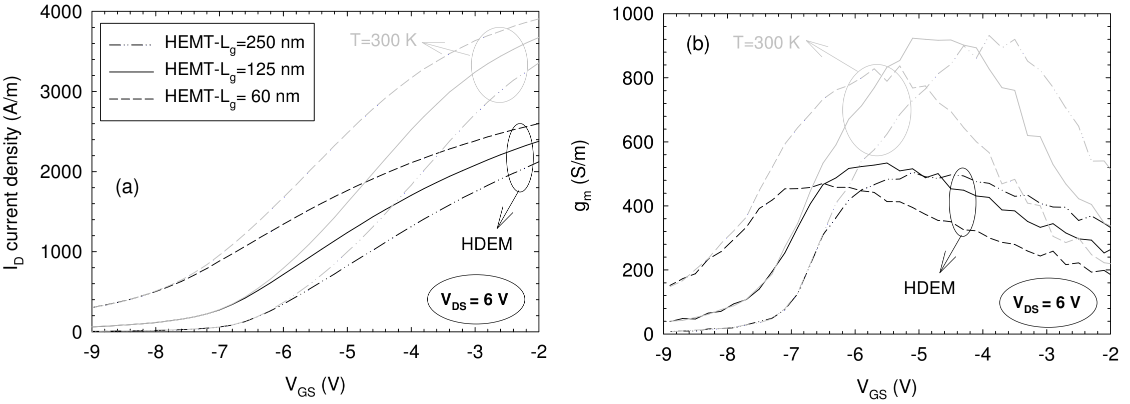

Figure 3. 39: Comparison of transfer characteristics of HEMT-L$_g$250, HEMT-L$_g$125 and HEMT-L$_g$60 when isothermal (at 300 K) and electro-thermal (HDEM) simulations are performed. (a) I_D *vs.* V_{GS}. (b) g_m. V_{DS}=6 V.

For the shorter gate-length (HEMT-L$_g$60), short-channel effects are clearly observed. The pinch-off voltage for the gate-to-source biases applied is not reached. This can be also observed in the transconductance, which is always over 0 S/m. For the same V_{GS} and V_{DS}, the current density, I_D, is always higher for the devices with shorter gates. This is due to a reduction in the modulation efficiency of the gate. At isothermal temperatures, the effect of the short-gate is also noticeable in g_m: for HEMT-L$_g$60, it is reduced to 835 S/m in comparison with the transconductances for HEMT-L$_g$250 and HEMT-L$_g$125, which are very similar (925 S/m). In addition, the maximum of g_m is always shifted to more negative gate-to-source biases when the gate-length is reduced.

Regarding thermal effects (HDEM), independently of the gate length, the pinch-off voltage is not modified because changes in temperature are irrelevant when the dissipated power is almost null. This is because a minimum level of dissipated power in the system is needed to produce a noticeable increase in the temperature. Heating starts when the gate-to-source biases V_{GS} are higher than -6.5 V, -7 V and -8 V for the HEMT-L$_g$250, HEMT-L$_g$125 and HEMT-L$_g$60, respectively. Moreover, the characteristics of devices using the HDEM show (i) a reduction in the value of the current density, (ii) a decrease in the maximum of g_m and (iii) a shift of the maximum of g_m to low gate-to-source biases. For the shorter length, transconductance is broadened.

At this point it is interesting to analyse the microscopic behaviour of the devices described above. The carrier concentration and the velocity along the channel of HEMT-L$_g$250, HEMT-L$_g$125 and HEMT-L$_g$60, under the bias conditions of V_{DS}=6 V and V_{GS}=-3 V, are of special interest, and are represented in Figure 3. 40 (a) and (b), respectively.

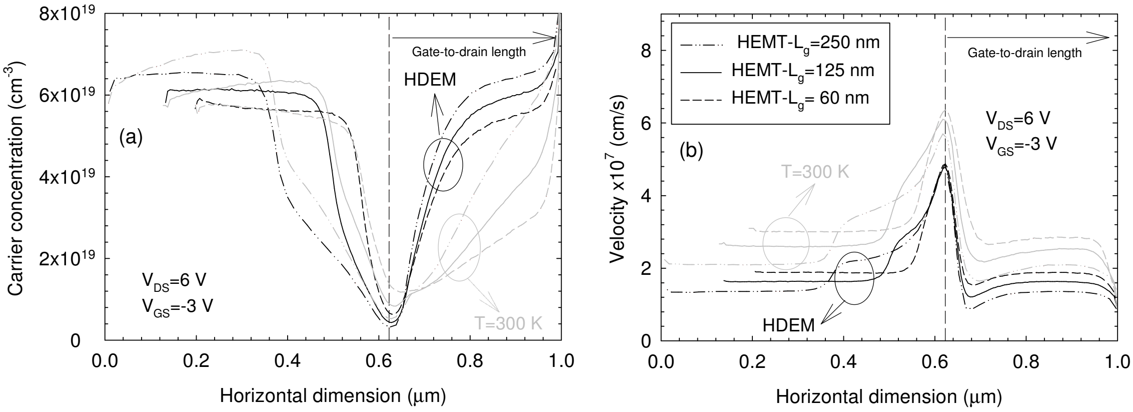

Figure 3. 40: Microscopic characteristics in the channel *vs*. horizontal length at V_{DS}=6 V and V_{GS}=-3 V. Isothermal (300 K) and electro-thermal (HDEM) simulations are compared. (a) Carrier concentration. (b) Velocity. The vertical dashed line indicates the end of the gate.

Isothermal (300 K) and electro-thermal (HDEM) simulations are compared. When the HDEM is considered, a higher depletion of electrons is observed close to the drain-edge of the gate. At room temperature, we remark the existence of an important velocity overshoot for the three gate-lengths: 6.4x10^7 cm/s (HEMT-L$_g$60), 6.1x10^7 cm/s (HEMT-L$_g$125) and 5.7x10^7 cm/s (HEMT-L$_g$250), where ballistic transport is likely to exist. The peak velocity is reduced when the gate length is increased. In contrast, this does not occur for the electro-thermal simulations, where the peak velocity is the same for the three gate-lengths~4.8x10^7 cm/s. Accordingly, the reason for the decrease in I_D for higher L_g can be attributed to a greater depletion of electrons close to the drain-edge of the gate.

In a HEMT, hot spots are located at the right side of the end of the gate. In order to analyse whether these hot spots (peak temperature) are affected by the gate lengths, in Figure 3. 41 (a) we show the peak temperature *vs.* V_{GS}, and, in Figure 3. 41 (b) its distance to the gate *vs.* V_{GS} for the three gate lengths considered previously. The peak temperature, under the same bias conditions, is always higher for the shortest gate, as expected from the high levels of dissipated power obtained for this device. For any gate length, the position of the hot spots coincides with the point of higher depletion of electrons. This is confirmed by inspection, for the HEMT-L$_g$250, of the carrier concentration in the channel *vs*. horizontal length at V_{DS}=6 V and V_{GS}=-6 V and -3 V (Figure 3. 42).

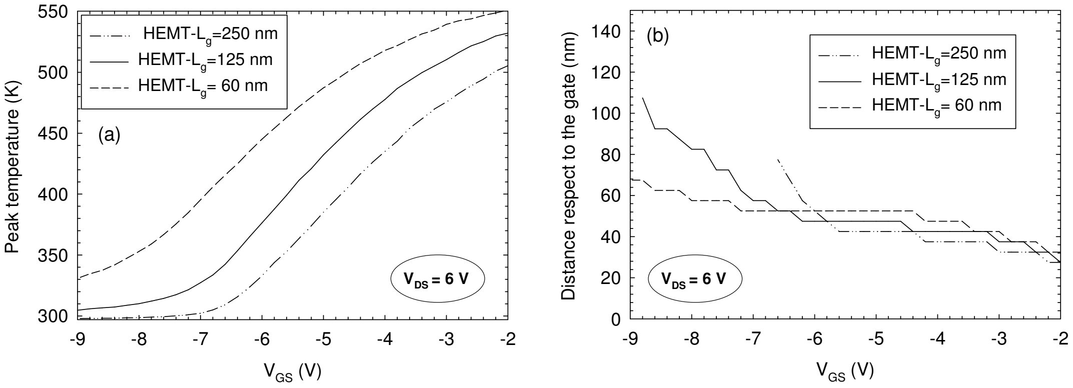

Figure 3. 41: (a) Peak temperature *vs.* V_{GS}. (b) Position where hot spots are located with respect to the gate *vs.* V_{GS}. V_{DS}=6 V.

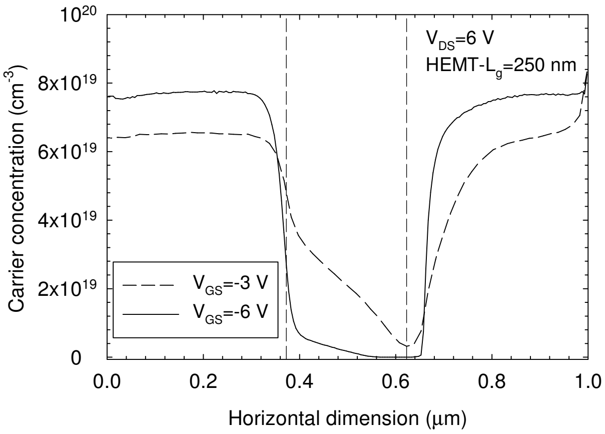

Figure 3. 42: Carrier concentration in the channel *vs*. horizontal length at V_{DS}=6 V and V_{GS}-6 V and -3 V for the HEMT with a gate length of 250 nm.

For all gate lengths, the hot spot or the most depleted point is shifted to the drain side when V_{GS} becomes more negative.

However, note that under ON-state operation the location of hot spots is almost independent of V_{GS} (see for example -5 V <V_{GS}<-2 V for HEMT-L_g250) while when close to or above the OFF-state operation the hot spots are strongly shifted to the drain side (see for example -6.5 V <V_{GS}<-5 V for HEMT-L_g250). In addition, under ON state operation (-4 V <V_{GS}<-2 V), when the gate-length is reduced the hot spots are slightly shifted to the drain side, see Figure 3. 41 (b).

(c) Temperature-dependent thermal conductivity

Finally, this section presents an analysis of the characteristics of the transistor presented in Figure 3. 24 when the temperature-dependent thermal conductivity of Eq. (III.12) is considered. As done for the diode before in Section 3.3.2 (b.6), we chose a value of α equal to 1.3 because this corresponds to the most relevant layer (Si). At room temperature, the thermal conductivities are those summarized in Table 3. 3.

We compare the results obtained with the temperature-independent and temperature-dependent thermal conductivity models. We focus our attention on the average temperature *vs.* dissipated power, when V_{GS} is swept from -2 V to -9 V, for V_{DS} values of 6 V and 8 V, see Figure 3. 43.

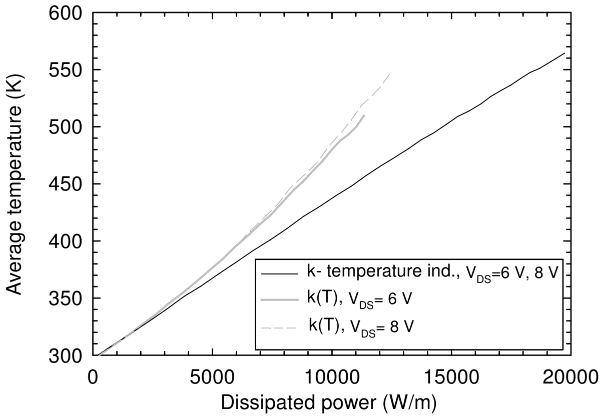

Figure 3. 43: Average temperature *vs.* dissipated power (V_{GS} is swept from -2 V to -9 V) for the two models: temperature-independent thermal conductivity *vs.* temperature-dependent thermal conductivity.

For both voltages, through the linear fitting T_{av}. *vs.* P_{diss}, the same R_{th}=14.25x10^{-3}K·m/W was extracted for the temperature-independent thermal conductivity model(19). However, when the temperature-dependent thermal conductivity model is used, it is not possible to extract a constant thermal resistance. The evolution of the average temperature is non-linear with the dissipated power. In fact, it exhibits a quadratic dependence that can be modelled by: T_{av}=300 K + 0.014 K·m/W x P_{diss} + 4.3x10^{-7} K·m^2/W^2 x P_{diss}^2 (for V_{DS}=6 V) and, T_{av}=300 K + 0.014 K·m/W x P_{diss} + 5.5x10^{-7} K·m^2/W^2 x P_{diss}^2 (for V_{DS}=8 V). Note that the equation is also a function of V_{DS}. Thus, the classical TRM does not reproduce the behaviour of the system. The variation in thermal conductivity in each mesh strongly affects the values of the average temperature, and therefore, the HDEM becomes essential to study thermal effects.

To conclude, we compare the transfer characteristics and transconductance obtained from both models, Figure 3. 44 (a) and (b), respectively, when V_{DS}=6 V and V_{GS} is swept from -2 V to -9 V. The current density is similar for V_{GS} lower than 6 V. Above this voltage, the temperature-dependent thermal conductivity model provides a smaller current and transconductance also decreases. The maximum of g_m [Figure 3. 44 (b)] is reduced from 505 S/m (V_{GS}=-5.1 V) to 475 S/m (V_{GS}=-5.5 V) for k=k(T). All this can be explained in terms of the average temperature, which is higher for the temperature-dependent thermal conductivity model, see inset of Figure 3. 44 (a).

---

(19) Note that, for V_{DS}=6 V, the average temperature *vs.* P_{diss} is also plotted in Figure 3. 31 (c).

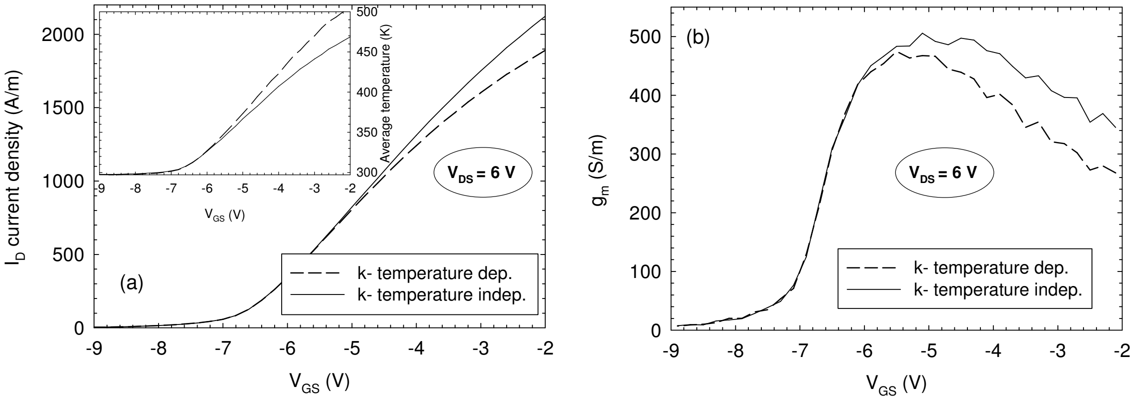

Figure 3. 44: Temperature-independent *vs.* temperature-dependent thermal conductivity models. (a) Transfer characteristics I_D *vs.* V_{GS}. The inset shows the average temperature *vs.* V_{GS}. (b) Transconductance g_m. V_{DS}=6 V.

3.5. Conclusions

In this chapter we present simulations of AlGaN/GaN diodes and HEMTs. The main goal has been to implement two self-consistent electro-thermal methods in our in-house MC tool: one based on a thermal resistance (TRM), and the other based on the solution of the steady-state heat diffusion equation (HDEM) under two cases for the thermal conductivity to be temperature-independent and temperature-dependent. The next step was the validation and calibration of our simulator with experimental values of sheet electron density, n_s, mobility, μ, sheet resistance, R_s (all at 300 K) and the *I-V* curve of an AlGaN/GaN diode with a length of 2 µm. Once calibrated, a HEMT was studied. The most important conclusions are summarized below.

- The validation and calibration of our software were made through isothermal simulations by varying the polarization charges, surface states and surface roughness. For P=12.12×10^{12} cm^{-2}, σ=-4.12×10^{12} cm^{-2} and PDR=3 % it was found that the values through isothermal simulation (300 K) of n_s=8×10^{12} cm^{-2}, μ=819 cm^2/V·s and R_s= 952 Ω/sq are in good accordance with the experimental ones (n_s=8×10^{12} cm^{-2}, μ=1000 cm^2/V·s and R_s= 780.2 Ω/sq). However, the isothermal simulations are not capable of reproducing experimental DC behaviour for the whole bias range.
- Once the heating phenomenon were included in our computational models, the results confirm that both thermal models show better agreement with the experimental *I-V* curve than the isothermal simulations. In particular, the simulation in which temperature-dependent thermal conductivity is considered provides a very satisfactory reproduction of the experimental saturation at high voltages. The temperature is as high as 595 K at V_{DS}=10 V.
- The TRM is based on the use of an ad-hoc thermal resistance and only a global value of the lattice temperature is calculated, it not being possible to identify hot-spots. Using temperature-independent thermal conductivity in the HDEM allowed us to extract a constant equivalent R_{th} for each geometry. This extracted R_{th} provides, within a TRM based model, the same results in the simulations as the HDEM ones.

- When a temperature-dependent thermal conductivity is employed, it is not possible to extract a constant equivalent R_{th}. Thus, the simple TRM presented in this study cannot be employed.
- The HDEM provides a local temperature map and is able to identify hot spots inside the device, which is very useful in the analysis of more complex devices such as HEMTs. However, although the temperature varies along the channel, the electronic transport of the device is dominated by the average temperature.
- With the HDEM it is possible to evaluate the effect of thermal conductivities of materials, die length and die thickness on the local lattice temperature with the aim of reducing self-heating effects and ensuring low temperatures in the ohmic contact areas. For example, the fact of considering SiC instead of Si as substrate in the diode means that the extracted thermal resistance is reduced by a factor 51 % (from $17.45\mathrm{x}10^{-3}$ K·m/W to $8.9\mathrm{x}10^{-3}$ K·m/W). If PCD or diamond substrates are employed, the current density and the extracted R_{th} do not change significantly, reflecting the notion that both substrates are excellent heat sinks. Some recommendations, when possible, for manufacturing purpose would be (i) the use of high thermal conductivities substrates and (ii) a reduction in substrate depth.
- The effect of the TBR has been included in the simulations of a diode. For temperature-independent thermal conductivity, the results show that the TBR may exert a strong influence, limiting the thermal flux in the interface where it appears. Although the effect of the TBR is higher for the SiC substrate, the temperature reached in the electronic domain is lower in comparison with the temperature obtained with the Si substrate. The TBR has a strong influence on R_{th}. For a TBR=$15\mathrm{x}10^{-8}$ m^2K/m, R_{th} is increased with respect to the case w/o TBR by a factor 1.5 for Si and 1.89 for SiC.
- For temperature-dependent thermal conductivity and at high voltages (V>8 V), we found that the simulation becomes unstable as a consequence of the very high temperatures (~600 K), due to the combination of the reduction of the thermal conductivity and the blocking of heating flow by the TBR.
- In addition, for the AlGaN/GaN HEMTs studied, we observed that hot-spots are always located at the drain side of the gate. The values of the maximum of g_m,

when electro-thermal modes are included, are well within the range of typical values of manufactured AlGaN/GaN HEMTs (500 S/m). When the gate length is reduced, the g_m maximum is always shifted to more negative gate-to-source biases. Regardless of the gate length, the pinch-off voltage does not change with the different isothermal and electro-thermal models. When the device is cooled, although the temperature along the channel varies significantly it seems that the level of the current is determined by the average temperature.

CONCLUSIONS AND FUTURE WORK

Conclusions

In this section we summarize the main conclusions of the whole thesis. More details can be found at the end of Chapter 2 and Chapter 3.

In Chapter 2 we focused our attention on the study, by means of Monte Carlo simulations, of two types of GaN and InP Gunn diodes as candidates for developing emitters in the THz range at medium- high-power applications. For a 0.75 µm length InP diode w/o notch a fundamental frequency of 400 GHz is reached. Also, for this material, the maximum DC to AC conversion efficiency achieved in simulations is 5.5 % for a frequency of 225 GHz. In a 1.5 µm-long GaN diode a significant amplitude is found in the power spectral density at the tenth harmonic (~1 THz). In addition, an efficiency of 0.1 % can be reached in a 0.9 µm-long GaN diode at the sixth generation band (675 GHz), supporting our expectations about achieving emissions near the THz band. Overall, it was found that notched structures provide (i) a higher number of harmonics, (ii) more generation bands, and (iii) higher spectral purity, at the expense of a lower frequency at the first harmonics. Although thermal effects lead to a reduction in performance, Gunn devices are still operative at 500 K and their expected figures of merit are very promising.

Generally, when an AlGaN/GaN diode or HEMT was operating at high power, we observed that heating effects reduced its performance. Thermal models are crucial to investigate heating limits and to properly simulate physical phenomena inside the device. In Chapter 3 we studied self-heating effects in AlGaN/GaN structures with two and three terminals. We implemented a simple thermal resistance method (TRM) and a more complex procedure based on the solution of the steady-state heat diffusion equation (HDEM) under two scenarios: temperature-independent and temperature-dependent thermal conductivities. On the one hand, when a temperature-independent thermal conductivity was used in the HDEM, it was found that by a linear fitting of the average temperature (T_{av}) with respect to the intrinsic dissipated power it was possible to extract the value of the thermal resistance, R_{th}. Within a TRM based model, this extracted R_{th} provided the same results in the simulations as the HDEM ones. For the substrates studied (polycrystalline diamond, diamond, silicon carbide, silicon and saphire), R_{th} took values ranging from 3.58x10^{-3} K·m/W (polycrystalline diamond) to 14.1x10^{-3} K·m/W (silicon), except in the case of sapphire, where R_{th} was ~40x10^{-3} K·m/W. In addition, we have discussed the effect of the inclusion of the thermal boundary resistance, TBR, in our MC simulator. The results showed that the TBR had a strong influence, limiting the thermal flux in the interface where it appeared. The presence of the TBR generated a considerable increase in thermal resistance. In a HEMT, the hot-spots were always located at the drain side of the gate. When the device is cooled, a more significant variation of the temperature along the channel takes place, but in all cases we concluded that the level of the current is determined by the average temperature. On the other hand, when a temperature-dependent thermal conductivity was employed, R_{th} was function not only of the geometry and materials of the die, but also of the dissipated power. In this latter case, the extraction of R_{th} is not possible and it would be necessary to take into account the HDEM for a proper thermal study of the device. In fact, the experimental saturation at high voltages was only well reproduced when the temperature-dependent thermal conductivity model was used. Finally, we observed that the working temperature limit was ~600 K.

Future work

- This thesis has dealt, through MC simulations, with the analysis and optimization of the behaviour of Gunn diodes based on InP and GaN. It would be interesting to perform further studies addressing the manufacture of GaN vertical diodes following our recommendations with the aim of searching for Gunn oscillations in fabricated devices.

- The simulator is able to analyse heating effects in a variety of devices: vertical diodes, planar devices, transistors, self-switching diodes, etc. After validation/calibration of our in-house electro-thermal MC tool with experimental measurements at the DC level, next steps address the study of the dynamic behaviour and noise analysis.
- Although we carried out isothermal simulations (up to 500 K) in the vertical diodes, observing that heating effects are not limiting factors in the appearance of Gunn oscillations, a self-heating analysis through the electro-thermal models developed in this thesis can complete the optimization of the performance of such diodes.
- We showed that sufficient power can be obtained in the vertical diodes at high frequencies by generating an elevated number of harmonics. However, it is necessary to carry out a further study of the noise-floor in order to minimise its influence on the extraction of the harmonics of interest.
- Once the intrinsic potentialities of the presented Gunn diodes have been confirmed, the next task for practical applications could be to run circuit simulations taking into account resonant cavities and band-pass filters to extract, in the most suitable manner, the power of the harmonics of interest.
- In order to obtain satisfactory agreement with measurements in real devices, our models must include (i) the extrinsic parameters (contact resistances or parasitic capacitances), and (ii) gate-leakage current or barrier-lowering mechanisms.
- Our electro-thermal in-house tool should allow us to study advanced HEMTS. We should include in our simulations (i) the AlN layer, (ii) a double heterojunction, and (iii) the field-plate.

APPENDIX: MEASUREMENTS OF HEMTS

In this appendix the measurements of the HEMTs characterized during my research stay at the Institut d'Electronique du Sud (IES) in Montpellier are presented.

Figure A. 1 shows the geometry of the $Al_{0.24}Ga_{0.76}N$/GaN HEMTs, fabricated at IEMN, Lille (France). Under equilibrium conditions, both structures have a sheet density n_s of $10\text{x}10^{16}$ m^{-2}. In both cases, the contact resistances are R_C=0.4 Ω·mm. Four wafers were measured, and each wafer contained the two HEMTs presented.

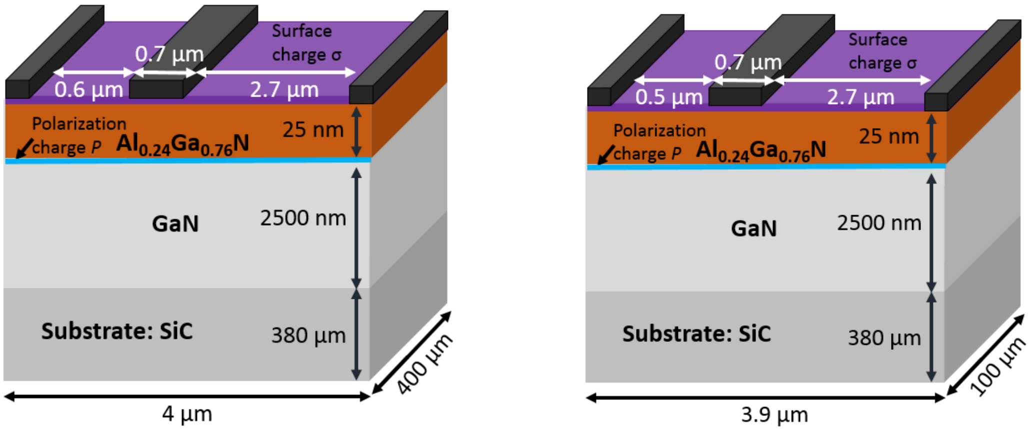
Surface charge σ
0.7 µm
0.6 µm
2.7 µm
Polarization charge P
Al0.24Ga0.76N
25 nm
GaN
2500 nm
Substrate: SiC
380 µm
400 µm
4 µm
Surface charge σ
0.7 µm
0.5 µm
2.7 µm
Polarization charge P
Al0.24Ga0.76N
25 nm
GaN
2500 nm
Substrate: SiC
380 µm
100 µm
3.9 µm

Figure A. 1: Geometry of the HEMTs. HEMT A (left), HEMT B (right) characterized.

In Figure A. 2, we plot the experimental measurements of HEMTs A and B presented in Figure A. 1. For the four wafers, HEMTs A and B were first characterized by measuring the current density I_D *vs.* drain-to-source bias V_{DS}. HEMT A of wafer 4 was damaged and no measures could be obtained.

In all cases, mainly for the highest V_{GS}, the thermal drop in the current density can be observed. Similar current levels and behaviour of the devices are detected when measurements of HEMTs with the same geometry are compared.

Below, by focusing our attention on HEMTs of wafer 1, we represent the current density I_D *vs.* drain-to-source bias V_{DS} when V_{GS} is swept from 0 V to -6 V, ΔV=1 V; I_D *vs.* V_{GS} for V_{DS}=2 V, 3 V, 4 V and 5 V; and g_m *vs.* V_{GS} for V_{DS}=5 V (see Figure A. 1).

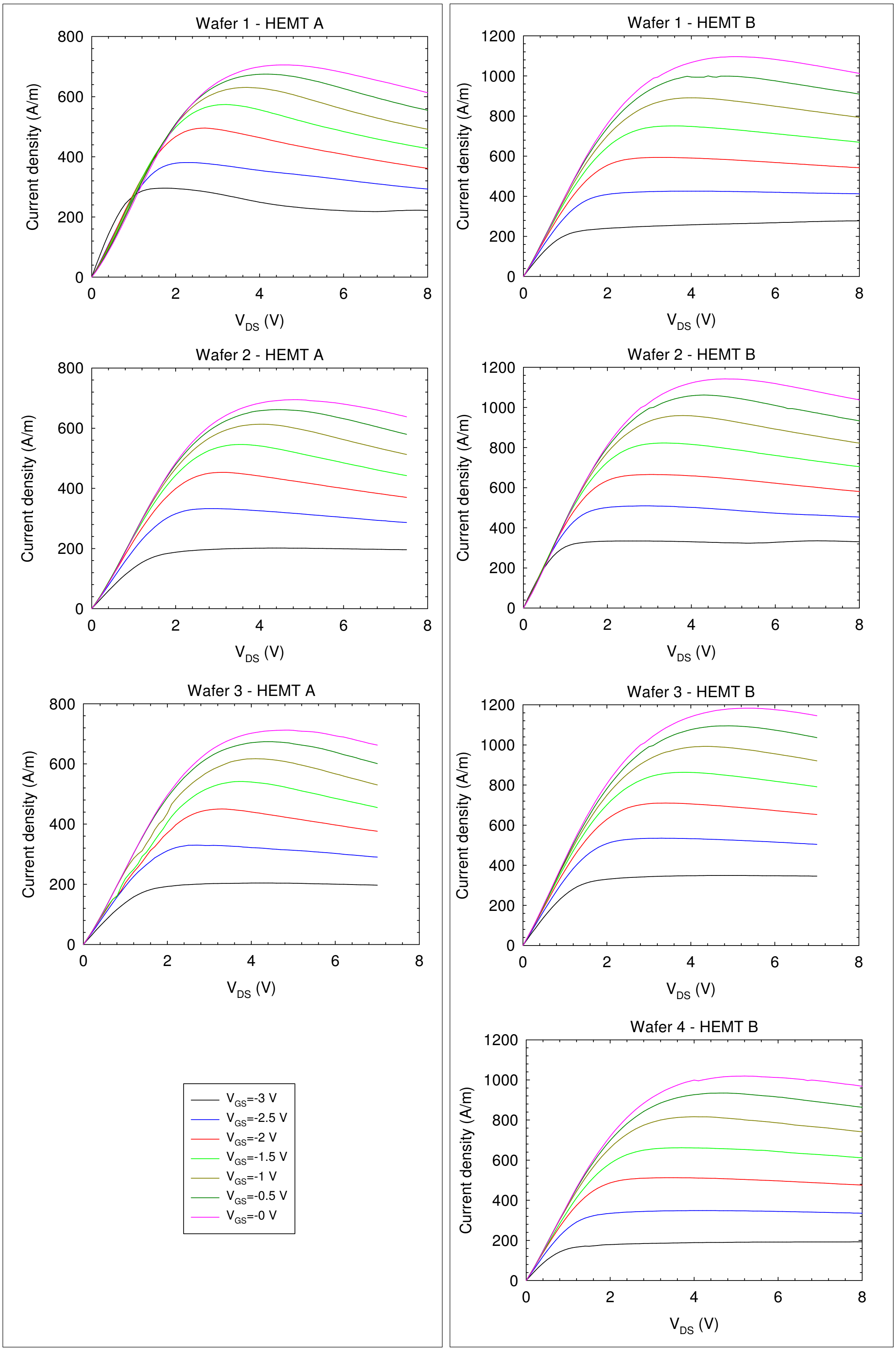

Figure A. 2: Experimental measurements. Current density I_D *vs.* drain-to-source bias V_{DS}.

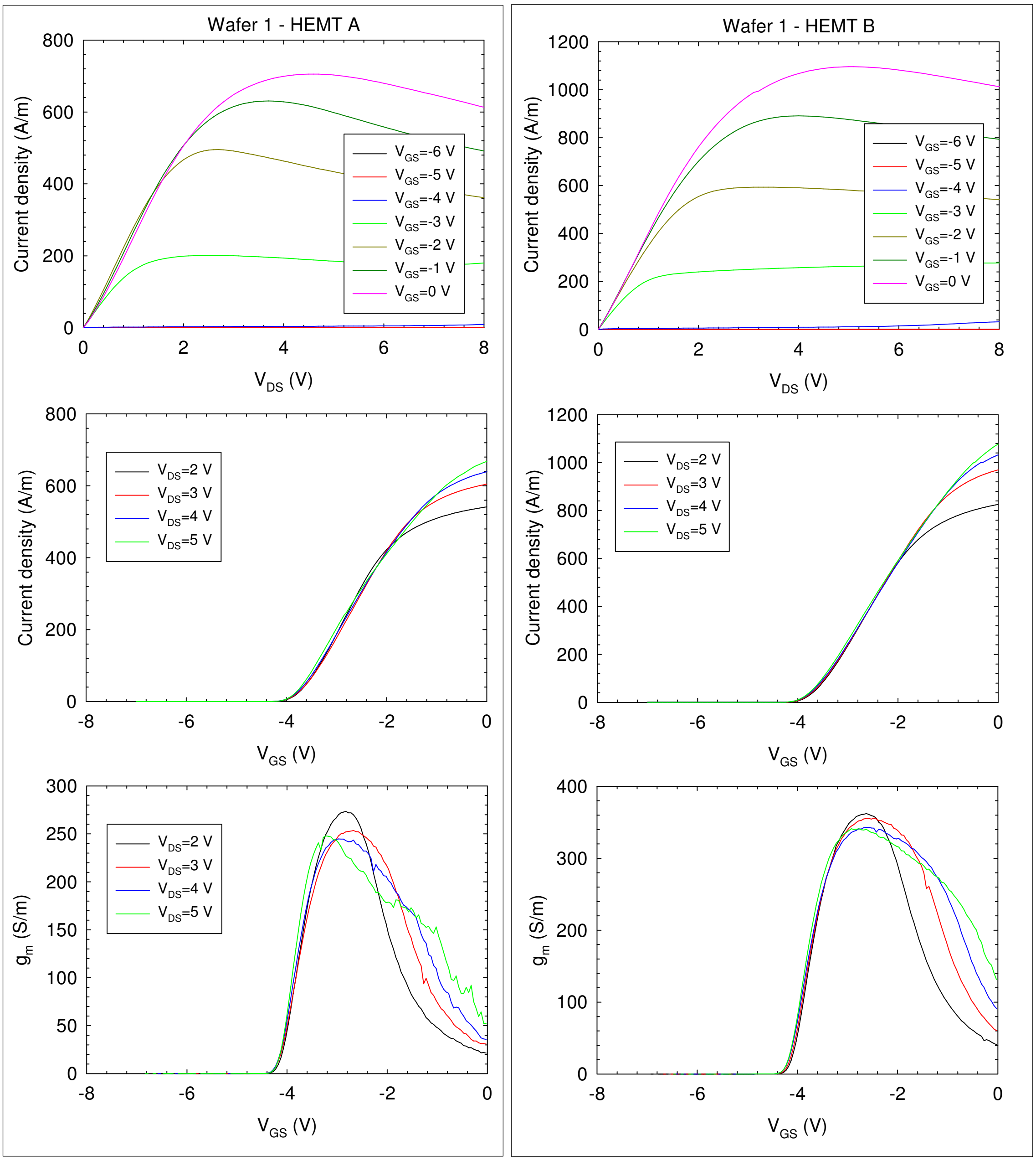

Figure A. 3: Experimental measures of HEMTs A and B of wafer 1. Current density I_D *vs*. drain-to-source bias V_{DS} when V_{GS} is swept from 0 V to -6 V, ΔV=1 V. I_D *vs.* V_{GS} for V_{DS}=2 V, 3 V, 4 V and 5 V. Transconductance g_m *vs.* V_{GS} for V_{DS}=5 V.

The pinch-off takes place at V_{GS}=-4.2 V in both HEMTs. Regarding g_m, the maximum values reached are ~250 S/m (V_{GS}≈-3V) and ~350 S/m (V_{GS}≈-2.8 V) for the HEMT A and B, respectively. In both cases, as V_{DS} becomes higher, the transconductance is widened.

This thesis has been produced with the financial assistance of a Research Staff Training (FPI) Grant from the Ministerio de Economía y Competitividad (BES-2011-045041).

This is part of the work carried out by the Research Group on Semiconductor Devices of the University of Salamanca (http://campus.usal.es/~gelec/ingles/webgrupo.htm) in the following research projects:

1- Nanoelectrónica de gap ancho y estrecho para la mejora de la eficiencia en aplicaciones de RF y THz (TEC2013-41640-R). Ministerio de Economía y Competitividad.
2- Estudio de efectos térmicos en dispositivos de RF. Modelado y caracterización experimental (SA052U13). Consejería de Educación y Cultura la Junta de Castilla y León.
3- Nanodispositivos semiconductores para la emisión y detección de radiación de THz a temperatura ambiente (SA183A121). Consejería de Educación y Cultura la Junta de Castilla y León.
4- Diodos y transistores avanzados para generación, detección y procesado de señales milimétricas y submilimétricas (TEC2010-15413). Ministerio de Economía y Competitividad.
5- Semiconductor Nanodevices for Room temperature THz Emission and Detection, ROOTHz (ICT-243845). European Union.

Some of the results presented in this work have been published in the **following scientific international journals**:

1- **S. García**, I. Íñiguez-de-la-Torre, Ó. García-Pérez, J. Mateos, T. González, S. Pérez, Modelling of thermal boundary resistance in a GaN diode by means of electro-thermal Monte Carlo simulations, *Journal of Physics: Conference Series*, 609 012005 (2015).

2- **S. García**, I. Íñiguez-de-la-Torre, Ó. García-Pérez, J. Mateos, T. González, P. Sangaré, C. Gaquière, S. Pérez, Self-consistent electro-thermal simulations of AlGaN/GaN diodes by means of Monte Carlo method, *Semiconductor Science and Technology*, 30, 035001 (2015).

3- **S. García**, S. Pérez, I. Íñiguez-de-la-Torre, J. Mateos, and T. González. Comparative Monte Carlo analysis of InP- and GaN-based Gunn diodes. *Journal of Applied Physics* 115, 044510 (2014).

4- **S. García**, I. Íñiguez-de-la-Torre, S. Pérez, J. Mateos, and T. González. Numerical study of sub-millimiter Gunn oscillations in InP and GaN vertical diodes: dependence on bias, doping and length. *Journal of Applied Physics* 114, 074503 (2013).

Some of these results have been presented in the following **communications at national and international congresses** and are summarized in the corresponding **conference proceedings**:

1- A. Rodríguez, I. Íñiguez-de-la-Torre, Ó. García-Pérez, **S. García**, A Westlund, P-Å. Nilsson, J. Grahn, T. González, J. Mateos and S. Pérez. Temperature and Surface Traps Influence on the THz Emission from InGaAs Diodes. *19th International Conference on Electron Dynamics in Semiconductors, Optoelectronics and Nanostructures* (*EDISON'19*), Salamanca (2015). **Poster presentation.**

2- **S. García**, I. Íñiguez-de-la-Torre, Ó. García-Pérez, J. Mateos, T. González and S. Pérez. Evaluation of the thermal resistance in GaN-diodes by means of electro-thermal Monte Carlo simulations. *10th Spanish Conference on Electron Devices*, Aranjuez IEEE Catalog 15589ART, 2015. ISBN: 978-1-4799-8108-3. **Poster presentation.**

3- **S. García**, I. Íñiguez-de-la-Torre, Ó. García-Pérez, J. Mateos, T. González and S. Pérez. Modelling of thermal boundary resistance in a GaN diode by means of electro-thermal Monte Carlo simulations. *EURO-TMCS I* (*Theory, Modelling and Computational Methods for Semiconductors*), Granada (2015). **Oral presentation.**

4- **S. García**, I. Íñiguez-de-la-Torre, O. García-Pérez, J. Mateos, T. González, P. Sangaré, C. Gaquière and S. Pérez. Examination of thermal effects in GaN-based devices by means of electro-thermal Monte Carlo simulators. *Workshop on Compound Semiconductor Devices and Integrated Circuit. 38th WOCSDICE*, Delphi (2014). **Oral presentation.**

5- **S. García**, I. Íñiguez-de-la-Torre, S. Pérez, J. Mateos and T. González. Performance of InP and GaN Gunn diodes: efficiency, power spectral density and thermal effects. *Compound Semiconductor Week 2014* (*IPRM/ISCS 2014*), Montpellier (2014). **Oral presentation.**

6- **S. García**, I. Íñiguez-de-la-Torre, S. Pérez, J. Mateos and T. González. Monte Carlo simulations of InP and GaN-based vertical Gunn diodes for THz power emission. *GDR-I THz Workshop*, Montpellier (2013). **Poster presentation.**

7- **S. García**, B. G. Vasallo, J. Mateos and T. González. Time-domain Monte Carlo simulations of resonant-circuit operation of GaN Gunn diodes.*2013 Spanish Conference on Electron Devices*, Valladolid. IEEE Catalog CFP13589, 2013. ISBN: 978-1-4673-5. **Poster presentation.**

A research stay of 96 days (21/04/2014-25/07/2014) was carried out at the *Institut d'Électronique du Sud*, Université Montpellier 2, Montpellier (France) through a scholarship from the Ministerio de Economía y Competitividad (Ayudas Movilidad Predoctoral para Estancias Breves en Centros I+D 2013 - Ref. EEBB-I-14-0786).

To run the simulations of this work two Cluster computers (Linux) were employed.

1) The oldest consists of 8 nodes with 2 CPUs Intel Xeon 5140 with 2 cores at 2.33 GHz (1 Gb RAM); the other 8 with 2 CPUs Intel Xeon 5520 with 4 cores at 2.26 GHz (1Gb RAM) and 2 nodes with 2 CPUs Intel Xeon 5650 with 6 cores at 2.66 GHz (2 Gb RAM).
2) The newest has 3 nodes with 2 CPUs Intel Xeon ES-2680 with 8 cores at 2.7 GHz (32 Gb RAM).

The compiler is Intel ® Fortran Compiler 10.1.011 for Linux.

BIBLIOGRAPHY

(1) Dunleavy L, Baylis C, Curtice W, Connick R. Modeling GaN: Powerful but challenging. Microwave Magazine, IEEE 2010;11(6):82-96.

(2) Shen L, Heikman S, Moran B, Coffie R, Zhang N, Buttari D, et al. AlGaN/AlN/GaN high-power microwave HEMT. Electron Device Letters, IEEE 2001;22(10):457-459.

(3) Duboz J. GaN as seen by the industry. Comptes Rendus de l'Académie des Sciences - Series IV - Physics 2000;1(1):71-80.

(4) Transparency Market Research. GaN semiconductor devices market (Power semiconductors, Opto semiconductors) - Global Industry Analysis, Size, Share, Growth, Trends and Forecast 2013 - 2019. 2014. http://www.transparencymarketresearch.com.

(5) Palacios T, Chakraborty A, Heikman S, Keller S, DenBaars S, Mishra U. AlGaN/GaN high electron mobility transistors with InGaN back-barriers. Electron Device Letters, IEEE 2006;27(1):13-15.

(6) Palacios T, Chakraborty A, Rajan S, Poblenz C, Keller S, DenBaars S, et al. High-power AlGaN/GaN HEMTs for Ka-band applications. Electron Device Letters, IEEE 2005;26(11):781-783.

(7) Wu Y, Saxler A, Moore M, Smith R, Sheppard S, Chavarkar P, et al. 30-W/mm GaN HEMTs by field plate optimization. Electron Device Letters, IEEE 2004;25(3):117-119.

(8) Sun Y, Eastman LF. Large-signal performance of deep submicrometer AlGaN/AlN/GaNHEMTs with a field-modulating plate. Electron Devices, IEEE Transactions on 2005;52(8):1689-1692.

(9) Chuang RW, Chang S, Chang S, Chiou Y, Lu C, Lin T, et al. Gallium nitride metal-semiconductor-metal photodetectors prepared on silicon substrates. J Appl Phys 2007;102(7):073110.

(10) Davis RF. III-V nitrides for electronic and optoelectronic applications. Proc IEEE 1991;79(5):702-712.

(11) Fitch MJ, Osiander R. Terahertz waves for communications and sensing. Johns Hopkins APL Tech Dig 2004;25(4):348-355.

(12) Shealy J, Smart J, Poulton M, Sadler R, et al. Gallium nitride (GaN) HEMT's: progress and potential for commercial applications. Technical digest-IEEE Gallium Arsenide Integrated Circuit Symposium; 2002.

(13) Vetury R, Wei Y, Green DS, Gibb SR et al. High power, high efficiency, AlGaN/GaN HEMT technology for wireless base station applications. Microwave Symposium Digest, 2005 IEEE MTT-S International: IEEE; 2005.

(14) Eastman LF, Mishra UK. The toughest transistor yet [GaN transistors]. Spectrum, IEEE 2002;39(5):28-33.

(15) Aichele D, Krishnamurthy K. Wideband GaN power amplifiers for software-defined radios. Microwave Product Design 2011:1-4.

(16) Kneissl M, Treat DW, Teepe M, Miyashita N, Johnson NM. Ultraviolet AlGaN multiple-quantum-well laser diodes. Appl Phys Lett 2003;82(25):4441-4443.

(17) Marso M. GaN for THz sources. SPIE OPTO: International Society for Optics and Photonics; 2011.

(18) El Fatimy A, Tombet SB, Teppe F, Knap W, Veksler D, Rumyantsev S, et al. Terahertz detection by GaN/AlGaN transistors. Electron Lett 2006;42(23):1342-1344.

(19) Samoska LA. An overview of solid-state integrated circuit amplifiers in the submillimeter-wave and THz regime. Terahertz Science and Technology, IEEE Transactions on 2011;1(1):9-24.

(20) Sakai K. Terahertz optoelectronics. Berlin: Springer; 2005.

(21) Carr GL, Martin MC, McKinney WR, Jordan K, Neil GR, Williams GP. High-power terahertz radiation from relativistic electrons. Nature 2002;420(6912):153-156.

(22) Gružinskis V, Starikov E, Shiktorov P, Reggiani L, Saraniti M, Varani L. Generation and amplification of microwave power in submicron n^+nn^+ diodes. In: Selberherr S, Stippel H, Strasser E, editors. Vienna: Springer Vienna; 1993.

(23) Gružinskis V, Starikov E, Shiktorov P, Reggiani L, Varani L. Linear and nonlinear analysis of microwave power generation in submicrometer n^+nn^+ InP diodes. J Appl Phys 1994;76(9):5260-5271.

(24) Liu Z, Su K, Gary DE, Federici JF, Barat RB, Michalopoulou Z. Video-rate terahertz interferometric and synthetic aperture imaging. Appl Opt 2009;48(19):3788-3795.

(25) Tonouchi M. Cutting-edge terahertz technology. Nature photonics 2007;1(2):97-105.

(26) Belkin MA, Capasso F, Belyanin A, Sivco DL, Cho AY, Oakley DC, et al. Terahertz quantum-cascade-laser source based on intracavity difference-frequency generation. Nature Photonics 2007;1(5):288-292.

(27) Siegel PH. Terahertz technology in biology and medicine. Microwave Symposium Digest, 2004 IEEE MTT-S International: IEEE; 2004.

(28) Eisele H. State of the art and future of electronic sources at terahertz frequencies. Electronics Letters 2010;46(26):s8-s11.

(29) Crowe TW, Poterfield DW, Hesler JL. Multiplier-based sources of terahertz power. Infrared, Millimeter and Terahertz Waves, 2008. IRMMW-THz 2008. 33rd International Conference on; 2008.

(30) Crowe TW, Bishop WL, Porterfield DW, Hesler JL, Weikle RM. Opening the terahertz window with integrated diode circuits. Solid-State Circuits, IEEE Journal of 2005;40(10):2104-2110.

(31) Maestrini A, Ward JS, Gill JJ, Lee C, Thomas B, Lin RH, et al. A frequency-multiplied source with more than 1 mW of power across the 840-900-GHz band. Microwave Theory and Techniques, IEEE Transactions on 2010;58(7):1925-1932.

(32) Chen YC, Ingram DL, Lai R, Barsky M, Grunbacher R, Block T, et al. A 95-GHz InP HEMT MMIC amplifier with 427-mW power output. Microwave and Guided Wave Letters, IEEE 1998;8(11):399-401.

(33) Radisic V, Leong KMKH, MEi X, Sarkozy S. A 50 mW 220 GHz power amplifier module. Microwave Symposium Digest (MTT), 2010 IEEE MTT-S International; 2010.

(34) Radisic V, Deal WR, Leong KMKH, Mei XB, Yoshida W, Po-Hsin Liu, et al. A 10-mW submillimeter-wave solid-state power-amplifier module. Microwave Theory and Techniques, IEEE Transactions on 2010;58(7):1903-1909.

(35) Brown E, Söderström J, Parker C, Mahoney L, Molvar K, McGill T. Oscillations up to 712 GHz in InAs/AlSb resonant-tunneling diodes. Appl Phys Lett 1991;58(20):2291-2293.

(36) Orihashi N, Suzuki S, Asada M. One THz harmonic oscillation of resonant tunneling diodes. Appl Phys Lett 2005;87(23):233501.

(37) Suzuki S, Teranishi A, Hinata K, Asada M, et al. Fundamental oscillation up to 831 GHz in GaInAs/AlAs resonant tunneling diode. Indium Phosphide & Related Materials, 2009. IPRM'09. IEEE International Conference on: IEEE; 2009.

(38) Saglam M, Schumann B, Duwe K, Domoto C, Megej A, Rodriguez-Girones M, et al. High-performance 450-GHz GaAs-based heterostructure barrier varactor tripler. Electron Device Letters, IEEE 2003;24(3):138-140.

(39) Qun X, Hesler JL, Crowe TW, Yiwei Duan, et al. High-efficiency heterostructure-barrier-varactor frequency triplers using AlN substrates. Microwave Symposium Digest, 2005 IEEE MTT-S International; 2005.

(40) Vukusic J, Bryllert T, Stake J. High power heterostructure barrier varactor quintupler sources for G-band operation. Proceedings of the 19th International Symposium on Space Terahertz Technology,[ISSTT 2008], Groningen, the Netherlands; 2008.

(41) Munkyo Seo, Urteaga M, Young A, Jain V, et al. > 300GHz fixed-frequency and voltage-controlled fundamental oscillators in an InP DHBT process. Microwave Symposium Digest (MTT), 2010 IEEE MTT-S International: IEEE; 2010.

(42) Eisele H, Rydberg A, Haddad GI. Recent advances in the performance of InP Gunn devices and GaAs TUNNETT diodes for the 100-300-GHz frequency range and above. Microwave Theory and Techniques, IEEE Transactions on 2000;48(4):626-631.

(43) Lee C, Ward J, Lin R, Schlecht E, et al. A wafer-level diamond bonding process to improve power handling capability of submillimeter-wave Schottky diode frequency multipliers. Microwave Symposium Digest, 2009. MTT'09. IEEE MTT-S International: IEEE; 2009.

(44) Alderman B, Henry M, Maestrini A, Grajal J, et al. High power frequency multipliers to 330 GHz. Microwave Integrated Circuits Conference (EuMIC), 2010 European; 2010.

(45) Hacker J, Urteaga M, Mensa D, Pierson R, et al. 250 nm InP DHBT monolithic amplifiers with 4.8 dB gain at 324 GHz. Microwave Symposium Digest, 2008 IEEE MTT-S International; 2008.

(46) Oo WL, Eisele H, Haddad GI, Wu YR, Pollard RD. Schottky barrier heights on AlGaN/GaN heterojunctions and their effect on high-performance GaN TUNNETT devices. Proc. 2nd UK/ Europe-China Workshop on Millimetre Waves and Terahertz Technologies, Didcot, UK; 2009.

(47) Mishra UK, Shen L, Kazior TE, Wu Y. GaN-based RF power devices and amplifiers. Proc IEEE 2008;96(2):287-305.

(48) Wu YF, Moore M, Saxler A, Wisleder T, et al. 40-W/mm double field-plated GaN HEMTs. Device Research Conference, 2006 64th; 2006.

(49) Siles JV, Grajal J. Physics-based design and optimization of Schottky diode frequency multipliers for terahertz applications. Microwave Theory and Techniques, IEEE Transactions on 2010;58(7):1933-1942.

(50) Pukala D, Samoska L, Gaier T, Fung A, Mei X, Yoshida W, et al. Submillimeter-wave InP MMIC amplifiers from 300-345 GHz. Microwave and Wireless Components Letters, IEEE 2008;18(1):61-63.

(51) Schwierz F. An electron mobility model for wurtzite GaN. Solid-state electronics 2005;49(6):889-895.

(52) Siles JV, Grajal J. Capabilities of GaN Schottky multipliers for LO power generation at millimeter-wave bands. Proc. 19th International Symposium on Space Terahertz Technology; 2008.

(53) Kai C, Thrower WF, Hayashibara GM. Millimeter-wave silicon IMPATT sources and combiners for the 110-260 GHz range. Microwave Symposium Digest, 1981 IEEE MTT-S International; 1981.

(54) Ino M, Ishibashi T, Ohmori M. C.W. oscillation with $p^{+-}p^{-}n^{+}$ silicon IMPATT diodes in 200 GHz and 300 GHz bands. Electronics Letters 1976;12(6):148-149.

(55) Khalid A, Pilgrim NJ, Dunn GM, Holland MC, Stanley CR, Thayne IG, et al. A planar Gunn diode operating above 100 GHz. Electron Device Letters, IEEE 2007;28(10):849-851.

(56) Maricar MI, Glover J, Khalid A, Li C, Evans G, Cumming DS, et al. An AlGaAs/GaAs-based planar Gunn diode oscillator with a fundamental frequency operation of 120 GHz. Microwave Opt Technol Lett 2014;56(10):2449-2451.

(57) Yilmazoglu O, Mutamba K, Pavlidis D, Karaduman T. Measured negative differential resistivity for GaN Gunn diodes on GaN substrate. Electronics Letters 2007;43(8):480-482.

(58) Yilmazoglu O, Mutamba K, Pavlidis D, Karaduman T. First observation of bias oscillations in GaN Gunn diodes on GaN substrate. Electron Devices, IEEE Transactions on 2008;55(6):1563-1567.

(59) Long S, Guo X, Hao Y. A comparative investigation on sub-micrometer InN and GaN Gunn diodes working at terahertz frequency. J Appl Phys 2012;111(10):104514.

(60) Maier D, Alomari M, Grandjean N, Carlin J, Diforte-Poisson M, Dua C, et al. Testing the temperature limits of GaN-based HEMT devices. Device and Materials Reliability, IEEE Transactions on 2010;10(4):427-436.

(61) Tang X, Rousseau M, Defrance N, Hoel V, Soltani A, Langer R, et al. Thermal behavior analysis of GaN based epi-material on different substrates by means of a physical-thermal model. Physica status solidi (a) 2010;207(8):1820-1826.

(62) Sadi T, Kelsall R, Pilgrim N. Simulation of electron transport in InGaAs/AlGaAs HEMTs using an electrothermal Monte Carlo method. Electron Devices, IEEE Transactions on 2006;53(8):1768-1774.

(63) Lindefelt U. Heat generation in semiconductor devices. J Appl Phys 1994;75(2):942-957.

(64) Rosker M, Bozada C, Dietrich H, Hung A, et al. The DARPA Wide Band Gap Semiconductors for RF Applications (WBGS-RF) Program: Phase II Results. Proc. CS MANTECH Conference, Tampa; 2009.

(65) Mateos J, Pérez S, Pardo D, González T. Monte Carlo analysis of thermal effects in GaN HEMTs. Electron Devices, 2009. CDE 2009. Spanish Conference on; 2009.

(66) Sadi T, Kelsall RW, Pilgrim NJ. Investigation of self-heating effects in submicrometer GaN/AlGaN HEMTs using an electrothermal Monte Carlo Method. Electron Devices, IEEE Transactions on 2006;53(12):2892-2900.

(67) Bonani F, Ghione G. On the application of the Kirchhoff transformation to the steady-state thermal analysis of semiconductor devices with temperature-dependent and piecewise inhomogeneous thermal conductivity. Solid-State Electronics 1995;38(7):1409-1412.

(68) Batty W, Christoffersen CE, Panks AJ, David S, Snowden CM, Steer MB. Electrothermal CAD of power devices and circuits with fully physical time-dependent compact thermal modeling of complex nonlinear 3-d systems. Components and Packaging Technologies, IEEE Transactions on 2001;24(4):566-590.

(69) McGaughey AJ, Kaviany M. Quantitative validation of the Boltzmann transport equation phonon thermal conductivity model under the single-mode relaxation time approximation. Physical Review B 2004;69(9):094303.

(70) Sadi T, Kelsall R, Pilgrim N, Thobel J, Dessenne F. Monte Carlo study of self-heating in nanoscale devices. Journal of Computational Electronics 2012;11(1):118-128.

(71) Jacoboni C, Lugli P. The Monte Carlo method for semiconductor device simulation. New York: Springer-Verlag; 1989.

(72) Íñiguez-de-la-Torre A, Íñiguez-de-la-Torre I, Mateos J, González T, Sangaré P, Faucher M, et al. Searching for THz Gunn oscillations in GaN planar nanodiodes. J Appl Phys 2012;111(11):113705.

(73) Perez S, González T, Pardo D, Mateos J. Terahertz Gunn-like oscillations in InGaAs/InAlAs planar diodes. J Appl Phys 2008;103(9):094516.

(74) García S, Pérez S, Íñiguez-de-la-Torre I, Mateos J, González T. Comparative Monte Carlo analysis of InP-and GaN-based Gunn diodes. J Appl Phys 2014;115(4):044510.

(75) García S, Íñiguez-de-la-Torre I, Pérez S, Mateos J, González T. Numerical study of sub-millimeter Gunn oscillations in InP and GaN vertical diodes: Dependence on bias, doping, and length. J Appl Phys 2013;114(7):074503.

(76) García S, Íñiguez-de-la-Torre I, García-Pérez O, Mateos J, González T, Sangaré P, et al. Self-consistent electro-thermal simulations of AlGaN/GaN diodes by means of Monte Carlo method. Semiconductor Science and Technology 2015;30(3):035001.

(77) García S, Íñiguez-de-la-Torre I, García-Pérez Ó, Mateos J, González T and Pérez S. Modelling of thermal boundary resistance in a GaN diode by means of electro-thermal Monte Carlo Simulations. Journal of Physics: Conference Series: IOP Publishing; 2015.

(78) García S, Íñiguez-de-la-Torre I, García-Pérez Ó, Mateos J, González T and Pérez S. Evaluation of the thermal resistance in GaN-diodes by means of electro-thermal Monte Carlo simulations. Electron Devices (CDE), 2015 10th Spanish Conference on: IEEE; 2015.

(79) Miranda JM, Sebastián JL, Sierra M, Margineda J. Ingeniería de Microondas. Técnicas Experimentales. Madrid: Prentice Hall. PEARSON EDUCATION, S. A.; 2002.

(80) Íñiguez-de-la-Torre A. Nanodispositivos de GaN para generación de señales de THz. Simulación Monte Carlo y experimental. Universidad de Salamanca. Salamanca: Dissertation; 2012. http://hdl.handle.net/10366/121375.

(81) Shockley W. Negative resistance arising from transit time in semiconductor diodes. Bell System Technical Journal 1954;33(4):799-826.

(82) Ridley BK, Watkins TB. The possibility of negative resistance effects in semiconductors. Proceedings of the Physical Society 1961;78(2):293.

(83) Hilsum C. Transferred electron amplifiers and oscillators. Proceedings of the IRE 1962;50(2):185-189.

(84) Gunn JB. Microwave oscillations of current in III-V semiconductors. Solid State Commun 1963;1(4):88-91.

(85) Kroemer H. Theory of the Gunn effect. Proceedings of the IEEE 1964;52(12):1736-1736.

(86) Pardo D, Bailón LA. Elementos de Electrónica. Valladolid: Secretariado de Publicaciones e Intercambio Editorial, Universidad de Valladolid; 1999.

(87) Sze SM, Ng KK. Physics of Semiconductor Devices, 3rd ed. New Jersey: Wiley & Sons, Inc., Publication; 2007.

(88) Alekseev E, Pavlidis D. Large-signal microwave performance of GaN-based NDR diode oscillators. Solid-State Electronics 2000;44(6):941-947.

(89) Kurosawa T editor. Proc. Int. Conf. Phys. of Semiconductors. Kyoto: J. Phys. Soc. Japan, Sup. A 49, 345; 1966.

(90) Kurosawa T. Monte Carlo calculation of hot electron problems. J. Phys. Soc. JPN. 1996;21:424.

(91) González T. Análisis del ruido electrónico en materiales y dispositivos semiconductores unipolares mediante el método de Monte Carlo. Universidad de Salamanca. Salamanca: Dissertation; 1994.

(92) Martín MJ. Análisis del transporte de carga y de los fenómenos del ruido electrónico en estructuras Si/Si$_{1-x}$ Gex bipolares. Universidad de Salamanca. Salamanca: Dissertation; 1996.

(93) Mateos J. Modelización microscópica del ruido electrónico en estructuras MESFET y HEMT submicrométricas. Análisis numérico y experimental. Universidad de Salamanca. Salamanca: Dissertation; 1997.

(94) Íñiguez-de-la-Torre I. Análisis de efectos de carga superficial en nanodispositivos semiconductores modelizados mediante simulaciones Monte Carlo. Universidad de Salamanca. Salamanca: Dissertation; 2008. http://hdl.handle.net/10366/19262.

(95) Rodilla H. Estudio de HEMTs basados en semiconductores de gap estrecho. Desde los materiales al dispositivo. Universidad de Salamanca. Salamanca: Dissertation; 2010. http://hdl.handle.net/10366/83172.

(96) Boardman AD editor. Computer simulation of hot electron behavior in semiconductor using Monte Carlo methods, in Physics Programs. Boardman A D ed. New York: Physics Programs; 1980.

(97) MacKay DJ. Introduction to Monte Carlo methods. Learning in graphical models: Springer; 1998.

(98) Lahoz-Beltrá R. Bioinformática: Simulación, vida artificial e inteligencia artificial. Madrid: Ediciones Díaz de Santos; 2010.

(99) Tomizawa K. Numerical Simulation of Submicron Semiconductor Devices. Boston: Artech House Materials Science; 1993.

(100) Moglestue C. Monte Carlo simulation of semiconductor devices. London: Chapman & Hall; 1993.

(101) Madelung O. Semiconductors: Data Handbook. Berlin: Springer Berlin Heidelberg; 2004.

(102) Xing H, Keller S, Wu Y, McCarthy L, Smorchkova I, Buttari D, et al. Gallium nitride based transistors. Journal of Physics: Condensed Matter 2001;13(32):7139.

(103) López E, Arriaga J, Olguín D. Cálculo de primeros principios de las propiedades electrónicas de nitruros del grupo III-V. Superficies y vacío 2004;17(1):21-26.

(104) Sadi T, Dessenne F, Thobel J. Three-dimensional Monte Carlo study of three-terminal junctions based on InGaAs/InAlAs heterostructures. J Appl Phys 2009;105(5):053707.

(105) Press WH, Flannery BP, Teukolski SA, Vetterling WT. Numerical recipes. The Art of Scientific Computing. New York: Cambridge University Press; 1989.

(106) Turin VO, Balandin AA. Electrothermal simulation of the self-heating effects in GaN-based field-effect transistors. J Appl Phys 2006;100(5):054501.

(107) Constant E. Modelling of Sub-Micron Devices. Berlin: Springer; 1988.

(108) Hess K. Monte Carlo device simulation: full band and beyond. New York: Springer Science & Business Media; 2012.

(109) Hockney RW, Eastwood JW. Computer simulation using particles. Bristol: IOP; 1988.

(110) Dunn GM, Kearney MJ. A theoretical study of differing active region doping profiles for W-band (75-110 GHz) InP Gunn diodes. Semiconductor Science and Technology 2003;18(8):794.

(111) Ramo S. Currents induced by electron motion. Proc.Ire 1939;27(9):584-585.

(112) Shockley W. Currents to conductors induced by a moving point charge. J Appl Phys 1938;9(10):635-636.

(113) He Z. Review of the Shockley-Ramo theorem and its application in semiconductor gamma-ray detectors. Nuclear Instruments and Methods in Physics Research Section A: Accelerators, Spectrometers, Detectors and Associated Equipment 2001;463(1):250-267.

(114) Kim H, Min HS, Tang TW, Park YJ. An extended proof of the Ramo-Shockley theorem. Solid-State Electronics 1991;34(11):1251-1253.

(115) Babiker S, Asenov A, Cameron N, Beaumont SP, Barker JR. Complete Monte Carlo RF analysis of “real” short-channel compound FET's. Electron Devices, IEEE Transactions on 1998;45(8):1644-1652.

(116) Yoder P, Gärtner K, Fichtner W. A generalized Ramo-Shockley theorem for classical to quantum transport at arbitrary frequencies. J Appl Phys 1996;79(4):1951-1954.

(117) Yoder P, Gärtner K, Krumbein U, Fichtner W. Optimized terminal current calculation for Monte Carlo device simulation. Computer-Aided Design of Integrated Circuits and Systems, IEEE Transactions on 1997;16(10):1082-1087.

(118) Brigham EO. The Fast Fourier Transform. New Jersey: Prentice-Hall, Inc., Englewood Cliffs, N. J.; 1974.

(119) James JF. A student's guide to Fourier transforms. Cambridge: Press Syndicate of the University of Cambridge; 1995.

(120) Bracewell RN. The Fourier Transform and its Applications. Singapore: MCGraw-Hill International Editions; 1986.

(121) Rao KR, Kim DN, Hwang JJ. Fast Fourier Transform: Algorithms And Applications. Dordrecht, Heidelberg, London, New York: Springer; 2010.

(122) Kurokawa K. Some basic characteristics of broadband negative resistance Oscillator circuits. Bell System Technical Journal 1969;48(6):1937-1955.

(123) Shur M. GaAs devices and circuits. New York: Springer; 1987.

(124) Masayuki A, Shintaro Y, Osamu W, Hirobumi T. Monte Carlo simulation of Gunn domain formations. Japanese Journal of Applied Physics 1975;14(1):70.

(125) Rydberg A. High efficiency and output power from second- and third-harmonic millimeter-wave InP-TED oscillators at frequencies above 170 GHz. Electron Device Letters, IEEE 1990;11(10):439-441.

(126) Rydberg A. A contribution to the design of wideband tunable second harmonic mode millimeter-wave InP-TED oscillators above 110 GHz. Int J Infrared Millim Waves 1990;11(3):383-404.

(127) Kamoua R. Monte Carlo-based harmonic-balance technique for the simulation of high-frequency TED oscillators. Microwave Theory and Techniques, IEEE Transactions on 1998;46(10):1376-1381.

(128) Macpherson R F, Dunn G M, Pilgrim N J. Simulation of gallium nitride Gunn diodes at various doping levels and temperatures for frequencies up to 300 GHz by Monte Carlo simulation, and incorporating the effects of thermal heating. Semiconductor Science and Technology 2008;23(5):055005.

(129) Sevik C, Bulutay C. Efficiency and harmonic enhancement trends in GaN-based Gunn diodes: Ensemble Monte Carlo analysis. Appl Phys Lett 2004;85(17):3908-3910.

(130) Gruzinskis V, Shiktorov P, Starikov E, Zhao JH. Comparative study of 200-300 GHz microwave power generation in GaN TEDs by the Monte Carlo technique. Semiconductor science and technology 2001;16(9):798.

(131) Joshi R, Sridhara V, Shah P, Del Rosario R. Monte Carlo analysis of GaN-based Gunn oscillators for microwave power generation. J Appl Phys 2003;93(8):4836-4842.

(132) Teoh YP, Dunn GM, Priestley N, Carr M. Multiple transit regions Gunn diodes. Semiconductor Electronics, 2002. Proceedings. ICSE 2002. IEEE International Conference on; 2002.

(133) Vaidyanathan R, Joshi RP. Simulations for improved heterostructure Gunn oscillator based on transit region doping variations. Electronics Letters 1991;27(17):1555-1557.

(134) Sevik C, Bulutay C. Gunn oscillations in GaN channels. Semiconductor science and technology 2004;19(4):S188.

(135) Macpherson RF, Dunn GM. The use of doping spikes in GaN Gunn diodes. Appl Phys Lett 2008;93(6):062103-062103-2.

(136) Dalle CF. Differentiated doping profile for vertical terahertz GaN transferred-electron devices. Electron Devices, IEEE Transactions on 2015; (99):1-1.

(137) Pilgrim N J, Khalid A, Dunn G M, Cumming D R S. Gunn oscillations in planar heterostructure diodes. Semiconductor Science and Technology 2008;23(7):075013.

(138) Montes M, Dunn G, Stephen A, Khalid A, Li C, Cumming D, et al. Reduction of impact ionization in GaAs-based planar Gunn diodes by anode contact design. Electron Devices, IEEE Transactions on 2012;59(3):654-660.

(139) Li C, Khalid A, Paluchowski Caldwell SH, Holland MC, Dunn GM, Thayne IG, et al. Design, fabrication and characterization of $In_{0.23}Ga_{0.77}As$-channel planar Gunn diodes for millimeter wave applications. Solid-State Electronics 2011 10;64(1):67-72.

(140) Reggiani L, Golinelli P, Faucher E, Varani L, González T, Pardo D. Proceedings of the 13th International Conference of Noise in Physical Systems and 1/f Fluctuations. Singapore: World Scientific; 1995.

(141) Wang Y, Yang L, Mao W, Long S, Hao Y. Modulation of multidomain in AlGaN/GaN HEMT-like planar Gunn diode. Electron Devices, IEEE Transactions on 2013;60(5):1600-1606.

(142) Shiktorov P, Starikov E, Gružinskis V, Pérez S, González T, Reggiani L, et al. Theoretical investigation of Schottky-barrier diode noise performance in external resonant circuits. Semiconductor Science and Technology 2006;21(4):550.

(143) Harlow JH. Electric Power Transformer Engineering, Third Edition. Florida: Taylor & Francis; 2012.

(144) Vitanov S, Palankovski V, Maroldt S, Quay R. High-temperature modeling of AlGaN/GaN HEMTs. Solid-State Electronics 2010;54(10):1105-1112.

(145) Cuerdo R, Sillero E, Romero MF, Uren MJ, Di Forte Poisson MA, Munoz E, et al. High-temperature microwave performance of submicron AlGaN/GaN HEMTs on SiC. Electron Device Letters, IEEE 2009;30(8):808-810.

(146) Wang A, Tadjer M, Calle F. Simulation of thermal management in AlGaN/GaN HEMTs with integrated diamond heat spreaders. Semiconductor Science and Technology 2013;28(5):055010.

(147) Sadi T, Kelsall R, Pilgrim N. Electrothermal Monte Carlo simulation of submicron wurtzite GaN/AlGaN HEMTs. Journal of Computational Electronics 2007;6(1-3):35-39.

(148) Mateos J, González T, Pardo D, Hoel V, Cappy A. Monte Carlo simulator for the design optimization of low-noise HEMTs. Electron Devices, IEEE Transactions on 2000;47(10):1950-1956.

(149) Mishra UK, Parikh P, Yi-Feng Wu. AlGaN/GaN HEMTs-an overview of device operation and applications. Proceedings of the IEEE 2002;90(6):1022-1031.

(150) Pilgrim N, Batty W, Kelsall R. Electrothermal Monte Carlo simulations of InGaAs/AlGaAs HEMTs. Journal of Computational Electronics 2003;2(2-4):207-211.

(151) Asgari A, Kalafi M, Faraone L. A quasi-two-dimensional charge transport model of AlGaN/GaN high electron mobility transistors (HEMTs). Physica E: Low-dimensional Systems and Nanostructures 2005;28(4):491-499.

(152) Ashok A, Vasileska D, Hartin OL, Goodnick SM. Electrothermal Monte Carlo simulation of GaN HEMTs including electron-electron interactions. Electron Devices, IEEE Transactions on 2010;57(3):562-570.

(153) Marino FA, Guerra D, Goodnick S, Ferry D, Saraniti M. RF and DC characterization of state-of-the-art GaN HEMT devices through cellular Monte Carlo simulations. Physica status solidi (c) 2010;7(10):2445-2449.

(154) Wang X, Hu W, Chen X, Lu W. The study of self-heating and hot-electron effects for AlGaN/GaN double-channel HEMTs. Electron Devices, IEEE Transactions on 2012;59(5):1393-1401.

(155) Giuliani F, Delmonete N, Cova P, Menozzi R. GaN HEMTs for power switching applications: from Device to System-Level Electro-Thermal Modeling. 2013 CSManTech,

International Conference on Compound Semiconductor MANufactoring TEChnology: MANTECH Inc.; 2013.

(156) Gao F, Lo H, Ram R, Palacios T. Self-consistent electro-thermal simulation of AlGaN/GaN HEMTs for reliability prediction. 2010.

(157) Heller E, Crespo A. Electro-thermal modeling of multifinger AlGaN/GaN HEMT device operation including thermal substrate effects. Microelectronics Reliability 2008;48(1):45-50.

(158) Liyuan Y, Shan A, Yonghe C, Mengyi C, Kai Z, Xiaohua M, et al. A self-heating study on multi-finger AlGaN/GaN high electron mobility transistors. Journal of Semiconductors 2013;34(7):074005.

(159) Ferrer JA. Thermal study of a GaN-based HEMT. Notre Dame, Indiana: Thesis work; 2012.

(160) Rodilla H, González T, Pardo D, Mateos J. High-mobility heterostructures based on InAs and InSb: A Monte Carlo study. J Appl Phys 2009;105(11):113705.

(161) Asbeck P, Yu E, Lau S, Sullivan G, Van Hove J, Redwing J. Piezoelectric charge densities in AlGaN/GaN HFETs. Electron Lett 1997;33(14):1230-1231.

(162) Yu E, Dang X, Asbeck P, Lau S, Sullivan G. Spontaneous and piezoelectric polarization effects in III-V nitride heterostructures. Journal of Vacuum Science & Technology B 1999;17(4):1742-1749.

(163) Fiorentini V, Bernardini F, Ambacher O. Evidence for nonlinear macroscopic polarization in III-V nitride alloy heterostructures. Appl Phys Lett 2002;80(7):1204-1206.

(164) Miller E, Yu E, Poblenz C, Elsass C, Speck J. Direct measurement of the polarization charge in AlGaN/GaN heterostructures using capacitance-voltage carrier profiling. Appl Phys Lett 2002;80(19):3551-3553.

(165) Gold A. Electronic transport properties of a two-dimensional electron gas in a silicon quantum-well structure at low temperature. Physical Review B 1987;35(2):723.

(166) Bolognesi C, Kroemer H, English J. Interface roughness scattering in InAs/AlSb quantum wells. Appl Phys Lett 1992;61(2):213-215.

(167) Smirnov BM. Principles of Statistical Physics: Distributions, Structures, Phenomena, Kinetics of Atomic Systems. Weinheim: Wiley; 1989.

(168) Sadi T, Kelsall RW. Hot-phonon effect on the electrothermal behavior of submicrometer III-V HEMTs. Electron Device Letters, IEEE 2007;28(9):787-789.

(169) Liu W, Balandin AA. Temperature dependence of thermal conductivity of $Al_xGa_{1-x}N$ thin films measured by the differential 3ω technique. Appl Phys Lett 2004;85(22):5230-5232.

(170) Sarua A, Ji H, Hilton KP, Wallis DJ, Uren MJ, Martin T, et al. Thermal boundary resistance between GaN and substrate in AlGaN/GaN electronic devices. Electron Devices, IEEE Transactions on 2007;54(12):3152-3158.

(171) Muzychka YS, Bagnall KR, Wang EN. Thermal spreading resistance and heat source temperature in compound orthotropic systems with interfacial resistance. Components, Packaging and Manufacturing Technology, IEEE Transactions on 2013;3(11):1826-1841.

(172) Mion C. Investigation of the thermal properties of gallium nitride using the three omega technique. North Carolina State University, United States: Thesis work; 2005.

(173) Shrestha NM, Wang YY, Li Y, Chang E. Simulation study of AlN spacer layer thickness on AlGaN/GaN HEMT. Himalayan Physics 2013;4:14-17.

(174) Ganguly S, Verma J, Xing HG, Jena D. Plasma MBE growth conditions of AlGaN/GaN high-electron-mobility transistors on silicon and their device characteristics with epitaxially regrown ohmic contacts. Applied Physics Express 2014;7(10):105501.

(175) Hasegawa H, Akazawa M. Current transport, Fermi level pinning, and transient behavior of group-III nitride Schottky barriers. Journal of Korean Physical Society 2009;55:1167.

(176) Okita H, Kaifu K, Mita J, Yamada T, Sano Y, Ishikawa H, et al. High transconductance AlGaN/GaN-HEMT with recessed gate on sapphire substrate. Physica status solidi (a) 2003;200(1):187-190.

(177) Juncai M, Jincheng Z, Junshuai X, Zhiyu L, Ziyang L, Xiaoyong X, et al. Characteristics of AlGaN/GaN/AlGaN double heterojunction HEMTs with an improved breakdown voltage. Journal of Semiconductors 2012;33(1):014002.

(178) Kuball M, Rajasingam S, Sarua A, Uren M, Martin T, Hughes B, et al. Measurement of temperature distribution in multifinger AlGaN/GaN heterostructure field-effect transistors using micro-Raman spectroscopy. Appl Phys Lett 2003;82(1):124-126.

(179) Aubry R, Jacquet J, Weaver J, Durand O, Dobson P, Mills G, et al. SThM temperature mapping and nonlinear thermal resistance evolution with bias on AlGaN/GaN HEMT devices. Electron Devices, IEEE Transactions on 2007;54(3):385-390.

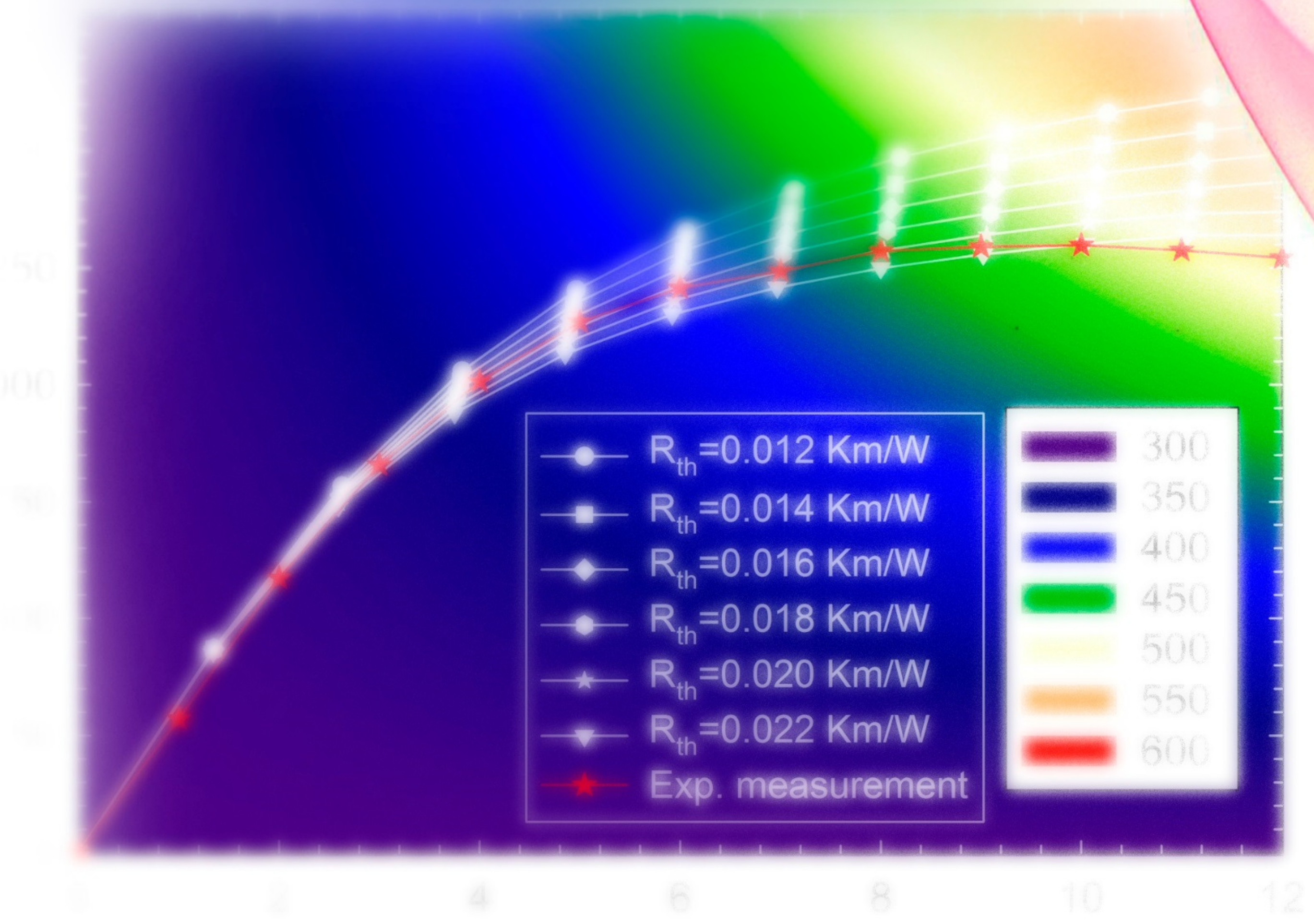
R_{th}=0.012 Km/W
R_{th}=0.014 Km/W
R_{th}=0.016 Km/W
R_{th}=0.018 Km/W
R_{th}=0.020 Km/W
R_{th}=0.022 Km/W
Exp. measurement
300
350
400
450
500
550
600
0
2
4
6
8
10
12